NEW TOOLSETS TO UNDERSTAND ENVIRONMENTAL SENSATION AND VARIABILITY IN THE AGING PROCESS

A Dissertation
Presented to
The Academic Faculty

By

Mei Zhan

In Partial Fulfillment
Of the Requirements for the Degree
Doctor of Philosophy in Bioengineering

Georgia Institute of Technology

December 2014

NEW TOOLSETS TO UNDERSTAND ENVIRONMENTAL SENSATION AND VARIABILITY IN THE AGING PROCESS

Approved by:

Dr. Hang Lu, Advisor
School of Chemical and Biomolecular Engineering
Georgia Institute of Technology

Dr. Robert Butera
School of Electrical and Computer Engineering
Georgia Institute of Technology

Dr. Philip Santangelo
Wallace H. Coulter Department of Biomedical Engineering
Georgia Institute of Technology

Dr. Patrick McGrath
School of Biology
Georgia Institute of Technology

Dr. Harold Kim
School of Physics
Georgia Institute of Technology

Dr. QueeLim Ch'ng
MRC Centre for Developmental Neurobiology
Kings College London

Date Approved: November 7, 2014

ACKNOWLEDGEMENTS

This work owes immensely to the advice, support, encouragement and, at times, forbearance of my advisor, Hang Lu. I would also like to thank my wonderful partner in nearly everything, Dhaval Patel, for keeping me happy, fed and entertained during this time (harder than it sounds, especially at a distance). Also, I am grateful to all of my friends, loved ones and work colleagues (not mutually exclusive categories) who have supported me through the years. In particular, I would like to thank Loice Chingozha, Kwanghun Chung, Jeffrey Stirman and Matt Crane, whose intellectual and emotional support have been instrumental to the completion of this work. Additionally, I would like to thank Tom Levario for helping to keep the lab running smoothly and making it a more entertaining work environment. Finally, I am grateful to Rochelle Moses, Brad Parker and Jeff Andrews for providing critical support and picking up some of the balls I inevitably drop.

TABLE OF CONTENTS

LIST OF TABLES

LIST OF FIGURES

SUMMARY

Aging is a complex process by which a combination of environmental, genetic and stochastic factors generate whole-system changes that modify organ and tissue function and alter physiological processes. Over the last few decades, many genetic and environmental modulators of aging have been found to be highly conserved between humans and a diverse group of model organisms. Yet, an integrative understanding of how these environmental and genetic variables interact over time in a whole organism to modulate the systemic changes involved in aging is lacking. The goal of this thesis project is to advance a systems perspective of aging by providing the experimental tools and conceptual framework for dissecting the regulatory connection between environmental inputs, molecular outputs and long term aging phenotypes in *Caenorhabditis elegans*, an experimentally tractable multi-cellular model for aging.

Specifically, this work advances the quantitative imaging toolsets available to biologists by developing and refining microfluidic, hardware, computer vision, and software integration tools for high-throughput, high-content imaging of *C. elegans*. Compared to previously described imaging systems, significant engineering improvements to the components themselves and to the integration and interfacing of these components at the systems level were made. By facilitating scalability in the manufacture of these technologies and dramatically improving their operational robustness, these improvements have enabled the dissemination and utilization of these technologies by non-experts. As a result of these technological advances, new roles for the TGF-beta and

serotonin signaling pathways in encoding environmental food signals to influence longevity were uncovered and quantitatively characterized.

Moreover, this work develops and integrates new microfluidic technologies with off-chip support systems to establish a platform for long-term tracking of the health and longevity trajectories of large numbers of individual *C. elegans*. The capabilities of this platform have the potential to address many important questions in aging including addressing environmental determinants of aging, the sources of inter-individual variability, the time course of aging-related declines and the effects of interventional strategies to improve health outcomes. Together, the toolsets for quantitative imaging and the long-term culture platform permit the large-scale investigation of both the internal state and long-term behavioral and health outputs of an important multicellular model organism for aging.

CHAPTER 1: INTRODUCTION AND BACKGROUND

The aging process, both in terms of absolute longevity and the physiological integrity of an organism as it ages, has important consequences for human health and society. Yet, aging is a complex process by which a combination of environmental, genetic and stochastic factors generate whole-system changes that modify organ and tissue function and alter physiological processes. The extent and diversity of the potential extrinsic environmental and lifestyle inputs into this process, a similarly large list of potential intrinsic genetic and epigenetic modulators, and the necessity to observe long-term and often subtle outputs has made aging intrinsically difficult to study in human or mammalian models. Compounding these problems, aging and longevity is subject to large individual-to-individual variability (Figure 1.1). While some of the variability in humans may be due to a combination of underlying lifestyle and genetic factors (Figure 1.1a), substantial variability persists even when these factors are controlled in model organisms (Figure 1.1b), suggesting other poorly understood sources of underlying biological variability (*1-3*). Dissecting these components of lifespan variability and potentially opening them up to clinical intervention thus requires large-scale longitudinal aging studies with careful control of both lifestyle and genetic contributions.

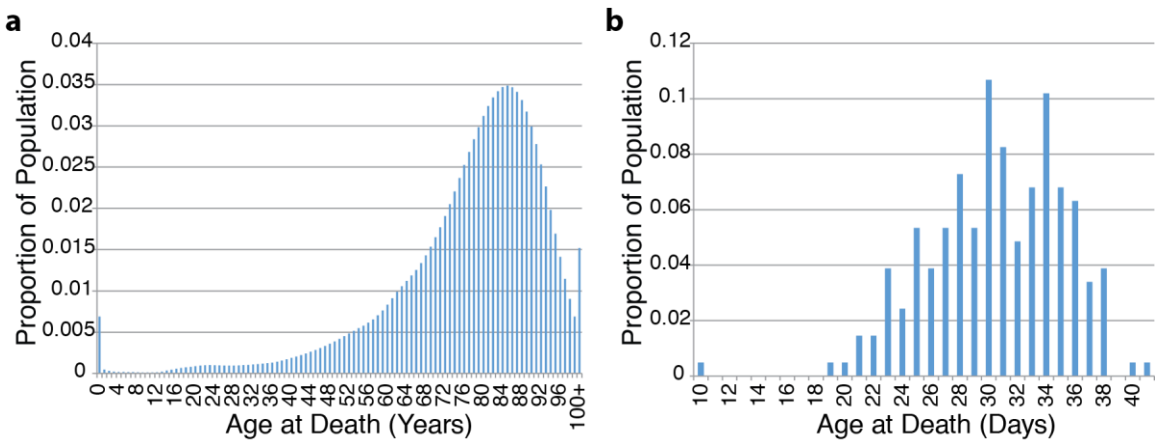

Figure 1.1: Both human populations subject to underlying genetic and lifestyle differences (a) and genetically and environmentally controlled laboratory populations of *Caenorhabditis elegans* (b) exhibit significant individual to individual variability in longevity outcomes. Data in (a) based on total mortality in the US population for 2005 from CDC National Vital Statistics. Data in (b) contributed by Dr. Eugeni Entchev and Dr. Dhaval Patel.

Due to the intrinsic difficulty of controlling critical environmental and genetic experimental variables in mammals, much of our mechanistic understanding of the aging process has been derived from studies in more tractable model organisms. From initial results from simple models such as yeast, worms and flies, subsequent studies have pointed to a high degree of conservation for many mechanisms of aging modulation (*4-7*). Over the last few decades, many genetic components of aging have been found to be highly conserved between humans and a diverse group of model organisms (*4*, *5*). Moreover, many conserved environmental modulators of aging, including diet and temperature, have been discovered (*7-9*). To begin to understand how these genetic and environmental modulators interact in an integrative way, some of the genetic targets that sense, store and translate environmental signals into lifespan alterations have started to be characterized in model organisms.

In particular, the nematode *Caenorhabditis elegans* serves as an extremely convenient multicellular model system for aging. Its ease of culture and amenability to genetic manipulation permit a high degree of control over both environmental and genetic factors. Moreover, its optical transparency permits minimally invasive, *in vivo* assessment of gene activity and other functional outputs via the use of fluorescent reporters and biosensors. Finally, the multicellular nature of *C. elegans* permits the modeling of complex inter-cellular and inter-tissue responses and observation of changes in functional behavior and mobility that would be impossible to appreciate within even simple single-cell models. Thus, the worm, *C. elegans*, serves as a model system for aging that encapsulates both sufficient levels of biological complexity and experimental tractability.

Yet, despite the identification of some important modulators of aging and the availability of a tractable model organism, an integrative understanding of how environmental and genetic variables interact over time in a whole organism to modulate the systemic changes involved in aging is lacking. In part, the large-scale longitudinal studies necessary to address questions of gene-environment interactions and biological variability have been hindered by the inability of existing experimental tools to address the specific experimental challenges of a multicellular model such as *C. elegans*. In particular, some of the same traits that make the worm an attractive model organism, such as its small size and its relatively short lifespans, have simultaneously posed particular experimental challenges such as difficulty of manipulation and necessity for high temporal resolution (Table 1.1). Moreover, the millimeter-long nematode is not

compatible with many existing commercial toolsets for single-cell studies, requiring the development of new hardware tools to serve some of the same experimental functions. Dissecting relevant cell- or tissue-specific information from the multicellular worm also poses diverse, experiment-specific image processing problems that have been difficult to address to current ready-to-use image processing packages.

Table 1.1: Traits of C. elegans as a model organism results in both intrinsic experimental advantages and challenges.

Traits	Experimental Advantages	Experimental Challenges
Small (~1 mm long)	Allows for large-scale, rapid experimentation	Difficulty of physical manipulation
Short Lived (2-3 weeks)		Necessity for high temporal resolution
Freely Moving	Permits modeling of complex inter-cellular and inter-tissue responses and meaningful behavioral metrics for healthspan	Diffculty of tracking individual worms for longitudinal assays
Multicellular		Not generally compatible with tools available for single cells
Optically Transparent	Imaging-based cell- and tissue-specific readout of functional information from intact worms	High-content imaging data sets that require extraction of relevant information
Easily genetically manipulated		
Availability of genetically encoded fluorescent proteins		

The work presented in this thesis is aimed at advancing a systems perspective of aging by providing the experimental tools and conceptual framework for dissecting the regulatory connection between environmental inputs, molecular outputs and long term aging phenotypes. To address the aforementioned experimental challenges, this work applies and integrates microfluidics and computer vision techniques to develop two automated experimental platforms capable of dissecting cell-specific functional readouts in *C. elegans* via fluorescence imaging and following the long term health trajectories of individual *C. elegans* as it ages. This work also demonstrates the application of some of

these tools towards understanding the genetic mechanisms of diet-induced modulation of longevity in *C. elegans*. The following sections serve to broadly contextualize and highlight the overall significance of the work presented in this thesis by briefly reviewing the history of aging studies in *C. elegans* and introducing the limitations of previously available methods for experimental investigation in the worm.

1.1: *C. elegans* as a Model for Aging

The aging process is modulated by genetic and environmental variables. Genetically, the early discovery of extreme longevity in *C. elegans daf-2* insulin receptor mutants (*10*) has led to the discovery of a conserved insulin pathway that regulates aging in other invertebrates and mammals (*4, 5*). Since then, many other genetic modulators of lifespan have been characterized (*5, 11, 12*). Environmentally, a broad range of model organisms have been found to respond to food and temperature manipulations in similar ways. Specifically, dietary restriction has been demonstrated to increase lifespan in yeast, *C. elegans, Drosophila melanogaster* and mammalian models (*7*). Similarly, modulating body temperature has been shown to have similar lifespan responses in both invertebrate and mammalian models (*8, 9*).

In the discovery of these mechanisms underlying aging, the nematode *C. elegans* has undoubtedly been the source of the most information. Importantly, its short (2-3 week) lifespan enables rapid lifespan analysis while its hermaphroditic reproduction permits the generation of large isogenic populations for lifespan assays. Moreover, it is extremely susceptible to genetic manipulation and its optical transparency permits visualization of intermediate aging phenotypes.

In *C. elegans*, there is evidence that the link between environmental variables and lifespan is based on active sensation by genetic components and subject to regulation. Mutants with defects in the sensory cilia and environmental perception have been shown to have increased lifespans (*13*) and ablation of specific sensory neurons also produce lifespan phenotypes (*14*). Moreover, the lifespan response to environmental temperature has been shown to be modulated by the presence of thermosensory neurons (*8*). The transcriptional activity of several lifespan-altering genes has also been found to be environmentally responsive (*15-21*). In particular, abundance of *tph-1* and *daf-7* have been shown to be both food and temperature responsive (*16, 18*) and implicated to have functional connections to the *daf-2* insulin signaling pathway that is a conserved modulator of lifespan (*11, 17*). The *tph-1* gene encodes the serotonin-synthesizing enzyme tryptophan hydroxylase and is specifically expressed in the ciliated sensory ADF neuron pair and in the NSM neuron pair. The level of *tph-1* transcriptional activity in the ADF neurons has previously been implicated in mediating serotonin-dependent environmental stress responses via the *daf-2* insulin pathway (*17*). The *daf-7* gene encodes a member of the TGF-beta superfamily that is expressed in the ciliated sensory ASI neurons. The responsiveness of daf-7 transcriptional activity to environmental conditions has been established in early developmental decision-making (*18, 19*). Recently, its role in mediating longevity responses via the insulin signaling pathway has been uncovered (*11*).

1.2: Conventional Approaches for Experimental Investigation of C. elegans

C. elegans has many intrinsic experimental advantages that make it a particularly attractive model organism for the study of the genetic and environmental regulation of aging. In particular, its optical transparency permits readouts of transcriptional activity and other phenotypes via non-invasive fluorescent imaging techniques. However, the micron-scale worm is at a size scale below that of effective human manipulation, making handling and imaging of large populations difficult. Traditionally, *C. elegans* have been subjected to high resolution imaging via mounting and anesthetization on a thin agar pad (*22*). Using this technique, a small population of tens of animals can be quickly mounted via pipetting or picking. However, the resulting arrangement and orientation of worms on the slide tend to be haphazard, resulting in occasionally poor and variable imaging results. While worms can also be carefully manually manipulated into more desirable positions and orientations, this process is tedious and time-consuming, limiting the number of animals that can be imaged without a reasonable experimental time frame. Finally, in both cases, recovery of animals from the imaging pad is also time-consuming and animals may be subject to physiological alterations due to anesthetic exposure.

At this time, only one commercially available system permits high throughput imaging of *C. elegans*. The COPAS system is a modified flow cytometer that allow fluorescent readouts along the anterior-posterior axis of the animal and sorting of populations based on these imaging readouts (*23*). The advantages of the COPAS system has enabled intensity based sorting in *C. elegans* and has been a critical enabling technique in previous studies on phenotypical variability in the worm (*24*, *25*). However, the

fluorescent readouts of the COPAS system is inherently low resolution, eliminating the possibility for reading cell- or tissue- specific signals. This is a major limitation as most phenotypes of interest in a multicellular model require higher resolution images with more sophisticated signal readouts.

Owing to its small size, hermaphroditic reproduction, large brood size, low culture requirements and short lifespan, *C. elegans* also has the potential to enable highly genetically controlled, large-scale aging experimentation. However, the limitations of conventional culture techniques available for *C. elegans* have hindered the ability to both control environmental variables and work with large populations in a longitudinal way. In the laboratory, populations of worms are typically maintained on Nematode Growth Medium (NGM) agar plates. While individual worms can be cultured separately, this is costly in terms of materials, time and space. Thus, worms are typically maintained as small populations for lifespan assays, prohibiting truly longitudinal data acquisition. Furthermore, the natural behaviors of the freely moving worm can occasionally result in individuals escaping from the agar surface under unfavorable environmental conditions. These experimental limitations fundamentally limit the potential scale of each study and the robustness of the culture technique for different environmental conditions.

While food and temperature have been identified as important modulators of aging in *C. elegans (7, 8)*, the ability to precisely control these inputs is also fundamentally limited using standard techniques. As a food source, the NGM plates are spotted with liquid cultures of specific bacterial strains such as *Escherischia coli* OP50. These spots are then allowed to dry and grow into a confluent bacterial lawn on the agar. To control for

environmental food supply, liquid bacterial cultures can be adjusted to defined concentrations prior to seeding and the NGM media can be altered and supplemented with antibiotics to inhibit unwanted bacterial growth (*26*). However, the final concentrations of bacteria on plate may not be well defined due to uneven or inconsistent drying of the plates, the potential for continued bacterial growth and continual depletion of the food source with time.

To control for temperature, these plates are typically kept in standard incubators maintained at set temperatures typically ranging from 15°C to 25°C. Inspecting the worms for lifespan or healthspan metrics or transferring worms to different plates to maintain food concentration using a microscope thus requires disruption of temperature control. Along with the time-consuming nature of manual inspection and worm transfer, this inability to continuously maintain environmental control fundamentally limits the temporal resolution of assays. As a result of these limitations, lifespan studies in *C. elegans* have typically been limited to population studies of tens of worms with only daily time resolution.

1.3: Microfluidic Approaches for Experimental Investigation of *C. elegans*

To address the fundamental limitations of macro-scale traditional handling techniques for micro-scale biological specimens, miniaturization of experimental platforms using microfabrication techniques has gained popularity (*27*). Specifically, microfluidics describes a subclass of microtechnologies that handle small volumes of liquids and control flow at the micro-scale. Although the term is generally applied to any system involving micro-scale liquid handling, one of the most common realizations in biological

applications involves the use of standard photolithographic processes to form micron-scale features on a silicone substrate, which is then used to mold these features in elastomeric materials (*28*). In particular, the soft elastomer polydimethylsiloxane (PDMS) has gained popularity as a microfluidics material in biological applications due to its biocompatibility and tunable mechanical properties (*29*).

The capability for producing features at the micron-scale allows for the design of experimental platforms on the same size scales with the specimens and phenomena of interest. Along with highly controllable transport phenomena associated with operating at small scales, this can also often result in a higher degree of environmental control with lower reagent consumption. Importantly, technologies have also been developed to allow for active manipulation of flow and specimens on chip, bridging the size-scales of active human manipulation with the size-scales of the specimens of interest. One of the foundational principles underlying various types of on-chip actuators has been the pneumatically driven membrane, which can form on-chip valves to gate flow paths in a controlled manner (Figure 1.2a) (*30, 31*).

Many groups have applied these microfluidics capabilities to address specific experimental challenges for *C. elegans*. Specifically, to address the need for both high throughput and high resolution imaging of individual worms, many specific toolsets have been developed for handling large populations worms for imaging in conventional microscopy setups (*32-38*). In general, these devices leverage the availability of on-chip valves (*30*) for serial positioning of individual *C. elegans* within a fixed field of view (Figure 1.2b). Many of these tools can also facilitate sorting of individual worms based

on imaging results (Figure 1.2c) and allow for functionality similar to flow cytometry. Moreover, the micro-environmental control enabled by microfluidics has enabled the use of non-anesthetic immobilization techniques for the worm such as cooling, carbon dioxide and compression (*32*, *34-36*). Together, these developments demonstrate the viability of critical concepts for high throughput, minimally invasive collection of imaging data from large populations of *C. elegans*. However, despite these conceptual advances, these tools often lack fabrication and operational robustness, resulting in a poor success rate in practice. Furthermore, these tools require off-chip hardware and software support systems to integrate on-chip actuation with image acquisition. The difficulty of adapting and transporting these support systems to different lab environments have hindered adoption of these tools. As a result, these technologies have mainly been utilized within the hands of the technology developers themselves.

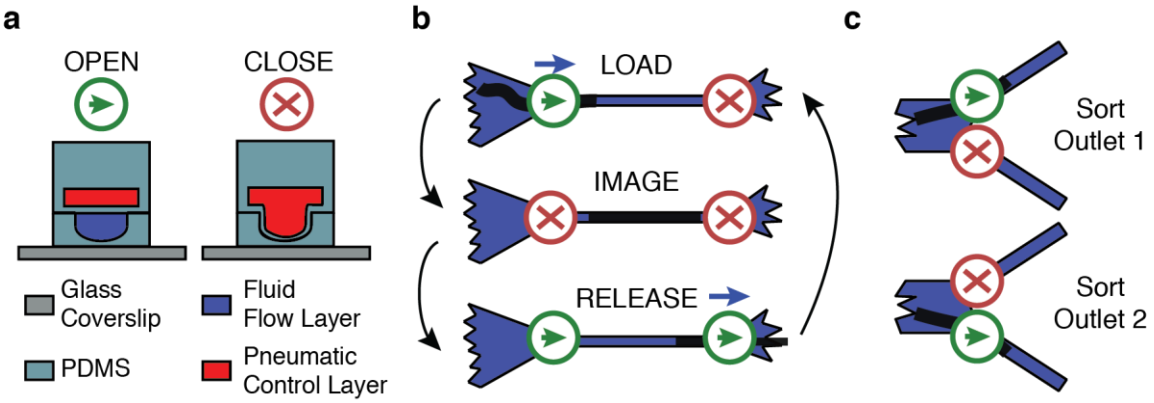

Figure 1.2: Schematic overview of microfluidics technologies for high-throughput serial worm imaging. a) Schematic of traditional microfluidic control valves utilize pressure-induced deflection of a PDMS membrane. b) Sequence of operation for sequencing loading, imaging and releasing worms in a microfluidic device using valve actuators. c) Downstream capability for sorting worms into different outlets depending on imaging results.

In addition to toolsets facilitating high resolution imaging, microfluidics tools have also been developed to assess functional outputs such as neuronal responses to specific stimuli and behavior, which may contribute to assessments of organismal health with age (*39-43*). To address longevity, platforms have also been adapted to permit long-term culture of *C. elegans* on chip via perfusion of the bacterial food source suspended in liquid media (*44-46*). While some of these long-term culture platforms demonstrate the capacity for longitudinal tracking of individual worms (*44, 45*), the hardware requirements associated with these platforms are not compatible with scaling up for higher sample sizes or a large range of experimental conditions. Moreover, none of these tools demonstrate the capacity for controlling environmental temperature.

1.4: Image Processing Approaches for Data Extraction in *C. elegans*

The potential capability for high throughput, high resolution imaging permits the extraction of many sophisticated imaging readouts from large data sets. However, the large data sets that are enabled by new experimental technologies puts the bottleneck of discovery on the data processing end. Information within these imaging datasets may also surpass the human ability for objective visual processing and be difficult to consistently ascertain using manual processing. Moreover, to realize the full capabilities of many new tools, it is advantageous to facilitate high throughput decision-making using automated image processing. Thus, software capabilities for unsupervised extraction of relevant data from biological images serve a critical role in facilitating the intrinsic functionality and effective utilization of new experimental hardware.

To address the need for both fast and objective biological image processing, ready-to-use toolsets have been developed to address some general needs of biologists (*47-49*). While much development have been focused on single-cell studies (*47*), some of these have been extended to perform general quantification functions in the worm (*48*). Other worm-specific toolsets have also been developed to address specific needs such as assessing growth, behavioral classification and worm tracking (*42, 50-53*).

Despite the availability of technologies to serve common image processing needs in the worm, the diverse range of biological experimentation in the worm and biological communities poses many specific image analysis problems that are beyond the scope of these general toolboxes. To enable problem-specific data extraction and decision-making, computer vision techniques such as Support Vector Machines (SVM) have been applied to extract readouts of interest and perform real-time experimental decision-making (*37, 54*). However, the resulting image analysis algorithms tend to be highly specific, requiring alteration for use in other experimental contexts. Compounding this problem, there is also no clear way by which the computer vision techniques can be applied to alter or develop new tools to address specific problems on the part of the end-user.

1.5: Thesis Contributions and Significance

These thesis provides a collection of microfluidic, hardware and software technologies to address the experiment challenges hindering large-scale, longitudinal tracking of health and longevity of individual worms. In addition to the development and validation of these technologies, this work demonstrates the utilization of the combination of these technologies to derive new biological insight about the mechanisms of food sensation in

modulating longevity. Moreover, this work demonstrates the construction of robust, integrated systems that have been disseminated and successfully used in the hands of non-engineers in the course of this work. Thus, in addition to serving the immediate aims of the work presented here, the hardware and software packages developed in the course of this work have the potential to facilitate wider adoption of microfluidic technologies in biology labs.

The work here also presents several conceptual advances for the general microfluidics and biological communities. For the microfluidics community, this work extends the design and application of single layer microfluidic valves, which have the capability to both increase the potential range of microfluidic functionality and increase the fabrication and operational robustness of existing technologies. For the biological community at large, this work presents a new image processing framework capable of address many problems in biological image processing. Finally, for the *C. elegans* community in particular, this work presents a new micro-scale multi-well experimental platform for *C. elegans* which is capable of robustly isolating individual worms within discrete chambers over a long period time. Additionally, this work provides a toolset that allows for precise temperature control of microfluidic chips alongside continuous monitoring using darkfield microscopy. These technologies provide a degree of environmental control that was not easily accessible for microfluidic platforms before and permit higher temporal resolution of experimental studies without disruption of environmental control. Overall, the applications of the technologies in this work go well beyond the study of aging

process and the work in this thesis presents a significant advance to the microfluidics and biological toolbox in general.

CHAPTER 2: INTEGRATED MICROFLUIDIC SYSTEMS FOR HIGH-THROUGHPUT IMAGING OF *C. ELEGANS*

2.1: Introduction

While many chip designs have been introduced to accelerate different forms of experimentation in *C. elegans* (*55*), the demonstration of these technologies are usually based on limited studies performed without the laboratory of the technology developers themselves. In this context, issues of fabrication and operational robustness and common failure modes are not particularly relevant or widely discuss due to the existence of on-site fabrication and expert troubleshooting capabilities. However, the yield of functional devices from the fabrication process and the design of friendly user interfaces that address common errors and failure modes is vital to the dissemination of these chips outside of the hands of technologists. Thus, the ultimate impact of microfluidic technology concepts depends on refinement of early designs and the integration of new functions in a way that facilitates robustness and usability.

Additionally, accessing the capabilities of microfluidic chips in practice often requires many chip-extrinsic systems that support the functions of the chip itself. Much of the time, the hardware and software support systems that truly comprise a full microfluidics system are presented conceptually as in Figure 2.1 and are not developed in a physical manifestation that is easily disseminated to other labs or users without an engineering background. Conversely, the commercialization and general adoption of microfluidic digital PCR technologies relied on the development of a packaged system for robustly

interfacing with the digital PCR chip (*56*). Thus, expanding the adoption of other microfluidic technologies in general will likely require the development of some generalizable, packaged off-chip support systems that extend public access to and understanding of these systems beyond the concept stage.

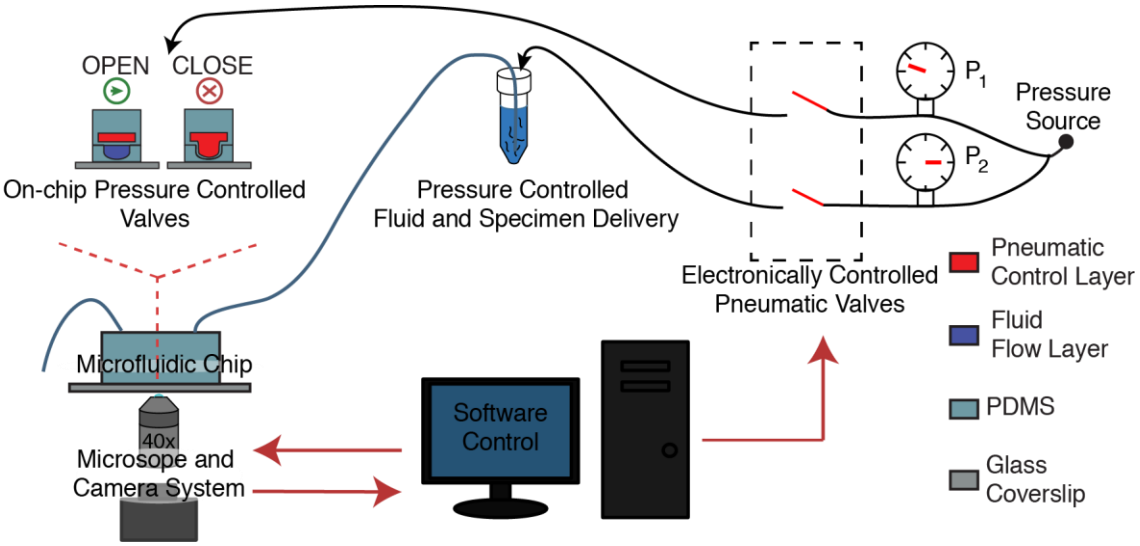

Figure 2.1: Conceptual overview of a microfluidics system. The utility of the microfluidic chip requires the coordination of different off-chip hardware systems via software control.

This chapter will discuss the development of both on-chip features and off-chip hardware and software support systems to address some of the issues associated with technology dissemination. While the discussion here will focus around the refinement of technologies for high-throughput serial worm imaging conceptualized in Figure 1.2, many of the specific developments here are generalizable to different chip designs and have been adopted for other purposes within the laboratory.

2.2: Optimizing and Increasing On-Chip Functionality

2.2.1: The Single Layer Valve and Increasing On-Chip Functionality

The capability to actively control flow on microfluidic chips using microfabricated valves has become a critical part of microfluidic chip design (*30*). It is a critical enabling technology for the function of previously published serial imaging devices (Figure 1.2) (*32, 33, 35-37, 54*). However, the traditional microfluidic valve, which fully occludes flow in a channel as shown in Figure 1.2a, is not ideal for controlled loading of biological specimens. While closure of the valve is necessary to physically define the position of the loaded specimen, the complete restriction of flow by the valve precludes entry of the specimen in the first place. Thus, secondary flow paths such as those shown in Figure 2.2a have to be created to permit entry of the specimen (*32*). In addition to requiring additional design features, the traditional microfluidic valve involves a complicated fabrication process that requires the assembly of three different components fabricated in polydimethylsiloxane (PDMS) (Figure 2.2b, Appendix A). Furthermore, in the fabrication process, a film of PDMS is left in the optical pathway, which can induce imaging aberrations (Figure 2.2b) (*57-59*).

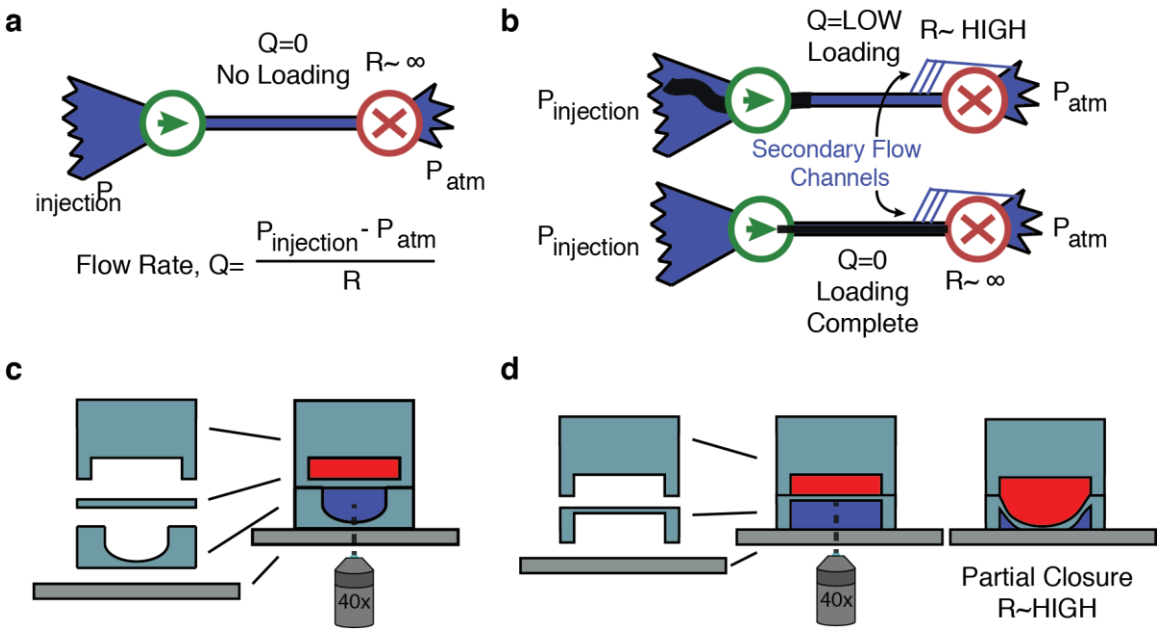

Figure 2.2: Utilization of microfluidic valves for worm handling. a) Tradition full closure microfluidic values do not permit direct loading due to complete flow obstruction. b) Addition of secondary flow channels facilitate loading. c) Fabrication and optical pathway of traditional full closure valves. d) Fabrication and optical pathway of simplified partial closure valves.

To combat the flow and optical problems, previous work in the laboratory of Dr. Hang Lu have resulted in the development partial closure valves for worm handling applications (Figure 2.2c). While this design obviates the need for secondary flow channels and leaves an unobstructed optical path between the coverslip and the worm itself, the fabrication process still requires the precise assembly of two components fabricated in PDMS (Figure 2.2d, Appendix A.3).

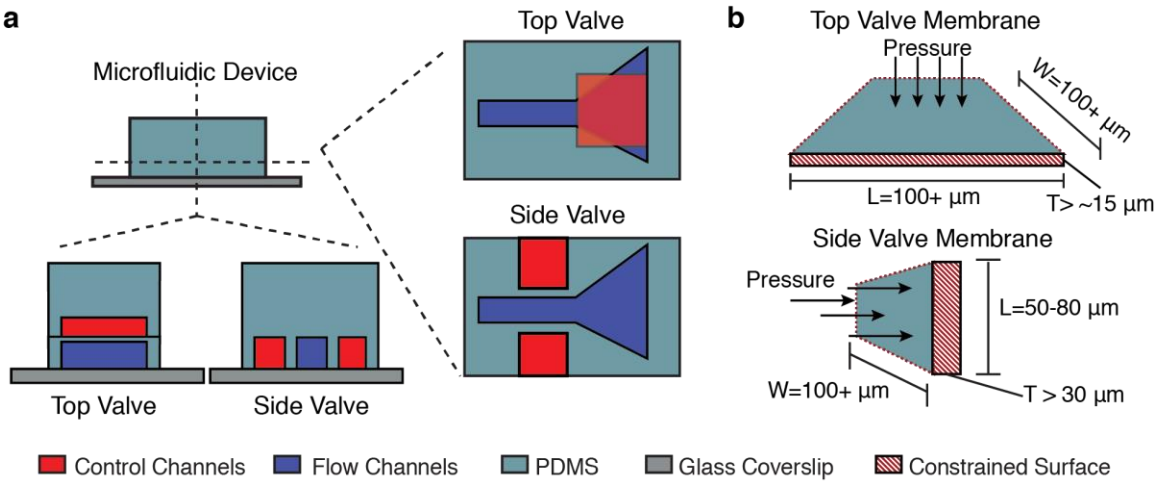

Figure 2.3: Physical constraints of laterally deflected membranes. a) Schematic comparison of top and side valves for controlling flow in microfluidic devices. b) Physical constraints of membranes for top and side valves. Membranes for second layer (top) valves afford more dimensional flexibility to allow higher deflections in comparison to lateral (side) valves.

To permit fast and robust fabrication of devices, fabrication of active membranes in a single PDMS molding process is ideal (Figure 2.3a). However, the ability to fabricate effective membranes with single-step molding is limited by several constraints (Figure 2.3b). First, one of the dimensions of the membrane is fundamentally limited by the height of the microfabricated channel. In practice, this height is constrained both by the size of the worm and the height limitations of the fabrication process. Typically, imaging devices must be 50 to 80 µm tall to enable effective handling of adult worms. Second, the thinness of the membrane is limited by the resolution of the micro-fabrication process. For features 50 to 80 µm tall, the minimum thickness of a membrane is typically 30 µm. Thus, as shown in Figure 2.3b, the dimensions of a single layer membrane is inherently more restrained in a way that is less conducive to effective deflection under pressure. Finally, the pressures that can be applied to a single layer membrane is also

fundamentally limited by the strength of the bond between PDMS and glass. Typically, reliable operation requires that these pressures be maintained under 40 psi.

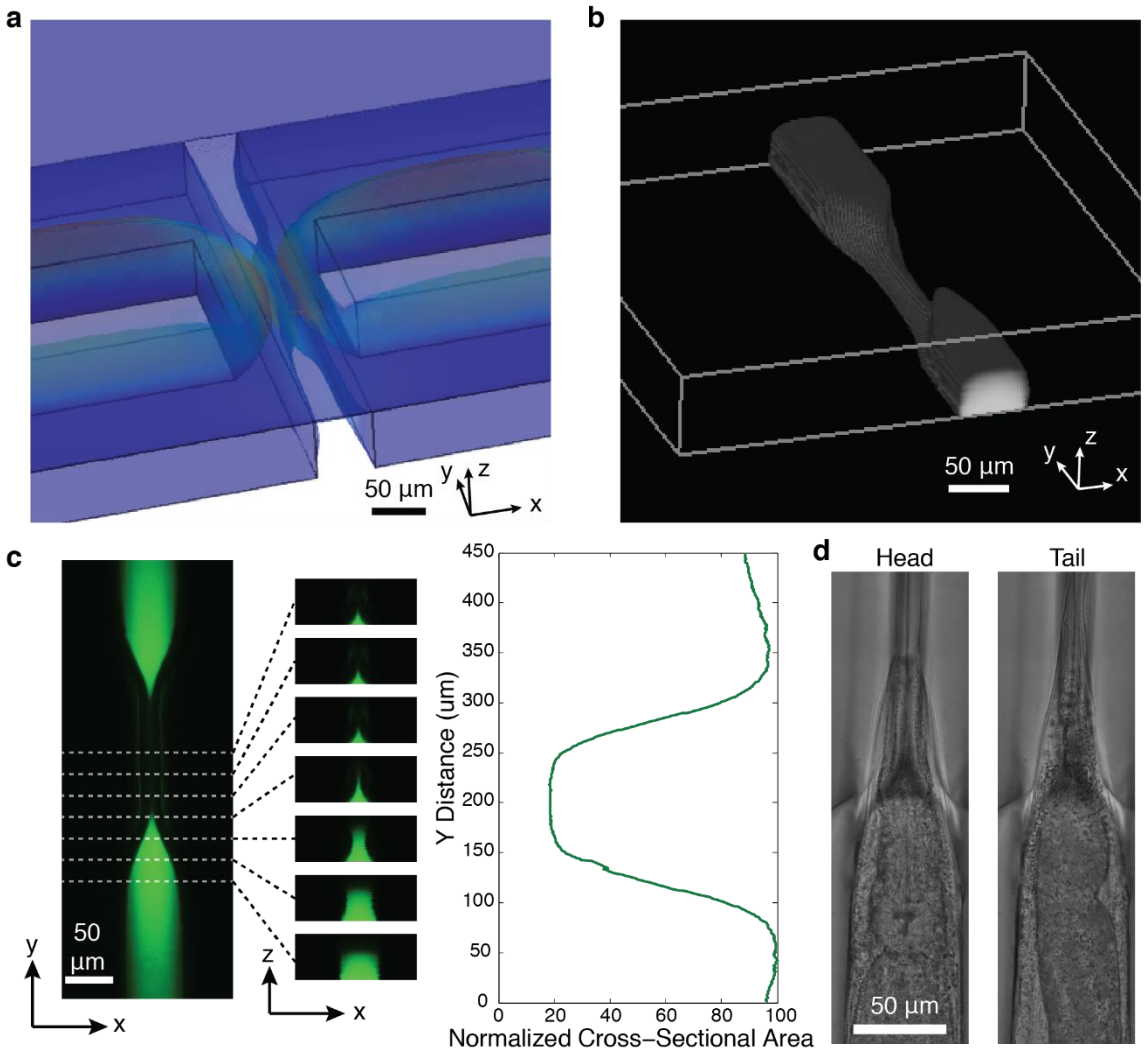

Figure 2.4: Laterally deflected membranes for single layer loading of *C. elegans*. a) Finite element model in COMSOL showing the ability of two opposing membrane structures to obstruct a flow path. b) Three dimensional reconstruction of confocal images showing a channel filled with FITC solution obstructed by a pair of laterally deflected membranes. c) Visualization of effect valve closure derived from confocal images showing a tapered closure of the channel. d) The tapered profile of side valve closure effective traps the head or the tail of a worm.

However, fabrication in PDMS permits tuning of the elastic modulus of the final material by altering crosslinker availability (*60*). Thus, the dimensional constraints of laterally deflected side membranes can be partially compensated for by changing the prepolymer to crosslinker ratio from standard 5:1 and 10:1 mixtures to 20:1 (see Appendix A.2). Under these conditions, modeling of membrane deflection using a finite element model in COMSOL indicates the potential of two-sided valves to create effect flow path closure under even under appropriate dimensional and pressure constraints (Figure 2.4a). Compared to previous attempts to characterize single layer membranes, the model shows the capability for higher deflections at more restrictive membrane and channel dimensions that facilitate robust fabrication and the accommodation of single worm loading (*61-63*). The ability of two laterally deflected side membranes to create effective channel closure was then confirmed via confocal microscopy of a microchannel filled with FITC solution. As shown in the three dimensional reconstruction in Figure 2.4b, empirical profiles of channel closure by side valves are similar to those from the finite element model in Figure 2.4a. As shown in Figure 2.4c, this profile indicates a tapered closing of the channel along the length of the valve. When used for loading of *C. elegans*, this closing profile effective captures and constrains the tapered worm head and tail (Figure 2.4d).

In addition to active valves to control sequential worm loading, previous generations of serial worm imaging devices also took advantage of low thermal masses and small transport distances on chip to permit rapid cooling and immobilization of the freely moving worm within the imaging channel (*32, 37, 54, 64, 65*). To do this, fluid that is

chilled off-chip can be cycled through a cooling channel adjacent to imaging channel. This was typically accomplished using a cooling channel fabricated on the same layer as two-layer valve structures. However, the ability to move this functionality onto one feature layer using a side cooling channel as shown in Figure 2.5a has the potential to fully eliminate a layer of features and reduce the fabrication complexity of a device without compromising any functionality.

Finite element modeling in COMSOL demonstrates the potential of a single layer cooling scheme to effectively cool the imaging channel (Figure 2.5b and c). In both the models in Figure 2.5b and 2.5c, the fluid entering the channel is assumed to be chilled to 0°C off-chip and enters at a rate of 1.3 ml/minute, a typical flow rate with common small form factor peristaltic pumps. The model in Figure 2.5b accounts for only thermal transfer and emission to the ambient air beneath the glass coverslip and is representative of imaging with an air objective. The model in Figure 2.5c, which shows diminished cooling performance, also accounts for contact with an objective lens through a thin layer of oil and is representative of imaging with an oil objective.

In practice, when using the same external hardware and settings for off-chip cooling and cycling of the cooling liquid, the side cooling channel is sufficient for robust immobilization of the tail of the worm. However, the imaging channel temperatures achieved using an oil objective under slightly elevated room temperatures near 25°C is insufficient to fully eliminate pharyngeal pumping or head movement in the worm. The diminished efficiency of cooling from a side channel can be addressed by increasing the performance specifications of the off-chip hardware for cooling and flow (Section 2.3.2).

However, as an alternative approach to optimize heat transport on-chip, this work also demonstrates the compatibility of laterally deflected side valves with additional second layer features via the incorporation of second-layer cooling with single-layer valves (Figure 2.6a).

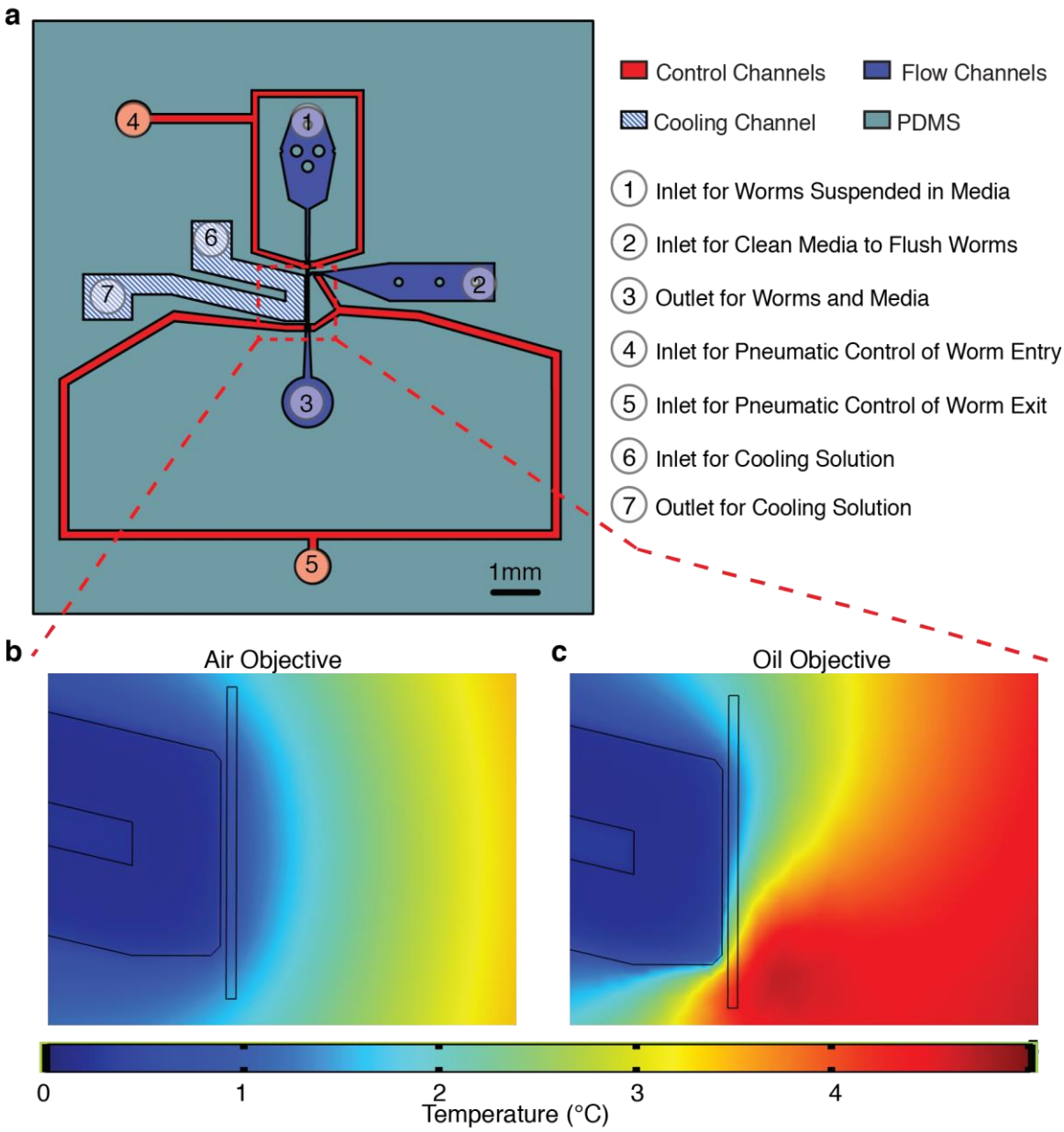

Figure 2.5: Incorporating complete imaging functionality onto a single layer of fabrication using lateral cooling for immobilization of C. elegans. a) Layout of single layer imaging device showing flow, control and cooling channels and numbered inlet and outlet ports for fluid introduction and pneumatic control. b) COMSOL model of single layer cooling performance shows effective cooling of the worm channel under imaging with an air objective. c) COMSOL model of single layer cooling performance showing diminished cooling of the worm channel under imaging with an oil objective.

Figure 2.6a shows a two-layer device utilizing single-layer, laterally deflected valves for flow control and a second layer cooling channel for immobilization. As opposed to the lateral cooling scheme presented in Figure 2.5b, a second layer cooling channel can overlap valve structures on the first layer. This overlap permits more effective cooling of the portions of worm that are trapped under the valve structures themselves (Figure 2.4d). Moreover, a second layer cooling scheme can simultaneously cool both the top and the two side surfaces of the imaging channel. As a result, COMSOL modeling results in Figure 2.6b and 2.6c demonstrates consistently higher cooling performance of this two layer scheme compared with the side cooling scheme in Figure 2.5b and c. The same model setup, accounting for thermal emission and transform to a layer of air below the coverslip, and the same flow rates were used for the models in Figure 2.5 and Figure 2.6.

In practice, a second layer cooling scheme results in robust immobilization of both the head and tail of the worm despite variations in ambient temperature. Moreover, while fabrication of a second layer cooling channel does involve an additional molding step and requires the alignment of two feature layers, alignment tolerances for a single, large cooling channel are substantially higher than for multiple, small valve control channels throughout the chip. Thus, the use of single layer valves in this case still offers substantial increases in fabrication and operational robustness despite the utilization of a second feature layer for cooling. Moreover, as the following section (2.2.3) demonstrates, the ability to segregate functional features into two layers adds a degree of freedom to device design that permits the incorporation of more complex operational capabilities within the same physical space.

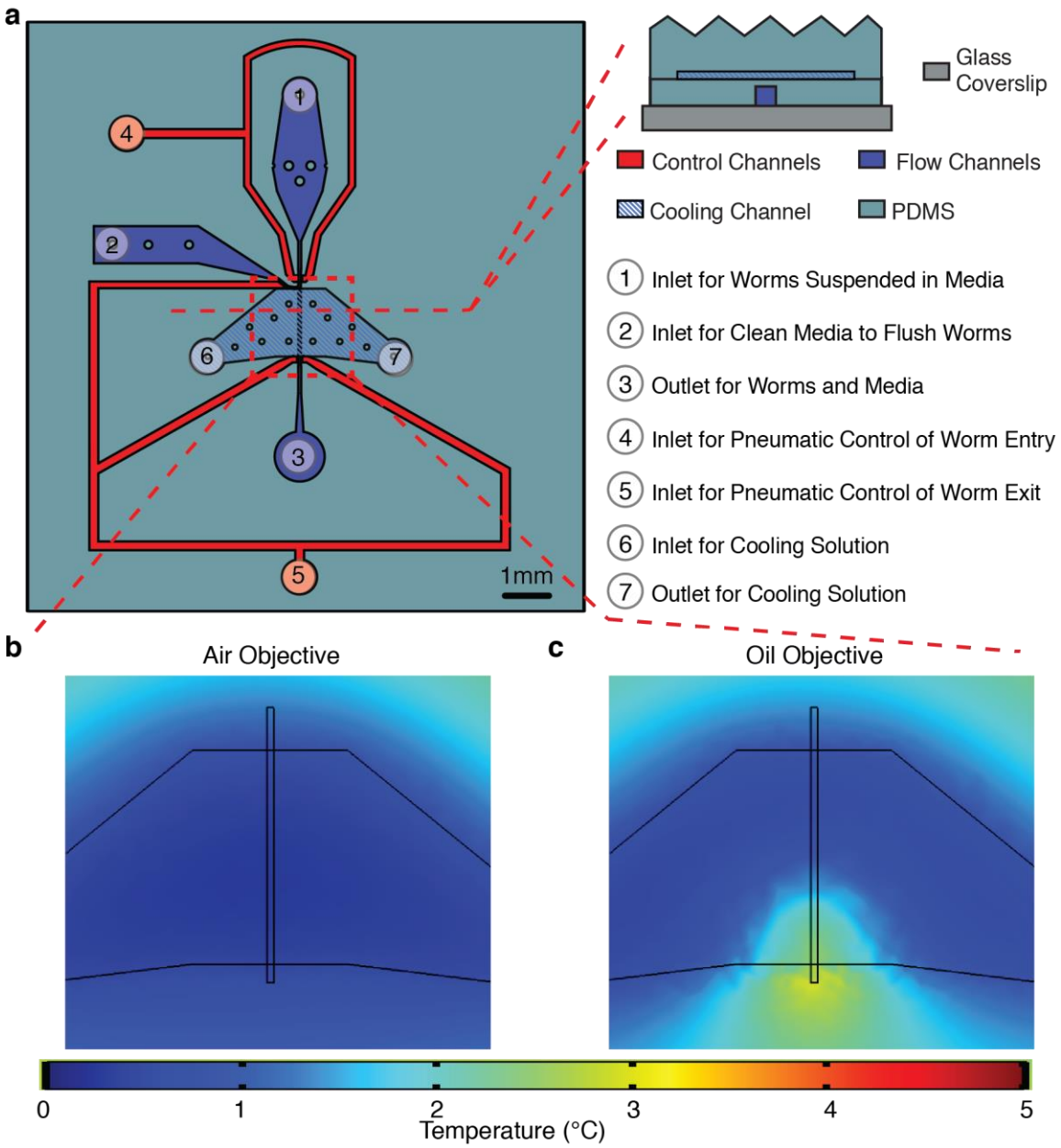

Figure 2.6: Incorporation of second layer cooling with laterally deflected valves for optimizing on-chip heat transfer. a) Layout of imaging device utilizing laterally deflected side valves and a second layer cooling channel, which is also diagrammed in a cross-sectional view. Flow, control and cooling channels as well as inlets and outlets ports for fluid and pneumatic pressure are indicated. b) The second layer cooling scheme results in high cooling performance when used with an air objective. c) Even with additional deleterious heat transfer using an oil objective, the second layer cooling scheme maintains low imaging channel temperatures.

2.2.3: Increasing Sorting Functionality

In addition to facilitating rapid end-point imaging experiments, the serial imaging devices presented in the previous section have often been utilized to conduct forward genetic screens (*32, 37, 38, 54, 64, 65*). These applications require binary sorting of a worm population into one population that is recovered for further study and another population that contains animals deemed to be not useful or interesting (Figure 2.7a). However, to extend sorting based on high-content imaging readouts to the recovery of multiple populations of interest, binary sorting devices are insufficient. For example, to cleanly recover two interesting populations, at least three sorting outlets must be present to accommodate the two populations of interest and the subset of animals that have been loaded or imaged improperly or otherwise cannot be assessed properly for sorting. Yet, due to the physical limitations of arranging independent control and flow lines on chip and robustly directing appropriate movement of the worms themselves via flow, increasing the number of outlets is non-trivial. In general, for robust independent gating of each, each flow line can only be split into two outlets. To increase the number of outlets despite this restriction, Figure 2.7b shows how taking advantage of the compatibility of laterally deflected valves and second layer features can ease physical constraints to accommodate additional flow paths and outlets from the imaging channel.

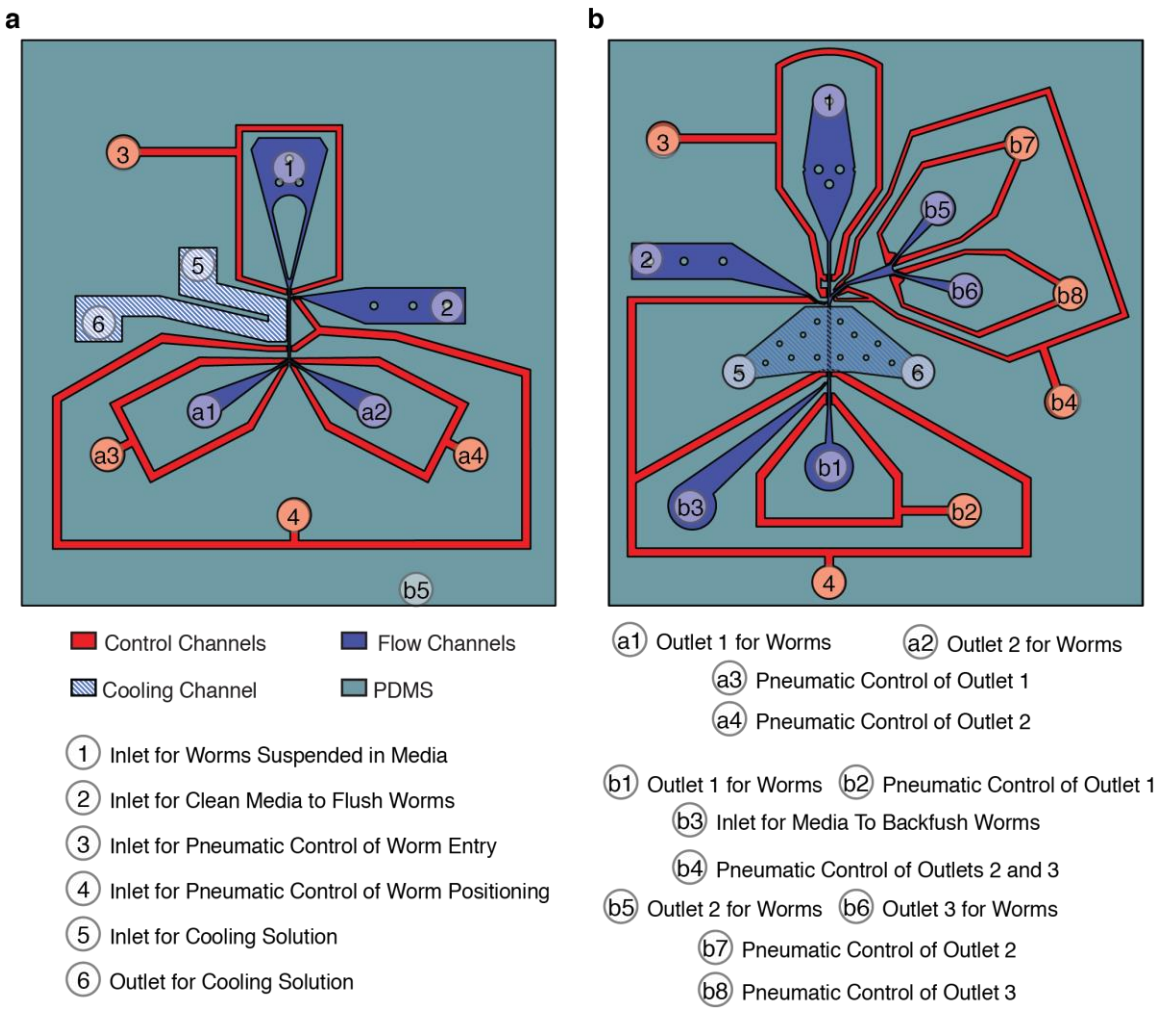

Figure 2.7: Comparison of binary sorting with single-layer cooling and mutli-population sorting with second-layer cooling. a) Single-layer devices intrinsically restrict the dimensionality of design and limit the ability to physically accommodate flow and control paths for independent sorting. b) Increasing the dimensionality of fabrication using second-layer cooling can ease physical restraints and accommodate addition flow paths and increase sorting capability.

The operation of the device in Figure 2.7b permits sorting of worms into at least three outlets while respecting space limitations and the inability of worms to be directed at very acute angles in the flow path. While loading worms, the side outlets are made inaccessible to the worms using a set of valves (Figure 2.8a). Worms that are trapped in

the imaging channel can be directed either forwards into a “discard” outlet (outlet b1 in Figure 2.7b) using flow from a forward flush inlet (inlet 2 in Figure 2.7b) or backwards towards sorting outlets from a backward flush inlet (inlet b3 in Figure 2.7b, Figure 2.8b). As a safety factor to prevent erroneous sorting, the “discard” outlet is located in the forward or default flow path from the worm inlet. This arrangement ensures that debris, eggs or worms that are not trapped by the positioning valve or are accidently pushed forward in the flow path are always discarded. Upon imaging and decision-making, worms that are appropriately loaded in the imaging channel can be actively sorted into the one of the sorting outlets via backflow. After the worms enter the sorting flow path, its trajectory into each of two independent outlets are directed by a second set of sorting valves (Figure 2.8c).

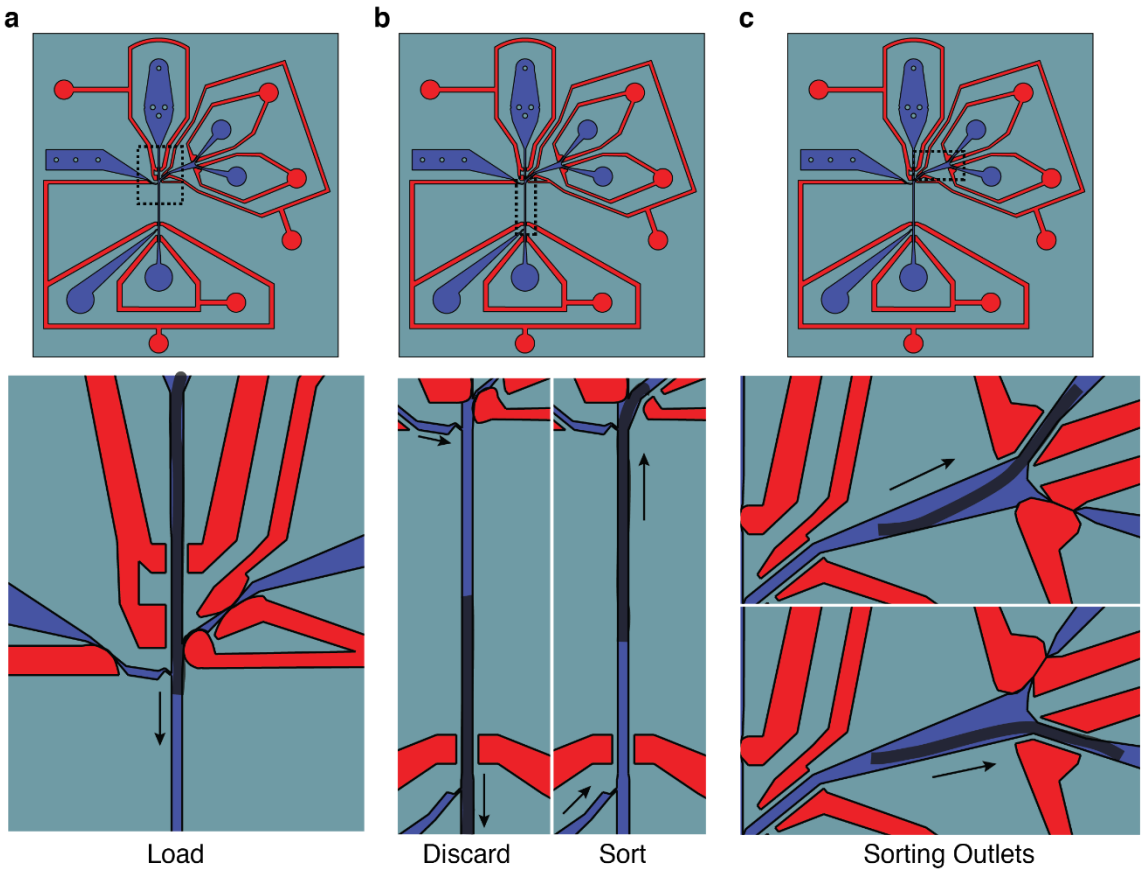

Figure 2.8: Operation of the multi-population sorting device. a) Upon loading, access to the sorting outlets is restricted by a sorting valve that directs the worm into the imaging channel. b) Worms that are in the imaging channel can be directed forwards to a discard outlet by a forward media flush inlet or backwards towards the sorting outlets by a backward media flush inlet. c) Once worms are guided by the backward fluid movement into the sorting area, independent sorting valves determine the specific outlet a worm enters.

While the device layout presented in Figures 2.7 and 2.8 only accommodate the recovery of two potentially interesting populations, it embodies design concepts that can be extended for the accommodation of a larger set of populations. The utilization of second layer cooling frees up physical space on the flow layer for the sorting design to be

reflected across the imaging channel, resulting in the recovery of four populations. Moreover, the demonstrations of laterally deflected valves and their compatibility with second layer features creates additional opportunities to increase sorting and other on-chip capabilities in general by using a combination of lateral and second-layer control features.

2.2.2: Optimizing Loading and Orientation

While the adult worm is a relatively large, millimeter-long specimen, understanding biological processes within the multicellular worm often requires the extraction of local information from specific sub-cellular, cellular or tissue-level structures at the micron-scale. Thus, the size an intact worm is usually large with respect to both the lateral x-y and axial z resolutions of the microscopy setups necessary to obtain detailed local information of interest. This mismatch creates a need for orientating the worm in an optimal position for targeting imaging to relevant structures.

With respect to lateral x-y resolution, the ability to resolve spatial information in the final image is dependent upon both the intrinsic resolution of the optical system (*66*) and the resolution afforded by the digitization at the camera sensor. Common sensors used for quantitative imaging offer pixel sizes of roughly 6.5 μm^2 arrayed in configurations of roughly 1000x1000 pixels or fewer. Thus, to be able to resolve a 2-3 μm neuronal cell body in the worm with multiple pixels, magnifications of at roughly 20X must be utilized. Furthermore, quantitative fluorescence imaging applications are often signal-limited, requiring the use of higher magnification and numerical aperture lenses or digital binning for adequate signal. However, higher magnifications increase spatial resolution

and the light gathering ability of the system at the cost of decreasing the extent of the space that can be viewed within the limited size of the sensor. Thus, as shown in Figure 2.9a, the effective field of view of digital microscopy systems necessary to extract local information from fluorescence imaging is usually only in the hundreds of microns.

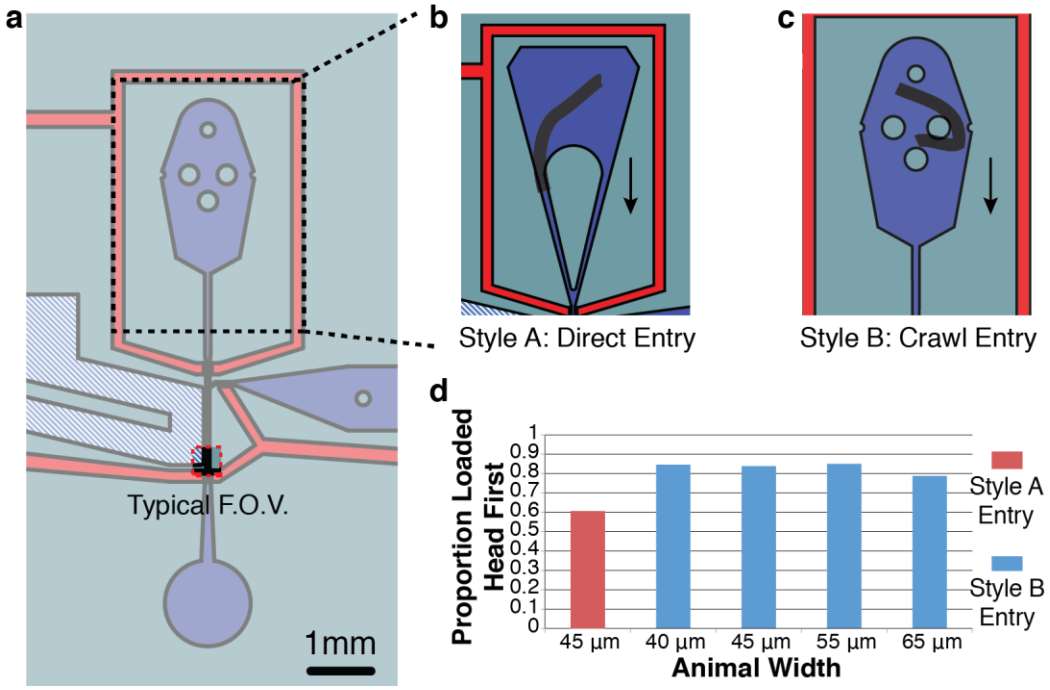

Figure 2.9: Biasing anterior-posterior orientation on chip to facilitate targeting of high resolution imaging. a) Under commonly used magnifications for single-cell analysis, the field of view (red dotted box) is limited to small regions along the anterior-posterior axis of the worm. To aid in targeting the field of view, loading orientation can be biased by the entry area for the worms (black dotted box). b) "Style A" entry area permitting relatively direct entry of the worm into the imaging. c) "Style B" entry area with pillar obstacles promoting the adoption of crawling behaviors in the worm prior to entry. d) Analysis of anterior-posterior loading orientation shows that direct, Style A entry areas offer little bias for specific orientations whereas crawl-promoting Style B entry areas offer consistent biasing of orientations towards head-first entry.

Thus, to facilitate high-resolution imaging in a high-throughput manner, it is necessary to target the field of view to specific locations of interest. If necessary, this can be accomplished using active movement of the stage guided by image recognition algorithms or manual control. However, physical orientation of the specimen on-chip provides another technique for expediting targeted data collection via the reduction of intermediate processing and stage movement steps. In particular, orientation of the long anterior-posterior axis of the worm along the imaging channel is important for providing rough anatomical positioning of the field of view along the length of the worm.

As shown in Figure 2.9b and c, the anterior-posterior orientation of the worm is governed by the microfluidic area for worm entry. Whereas entry areas that allow worms to directly enter the imaging channel offer relatively no bias for anterior-posterior orientation (Figure 2.9b and d), entry areas that provide flow path obstacles tend to increase the bias for a head-first entry into the imaging channel (Figure 2.9c and d). Specifically, sparse pillar arrangements within the entry area tend to slow worm movement and allow them to adopt forward crawling behaviors before entering the imaging channel. As shown in Figure 2.9d, these microfluidic features promote head-first entry of the worm across different ages and worm sizes.

With respect to axial *z* resolution, quantifying intensities in specific cells within the relatively thick (~50-70um) worm body poses particular imaging challenges. Imaging aberrations increase with distance of the target from the coverslip and targets far from the coverslip suffer from loss of contrast and intensity attenuation (*58, 67*). These effects can be observed in Figure 2.10, where fluorescence in a bilaterally symmetric pair of

neuronal cells located in the head of the worm (Figure 2.10a) is observed from two different orientations. When the cell pair is imaged in an orientation along the x-y plane, they exhibit similar intensities (Figure 2.10b). However, when the cell pair is imaged oriented along the *y-z* plane, the cell pair furthest from the coverslip shows diminished intensity (Figure 2.10c). Furthermore, z-axial resolution is more limited compared with lateral resolution in the *x-y* plane, diminishing the ability to resolve the two cells.

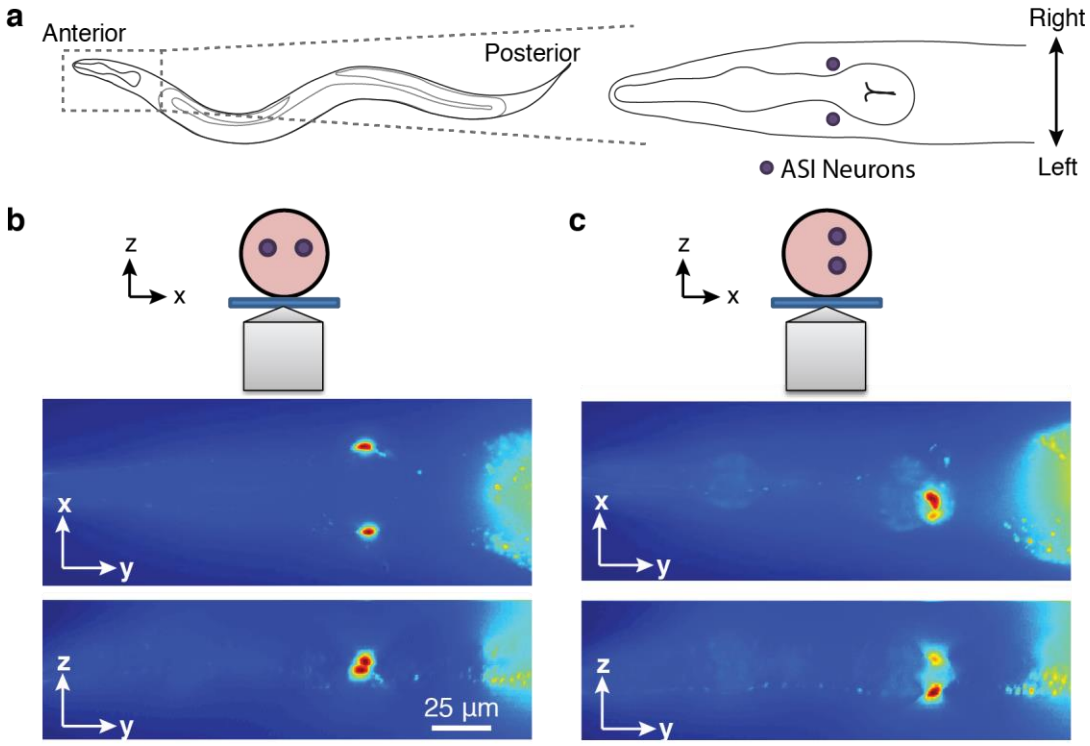

Figure 2.10: Imaging quality of bilaterally symmetric neuron pair under different imaging orientations. a) Schematic of the bilaterally symmetric ASI neurons, organized as a left-right pair of cells in the head of the worm. b) Imaging the cell pair oriented along the x-axis results in comparable intensities for both cells and good spatial resolution of the individual cells in the x-y plane. c) Imaging the cell pair oriented along the z-axis results in loss of intensity for the cell located furthest from the coverslip and poor spatial resolution of the individual cells in the y-z plane.

Compromises in both spatial resolution and signal loss in the z-axis of imaging suggest that consistent orientation of the worm is critical for both accurate intensity quantification and structural characterization. Previous work has demonstrated microfluidic features to laterally orient the worm along the z-axis as shown in Figure 2.10c in order to resolve particular biological structures on the left or right side of the worm (*38*). However, since many sensory neurons in *C. elegans* exist as bilaterally symmetric pairs, it is particularly advantageous to orient the animal such that both neurons are in the same plane of focus especially when studying potential asymmetries in neural processing. Figure 2.11a shows that imaging of worms in a straight rectangular imaging channel tends to induce a rotational skew such that the left and right neurons differ in z-position by roughly 20 μm. Moreover, the z-plane difference due to this small rotational skew is sufficient to bias the intensities of the neurons pairs such that quantifiable differences of ±50% between neuronal intensities can be observed due to differences in z location (Figure 2.11b).

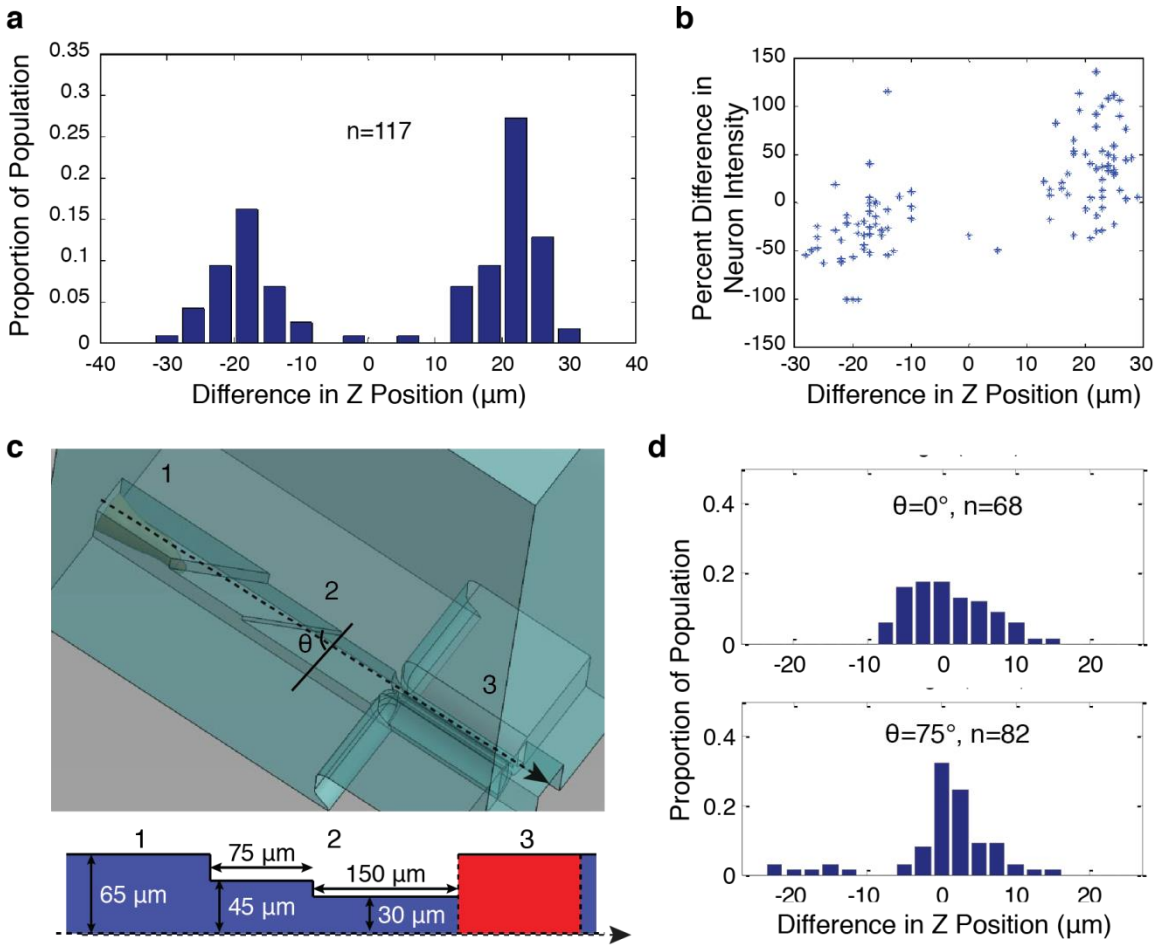

Figure 2.11: Reducing rotational asymmetry in imaging of bilaterally symmetric biological structures. a) Imaging in a straight rectangular imaging channel results in a rotational skew that puts bilaterally symmetric features roughly 20 µm apart from each other on the z-axis. b) The rotational skew and resulting z-axial differences observed straight imaging channels results in quantifiable neuron intensity differences of about ±50%. c) Diagram of scheme for restriction of the z range of motion via sequential tapering of the imaging channel. Worms progress from the inlet (1) through two downward and steps aligned at a specified angle θ in the imaging channel (2) before stopping at the positioning valve (3). d) In addition to reducing the total z-range for data acquisition, top down compression provided by sequential steps eliminate the rotational skew previously observed in the worm. Providing differential compression of the worm via angled steps can also alter the rotational profiles observed on-chip.

To reduce the confounding effects of z-dependent intensity changes, a vertical tapering of the imaging channel can be employed to restrict the z axial range at the imaging location.

As shown in Figure 2.11c, step-wise truncation of the height of the imaging channel can be accomplished using multi-layer soft lithography (Appendix A). In order to provide compression of the head of the worm while still allowing sufficient space for efficient loading and removal of the worm through the channel, 30 μm is used as the minimum height at the imaging location. At the same time, an overall device height of 10 to 15 μm above the width of the worm is necessary to facilitate efficient entry and loading of the worms into the device. In practice, a single height step down to 30 μm in the imaging channel tends to result in folding of the worm head upon loading, resulting in clogging and loss of worms. In order to robustly guide the worm head into the 30 μm restriction, two sequential height steps are used with no more than roughly 20 μm in height change at each step (Figure 2.11c bottom).

The configuration in Figure 2.11c both restricts the amount of z-deviation permissible between the two neurons and eliminates the rotational skew previously observed in simple rectangular imaging channels (Figure 2.11a). With height steps perpendicular to the length of the channel ($\theta=0$ in Figure 2.11c), the z-position deviation between two bilaterally symmetric neurons shown in Figure 2.11d is centered around 0 and the maximum z deviation is about half of those observed with simple rectangular imaging channels shown in Figure 2.11a. Furthermore, when the height steps are fabricated at an angle of 75° relative to the channel perpendicular, further refinement of the rotational distribution is observed (Figure 2.11d).

These results indicate that top-down compression of the worm during loading is an effective means of tuning the orientation of the dorsoventral axis of the worm relative to

the z imaging axis. In combination with the ability to tune anterior-posterior orientation using features at the worm inlet of the imaging device, the design and characterization of these microfluidic features provides another modular microfluidic toolset to manipulate worms on-chip to maximum imaging throughput and quality.

2.3: Hardware Support Systems for Microfluidic Imaging

2.3.1: Integrated Pressure and Solenoid Valve Controllers

The operation of the microfluidic devices presented thus far require controlled off-chip pressure sources for both on-chip membrane valve deflection and driving flow on chip. Typically, control of pneumatically driven valves on-chip require activation pressures of roughly 30-40 psi, which must be quickly applied and released for valve activation and deactivation. On the other hand, pressures necessary for driving flow on-chip range from 3-10 psi depending on the particular application and fluidic resistance of the microfluidic chip. Finally, off-chip, electrically activated solenoid pinch valves are often utilized as a method to rapidly start and stop flow on chip and prevent undesirable back-flow into certain flow paths. To accommodate all of these potential needs, an integrated controller incorporating multiple independent pressure controls, pneumatic valves, and accessory outlets to drive additional off-chip components is necessary.

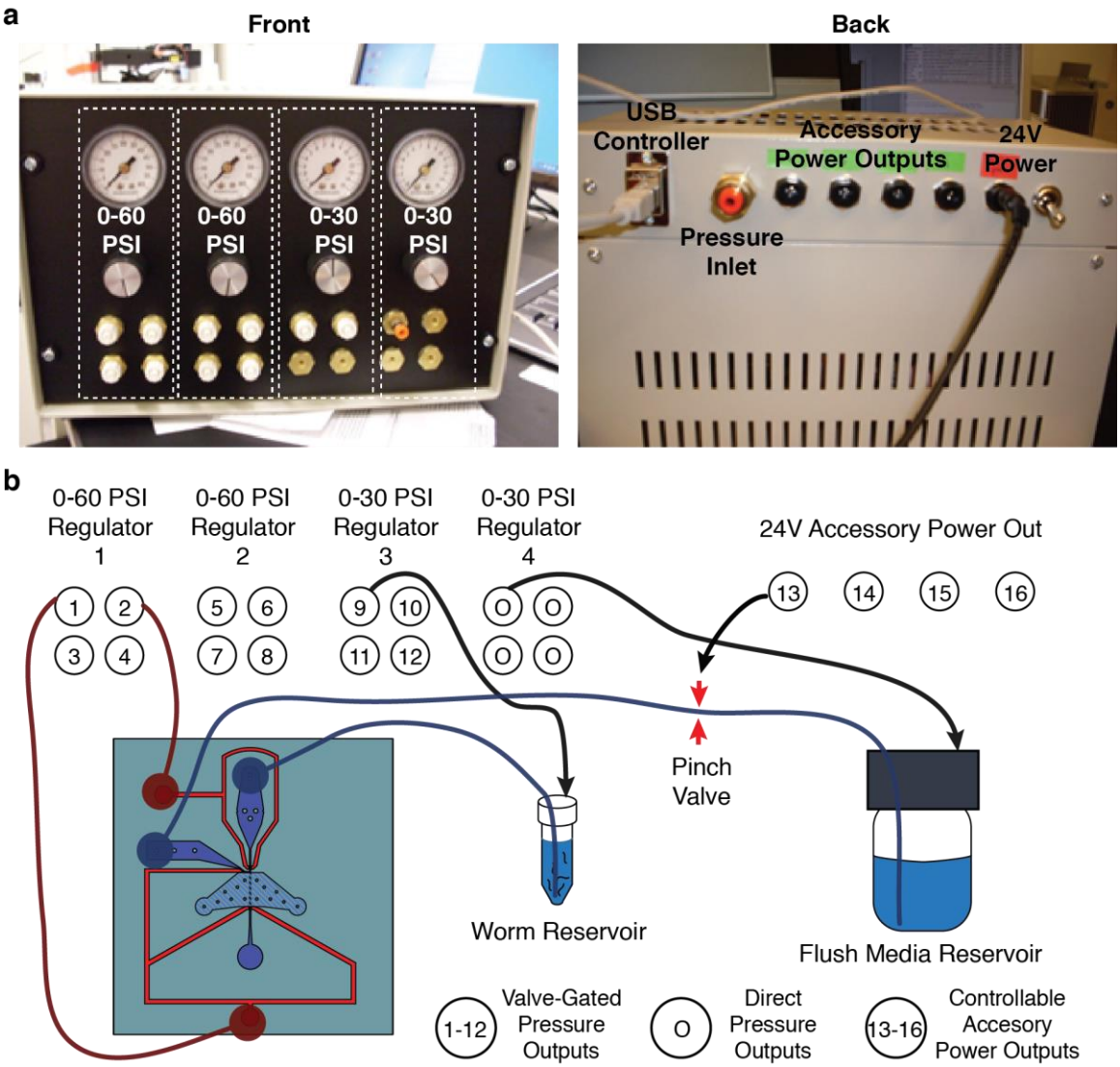

Figure 2.12: Integrated pressure and valve controller for integrating control of off-chip microfluidic flow control. a) Pictures of the front and back of the pressure and valve controller box showing relevant pressure controllers and inputs and outputs on the front and back panels. b) Schematic overview of the outputs of the pressure box demonstrating functional connections with a microfluidic imaging chip.

An integrated solution for both pressure, pneumatic and pinch valve control is presented in Figure 2.12a. This controller incorporates four independent pressure controllers operating at different pressure ranges to accommodate both high and low pressure

requirements. Additionally, the controller accommodates the independent operation of up to eight high pressure on-chip valves (outputs 1-8 in Figure 2.12b) and 2-4 low pressure sources for flow control (outputs 9-10 in Figure 2.12b). Additionally, 2-4 constant low pressure sources are supplied for continuous pressure ("O" outlets in Figure 2.12b). When necessary, flow lines driven by these constant pressure sources can be rapidly gated by off-chip solenoid pinch valves driven by the four electrical outlets for control of additional accessories (outputs 13-16 in Figure 2.12b). As shown in Figure 2.12b, these control elements accommodate full control of all of the microfluidic designs presented in this chapter and can be flexibly adapted to other chips requiring different pressure and flow inlets.

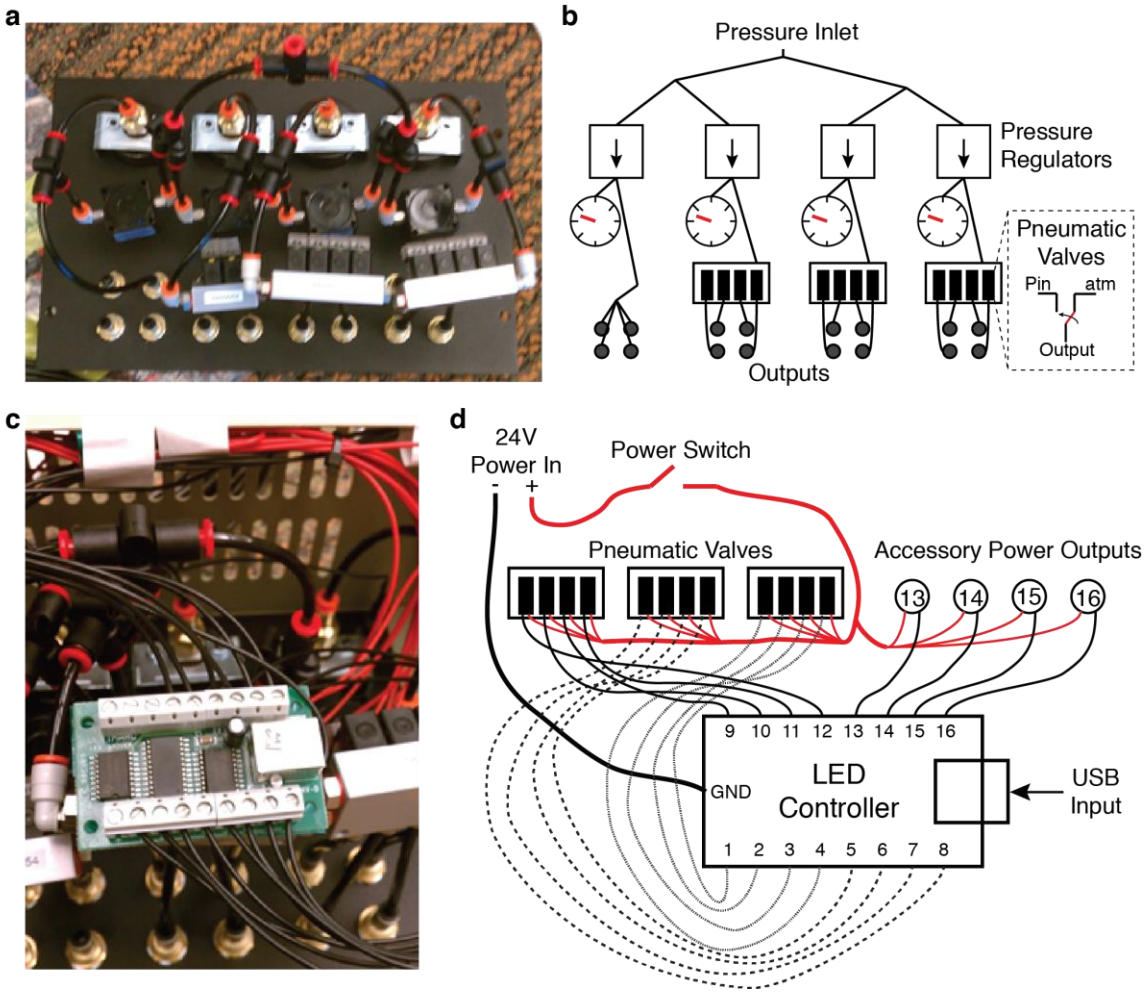

Figure 2.13: Internal view of pressure and valve control box. a) Picture of pneumatic connections on the interior of the valve box. b) Schematic of pneumatic connections showing the distribution of a single pressure source amongst four independent pressure regulators and 16 potential outputs. c) Picture of the electrical connections to the LED controller responsible for furnishing computer control of valve and accessory power output activation. d) Schematic of the electrical connections showing the independent control of 16 potential valve and external outputs using a single LED controller.

An internal view of the pneumatic connections in pressure and valve control box is shown in Figure 2.13a. A detailed schematic of the pressure distribution and control lines in the box is shown in Figure 2.13b. Pressure from the air inlet on the back of the box is distributed amongst four sets of four pressure outputs. The first three sets of pressure

outputs are gated by three-way pneumatic valves as shown in the inset in Figure 2.13b. These valves switch the pressure output between a regulated pressure input and atmospheric pressure in order to rapidly pressurize and de-pressurize media or worm reservoirs. The last set of pressure outputs is not electronically gated and directly connects the pressure output to the regulated pressure input. These outputs are intended for constant-flow applications or constant pressurization of large reservoirs, which have large dead volumes for pressurization and are more rapidly gated by off-chip pinch valves.

To facilitate computer control of the pneumatic valves and accessory power outputs in the box, the power lines for the valves and outputs are wired to a USB-controllable LED controller as shown in Figure 2.13c and d. The commercially available 16 output LED controller supplied by Ultimarc Limited gates the connection of the negative terminal of valve and power outputs to the ground of the power input and electronically closes each the circuit powering each valve or external output on demand. The LED controller integrates control of all electronic outputs in the box to one USB connection with the computer through the back of the box and provides a unified interface for software valve control.

2.3.2: Cooling Systems for Immobilization

The pressure and valve controller box described in the previous section serves to address two general microfluidic needs for pneumatically driving both flow and valves on chip. However, the ability to immobilize worms via cooling for worm imaging applications depends on a third off-chip support system generating and cycling chilled liquid through

the cooling channels discussed in Section 2.2.1. An overview of such a system is shown schematically in Figure 2.14.

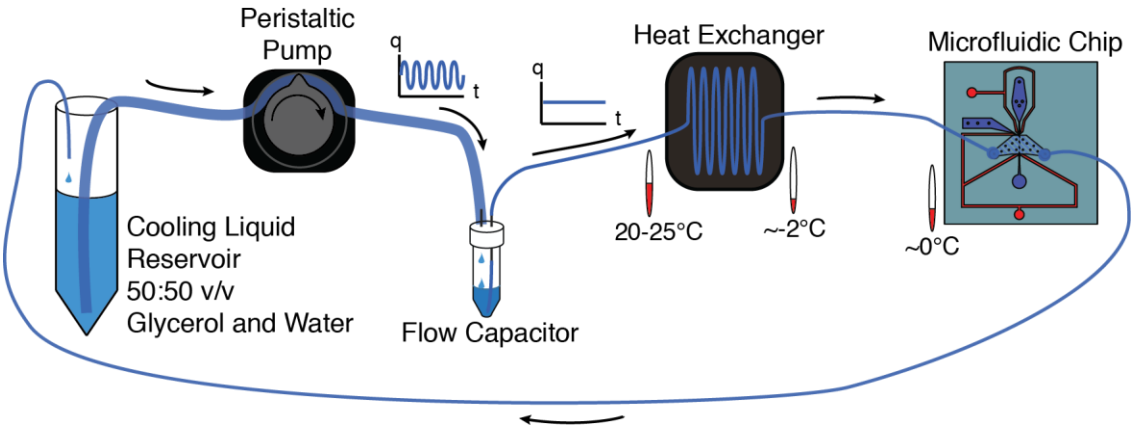

Figure 2.14: Overview of liquid cooling system for on-chip immobilization of *C. elegans*.

Through the system, a 50:50 v/v glycerol-water mixture is utilized as the cooling solution due to the need for freezing point depression in the heat exchanger. This cooling liquid is first pumped from a reservoir using a peristaltic pump. The use of a peristaltic pump facilitates the maintenance of constant flow despite changes in the viscosity of the cooling liquid when chilled and potential changes in the fluidic resistance of the on-chip cooling channel itself. Furthermore, as opposed to pressure-driven flow, which requires a closed vessel to maintain an upstream pressure, driving flow using a peristaltic pump also facilitates recycling of the cooling liquid back into the same open reservoir. However, despite the aforementioned advantages, the cyclical operation of peristaltic pumps often results in pulsatile flow profiles that may manifest in deleterious pulsatile vibrations in the cooling channel on-chip. To dampen the pulsatile nature of the flow, liquid from the

peristaltic pump is first directed into an air-tight flow-buffering container. This container acts as a flow capacitor, dampening the flow profile from the peristaltic pump.

After a steady flow of cooling liquid has been generated by the peristaltic pump and the downstream capacitance container, it must be chilled before being introduced into the microfluidic chip. Here, a heat exchanger module can be used to lower the temperature of the incoming liquid before delivering to the microfluidic chip. While various heat exchanger designs have been previously utilized in the lab to accomplish this goal (*64*), previous solutions tended to lack portability, repeatability and robustness. Specifically, the initial use of ice for fluid cooling lacked the ability to adjust cooling temperatures for different conditions and required frequent manual intervention to maintain cooling. Subsequent designs using a peltier module to chill fluid also suffered from a lack of long term stability due to degradation of the flow module joints and seals due to repeated thermal cycling over time. These initial peltier-based designs also required difficult assembly procedures and expensive off-chip voltage controllers or PID controllers that made the system difficult to replicate.

Figure 2.15a highlights the specific failure modes of the previous cooling designs in red. Early designs called for two-point compression assembly of all of the components of the heat exchanger. This mode of assembly required careful and simultaneous alignment of multiple pieces and often leads to improper sealing between the copper flow module and the peltier module. Moreover, the hand-fabricated PDMS seal used as a gasket for leak prevention had high rates of fabrication failure and could also shift or tear during assembly. Finally, the inlets and outlets of the flow module were initially created using an

epoxy seal with the copper flow module. While initially effective, the epoxy tended to separate from the copper flow module and the stainless steel inlet and outlet ports due to repeated thermal cycling.

To address these failure modes, Figure 2.15b shows the components of an independently sealed flow module. The flow module is sealed using 8-point compression against a commercially acquired Teflon tape sealant, resulting in an easy and robust assembly process and the maintenance of a continuous seal over time. Furthermore, inlets and outlets are created with screw-in gasketed barb fittings, eliminating the possibility of adhesive failure over time. Together, these components form an independently assembled and sealed flow module with inlet and outlet ports in the front and a highly conductive contact surface for the peltier module on the back (Figure 2.15c). To create a full heat exchanger assembly, this flow module can then be mounted to commercially available peltier modules via the standard fittings provided with commercially available CPU cooling assemblies as shown in Figure 2.15d.

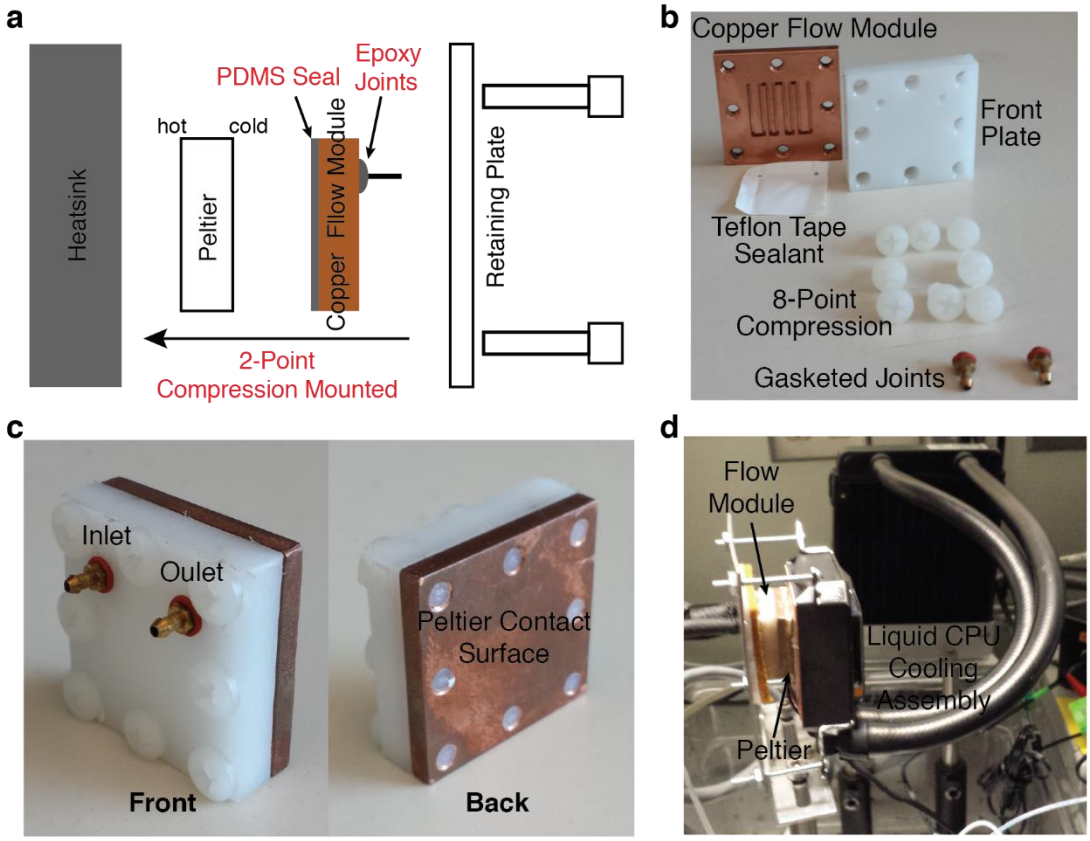

Figure 2.15: Improved heat exchanger module eliminates fabrication challenges and failure modes in previous designs. a) Early peltier heat exchanger design with failure modes highlighted in red. Two point compression, a hand-fabricated PDMS seal and epoxy joints lead to fluid leaks due to improper compression and degradation of epoxy contact with thermal cycling. b) Components of improved independently sealed flow module which eliminates the failure modes outlined in part a. c) Pictures of assembled flow module show flow inlets and outlets in the front and the contact surface for the peltier module on the back copper surface. d) Picture of flow module assembled with commercially available peltier module and liquid CPU cooling assembly.

Finally, to complete the cooling system, the peltier module must be driven by a power supply. To accommodate the potential need for increasing or decreasing cooling capacity for different chip designs or ambient temperatures, Figure 2.16 outlines a custom adjustable power supply to drive the peltier module. Figure 2.16a shows the circuit diagram for the voltage regulation and buffering steps. A LM317 linear voltage regulator

is used to adjust the output voltage from 1.25V to roughly 12V using a panel-mounted knob potentiometer. To account for the high current requirements of the peltier module, the low current output from the voltage regulation step is delivered to a voltage buffering step with a BJT transistor to increase current output. Pictures of the front and back panels and interior of the cooling voltage control box is shown in Figure 2.16b and c.

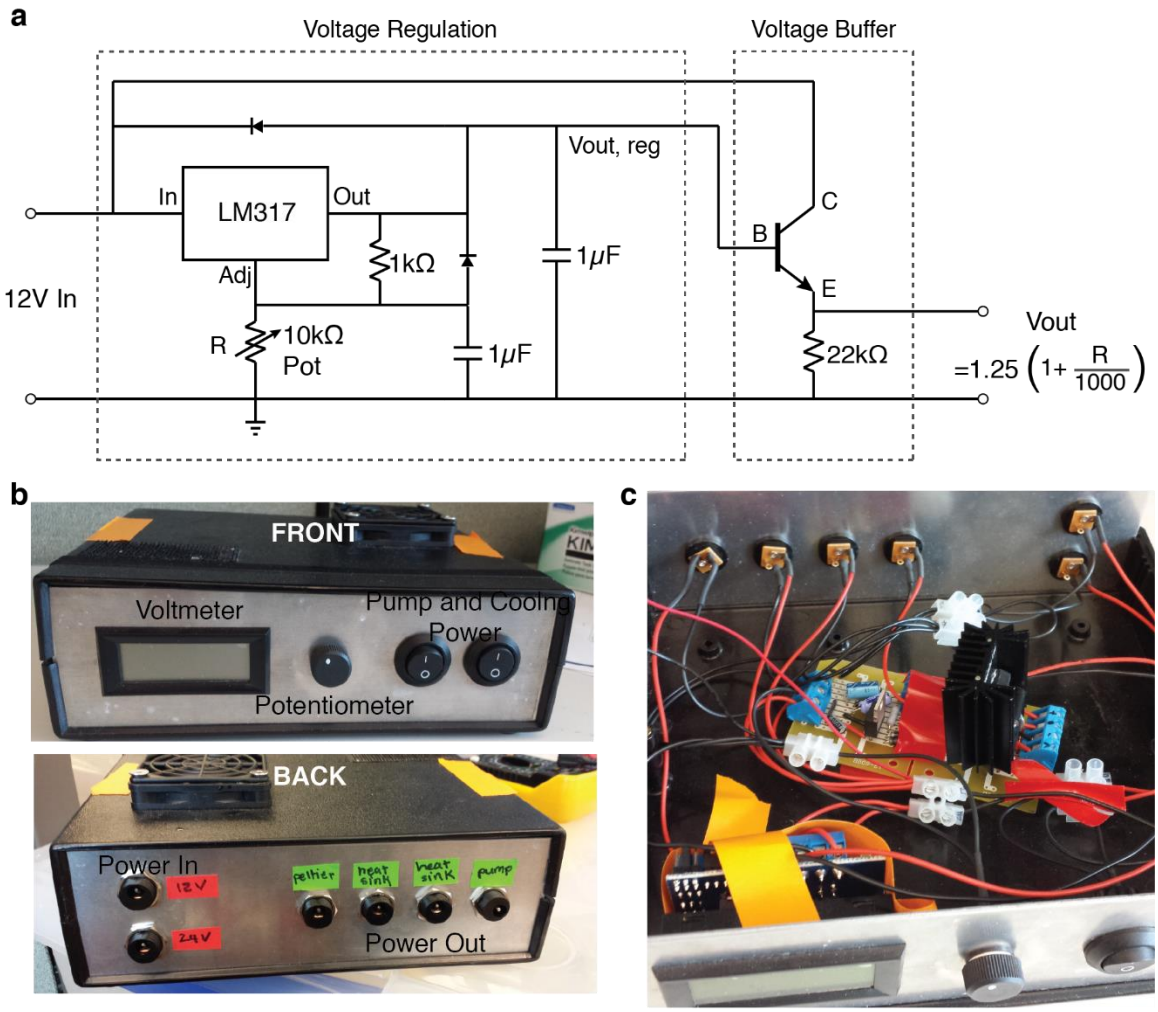

Figure 2.16: Electronic components for adjustable peltier cooling. a) Circuit diagram of voltage regulator and buffer used to generate an adjustable power supply for the peltier module. b) Front and back panels of the power supply box for cooling control. c) Interior view of the electronics in the cooling power supply box.

2.4: Software Support Systems for Microfluidic Imaging

In order to perform automated imaging tasks with the microfluidic tools and support hardware described in the previous sections, specific hardware components of the imaging system have be electronically controllable via computer control. A minimal list of hardware components that must be controllable via a computer interface is tabulated in Table 2.1 alongside typical actuation mechanisms for each component and the computer interfaces used. While the pressure and valve controller box described in Section 2.3.1 addresses the actuation of the microfluidic components via a common USB interface, the specific mechanisms and interfaces for the other components are dependent on the specific microscopy setup being used for microfluidic imaging.

Table 2.1: Microfluidic and microscopy hardware that must be electronically controllable via a computer interface for general automated imaging applications.

Component	Typical Actuation Mechanism	Typical Computer Interface
Microfluidic Valves	Solenoid Pneumatic Valves	USB LED Controller
Microfluidic Flow Control	Solenoid Pneumatic or Pinch Valves	USB LED Controller
Transmitted (Bright field) Light	LED or Shutter	USB, Serial or TTL
Incident (Fluorescence) Light	LED or Shutter	USB, Serial or TTL
Z-Stage	Stepper Motor or Piezo	USB or Serial
Camera	-	Firewire, USB or Framegrabber

In order to provide integrative computer control of all of the components listed in Table 2.1, custom control software is necessary. Commercial and open-source microscopy software packages typically only accommodate control of common microscopy components and are not easily customizable to permit full microfluidic control.

Furthermore, integration of custom on-demand image processing and decision-making can be difficult within the constraints of more narrowly tailored microscopy packages.

To develop modular, portable and customizable microfluidic control software, it is advantageous to select a software environment that is commonly available within academic environments, amenable to rapid design changes and testing and readily supports parallel instrument control with drivers available for common microscopy components. To address these specifications, Figure 2.17 shows an overview of control software developed in the LabVIEW development environment for integrative control of all of the components listed in Table 2.1. The code and the LabVIEW environment offers the flexibility to quickly change modules for different microscopy setups and the ability to incorporate custom image processing algorithms within the course of automation.

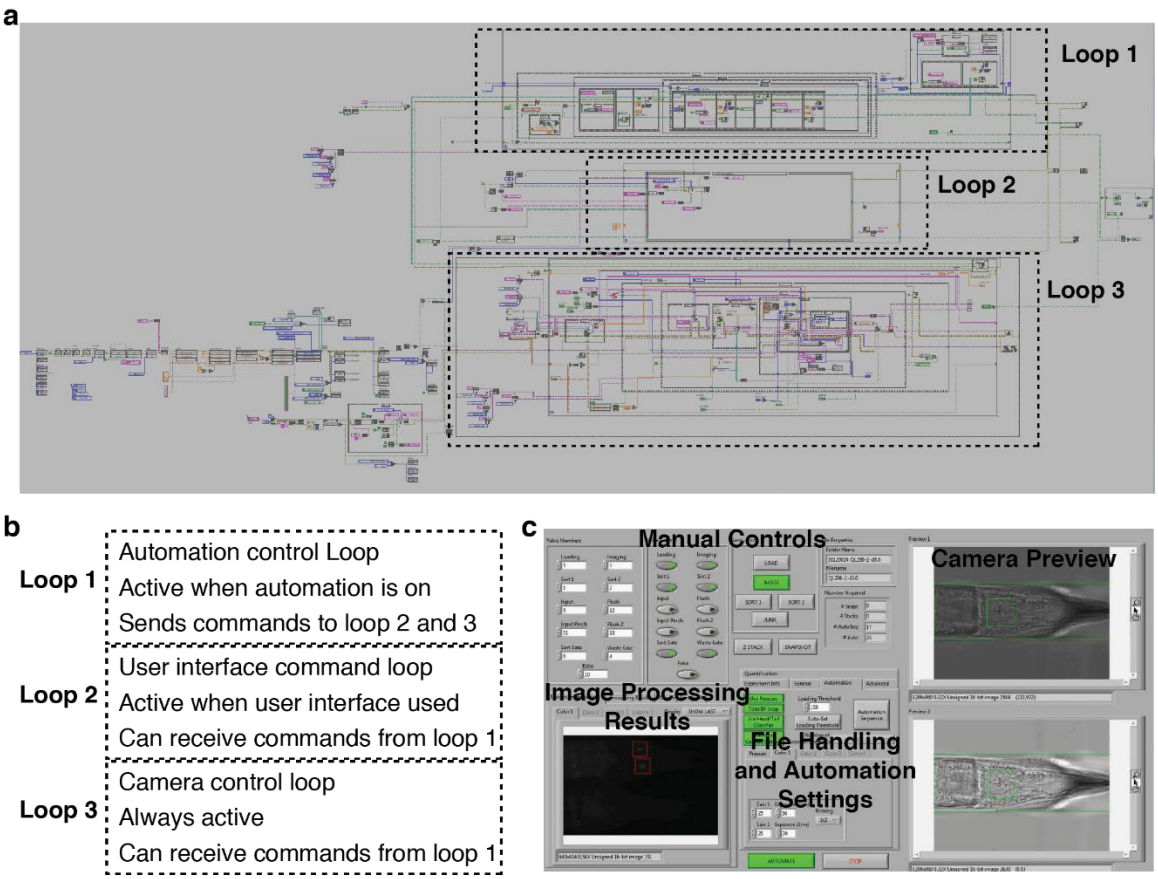

Figure 2.17: Custom LabVIEW software for automated fluorescence imaging of *C. elegans* on microfluidic chips. a) Block diagram underlying software operation showing three independent control loops. b) Outline of the functions and interdependencies of each loop. c) Overview of the user interface for the software.

Figure 2.17a shows an overview of the block diagram, which underlies the operation of the custom LabVIEW software. The block diagram consists of three independent control loops which operate according to the outline provided in Figure 2.17b. Briefly, the three loops are responsible for the coordination of automation functions, responding to user interface commands and continuous operation of the camera, respectively. In order to execute automation functions, the automation control loop can interact with the other two loops to mimic user interface commands in loop 2 or alter camera operation in loop 3.

The user interface to direct the function and operation of these three loops and receive visual feedback of camera and image processing results is shown in Figure 2.17c.

A more detailed block diagram of automation routines is shown in Figure 2.18 below. Figure 2.18a shows a high level description of how the automation loop interacts with the user interface and camera loops to facilitate coordinated function of the microfluidic device and other microscopy components. Blocks indicated by dotted boundaries indicate functions where image processing is necessary for decision-making. These image processing operations are discussed in more detail in Chapter 3. Figure 2.18b shows a lower level block diagram of z-stack collection, showing how all of the components listed in Table 2.1 are utilized in automated imaging.

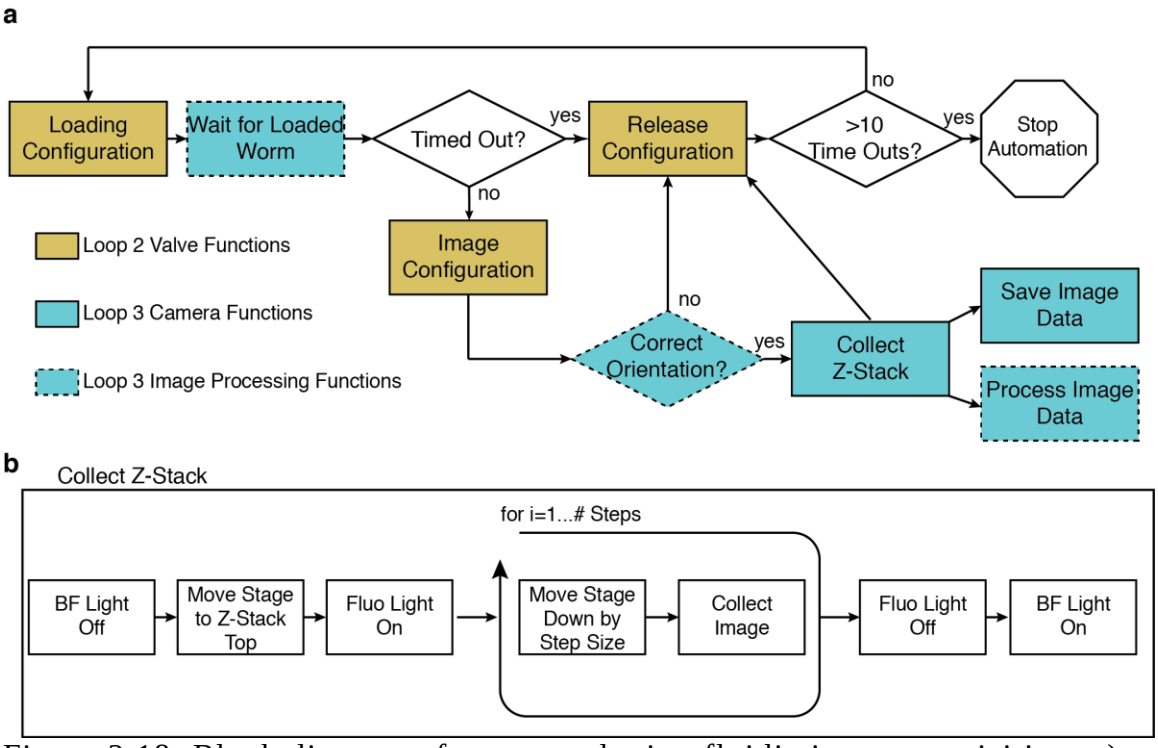

Figure 2.18: Block diagram of automated microfluidic image acquisition. a) High level block diagram of how the automation loop interacts with the user interface and camera loops to alter microfluidic chip configurations and interface with the camera. b) Lower level block diagram of z-stack collection procedure showing how other microscopy components are controlled in data acquisition.

2.5: Discussion and Conclusions

This chapter describes both the development of new microfluidic chip functionality and the construction of the off-chip ecosystem to support the function of microfluidic chips. Some of these developments such as the laterally deflected valve, pressure and valve controller system and the general the framework for integrative microfluidic and microscopy control have broader utilization beyond the handling and imaging of *C. elegans*. However, this chapter describes the specific utilization and refinement of these tools alongside other technological innovations to enable robust, high-throughput

imaging of *C. elegans*. While imaging and sorting of *C. elegans* on microfluidic platforms have been previously demonstrated, the body of work in this chapter refines and increases the robustness and usability of these technologies with the aim of ultimately increasing the dissemination and impact of microfluidic technology. As a demonstration of progress towards this goal, microfluidic imaging systems have been disseminated and successfully used in several non-engineering laboratories in the course of this work.

CHAPTER 3: TWO-LAYER CLASSIFICATION ARCHITECTURE FOR BIOLOGICAL IMAGE PROCESSING

This work has been submitted for publication in PLoS Computational Biology as of September 24, 2014.

3.1: Introduction

Diverse imaging techniques exist to provide functional and structural information about biological specimens in clinical and experimental settings. On the clinical side, new and augmented imaging modalities and contrast techniques have increased the types of information that can be garnered from biological samples (*68*). Similarly, many tools have recently been developed to enable new and accelerated forms of biological experimentation in both single cells and multicellular model organisms (*27, 43, 55, 69, 70*). Increasingly, the capacity for high-throughput experimentation provided by new optical tools, microfluidics and computer controlled systems has eased the experimental bottleneck at the level of physical manipulation and raw data collection. Still, the power of many of these toolsets lies in facilitating the automation of experimental processes. The ability to perform real-time information extraction from images during the course of an experiment is therefore a crucial computational step to harnessing the potential of many of these physical systems (Figure 3.1). Even when off-line data analysis is sufficient, the capability of these systems to generate large, high-content datasets places a large burden on the speed of the downstream analysis.

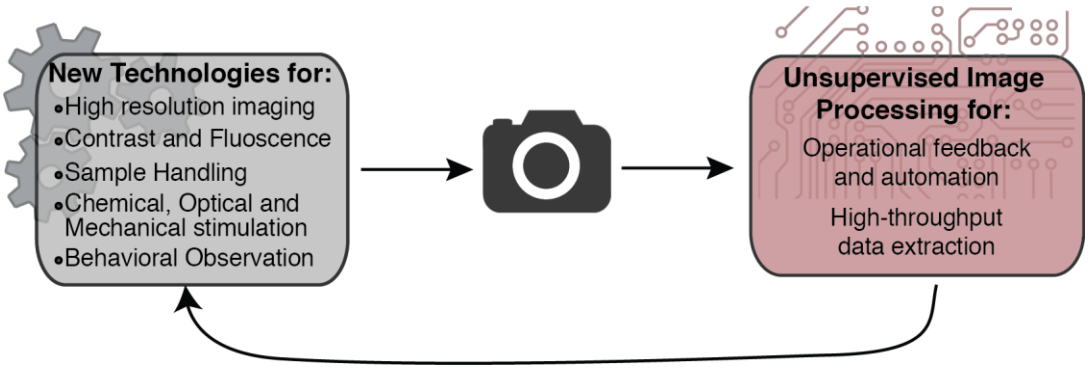

Figure 3.1: Unsupervised image processing techniques are often necessary to harness the power of emerging imaging and experimental technologies.

Automated image processing and the use of supervised learning techniques have the potential for bridging this gap between raw data availability and the limitations of manual analysis in terms of speed, objectivity and sensitivity to subtle changes (*71*). Yet, automated image processing solutions tend to be highly problem-specific, limiting the development of ready-to-use tools that are both broadly generalizable and robust (*71*). Compounding this problem, there is not a clear methodology by which these computational approaches can be applied to solving common problems in mining biological images (*72*). Thus, the development or adaptation of these tools for specific problems has thus far been relatively opaque to many potential end-users and require a high degree of expertise and intuition. Specifically, extraction of meaningful information from biological images usually involves the identification and calculation of metrics about particular structures rather than the usage of global image metrics. Depending on the specimen and the experimental platform, this may range in scale from molecular or sub-cellular structure recognition to the identification of individual cells within a field of view, specific cells or tissues within a heterogeneous specimen or free-moving organisms

within a culture area. While toolsets have already been developed to address some general needs of the biological community (*37, 42, 47, 48*) and powerful, general algorithmic tools exist for pattern and feature discrimination and decision-making (*73-75*), many specific biological image processing problems have been left unaddressed by existing toolsets.

Image analysis algorithms to address these specific individual needs have typically been developed on an *ad hoc* basis and relied on expertise and intuition that made it difficult for general end-users to adapt or generate new solutions to suit individual problems. In contrast, unified approaches and prescribed workflow architectures have the potential to both promote understanding and facilitate customization on the part of end-users and to assist in complex problem solving via formal modularization. This chapter presents a general scheme for the detection of specific biological structures that has the potential to be applied as a basis for solving a diverse set of problems. As opposed to finished, ready-to-use toolsets which address a limited problem definition by design, the image processing workflow devised here has the power to simultaneously address the need for accuracy, problem-specificity and generalizability by promoting the design and customization of toolsets by end-users.

This chapter also demonstrates the application of this formalized approach to specifically address the common image processing challenges associated with automated, high-throughput imaging of *C. elegans*. To address the problems of extracting region-, tissue- and cell-specific information within a multicellular context, image processing algorithms are developed to distinguish the head of the worm under bright-field imaging and enable

specific cell identification under fluorescence imaging. These developments demonstrate the flexibility of the two layer classification framework to accommodate different imaging modalities and disparate biological structures. The resulting toolsets also contribute directing to addressing two fundamental needs for automated studies in the worm and contribute specific concepts and modules that may be applied to a broader range of biological problems.

3.1: Generalizable Architecture for Biological Image Processing

Figure 3.2 outlines the two-tiered classification scheme developed to identify specific biological structures within an image. To identify biological structures of interest, images are first pre-processed to condition the data and generate candidates for the structure of interest. In general, candidates can either be individual pixels or discrete segmented regions generated via a thresholding algorithm applied during pre-processing. In the subsequent two layers of classification, these candidates are quantitatively described by two distinct sets of descriptive features, which may be derived from intuitive metrics designed to mimic human recognition or mathematical abstractions that capture additional information (*73, 76*). These features are mathematical descriptors that help delineate the structure or interest from other candidates and will form the basis for classification in each layer.

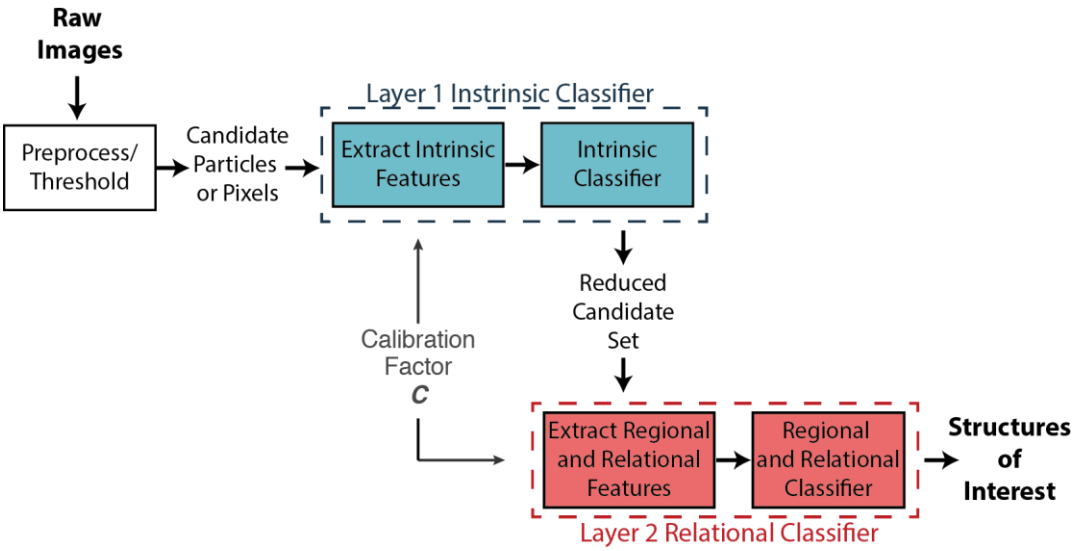

Figure 3.2: Overview of biological structure detection using multi-layered classification. Intrinsic, computationally simple features and relational or computationally expensive features are partitioned into two layers to accommodate both structural complexity and efficiency.

Separation of features into two distinct layers of classification in the classification scheme serves three purposes. First, it permits conceptual separation of intrinsic and extrinsic or relational properties of a biological structure. Second, it permits the inclusion of higher level descriptions of the relationships between structures identified from the first layer of classification. Finally, it reduces the number of times computationally expensive features must be calculated if they are associated with the second layer of classification and thus a reduced candidate set. Accordingly, the first layer of classification uses computationally inexpensive, intrinsic features of the candidates to generate a smaller set of candidates. To both address additional complexity and reduce computation time, computationally expensive features or extrinsic features that involve the relationship between different candidates are reserved for the second layer of classification. Overall, the workflow architecture presented in Figure 3.2 permits the

identification of generic biological structures and balances the capability for describing biological complexity with computational speed.

At each layer of classification, features calculated about each candidate are used in a trained classifier to make a decision about the candidate's identity. To accommodate different image acquisition setups and acquisition parameters in practice, the algorithm in Figure 3.2 utilizes an image calibration factor, C, in feature calculation. This calibration factor characterizes the relationship between the digitized and real-world length scales for a specific experimental setup and can be used to normalize feature and parameter scaling in all image processing steps (Section 1.4.3). With these normalized features, this work utilizes support vector machines (SVM) for all classification steps. SVM is supervised learning approach that involves minimal user input or manual parameter selection and offers relatively general utility due to its insensitivity to specific conditioning of feature sets (*74, 77*). However, for problems where constraints of the feature sets are well known, other models including Bayesian discriminators and heuristic thresholds can also be used.

3.2: Application for Head versus Tail Detection in *C. elegans*

Due to its relatively large size, only a limited portion of the worm body can be captured within the field of view under high resolution imaging and it is necessary to target specific regions along the anterior-posterior axis of the worm to capture specific cells or tissues of interest (Figure 3.3a). Even at lower resolution, it is also often desirable to target stimuli to and understand responses of specific regions of the worm body. Thus, image processing for orientation along the length of the worm is crucial to enabling the full potential of many of the toolsets for high resolution image and physical and optical

manipulation. To address this need, many *ad hoc* tactics such as the presence of fluorescent markers (*32, 33, 37, 43*) or the assumption of forward locomotion in freely moving worms (*42, 51, 78, 79*) are often used delineate between the head and tail and orient the anterior-posterior axis. However, these tactics are strain-specific, impose constraints on the magnification, imaging modality and experimental setup, and therefore lack generalizability. Moreover, image metrics based on fluorescence may cause unnecessary photobleaching of the sample before data acquisition and be confounded by age and condition-specific autofluorescence in the worm body (*80*).

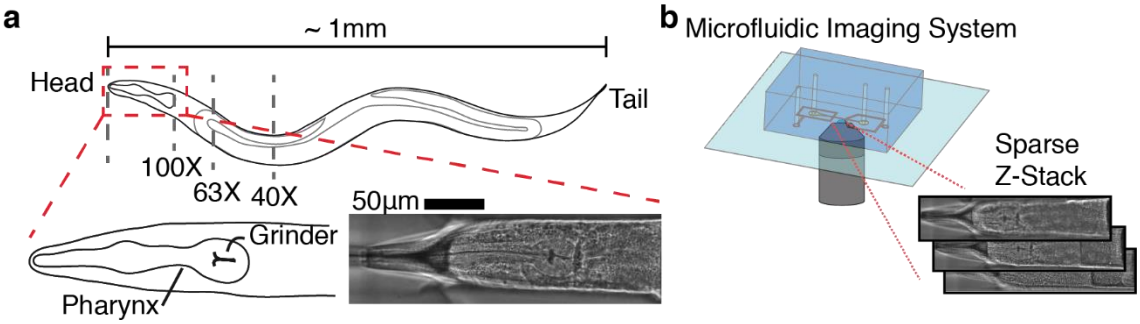

Figure 3.3: The necessity of head versus tail delineation under high resolution imaging. a) The limited field of view of high resolution imaging systems creates a need for spatial positioning along the anterior-posterior axis of the worm. As a landmark for orienting the A-P axis, the head of the worm is distinguished by the presence of the pharynx and a grinder structure (inset below). b) In an automated microfluidic imaging system, a sparse z-stack in bright field may be acquired to accommodate for z-focus uncertainty.

In order to approach this problem without a reliance on a specific experimental framework, there are several consistent morphological differences between the head and the tail of the worm that are observable under bright field imaging. While the shape of the head and the tail differs significantly, these differences are difficult to detect due to low contrast and may be physically obscured by some experimental platforms (*32*). Instead,

the head of the worm is more clearly distinguished by the presence of the pharynx, which has a stereotypical morphology that includes a biological structure for masticating food called the grinder (*81*). As shown in Figure 3.3a, the grinder is a dark, uniquely shaped, high-contrast structure under bright field imaging. This stereotypical feature of the head can serve as the target biological structure for the two layer classification scheme.

To construct and validate the classification solution for automated head versus tail detection, bright field images of the worm head and tail were collected using a custom microfluidic device (Figure 3.3b, Section 3.5). Following the classification architecture in Figure 3.2, application of the scheme involves three major steps: preprocessing of raw images to generate candidates for the structure of interest, selection and calculation of features to describe these candidates at both layers of classification, and optimization and training of the two classifiers based on these feature sets.

3.2.1 Preprocessing and Feature Selection for Pharyngeal Grinder Detection

First, in the preprocessing step, a minimum intensity projection is used to consolidate dark structures of potentially multi-plane bright field images into a single image (MP in Figure 3.4a) and Niblack local thresholding is used to generate discrete binary particles as potential candidates for the grinder (BW_0 in Figure 3.4a). This work utilizes the Niblack local thresholding procedure in both this and the following cell identification application to robustly segment particles despite the potential variability in local lighting, texture and background tissue intensity (Section 3.5). Following initial thresholding, preliminary filtering of the binary particles is then applied to remove segmented regions that are either too small (less than 37.5 μm^2) or too large (greater than 100 μm^2) to reduce

downstream computation (BW_1 in Figure 2b). The remaining particles are processed through the two-layer classification scheme to detect the presence of the pharyngeal grinder.

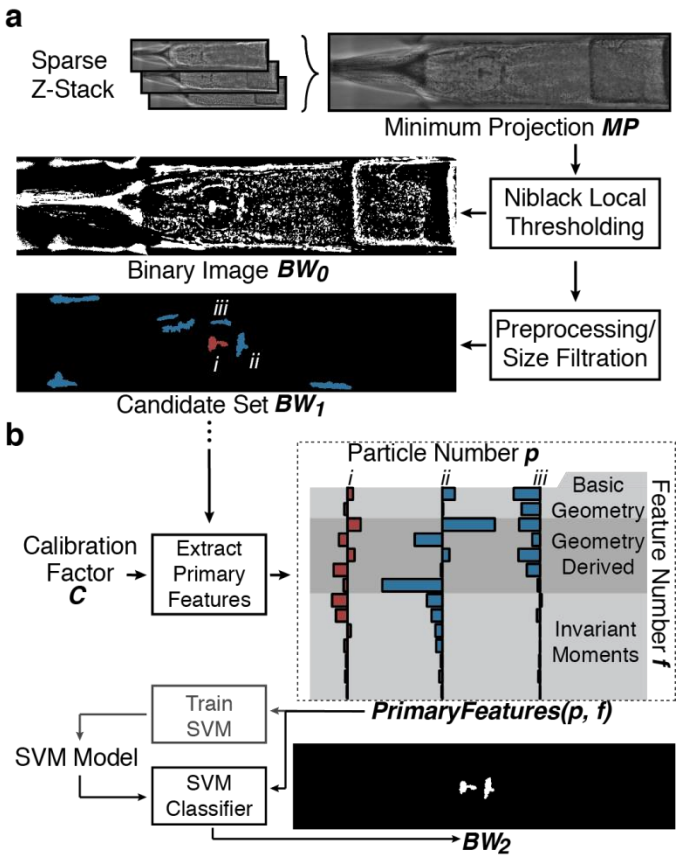

Figure 3.4: Preprocessing and first layer features for pharyngeal grinder detection. a) Preprocessing steps concatenate multi-plane images and binarizes the image to generate candidates for subsequent classification using. b) First layer features are based on describing only the intrinsic properties of each binary particle, which is insufficient to eliminate all non-grinder particles in classification.

Second, in the feature selection step, distinct mathematical features which may help to describe and distinguish the structure of interest are calculated for each layer of classification. In the first layer of classification, intrinsic and computationally

inexpensive metrics of the particles are computed and used as features (Figure 3.4b, Figure 3.5) in classification of the grinder shape. These features represent a combination of simple, intuitive geometric features, such as area and perimeter, in addition to higher level measures of the object geometry and invariant moments suitable for shape description and identification (*76*). Training and application of a classifier with this feature set eliminates candidates on the basis of intrinsic shape (BW_2 in Figure 3.4b).

a

#	Name	Definition	Scaling Factor
1	Area	$\sum_{(x,y)\in R_i} BW(x,y)$	C^2
2	Perimeter	$\sum_{(x,y)\in R_i} P(x,y)$ $P(x,y) = \begin{cases} 1 \text{ if } BW(x,y) = 1 \cap (BW(x\pm1, y\pm1) = 0) \\ 0 \text{ otherwise} \end{cases}$	C
3	Bounding Rectangle Width	$\max(\Delta x_{i,j})$ $\Delta x_{i,j} = x_i - x_j,\ (x_i, x_j) \in R_i$	C
4	Bounding Rectangle Height	$\max(\Delta y_{i,j})$ $\Delta y_{i,j} = y_i - y_j,\ (y_i, y_j) \in R_i$	C
5	Convex Area	$\sum_{(x,y)\in RC_i} 1$	C^2
6	Maximum Feret Diameter	$\max\left(\sqrt{\Delta x_{i,j}^2 + \Delta y_{i,j}^2}\right),\ (x_i, y_i, x_j, y_j) \in R_i$	C
7	Maximum Feret Diameter Orientation	$\tan^{-1}\left(\frac{\Delta y_{max}}{\Delta x_{max}}\right)$ $\Delta x_{max}, \Delta y_{max} = \arg\max_{\Delta x, \Delta y}\left(\Delta x_{i,j}^2 + \Delta y_{i,j}^2\right), (x_i, y_i, x_j, y_j) \in R_i$	-
8	Hu Moment 1	$\eta_{20} + \eta_{02}$	-
9	Hu Moment 2	$(\eta_{20} - \eta_{02})^2 + 4\eta_{11}^2$	-
10	Hu Moment 3	$(\eta_{30} - 3\eta_{12})^2 + (3\eta_{21} - \eta_{03})^2$	-
11	Hu Moment 4	$(\eta_{30} + \eta_{12})^2 + (\eta_{21} + \eta_{03})^2$	-
12	Hu Moment 5	$(\eta_{30} - 3\eta_{12})(\eta_{30} + \eta_{12})[(\eta_{30} + \eta_{12})^2 - 3(\eta_{21} + \eta_{03})^2] + (3\eta_{21} - \eta_{03})(\eta_{21} + \eta_{03})[3(\eta_{30} + \eta_{12})^2 - (\eta_{21} + \eta_{03})^2]$	-
13	Hu Moment 6	$(\eta_{20} - \eta_{02})[(\eta_{30} + \eta_{12})^2 - (\eta_{21} + \eta_{03})^2] + 4\eta_{11}(\eta_{30} + \eta_{12})(\eta_{21} + \eta_{03})$	-
14	Hu Moment 7	$(3\eta_{21} - \eta_{03})(\eta_{30} + \eta_{12})[(\eta_{30} + \eta_{12})^2 - 3(\eta_{21} + \eta_{03})^2] - (\eta_{30} + 3\eta_{12})(\eta_{21} + \eta_{03})[3(\eta_{30} + \eta_{12})^2 - (\eta_{21} + \eta_{03})^2]$	-

$$C = \frac{(Sensor\ Pixel\ Size)(Binning)}{(Optical\ Magnification)}$$

$$\mu_{pq} = \sum_x \sum_y (x - \bar{x})^p (y - \bar{y})^q$$

$$\eta_{pq} = \frac{\mu_{pq}}{\mu_{00}^{\gamma}}, \gamma = \frac{p+q}{2} + 1$$

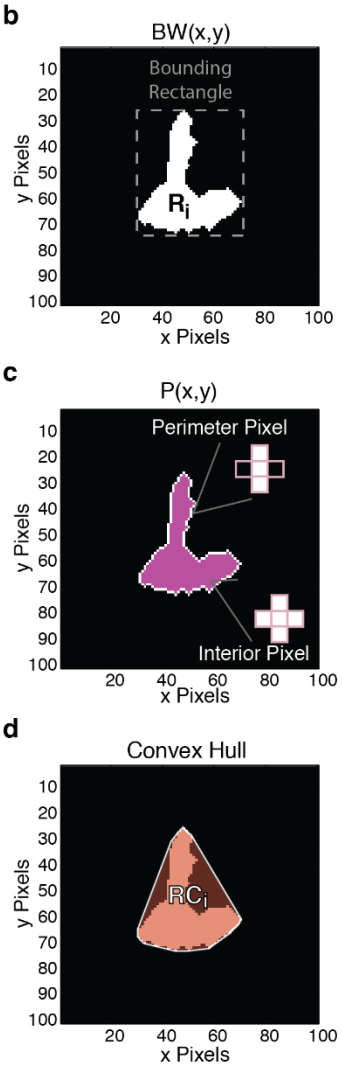

Figure 3.5: Robust descriptors for binary particle shape for layer 1 of classification scheme. a) Table of 14 features for binary shape description including low-level geometric descriptors, more complex derived measures of geometry and invariant moments. b) Diagram of binary particle indicating variables used for feature definition. c) Illustration and example of defining and calculating the perimeter of an irregular particle based on pixel connectivity. d) Illustration and example of the convex hull of a binary particle.

The resulting false positives in Figure 3.6a show that the information within the shape metrics used in layer 1 is insufficient to distinguish the grinder with high specificity. To refine the description of the biological structure in the second layer classification,

features that describe the relationship of candidate particles to nearby particles and texture are utilized (Figure 3.6b). Specifically, the grinder resides inside the terminal bulb of the pharynx, which is characterized by a distinct circular region of muscular tissue (Figure 3.3a). Based on this observation, second layer features are defined based on distributions of particle properties within a circular region around the centroid of the grinder candidate particle. Noting that the pharyngeal tissue is characterized by textural ranges in the radial direction and relative uniformity in the angular direction, layer 2 features describe both the radial and angular distributions the surrounding particles (Figure 3.7).

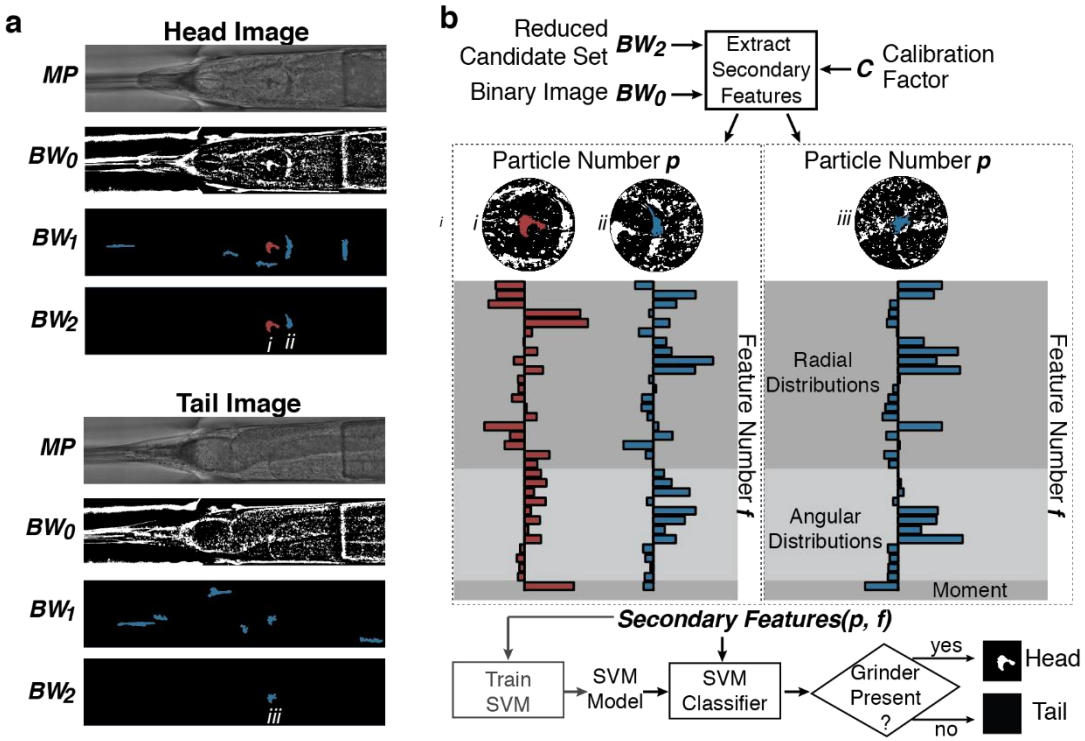

Figure 3.6 Utilization of second layer region features to refine classification of grinder structure. a) Classification based on the intrinsic shape of binary structures is insufficient to fully eliminate background particles and cannot adequately distinguish the head and the tail of the worm. b) Regional properties of the grinder used in layer 2 classification refine this classification decision to permit accurate head and tail detection.

a

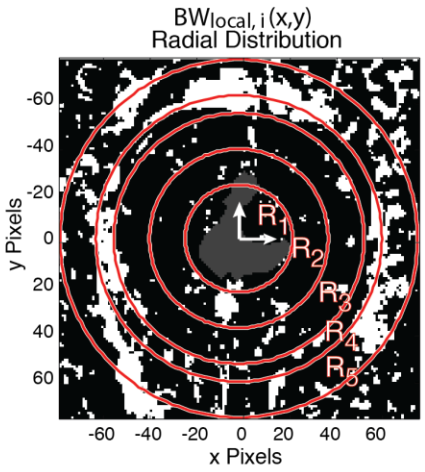

b

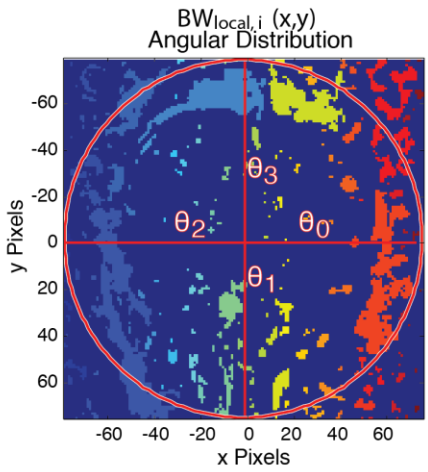

c

#	Name	Definition	Scaling Factor	Other Definitions
1-5 $i = 0 \ldots 4$	Radial Distribution of Binary Area	$RArea_i = \sum_{R_i \le r < R_{i+1}} BW_{local,i}(x,y)$	C^2	$C = \frac{(Sensor\ Pixel\ Size)(Binning)}{(Optical\ Magnification)}$ $R = \{0, 7.5, 12.5, 17.5, 20, 25\} \cdot C$ $\theta = \{0°, 90°, 180°, 270°, 360°\}$ x_c, y_c – List of centroid indices for individual particles within $r < R_5$ $r = \sqrt{x^2 + y^2}$, $r_c = \sqrt{x_c^2 + y_c^2}$ $\theta = \tan^{-1}\frac{y}{x}$, $\theta_c = \tan^{-1}\frac{y_c}{x_c}$, $A_{x_c y_c}$ – Areasof particles with centroids at x_c, y_c $P_{x_c y_c}$ – Perimeter of particles with centroids at x_c, y_c
6-10 $i = 0 \ldots 4$	Radial Distribution of Particle Number	$RNumber_i = \sum_{R_i \le r_c < R_{i+1}} 1$	-	
11-15 $i = 0 \ldots 4$	Radial Distribution of Mean Particle Size	$RSize_i = \frac{1}{RNumber_i} \sum_{R_i \le r_c < R_{i+1}} A_{x_c y_c}$	C^2	
16-20 $i = 0 \ldots 4$	Radial Distribution of Mean Particle Circularity	$RCirc_i = \frac{1}{RNumber_i} \sum_{R_i \le r_c < R_{i+1}} \frac{P_{x_c y_c}}{2\sqrt{\pi A_{x_c y_c}}}$	-	
21-24 $i = 0 \ldots 3$	Angular Distribution of Binary Area	$AArea_i = \sum_{\substack{\theta_i \le \theta < \theta_{i+1} \\ r \le R_5}} BW_{local,i}(x,y)$	C^2	
25-28 $i = 0 \ldots 3$	Angular Distribution of Particle Number	$ANumber_i = \sum_{\substack{\theta_i \le \theta_c < \theta_{i+1} \\ r_c \le R_5}} 1$	-	
29-33 $i = 0 \ldots 3$	Angular Distribution of Mean Particle Size	$ASize_i = \frac{1}{ANumber_i} \sum_{\substack{\theta_i \le \theta_c < \theta_{i+1} \\ r_c \le R_5}} A_{x_c y_c}$	C^2	
34	Normalized Moment of Inertia	$\frac{\sum_{r \le R_5} BW(x,y) \cdot r^2}{R_5^2 \sum_{r \le R_5} BW(x,y)}$	-	

Figure 3.7: Regional descriptors for structural detection of the pharyngeal grinder. a) Diagram of the region of interest around a grinder particle showing changes in texture and particle density along radial partitions. b) Diagram of the region of interest around a grinder particle distinguishing individual particles using different colors and showing particle distributions along angular partitions. c) Table of 34 features used to describe regional characteristics of the grinder particle for the second layer of classification.

3.2.2 Training of Support Vector Machine Classification Model

Using the features outlined in the previous section, each classification step is a mathematical model that is trained to distinguish between structures of interest such as the pharyngeal grinder and irrelevant structures generated represented the textures and boundaries of other tissues in the worm. To allow for supervised training of both the layer 1 and layer 2 classifiers, a training set is constructed by manually identifying particles that represent the pharyngeal grinder in a selection of images (n=1430). The classifiers can then be trained to associate properties of the feature sets with the manually specified identity of candidate particles. However, in addition to informative feature selection and the curation of a representative training set, the performance of SVM classification models is subject to several parameters associated with the model itself and its kernel function (*74*, *82*) Thus, to ensure good performance of the final SVM model, model parameters are first optimized based on five-fold cross-validation on the training set Figure 3.8, Section 3.5).

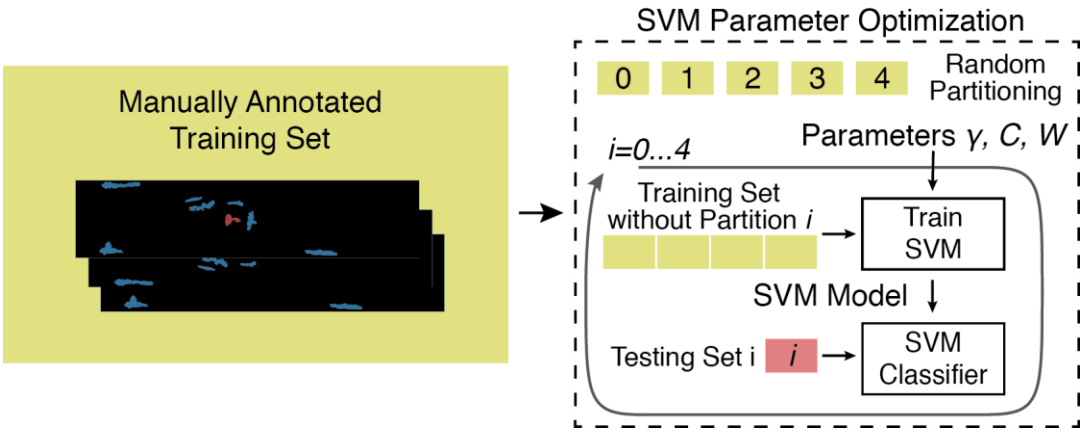

Figure 3.8: Schematic of SVM parameter optimization via five-fold cross-validation. Training sets are partitioned into five random sets which are each used as validation testing sets for five iterations of SVM model training and classification. Accuracy estimates derived from this process are used to select appropriate parameters for the SVM model.

Within the parameter selection process, the optimization metric can be design to reflect the goals of classification in each layer (Figure 3.9a). For the first layer of classification, the goal is to eliminate the large majority of background particles while retaining as many grinder particles in the candidate pool as possible for refined classification in the second layer. Therefore, SVM parameters are optimized via the minimization of an adjusted error rate that penalizes false negatives more than false positives (Figure 3.9a). With an appropriate parameter selection, the first layer of classification can eliminate over 90% of background particles while retaining almost 99% of the true grinder particles for further analysis downstream. (Figure 3.9a).

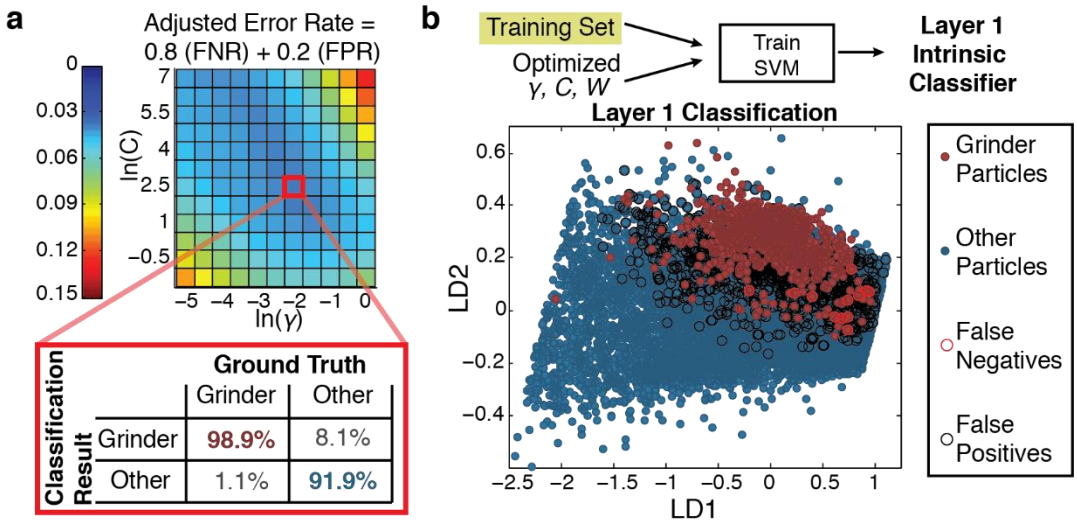

Figure 3.9: Parameter optimization and performance for first layer pharyngeal grinder classifier. a) Grid search of SVM parameters using an adjusted error rate that penalizes false negatives. b) Linear Discriminant Analysis visualization of the classification performance of the first layer SVM classifier trained with optimized parameters shows relatively high false positive rate.

To visualize feature and classifier performance, Fisher's linear discriminant analysis is employed to linearly project the 14 layer 1 features of the training set onto two dimensions that show maximum separation between grinder and background particles (Figure 3.9b). Significant overlap between the grinder particles and background particles in this projection suggest that shape-intrinsic features are insufficient to fully describe the grinder structure. Nevertheless, the first layer of classification enriches the true grinder structure candidates in the training set from roughly 6.2% of the original particle set to 40% of the particle set entering into the second layer of classification (Figure 3.9b). This enriched set of candidate particles is used to optimize and train the second layer of classification in a similar manner (Figure 3.10a). With appropriate parameter selection, the second layer of classification is capable of identifying the grinder with sensitivity and

specificity above 95% (Figure 3.10b). The final layer 2 classifier is trained with the reduced training set and these optimized parameters to yield high classification performance in combination with layer 1 (Figure 3.10c).

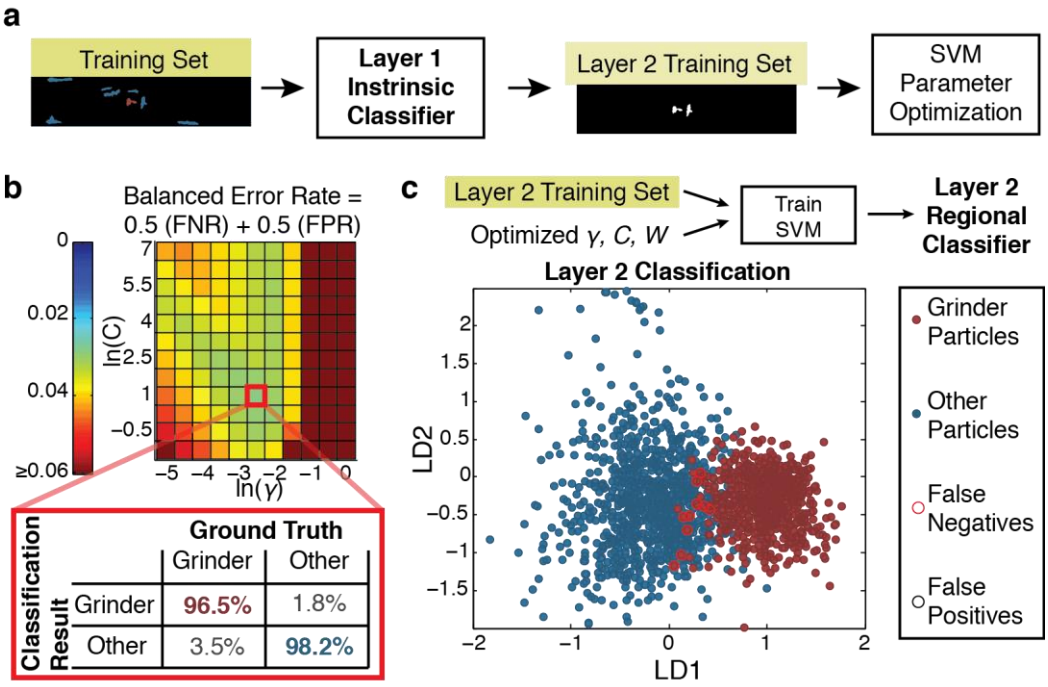

Figure 3.10: Parameter optimization and performance of the second layer of classification for pharyngeal grinder detection. a) Operating in cascade with the layer 1 classifier, the layer 2 training set consists of particles that are passed by layer 1 classification. b) Grid search of SVM parameters using a balanced error rate. c) Linear Discriminant Analysis visualization of layer 2 classifier performance demonstrates both high sensitivity and specificity.

3.2.3 Pharyngeal Grinder Classifier for Head versus Tail Detection

In spite of the performance of the classifier within the training set of images (Figure 3), the performance of the classifier in practice may be altered by changes in experimental conditions, the genetic background of the worms under study or changes to the imaging system. To account for some of this potential variability, worms imaged at different ages

and food conditions are included within the training set of images. To validate the utility the resulting classification scheme in practice, its performance is analyzed on new data sets acquired under difficult conditions. First, in spite of morphological changes due to experimental conditions (Figure 3.11a), the resulting classification scheme operates with consistently high performance in distinguishing the head and the tail of the worm in new testing data sets (Figure 3.11b). Second, while the training set only includes wildtype worms imaged under different conditions, the morphology and texture of the worm is also subject to genetic alteration (Figure 4c). To see whether the classification scheme can accommodate some of this genetic variability, the classification scheme was also validated against a mutant strain (*dpy-4(-)*) with large morphological changes in the body of the worm (Figure 3.11c). Finally, changes in the imaging system can alter the effective magnification and final digital representation of biological structures of interest (Figure 4e). The inclusion of a calibration factor adjusting for the pixel to micron conversion of the imaging system is sufficient for maintain classifier operation across a two-fold change in the effective magnification of the system (Figure 3.11g).

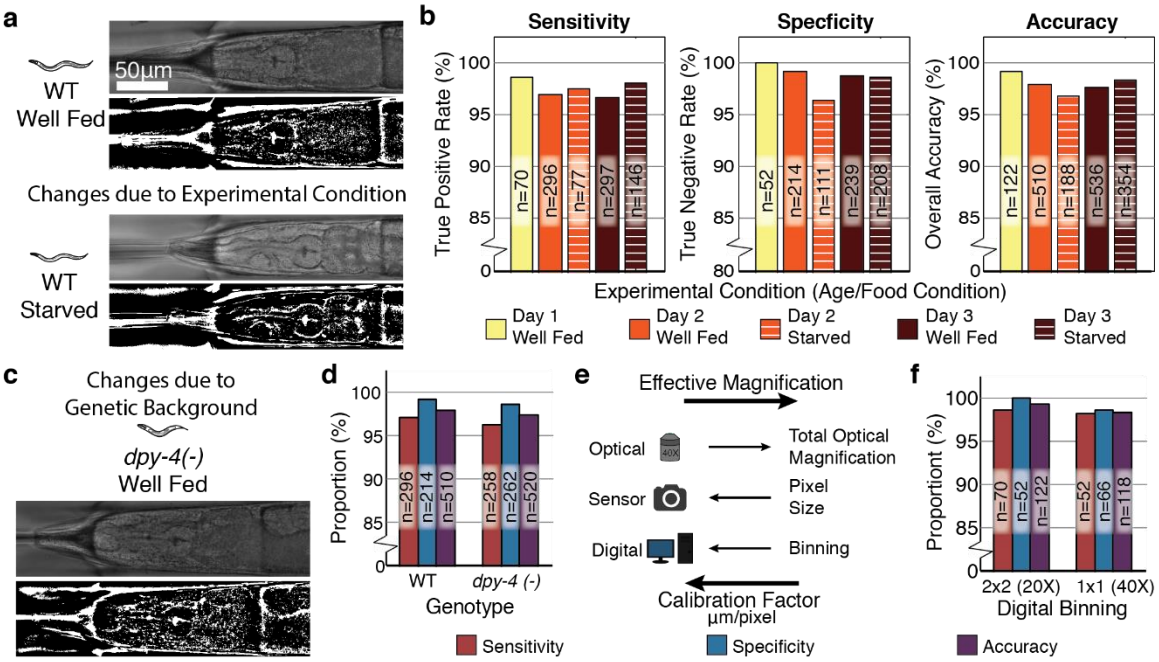

Figure 3.11: Head versus tail classification using grinder detection is robust to changes in experimental conditions and genetic background. a) Changes in experimental conditions, such as food availability, can alter the bulk morphology and the appearance of worm body in bright field, with potential consequences for classification accuracy. b) The head versus tail classification scheme maintains sensitivity and specificity at over 95% at different ages and feeding conditions despite these biological changes. c) Genetic changes can also induce changes in bulk morphology and texture of the worm. d) Despite not being represented within the training set, the performance of the classifier is maintained even for mutant worms (dpy-4 (-)) with major morphological changes. e) Changes in the optics, camera or acquisition parameters can alter the effective magnification and digitization of images. f) The inclusion of the calibration metric within feature calculation (Supplementary Figures 1 and 2) maintains classifier performance across a two-fold change in effective magnification due to alternations in digital binning.

3.3: Application for Cell-Specific Identification in *C. elegans*

The identification of the pharyngeal grinder and the ability to target imaging and stimulation along the anterior-posterior axis of the worm provides only provides rough anatomical resolution. To understand biological phenomena within a multi-cellular

context, cell-specific resolution is often needed to dissect individual components of organismal responses and functions. In particular, specific neuronal responses are important understanding information processing and coordination of biological function in a multicellular context. While such detailed information of neuronal function is difficult to obtain in mammalian models, the transparency and highly stereotypical nervous system of the worm makes it a convenient model to understand the nervous system. Yet, despite the demonstrated importance of understanding neuron-specific information processing in *C. elegans* (*15, 83-86*), these studies have relied on manual data extraction, which have limited the speed and breadth of these studies. To address this limitation, this work will develop a framework for neuronal cell identification within the worm with the aim of enabling fast, automated data extraction to accelerate these studies.

3.3.1 Single Cell-Pair Detection

A growing set of genetically encoded fluorescent reporters have increased the ability to obtain functional neuronal readouts from intact worms via fluorescence imaging (*43, 69, 70, 79*). To accelerate data extraction and enable automated experimentation with these new techniques, this work applies the two layer classification scheme in Figure 3.2 to the identification of neurons within fluorescently labelled images. In particular, many neurons in *C. elegans* are organized as bilaterally symmetric pairs of cells in the head region of the worm near the pharynx (Figure 3.12a) (*83*). As a stereotypical example of a bilaterally symmetric neuron pair, this work will first focus on the identification of the ASI neurons, a sensory pair of cells that have been implicated to be important environmental encoding and the coordination of appropriate physiological responses (*15,*

18, *83*, *86*). Figure 3.12b shows a corresponding set of bright field and fluorescent images showing the positioning of the neuron pair within the head region of the worm. The power of fluorescent reporters to provide functional readouts depends on the ability to accurately assessing intensities. The fluorescent maximum intensity projection in Figure 3.12b demonstrates that identification and extraction of intensities from specific cellular regions is important for eliminating confounding intensity effects from background autofluorescence.

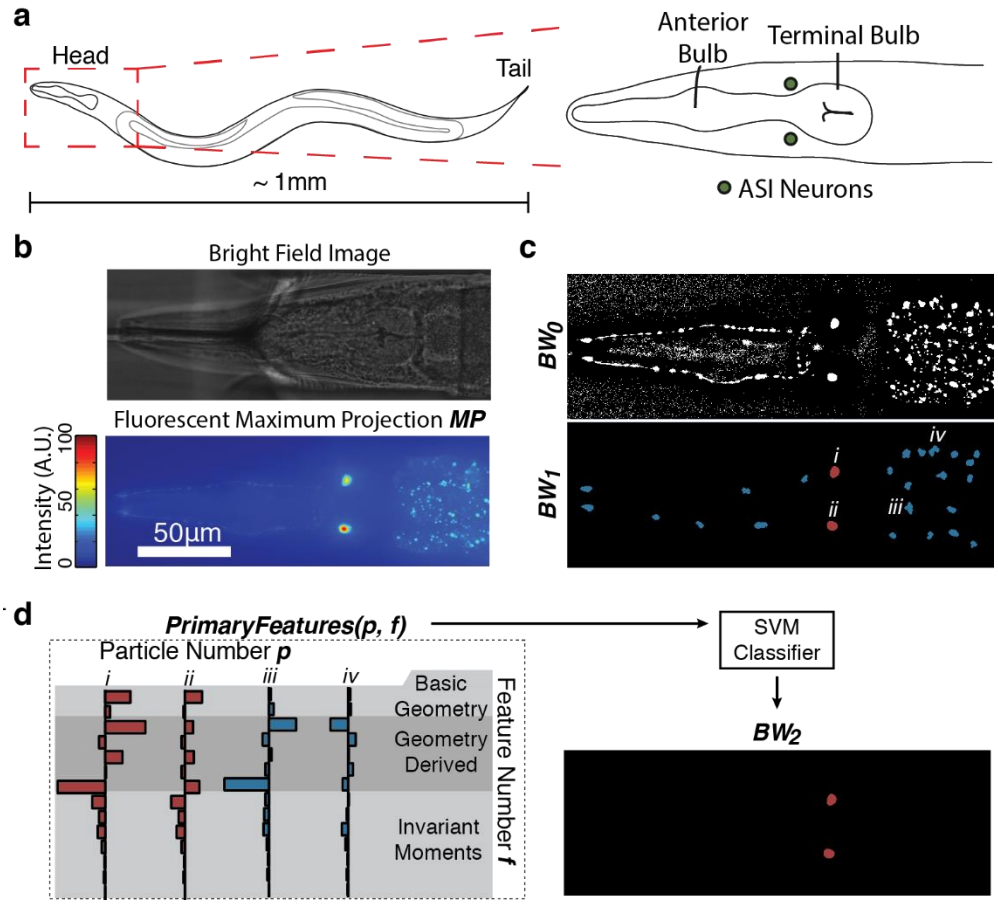

Figure 3.12: First layer classification for detection of fluorescently labelled neuronal cells demonstrates generalizability of first layer features for particle shape classification. a) Stereotypical positioning of the ASI neuron pair in the head of the worm. Many neuronal cells in the worm are organized as similar pairs near the pharynx. b) Bright field and fluorescent maximum intensity projection showing the appearance and positioning of fluorescently labelled ASI cells in the head of the worm. c) Preprocessing of raw fluorescent images showing binary image after Niblack thresholding (BW_0) and initial filtration of the candidate set by size (BW_1). d) First layer classification of fluorescently labeled neurons shows good generalizability of the first layer feature set developed for pharyngeal grinder detection for classification based on binary particle shape.

Again following the architecture from Figure 3.2, the construction of the cell identification toolset begins with preprocessing of the raw images by maximum intensity projection, Niblack thresholding and preliminary filtering of the resulting candidate

particles (Figure 3.12c, Section 3.5). In the selection of features for both layers of classification, this work takes advantage of the fact that the layer 1 feature set constructed for the detection of the pharyngeal grinder can be generally applied to the description of particle shape within other contexts (Figure 3.5). Using this feature set, a layer 1 SVM classifier is optimized and trained using a manually annotated training set (n=218) (Figure 3.13, Section 3.5). The resulting classifier is sufficient for identifying cellular regions with relatively high sensitivity and specificity (Figure 3.12d, Figure 3.13).

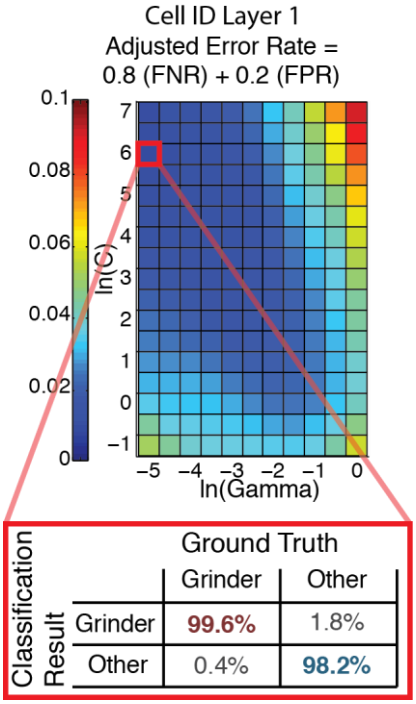

Figure 3.13: Parameter selection for the first layer of classification for fluorescent cell pair identification.

While layer 1 classification succeeds in eliminating many irrelevant background particles generated by the thresholding process, variable background intensity within the tissues surrounding the neurons can generate confounding binary particles that pass layer 1

classification (Figure 3.14a). To make a final identification of a true cell pair, a second layer of classification is applied based on the properties of candidate pairs of particles that pass layer 1 classification (Figure 3.14b). To describe the spatial arrangement and relative intensities of the cell pairs, the relative distances between the candidate neuron centroids and normalized mean intensity values for each candidate in the pair are used as features (Figure 3.14b). A detailed description of this relational feature set can be found in Figure 3.15. Unlike the secondary feature set for pharyngeal grinder detection (Figure 3.6, Figure 3.7), the relational features calculated for the candidate pairs are computationally simple. However, embedding relational features on the second layer of classification dramatically reduces the size of the paired candidate set. For example, for detection of cell pairs amongst n particles, there are $\binom{n}{2} = \frac{n!}{2(n-2)!}$ possible candidate pairs that require feature calculation.

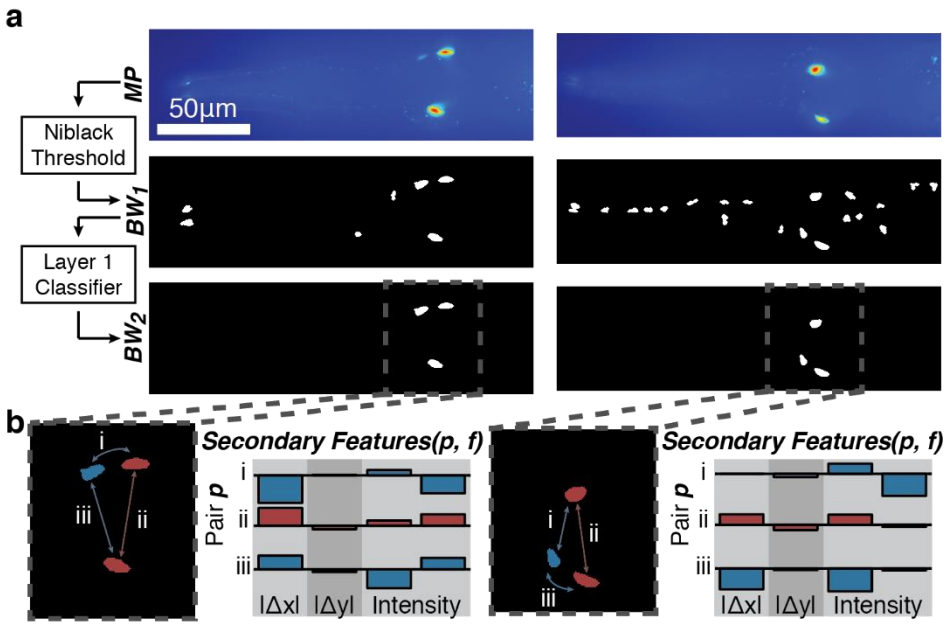

Figure 3.14: Relational features for second layer classification of neuron pairs. a) The first layer of classification is insufficient for rejection of all background particles. b) The reduced candidate set from the first layer of classification is used to form candidate cell pairs with feature sets describing their relative positioning and intensities

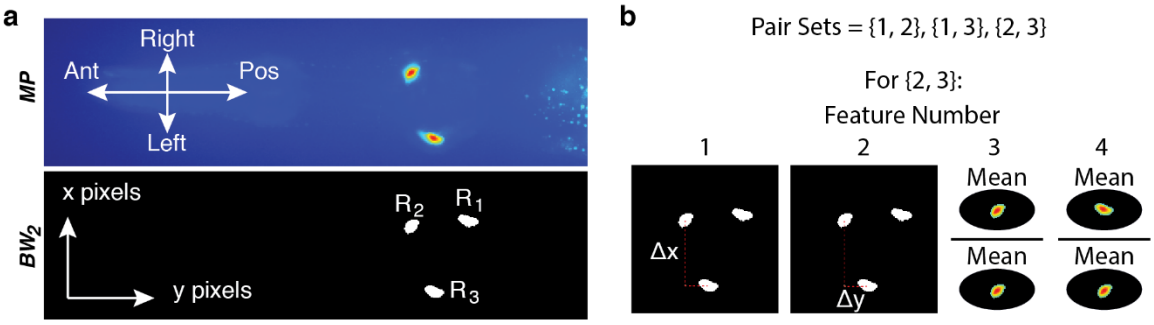

c

#	Name	Definition For Pair *{i, j}*	Scaling Factor	Other Definitions
1	Separation along the Left-Right Axis	$\lvert x_{c,i} - x_{c,j} \rvert$	C	$C = \frac{(Sensor\ Pixel\ Size)(Binning)}{(Optical\ Magnification)}$ x_c, y_c – List of centroid indices for individual particles I – List of mean intensities for individual particles $I_i = \frac{\sum_{(x,y)\in R_i} MP(x,y)}{\sum_{(x,y)\in R_i} BW_2(x,y)}$
2	Separation along the Anterior-Posterior Axis	$\lvert y_{c,i} - y_{c,j} \rvert$	C	
3	Normalized Intensity of Neuron 1	$\frac{I_i}{\max(I)}$	-	
4	Normalized Intensity of Neuron 2	$\frac{I_j}{\max(I)}$	-	

Figure 3.15: Relational features for pairs of neurons. a) Maximum intensity projection (MP) and binary image (BW_2) showing candidate particles after the first layer of classification with relevant axes and regions labeled. b) Identification of possible pairs for feature calculation and schematic of an example feature set for one pair. c) Table of the four relational features used to describe cell pair patterns.

To construct the layer 2 classifier, parameter optimization for the SVM model is done via five-fold cross-validation (Figure 3.16a) and these optimal parameters are used in training of the layer 2 classifier. In validation of the classifier against new test images, robust single cell pair detection occurs in the majority of cases (Figure 3.16b, left). However, in a minority of cases, multiple candidate pairs are identified as potential neuron pairs in each image (Figure 3.16b, right). In this case, the derivation of probability estimates from the SVM classifier (*77, 87*) and the selection of the most likely candidate in images with multiple positive classification results eliminates these false positives and boosts the

specificity of the classifier without compromising the high sensitivity (Figure 3.16c). This additional step incorporates the real-world constraint that, at most, one cell pair exists in each valid image and resolves any conflicts that may arise in direct classification.

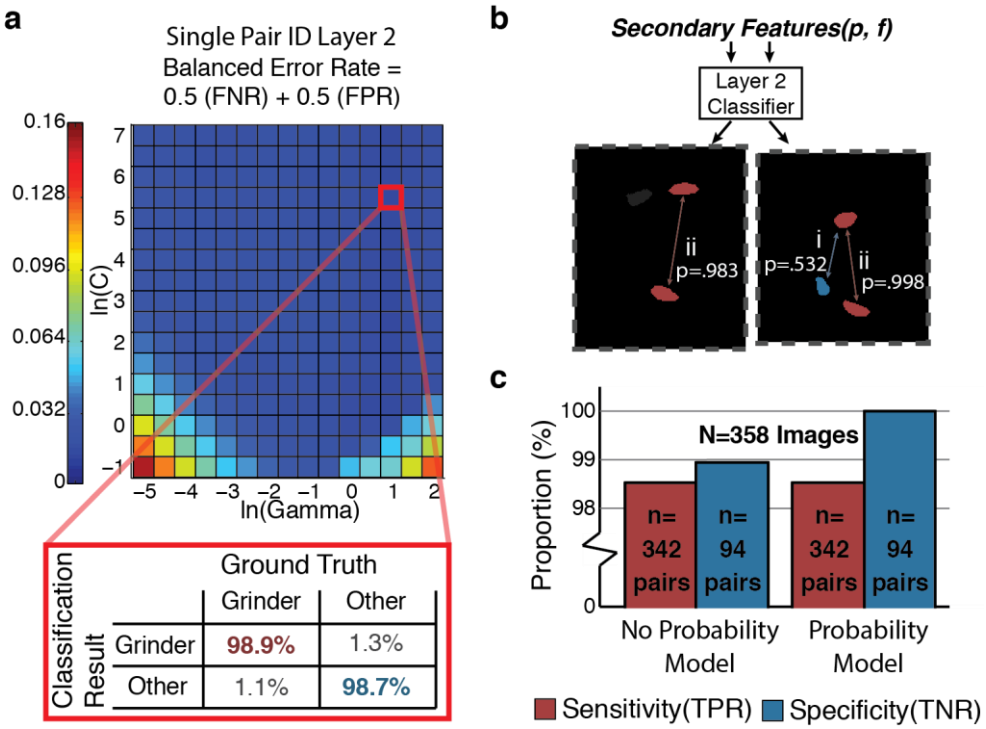

Figure 3.16: Optimization and performance of the second layer classifier for neuron pair detection. a) Parameter optimization for the second layer of classification for fluorescent cell pair identification. b) Although the second layer classifier is sufficient for accurate cell pair detection in the majority of cases (left), multiple potential cell pairs are sometimes classified within the same image (right). d) Incorporating probability estimates (shown in panel b) into the SVM model and selecting the most likely cell pair eliminates these false positives and increases the specificity of the classifier.

3.3.2 Multiple Cell-Pair Detection

The identification of single neuron pairs has the ability to facilitate neuron-specific information extraction for many applications in *C. elegans*. However, due to the

prevalence of bilaterally symmetric neuron pairs within the head of worm (*83*), applications where functional readouts are simultaneously acquired in multiple neuron pairs are also common. Figure 3.17a shows the expression pattern of a worm insulin-like protein (*ins-6*) in two bilaterally symmetric neuron pairs in the head of the worm (*85*). While this problem can be partially addressed via the use of multiple color channels and cell-specific promoters to facilitate cell identification, effective cell identification via pattern recognition can serve as a complementary technique that eases complexity in experimental design. Taking advantage of the modular two layer architecture, the neuron pair identification scheme developed previously can be extended to the detection of more complex cellular arrangements using the preprocessing and first layer classification tools that have already been constructed (Figure 3.17b).

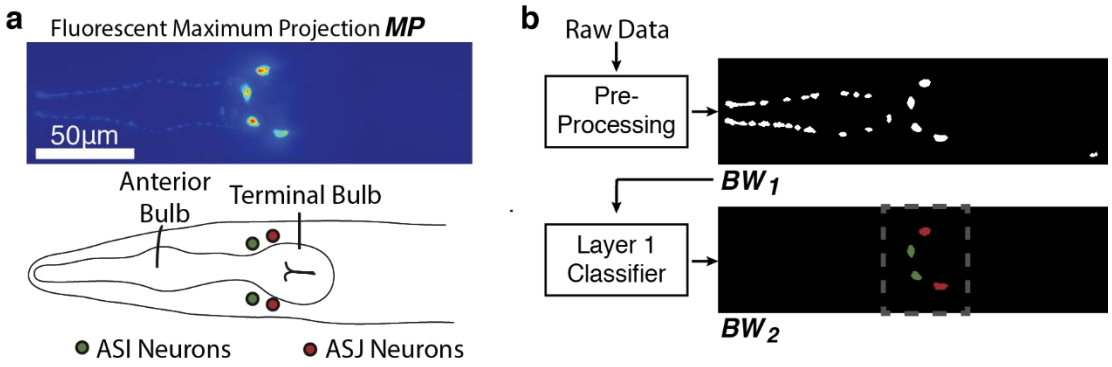

Figure 3.17: Utilization of modular layer 1 classifier for multiple cell pair detection. a) Fluorescent maximum projection and schematic showing ins-6 expression in two pairs of neurons. b) The same layer 1 classifier developed for single cell pair detection can be applied to this extended problem.

While the first layer of classification is based on the intrinsic features of cells themselves and can be re-utilized regardless of the cellular arrangement, the second layer of classification is based on relational features and is therefore highly problem-specific. To

detect the tetrad of cells with specificity for the ASI and ASJ neuron pairs as shown in Figure 3.17, a relational feature set based on combinations of neuron pairs is constructed (Figure 3.18). The mathematical details of these features are given in Figure 3.19. As shown in Figure 3.18 and 3.19b, accounting for both correct cell pair identification and non-repetition of individual cells within the tetrad set, there are $\binom{n}{2}\binom{n-2}{2} = \frac{n!}{4(n-4)!}$ tetrad sets that require feature calculation. The two layer architecture formalized in this work is therefore essential for the construction of such relational feature sets. Without layer 1 classification, description of such complex sets quickly becomes intractable: even 10 candidate particles generates 1260 different possible tetrad sets for feature calculation.

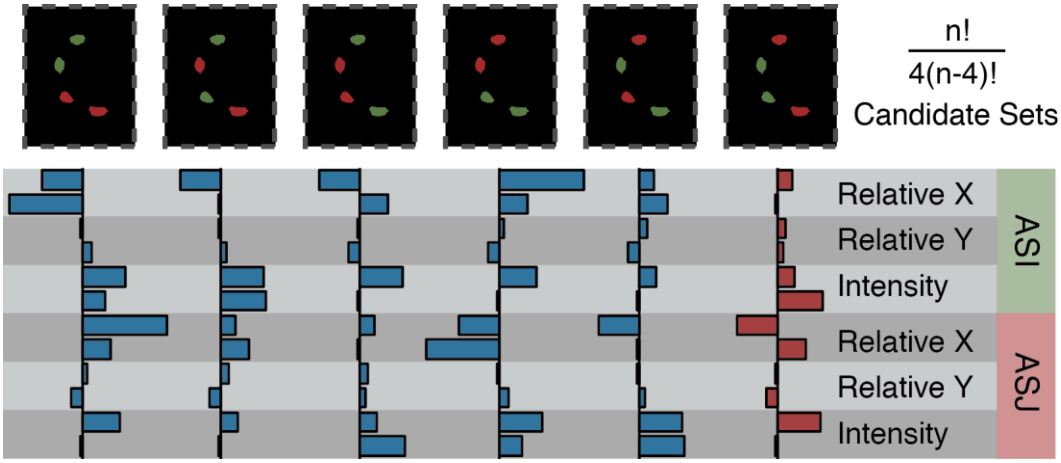

Figure 3.18: Overview of second layer feature set for detection of tetrad arrangement of two neuron pairs. Relational features are calculated for all potential arrangements of cells with different cell pair identifications.

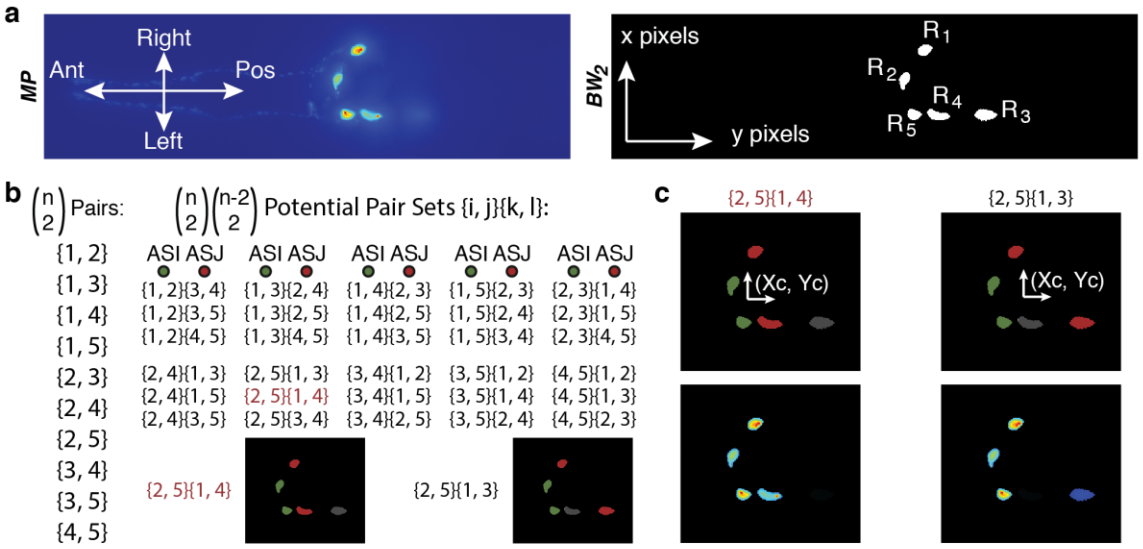

c

#	Name	Definition For Pair Set *{i, j, k, l}*	Scaling Factor	Other Definitions
1	Location of Neuron 1 Relative to the Set Centroid along Left-Right Axis	$x_{c,i} - X_c$	C	$C = \frac{(Sensor\ Pixel\ Size)(Binning)}{(Optical\ Magnification)}$ x_c, y_c – List of centroid indices for individual particles X_c, Y_c – Centroid of the set of 4 cells $X_c = \frac{1}{4}(x_{c,i} + x_{c,j} + x_{c,k} + x_{c,l})$ $Y_c = \frac{1}{4}(y_{c,i} + y_{c,j} + y_{c,k} + y_{c,l})$ I – List of mean intensities for individual particles $I_i = \frac{\sum_{(x,y)\in R_i} MP(x,y)}{\sum_{(x,y)\in R_i} BW_2(x,y)}$
2	Location of Neuron 2 Relative to the Set Centroid along Left-Right Axis	$x_{c,j} - X_c$	C	
3	Location of Neuron 1 Relative to the Set Centroid along Anterior-Posterior Axis	$y_{c,i} - Y_c$	C	
4	Location of Neuron 2 Relative to the Set Centroid along Anterior-Posterior Axis	$y_{c,j} - Y_c$	C	
5	Normalized Intensity of Neuron 1	$\frac{I_i}{\max(I)}$	-	
6	Normalized Intensity of Neuron 2	$\frac{I_j}{\max(I)}$	-	
7 … 12	Feature 1…6 for Pair *{k,l}*			

Figure 3.19: Relational features for multiple cell pair detection and identification. a) Maximum intensity projection (MP) and binary image showing candidate particles after layer 1 classification (BW_2) with relevant axes and regions labeled. b) Enumeration of the possible neuron pairs and the possible sets of neuron pairs with correct distinction between the ASI and ASJ pairs. c) Schematic showing the frame of reference (X_c, Y_c) for the calculation of the relative location of each neuron and the intensities of the neurons within two particular sets. d) Table showing that 6 properties are calculated for each neuron pair, resulting in a total of 12 relational features to identify the tetrad of neurons.

To construct a second layer classifier to detect the tetrad arrangement of cells, a new SVM model is optimized and trained based on a manually annotated training set (n=324) (Figure 3.20a). Subsequent validation of the two layer classifier against new test images shows that the two layer classification scheme operates with high specificity but relatively low sensitivity in comparison to the single cell pair classification problem (Figure 3.20b). Further analysis of the classifier performance within the test set of images shows that this low sensitivity is mainly due to more degrees of freedom for biological variability associated with this particular image processing problem. As shown in Figure 3.20c, while the second layer classifier accommodates some deviation from the stereotypical arrangement of the neurons shown in Figure 3.17a (positive identification on the left), maintenance of high classifier specificity necessitates the rejection of larger deviations (negative identification on the right). While this precludes automated data extraction from some images that may be usable in the context of manual annotation, it also serves the more important purpose of reducing the possibility misidentification and erroneous data.

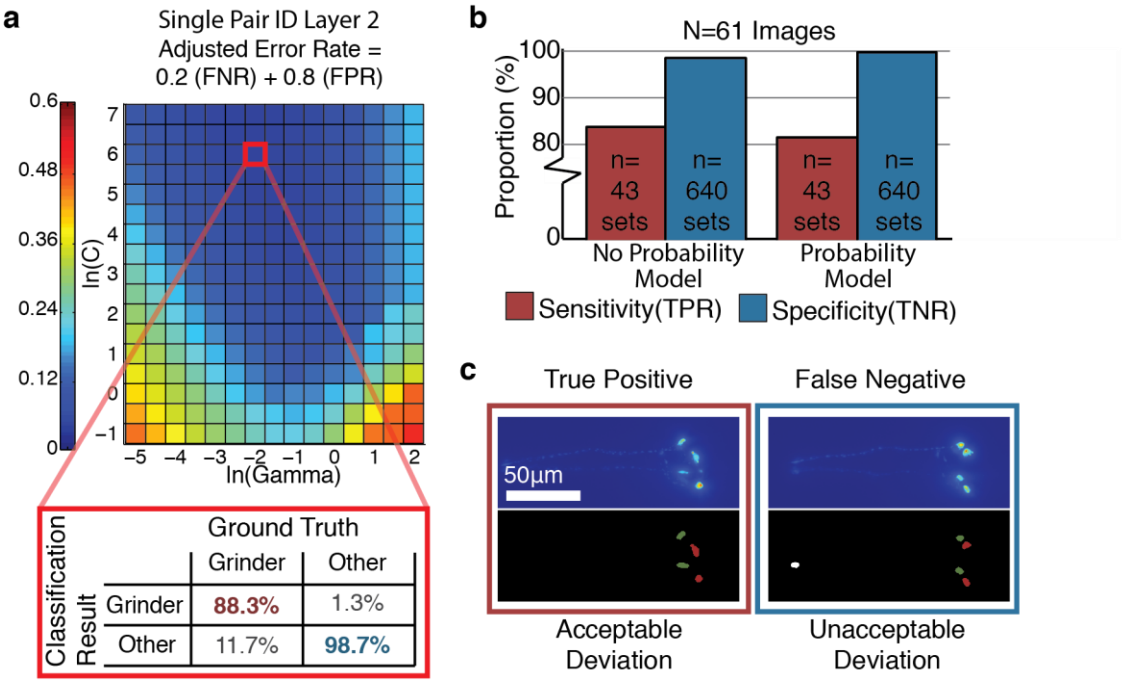

Figure 3.20: Optimization and performance of the second layer classifier for detection of two neurons pairs. a) Parameter optimization for the second layer classifier in the identification of two cell pairs. b) Validation of the SVM classifier shows high specificity but only moderate sensitivity. c) The lower sensitivity observed for this classification scheme is mainly due to the limit ability to accommodate biological deviations from the stereotypical arrangement of the neurons while still maintaining high specificity.

3.4: Discussion and Conclusions

This work has demonstrated the flexibility and computational benefits of a formal two layer architecture in handling two disparate image recognition problems. Using this pipeline, two specific tools have been developed to address common image processing problems in the *C. elegans* community. The contribution of a ready-to-use head versus tail classification scheme under bright field imaging enables automated high resolution imaging and stimulus application in a large range of biological experiments in the worm. The neuronal cell pair identification application forms the basis for approaching the general problem of cell-specific information extraction within a multicellular context

such as the worm. Together, these tools permit automated visual dissection of the multicellular worm at different resolutions that range from the targeting of rough anatomical regions to cell-specificity.

The two specific applications also highlight the effectiveness of the algorithm in segregating complex image recognition problems in both a computationally effective and conceptually convenient manner. In the detection of the pharyngeal grinder, two layer construction reduced the computation a large set of regional descriptors by associating them with the second layer of classification and therefore a smaller candidate set. In cell identification, reserving relational properties for the second layer of classifications dramatically reduced the number of pairs or sets for which relationships must be described. The two applications also demonstrate that the segregation of intrinsic and secondary or extrinsic properties of a structure onto two layers of classification reserves many problem-specific features for the second layer and renders the first layer feature set relatively generalizable. Moreover, this work demonstrated that by incorporating a calibration factor to normalize feature calculation, these classifiers can be adapted to different optical systems and sensor configurations with only the modification of the calibration factor itself (3.11f).

In both layers of classification, this work adopts a supervised learning approach that depends upon human annotation of training sets of data. This approach imposes user-defined structure onto the data-extraction problem and promotes familiarization with the condition and fundamental limitations on the information content of imaging datasets (*72, 88*). Moreover, having a small set of manually annotated images allows for the

assessment of the reliability of the final analysis (*72*). Thus, the user exercises control over higher level problem structure including the formulation of the overall classification question, the choice of the type of candidates and the features used. However, to constrain the construction of the solution, the specific workflow presented here and the integration of computational techniques that bypass much of the manual guesswork. Annotation and calculation of quantitative descriptors about particle or pixel candidates captures multivariate information about different structures. The use of this multivariate information with a classification model such as SVM obviates the need for manually assessing rectilinear thresholds for classification. Moreover, the performance of the resulting classifiers demonstrate that the potentially nonlinear, multi-dimensional classification provided by SVM prove more powerful than rectilinear thresholding of individual features or dimensionality reduction techniques (Figures 3.9b and 3.10c). Overall, methodology presented in this work provides a pipeline that streamlines and formalizes the image processing steps after the annotation of a training set.

Finally, while application of the framework will require feature selection and training for each particular application, the modularity and architecture of the framework permits aspects of the specific tools developed here to be reused. For example, the generalizability of the layer 1 feature set for binary particle classification has been established and can be used to train classifiers for the identification of different shapes. In general, the construction of the classification scheme affords layer 1 classifiers more general applicability. For example, the layer 1 classifier constructed in the cell identification scheme can be reused for the classification of different downstream cellular

arrangements. Even for the second layer of classification, where feature sets are problem-specific, this work has provided examples of both regional and relational feature set constructions that can form the basis of feature sets for other problems.

Beyond the specific applications discussed here, the methodology presented at the outset of this chapter can be a powerful way to tackle a broad range of biological image processing problems. For example, this scheme is a generalization of the previously reported application of SVMs towards the understanding of synaptic morphology in *C. elegans* (*37*). In this previous application, individual pixels within the image form the pool of candidates for potential synaptic pixels in the first layer classification. The second layer of classification then refines this decision on the basis of relational characteristics between candidates. Here, this classification approach is formalized and its ability to be applied to the detection of disparate structures imaged under different imaging modalities has been demonstrated. Overall, the imaging processing approach presented here has inherent structural advantages in terms of conceptual division, modularization and computational efficiency and demonstrates the application of a powerful supervised learning model to streamline biological image processing. This methodology can thus form the basis for detection algorithms for structures ranging from the molecular to the tissue or organismal level under different experimental methodologies.

3.5: Materials and Methods

3.4.1 Worm Maintenance and Culture

C. elegans worms used in this study were maintained and cultured according to standard techniques (*89*). Briefly, populations of worms were allowed to reach reproductive

maturity and lay eggs on NGM agar media overnight. Age-synchronized worms were then obtained by washing free-moving worms off of the agar plate, allowing the remaining eggs to hatch for one hour and then washing the resulting L1 stage larvae off of the plate. Age-synchronized L1 worms were then transferred onto new NGM plates seeded with OP50 *E. coli* bacteria as a standard food source and grown until the desired age for imaging. To avoid over-crowding and food depletion, adult worms were transferred onto new plates daily. For starvation experiments, worms were transferred onto fresh NGM plates lacking a bacterial food source the day before imaging.

C. elegans strains used in these studies were wild-type N2 worms, QH3833 *dpy-4*(*e1166*), QL296(*pdaf-7::GFP*) and QL617(*pins-6::mCherry; pgpa-4::GFP*).

3.4.2 Microfluidics and Image Acquisition

Standard soft lithographic techniques were used to produce polydimethylsiloxane (PDMS) imaging devices as described in Chapter 2. For automated imaging, worms are washed off of NGM plates using S Basal buffer and introduced via pressure injection into the microfluidic device. Sequential activation of pressure sources driving liquid delivery and on-chip pneumatic valves is then used to drive individual worms within the device for imaging.

Images were collected either on a Leica DMI 6000B microscope with a Hamamatsu Orca D2 camera and a 40X oil objective or on an Olympus IX-73 microscope with a Hamamatsu Flash 4.0 camera and a 40X oil objective. Relevant specifications and calibration metrics for these set-ups can be found in Table 3.1. Although not strictly necessary, for generalizability in cases where the center of focus is adjusted to specific

fluorescent targets and does not capture the pharynx well, a sparse three plane z-stack with a 15μm step size is used for bright field image acquisition. To fully capture neuronal cells, a dense z-stack was collected through the body of the worm. For fluorescence imaging of the single neuron pair in QL296, a 0.4μm step size was used over a 60μm thick volume. For fluorescence imaging of multiple neurons pairs in QL617, a 1μm step size was used over a 100μm thick volume.

3.4.3 Image Analysis and Computational Tools

Custom MATLAB code was used to perform all image preprocessing and feature extraction steps and enable the construction and testing of the classification schemes. In preprocessing, the three dimensional information in the acquired z-stacks were either maximum or minimum projected onto a single two dimensional image for further processing. For bright-field images, a minimum projection with respect to z was utilized to accentuate the appearance of dark objects throughout the stack. Conversely, for fluorescence images, a maximum projection was utilized to accentuate the appearance of bright objects throughout the stack:

$$MP_{BF}(x_i, y_i) = \min_{z_i}\big(I(x_i, y_i, z_i)\big), MP_{FLUO}(x_i, y_i) = \max_{z_i}\big(I(x_i, y_i, z_i)\big)$$

In order to generate binary particles for classification, this work utilizes a local thresholding algorithm that uses information about the mean and variability of pixel intensities within a local region around a pixel:

$$BW_{BF}(x_i, y_i) = MP_{BF}(x_i, y_i) \leq \mu_{local} - k\sigma_{local},$$

$$BW_{FLUO}(x_i, y_i) = MP_{FLUO}(x_i, y_i) \geq \mu_{local} + k\sigma_{local}$$

μ_{local} and σ_{local} are the means and standard deviations of all pixel values that fall within a square region of width $2R + 1$ centered around the pixel of interest x_i, y_i and k is a parameter specifying the stringency of the threshold. μ_{local} and σ_{local} can be derived using standard image filtering with a binary square filter $h(x_i, y_j)$ of width $2R + 1$:

$$\mu_{local} = \frac{1}{(2R+1)^2} filter(MP[i,j], h[i,j])$$

$$= \frac{1}{(2R+1)^2} \sum_{m=0}^{M} \sum_{n=0}^{N} MP[i,j]h(i-m, j-n)$$

$$\sigma_{local} = \sqrt{\frac{1}{(2R+1)^2} filter((MP[i,j] - \mu_{local}[i,j])^2, h[i,j])}$$

Using a Using local mean and standard deviation information in the binary decision affords robustness against local background intensity and texture changes.

The width of the local region, R, can be roughly selected on the basis of the size scale of the structure of interest. In accordance with the size scales of the pharyngeal structure and individual neurons, $R = 15\mu m$ for is used for detection of the pharyngeal grinder and $R = 5\mu m$ is used for fluorescent cell segmentation.

The parameter k can be roughly selected by visual inspection of segmentation results. Parameters $k = 0.75$ is used for the bright field application and $k = 0.85$ is used for the fluorescence application. Individual candidate particles in the resulting binary image are defined as groups of nonzero pixels that are connected to each other via any adjacent of diagonal pixel (8-connected). Changes in k can alter the size of segmented particles and

the connectivity of segmented particles. Particularly in bright field, where the contrast mechanism lacks specificity, decreases in k can cause particles to merge via small bridges of dark texture. In order to build in some robustness against changes in k and background texture in these scenarios, a form of a morphological opening operation is performed after thresholding to remove small bridges that may arise between otherwise distinct particles. To do this, a morphological erosion with a small circular structuring element is performed followed by a morphological dilation with a smaller structuring element (*90*).

In order to fully capture both intrinsic and secondary characteristics of biological structures, distinct sets of features are calculated for each of the two layers of classification. The first layer, which delineates structures of interest from other structures on the basis on its intrinsic geometric properties, is generally applicable to particle classification problems and is used for both the bright field and fluorescent structure detection outlined here. Details and equations for the calculation of the 14 features for layer 1 classification can be found in Figure 3.5.

Secondary characteristics of biological structures describe the context in which structures exist and their relationship to other structures. Due to the large variability in the secondary characteristics of biological structures, a generic set of features is not necessarily attainable or desirable due to concerns for computational efficiency. Rather, secondary features can be derived via a mathematical description of empirical observations of important structural properties. In the case of pharyngeal grinder detection, the secondary features are regional, forming a description of the image context

in which the grinder structure resides. The form of the features is based on an empirical understanding of this structural context and full details and equations for the calculation of the 34 features in layer 2 of the bright field classifier can be found in Figure 3.7. In the case of cell pair detection, the secondary features are mostly relational, describing how particles from layer 1 of classification may or may not exist as pairs on the basis of both positioning and intensity. Second layer features for single and double cell pair detection can be found in Figure 3.15 and Figure 3.19, respectively.

In this work, all calculated features are scaled using a calibration factor, C, derived from specifications of both the optics and sensors that form the imaging system:

$$C = \frac{(Sensor\ Pixel\ Size)(Binning)}{(Optical\ Magnification)}$$

The use of this calibration system renders the trained classifier relatively invariable to small changes in the imaging set-up via conversion of all features into real units. Calibration factors for all imaging systems and configurations used here can be found in Table 3.1.

Table 3.1: Calculation of the calibration metric for common changes in the imaging system and acquisition parameters. Setups used for this study are highlighted.

Optical Magnification		Camera Pixel Size (µm /Pixel)	Acquisition Parameters	Calibration Metric (µm/Pixel)
Objective	**Coupler**	**Hamamatsu Orca D2**	**Binning**	
20X	1X	6.45	1x1	0.3225
40X	1X	6.45	1x1	0.16125
40X	1X	6.45	2x2	0.3225
40X	0.5X	6.45	1x1	0.3225
Objective	**Coupler**	**Hamamatsu Flash 4.0**	**Binning**	
40X	1X	6.5	1x1	0.1625
40X	1X	6.5	2x2	0.325

To implement discrete classification steps using support vector machines, this work uses the LIBSVM library, which is freely available for multiple platforms including MATLAB (*77*). For general performance, this work uses a Gaussian radial basis function kernel for all of the trained classifiers (*82*). To ensure performance of the SVM model for each dataset, optimization is performed for the penalty or margin parameter, C, and the kernel parameter, γ, for each training set using the five-fold cross-validation performance of the classifier as the output metric. For efficient parameter optimization, a rough exponential grid search is used for initial parameter optimization followed by a finer grid search for parameter refinement. To adjust for the relative proportions of positive and negative candidates in unbalanced training sets, the relative weight, W, of the classes is adjusted according to their representation in the training set while training (*77*). Additionally, a small grid search for the optimal weighting factor is performed to fully optimize the following performance metric. Probability estimates for single and multiple neuron pair identification are derived according to the native LIBSVM algorithm (*77*).

For visualization of the high dimensionality feature sets (Figures 3.9b 3.10c), this work applies Fisher's linear discriminant analysis (*91*). The two projection directions are chosen to be the first two eigen vectors of:

$$S_w^{-1} S_B$$

$$S_B = (\mu_1 - \mu_2)(\mu_1 - \mu_2)^T$$

$$S_w = S_1 + S_2, \qquad S_i = \sum_{x \in class\ i} (x - \mu_i)(x - \mu_i)^T$$

S_B is a measure of inter-class separation and S_w is a measure of intra-class scatter.

CHAPTER 4: NEURAL REPRESENTATION OF ENVIRONMENTAL FOOD ABUNDANCE

This work is planned for future submission to a peer reviewed journal with collaborative contributions from Dr. Eugeni Entchev, Dr. Dhaval Patel, Dr. Andrew Steele and Dr. QueeLim Ch'ng.

4.1: Introduction

Decreasing food intake via dietary or caloric restriction (DR) is a highly conserved and effective modulator or aging and age-related physiological decline in a broad range of model organisms (*6, 7, 92-94*). Restriction of food abundance in models ranging from unicellular yeast (*95, 96*) and multicellular invertebrates (*26, 97-100*) to mammalian models such as mice and rats (*101-103*) results in robust increases in longevity. Moreover, while longevity increases tend to be more modest or have been difficult to experimentally observe in rodent and primate models (*104-106*), DR has been shown to confer protection against aging-associated ailments such as cancer, diabetes and cardiovascular disease (*104, 106-110*). These positive health effects have also been noted in human as well: DR has been shown to improve cardiovascular and glucoregulatory health and ameliorate cognitive decline in some studies (*111-114*). However, due to both logistical challenges in long-term compliance and participation, as well as concerns about quality of life and adverse social and psychological effects, studies of DR in humans are limited. For the same reasons, DR itself is not an attractive clinical intervention for preventing age-associated diseases or increasing longevity. Thus, one of primary aims of

DR studies has been to discover its underlying mechanisms in model organisms and extend this knowledge to permit clinical intervention in humans (*115*).

In worms, several genetic pathways have been implicated in the mediation of DR responses (*15, 26, 116-121*). However, a comprehensive understanding of how environmental variables and the genetic components of an organism interact to mediate the observed phenotypic effects of DR is still lacking (*120*). Moreover, the insulin/IGF-1 signaling (IIS) and Target of Rapamycin (TOR) pathways have been broadly implicated in regulating aging and perhaps mediating the link the between environmental sensation and phenotypes of interest (*10, 121-123*). These pathways represent important nodes for the regulation of multiple biological functions and physiological outputs (*124-126*) and non-specific intervention in these pathways can elicit detrimental effects (*127*). Thus, a refined understanding of upstream mediators of food sensation and information storage is necessary to increase the number of potential clinical targets and advance the goal of specifically and positively intervening in DR-mediated longevity.

Several candidate genes that specifically mediate the DR response have been previously reported (*15, 26, 118*). Loss of function mutations in these candidates have typically been shown to fully abrogate the lifespan response to DR by constitutively decreasing lifespan across all food levels. While these results indicate that these candidates are all necessary for DR-mediated changes in longevity, they also suggest that these genes act generically in processes that are broadly necessary for lifespan extension. In contrast, collaborators Dr. Eugeni Entchev and Dr. Dhaval Patel working in the laboratory of Dr. Queelim

Ch'ng have characterized the longevity responses of two mutants that show a unique bidirectional attenuation of the DR response (Figure 4.1).

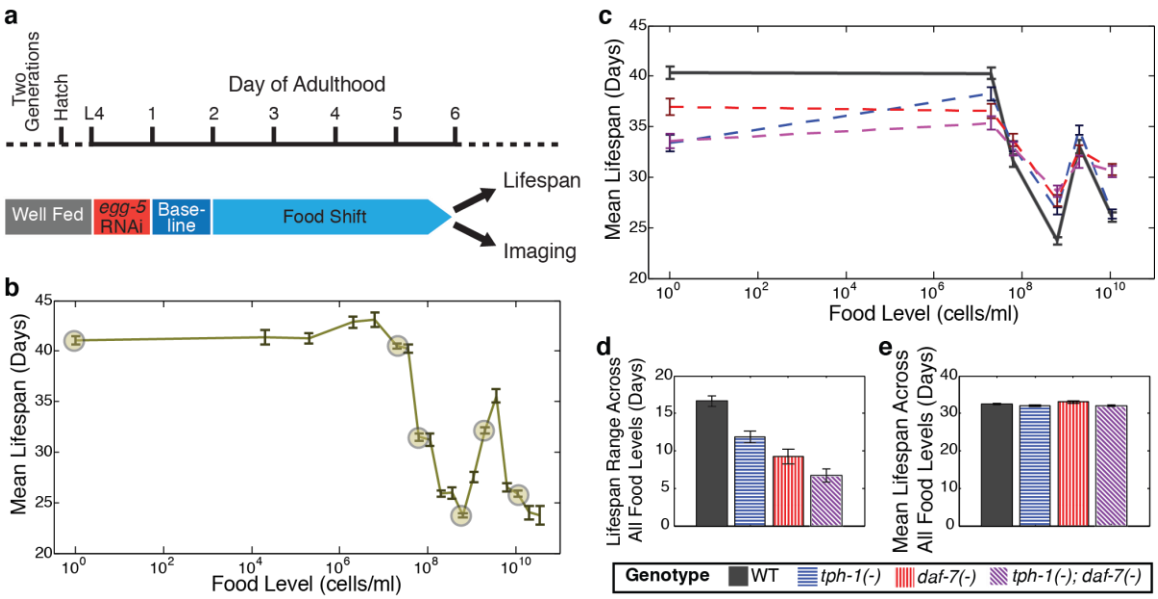

Figure 4.1: Two neuronal genes, daf-7 and tph-1, shape a complex, multiphasic relationship between lifespan and food availability. a) Protocol for maintaining animals at different food levels for lifespan and imaging experiments. b) Mean lifespan of wildtype worms subjected to 19 food levels ranging from 0 to 3.5x1010 bacterial cells/ml at 20°C. Points denoting key features in the food response and used as food conditions in subsequent experiments are highlighted. c) Mean lifespan of wildtype and mutant animals across the six food levels indicated in (b) show that loss of tph-1 and daf-7 preserves the pattern but attenuates the range of the lifespan response. Genotypes are indicated by the legends below (d) and (e). d) Range of food-induced lifespan modulation for each genotype. Range is defined by the difference between the highest and lowest mean lifespan response across the six food levels. e) Average of the mean lifespan responses across all food levels for each genotype reveals a consistent, food-independent baseline lifespan response.

The Ch'ng lab established a new DR protocol (Figure 4.1a, Section 4.5.2 and 4.5.3) to finely sample the lifespan effects of a broad range of bacterial concentrations that worms might encounter in the wild. The results, shown in Figure 4.1b, show a more complex DR

response than those previously reported using more limited sampling of the bacterial concentration range (*26, 100*). Using a subset of bacterial concentrations that reflect this complexity (circled in Figure 4.1b), the Ch'ng lab found attenuation of the lifespan response in mutants of two neuronally expressed genes, *tph-1* and *daf-7*. Figure 4.1c shows that single mutants in either *tph-1* (blue dashed line), which encodes an enzyme responsible for a rate-limiting step of serotonin synthesis (*128*), or *daf-7* (red dashed line), which encodes a TGF-beta homolog (*18*), bidirectionally alter the lifespan response to food. Additionally, animals with mutations in both genes (purple dashed line) shows further attenuation of the response. Figure 4.1d summarizes this lifespan response attenuation by showing the observed range of DR-modulated lifespans for each mutant. Furthermore, Figure 4.1e shows that as opposed to previously identified DR genes, the attenuation in food-responsiveness is bidirectional and the mean lifespan across all food levels is similar for all mutants.

The lifespan results in Figure 4.1 confirm previous indications that *tph-1* and *daf-7* may act as important carriers of food information in the worm (*81, 129, 130*) and loss of these functional genetic components result in a limited ability to generate appropriate physiological responses to food. More broadly, they may implicate the conserved serotonin and transforming growth factor beta pathways in mediating food responses in other organisms and humans. However, the manner in which these genes may mediate the link between food and longevity and the ways in which clinical interventions can act on these targets are unclear. Since previous studies have indicated that *tph-1* and *daf-7* activities are transcriptionally regulated by environmental cues (*17-19, 128, 131-137*) and

the timescales of regulated gene expression are well-matched with the long timescales of the physiological processes involved in aging, a mechanism involving food dependent transcriptional regulation is likely.

In this chapter, the hardware and software technologies developed in Chapters 2 and 3 are combined and applied to characterizing the cell-specific expression profiles of *tph-1* and *daf-7* using quantitative imaging of genetically encoded fluorescent reporters. As opposed to conventional gene expression profiling techniques, the quantitative imaging technique employed here permits easy spatial resolution of expression profiles, providing additional information about potential internal representation of food information. Furthermore, use of the technologies developed in the preceding chapters permits imaging of large numbers of animals, allowing for the assessment of expression variability and the fidelity of the food representation via *tph-1* and *daf-7* expression.

4.2: Quantitative Imaging of *tph-1* and *daf-7*

To assess food-dependent changes in the expression *tph-1* and *daf-7*, wildtype and mutant transgenic strains bearing single-copy fluorescent transcriptional reporters for both *tph-1* and *daf-7 (Ptph-1::mCherry* and *Pdaf-7::Venus*) were generated as described in Section 4.5.1. Different bacterial food levels were administered to these imaging strains using the same dietary restriction protocol used for the lifespan assays (Sections 4.5.2 and 4.5.3). As diagramed in Figure 4.2a, animals were then cultured on the experimental food condition for four days and then collected on day 6 of adulthood for quantitative imaging on a microfluidic chip as described in Section 4.5.5. The observed expression patterns were identical to published validated reporters (*18, 19, 128*) (Figure 4.2b). *tph-1* is

expressed in the ADF sensory neurons, the NSM neurons within the foregut, and the hermaphrodite-specific HSN motorneurons (*128*). *daf-7* is expressed in a single pair of ASI sensory neurons (*18, 19*). The ADF and ASI neurons are both ciliated sensory neurons with processes projecting into the external environment (*83*) and expression in these cells may be regulated by environmental sensation of food. Moreover, the NSM neurons are motor neurons that have processes closely associated with the pharynx and have been previously postulated to have a proprioceptive role in food sensation (*81, 83, 129*). Thus, quantitative imaging was specifically applied to the dissection of expression information from the NSM (red hexagons), ADF (red circles) and ASI (green squares) neurons.

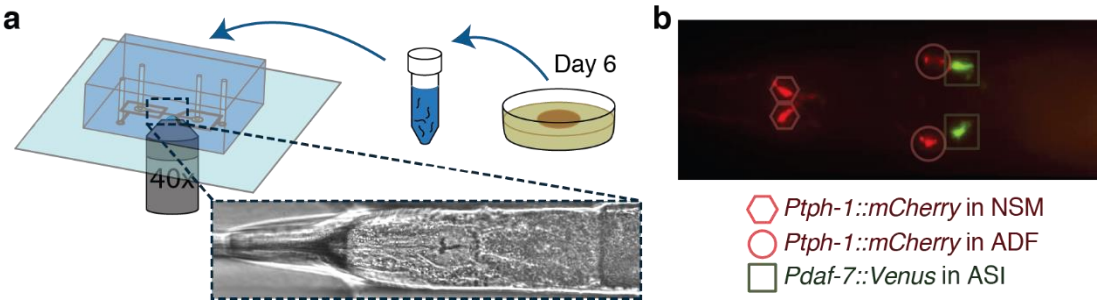

Figure 4.2: Outline of quantitative imaging scheme. a) Worms subjected to a solid DR protocol are harvested on day 6 of adulthood, suspended in liquid media and imaged using a microfluidic imaging system. b) The expression of *tph-1* and *daf-7* in three neuron pairs in the head of the worm are quantified to assess food responsiveness.

The integrated fluorescent intensities exhibited by each of the three neuron pairs shown in Figure 4.2b were calculated from fluorescent z-stack images as described in Section 4.5.6. The results in Figure 4.3a show that each neuron pair has a distinctive pattern of response to food inputs. Moreover, the expression changes in response to food were

largely non-monotonic, limiting the ability of the expression output in any single neuron pair to uniquely represent food levels across the entire range tested. The outputs also differed with respect dynamic range, indicating different limits on the natural variation of gene activity due to changes in food inputs. Additionally, the large populations of animals assayed in these imaging experiments showed considerable inter-individual variability in their expression levels, indicating the limited fidelity of individual gene expression outputs to represent environmental information (Figure 4.3b)

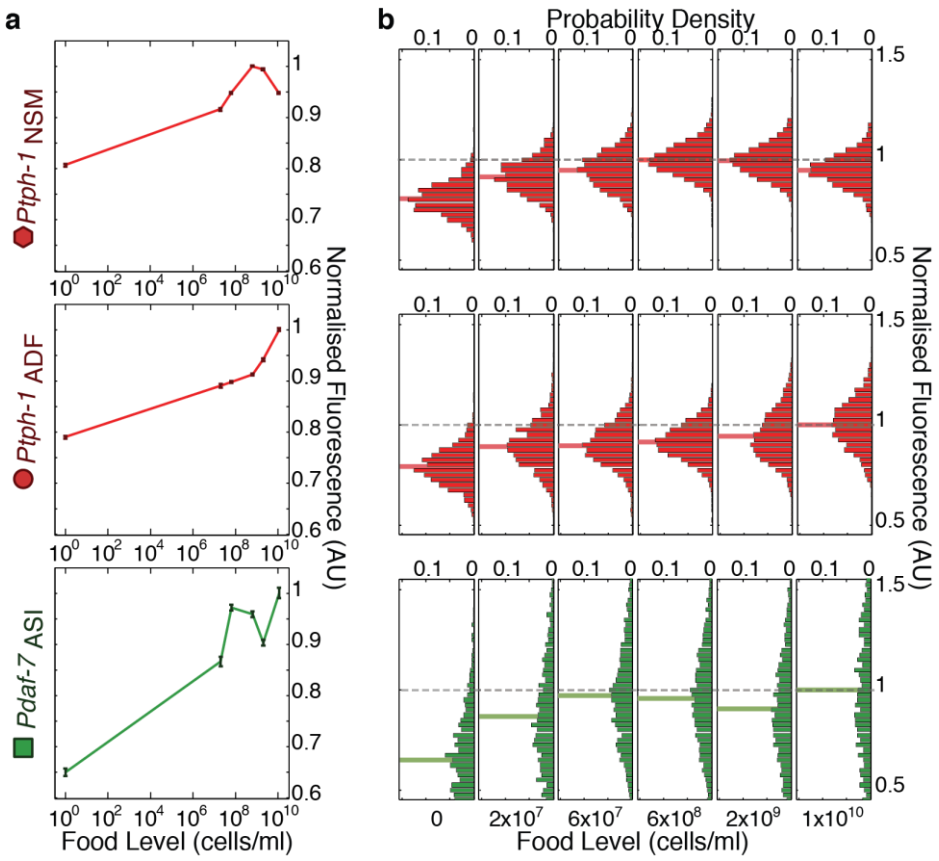

Figure 4.3: Food-dependent expression of *tph-1* and *daf-7* in the NSM, ADF and ASI neuron pairs. a) Mean expression profiles of *tph-1* in NSM (*Ptph-1*$_{NSM}$) and ADF (*Ptph-1*$_{ADF}$), and *daf-7* in ASI (*Pdaf-7*$_{ASI}$) across six different food levels are neuron-specific and largely non-monotonic. Measurements are normalized to the highest mean expression response observed in each respective neuron; error bars are SEM. b) Distribution of the expression responses of *tph-1* in NSM and ADF and *daf-7* in ASI at different food levels. Means are indicated by the solid lighter-shade lines behind the distributions. Dashed line denotes the highest mean expression for each neuron, which was used for normalization.

The non-monotonic gene expression responses shown in Figure 4.3a indicate that individual gene expression readouts are largely incapable of uniquely representing food conditions internally. However, since the lifespan responses observed in Figure 4.1b and c are also non-monotonic, it is possible that they correlate in a manner such that gene expression outputs can uniquely specify lifespan responses. Figure 4.4a shows that this is

also not the case. Not only are individual gene expression outputs insufficient for uniquely representing food inputs, they are also not sufficient for uniquely specifying the observed lifespan outputs. However, Figure 4.4b shows that, together, the three spatially defined set of gene expression outputs in NSM, ADF and ASI can form a unique multivariate code for food levels. The multivariate pattern of expression form a 3 bit pseudo-binary code that can specify the food levels that that correspond to critical features of the lifespan response curve shown in Figure 4.1b. Based on the ability of individual animals to adopt a continuous range of expression pattern (Figure 4.3b), intermediate food levels are likely represented by graded transitions in expression levels between these pseudo-binary extremes.

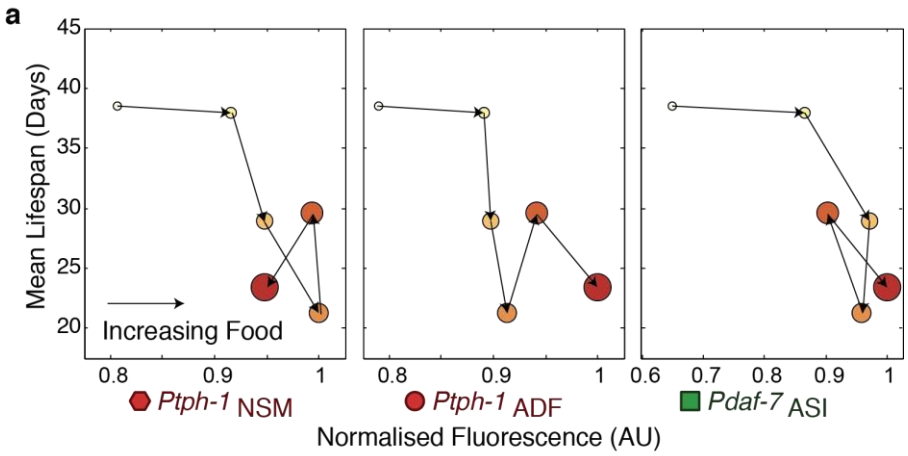

b

Input →	Internal Representation (Mean Expression)			→ Output
Food Level (cells/ml)	*Ptph-1* NSM	*Ptph-1* ADF	*Pdaf-7* ASI	Mean Lifespan
0	Low	Low	Low	High
$2x10^7$	Medium	Medium	Medium	High
$6x10^7$	Medium	Medium	High	Medium
$6x10^8$	High	Medium	Medium	Low
$2x10^9$	High	High	Medium	Medium
$1x10^{10}$	Medium	High	High	Low

Figure 4.4: Unique multivariate representation of food levels by spatially defined gene expression three neuron pairs. a) Relationship between individual gene expression profiles and the lifespan responses across the six food levels indicates that the individual readouts are insufficient to uniquely specify lifespan responses. b) The combination of *tph-1* in NSM ($Ptph\text{-}1_{NSM}$) and ADF ($Ptph\text{-}1_{ADF}$) and *daf-7* in ASI ($Pdaf\text{-}7_{ASI}$) create a non-monotonic multivariate encoding scheme capable of both uniquely representing food inputs and potentially specifying lifespan outputs.

Having established that *tph-1* and *daf-7* expression responses are food-sensitive and that the combination of expression responses in NSM, ADF and ASI is capable of uniquely capturing food information, quantitative imaging was performed in single and double mutants of *tph-1* and *daf-7* to assess potential changes in expression profiles. Figure 4.5

shows the changes in expression profiles for each of the three neuron pairs. Full gene expression distributions for all of the mutants can be found in Appendix B (Figures B.1-B.3). In this case, the use of an exogenous gene expression reporter for quantitative imaging permits the acquisition of gene expression data even in mutants where the genetic output is non-functional. This allows for the assessment of both cross-regulation and auto-regulation amongst *tph-1* and *daf-7*. Figure 4.5 shows that cross- and auto-regulatory effects can sometimes dramatically alter gene expression profiles. However, how these alterations impact the ability of the gene expression variables to represent the environment is unclear.

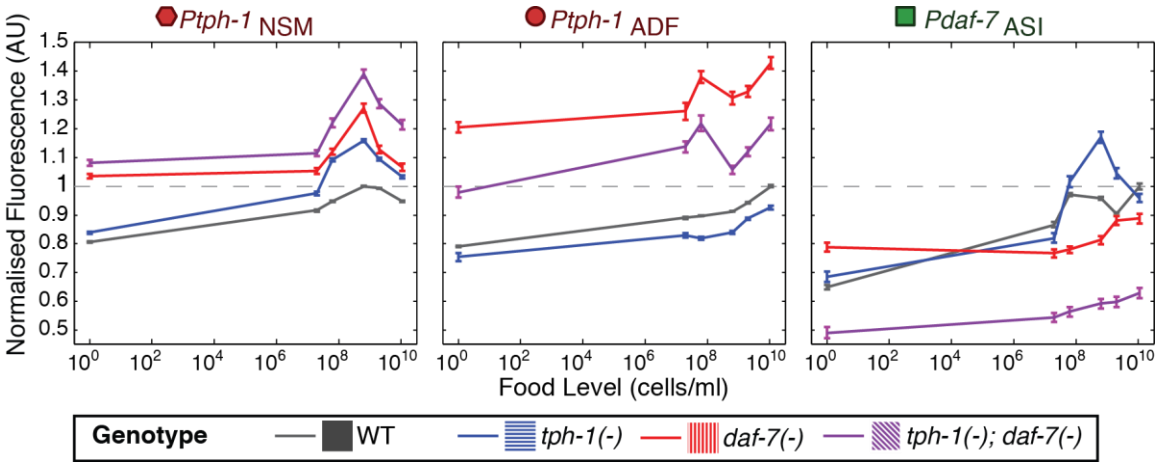

Figure 4.5: Food-responsive expression profiles of *tph-1* in NSM ($Ptph\text{-}1_{NSM}$) and ADF ($Ptph\text{-}1_{ADF}$), and *daf-7* in in ASI ($Pdaf\text{-}7_{ASI}$) for different genetic backgrounds, as indicated in the legend. All values are normalized to the highest wildtype mean expression response observed in the respective neuron (dotted line).

As discussed previously for the expression profiles and distributions in wildtype worms, the gene expression profiles from quantitative imaging can be described in terms of both their dynamic range and inter-individual variability. In terms of the ability of a particular

gene expression readout to represent environmental information, increases in dynamic range tend to increase representational ability, by increasing the range of outputs that a variable can adopt. At the same time, increases in inter-individual variable tend to indicate a decrease in representational capacity since it increases the overlap of gene expression distributions between two populations and lowers the ability to resolve the food conditions experienced by each animal. Figure 4.6 analyzes the changes in both dynamic range and expression variability between the wildtype and mutant populations in order to understand

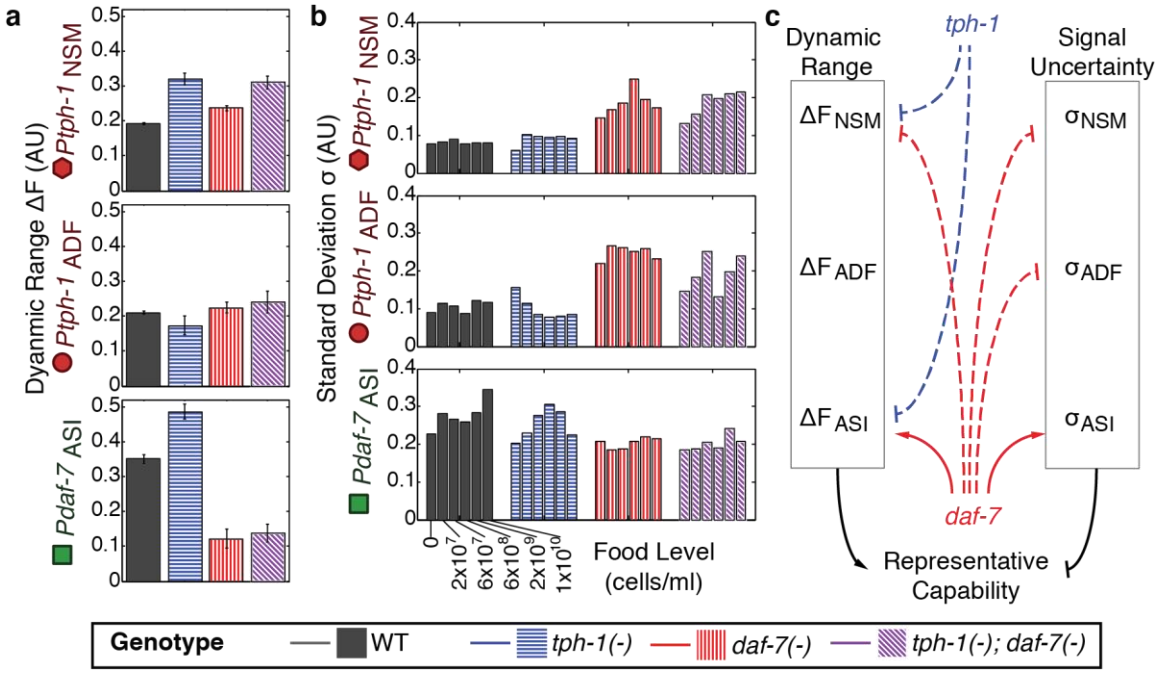

Figure 4.6: Auto- and cross-regulation amongst *tph-1* and *daf-7* alters both the dynamic range and variability of gene expression responses to food with consequences for representative capability. a) The dynamic range of all three gene expression profiles in each neuron pair for different mutants. b) The inter-individual variability of gene expression responses as measured by the standard deviation of the population response for each food condition and mutation. c) Schematic summary of the effect of the auto- and cross-regulatory effects of *tph-1* and *daf-7* on the dynamic range, variability and representative capability of gene expression responses.

Figure 4.6 analyzes the changes in the dynamic range and expression variability between the wildtype and mutant populations to understand potential changes in the ability of the *tph-1* and *daf-7* readouts to represent environmental food information. Figure 4.6a shows that loss of functional *tph-1* tends to increase the ability of both the *tph*-1 promoter and the *daf-7* promoter to respond to environmental food signals. Thus, the regulatory role of *tph-1* in an intact animal dampens the range of *tph-1* and *daf-7* transcriptional levels that an animal can adopt. These results indicate that *tph-1* is negatively auto-regulated in a cell-specific manner and is involved in negatively regulating the responsiveness of *daf-7*. On the other hand, mutants with loss of functional *daf-7* show marked decreases in the dynamic range of *daf-7* outputs. This indicates that *daf-7* is positively auto-regulated in a scheme where small perturbations in the output generated by changes in the environmental perception are amplified by the resulting activity of the output itself.

Figure 4.6b analyzes the changes in the variability of the gene expression responses between the wildtype and mutant animals. In general, loss of *tph-1* has little effect on the expression variability of any of the three readouts. However, loss of *daf-7* either alone or in combination with *tph-1* increases the gene expression variability of the both of the *tph-1* readouts in NSM and ADF. Thus, in an intact animal, *daf-7* activity dampens the variability of *tph-1* responses. This regulatory effect of daf-7 tends to maintain the ability of the serotonin signaling system to represent information about the environment. Moreover, despite the potential importance of this effect, it is not uncovered by more conventional analyses of changes in mean gene expression. For example, in the expression profiles in Figure 4.5, the *daf-7* mutants show increases in absolute *tph-1*

expression levels, and in the analysis in Figure 4.6a, *daf-7* mutants also show moderate increases in the food-responsiveness of these outputs. Analysis based on mean expression alone would therefore suggest that *daf-7* limited the environmental responsiveness of *tph-1* in a wildtype animal. However, the ability to assess large populations using high-throughput imaging permits the discovery of an opposing effect based on population distributions.

Figure 4.6c summarizes the effects of *tph-1* and *daf-7* on both the dynamic range and the variability or uncertainty of the gene expression outputs. As discussed previously, these two aspects of a gene expression profile tend to have opposing effects on the representative capability of the readouts. Thus, via this analysis, the regulatory role of *tph-1* would seem to have a negative effect on representative capability of the system primarily due to dampening of the *tph-1* and *daf-7* food responses in NSM and ASI. The regulatory role of *daf-7*, on the other hand, would seem to have a positive effect on the representative capability of the system primarily due to its effect on reducing variability and signal uncertainty in the *tph-1* readouts. However, this analysis does not give quantitative indications of the magnitudes of these effects or to total representative capability of the system in the wildtype animal.

4:3: Assessing the encoding capabilities of differential gene expression

In order to assess the food-representative capability of the largely non-monotonic, multivariate food encoding scheme formed by the combination of *tph-1* and *daf-7* readouts, a Bayesian inference framework is applied. Full details on this analysis can be found in Section 4.5.7. Via the construction of probability models based on the observed

expression profiles, Bayesian analysis assesses the ability of expression readouts to make inferences about upstream information such as food inputs. The results can be summarized as matrices showing the frequency of inferred versus actual food stimuli for each population (Figure 4.7a). If the expression distributions are distinct (non-overlapping) across food levels, a correct inference is always obtained, resulting in a strongly diagonalized matrix (Figure 4.7a top). If the distributions overlap entirely, then the food level inference is random and the values in the matrix are inversely related to the number of conditions tested (Figure 4.7a bottom).

Applying this framework to the individual expression profiles in NSM, ADF and ASI indicates that each readout alone provides some discriminatory power for food inputs (Figure 4.7b top). However, in accordance with the previous observation that each neuron pair contributes distinct information to a unique multivariate encoding scheme (Figure 4.4b), the inference accuracy is improved when information from multiple neuron pairs are combined (Figure 4.7b). This result confirms that non-redundant encoding by each neuron pair improves the accuracy of the overall representation of environmental conditions. This analysis also confirms that while the multivariate encoding scheme in Figure 4.4b would suggest unique representation of each food level, the ability of the encoding scheme to represent food inputs is limited by the variability observed in the expression outputs (Figure 4.3b). As shown in the final matrix in Figure 4.7b, the same Bayesian inference framework is also analyzed to analyze the amount of food information captured by the longevity outputs in Figure 4.1. This analysis shows that the combined inference accuracy of the three *tph-1* and *daf-7* outputs is slightly above the

inference accuracy of the final lifespan outputs and suggests that sufficient information is stored within these two genes to specify downstream physiological outputs such as lifespan.

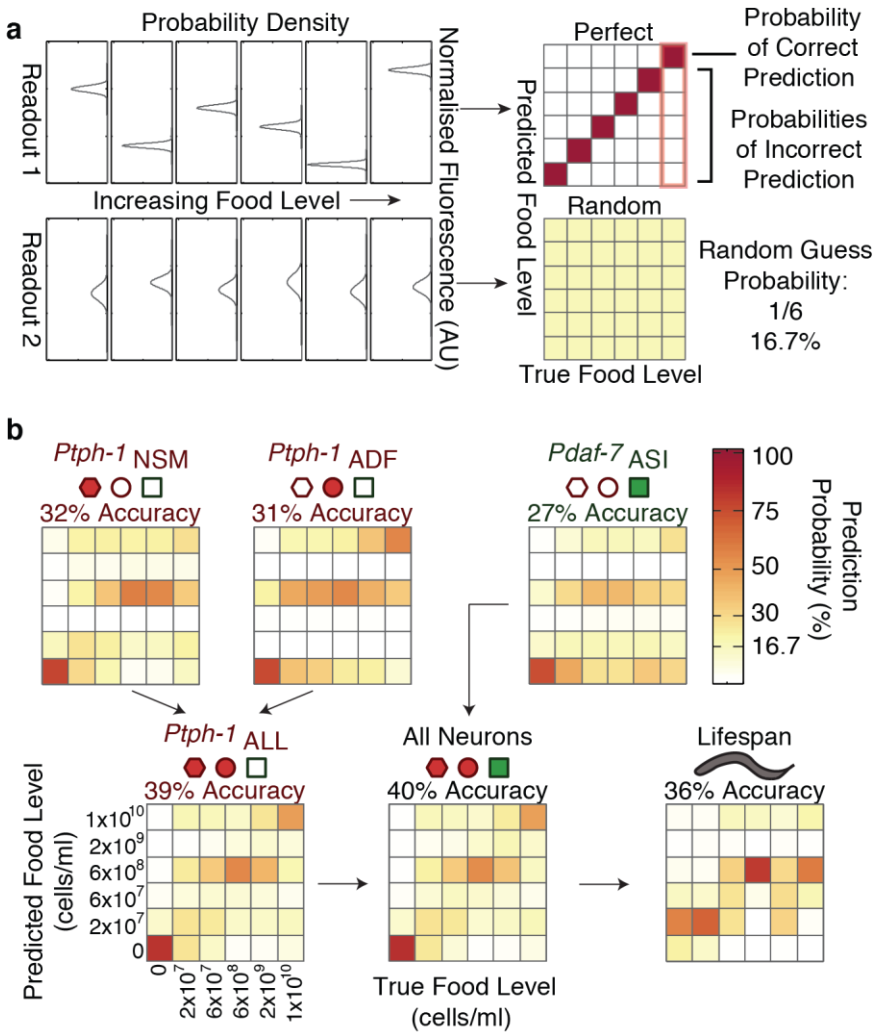

Figure 4.7: Expression readouts of *tph-1* and *daf-7* encode food information with higher accuracy than final lifespan phenotypes. a) The ability of expression and lifespan readouts to respond to and represent (encode) food conditions can be estimated by using the readouts of interest to infer the true food conditions. The results can be visually represented by matrices where the squares in each column indicate the frequency with which particular inferences are made for a given true food level. Distinct, non-overlapping readouts result in high discriminatory power, represented by a highly diagonalized matrix (top). Indistinct, overlapping response profiles result in low (random) discriminatory power, represented by a uniform matrix (bottom). b) Matrices indicating the representational capability of *tph-1* and *daf-7* readouts individually or in combination exhibit similar total encoding fidelity to that of lifespan outputs in wildtype animals.

To quantitatively assess changes in representative capacity in the mutants, the same Bayesian inference framework is applied to the expression profiles of the mutants. Figure 4.8a shows that the single or double mutants in *tph-1* and *daf-7* have similar effects on the representative capacity of each individual expression readout. Specifically, loss of *tph-1* functionality tends to increase the information carrying capacity of expression readouts, loss of *daf-7* functionality tends to decrease the information capacity of expression readouts and double mutants in *tph-1* and *daf-7* have an intermediate effect on the encoding accuracy. As with the wildtype animals, combining expression readouts tends to increase the information accuracy in all of the mutants (Figure 4.8b). Finally, consistent with the qualitative assessment of encoding fidelity changes in Figure 4.6, the Bayesian analysis indicates that loss of *tph-1* tends to increase encoding fidelity and loss of *daf-7* tends to decrease encoding fidelity when accounting for all functional and non-functional expression readouts (Figure 4.8c).

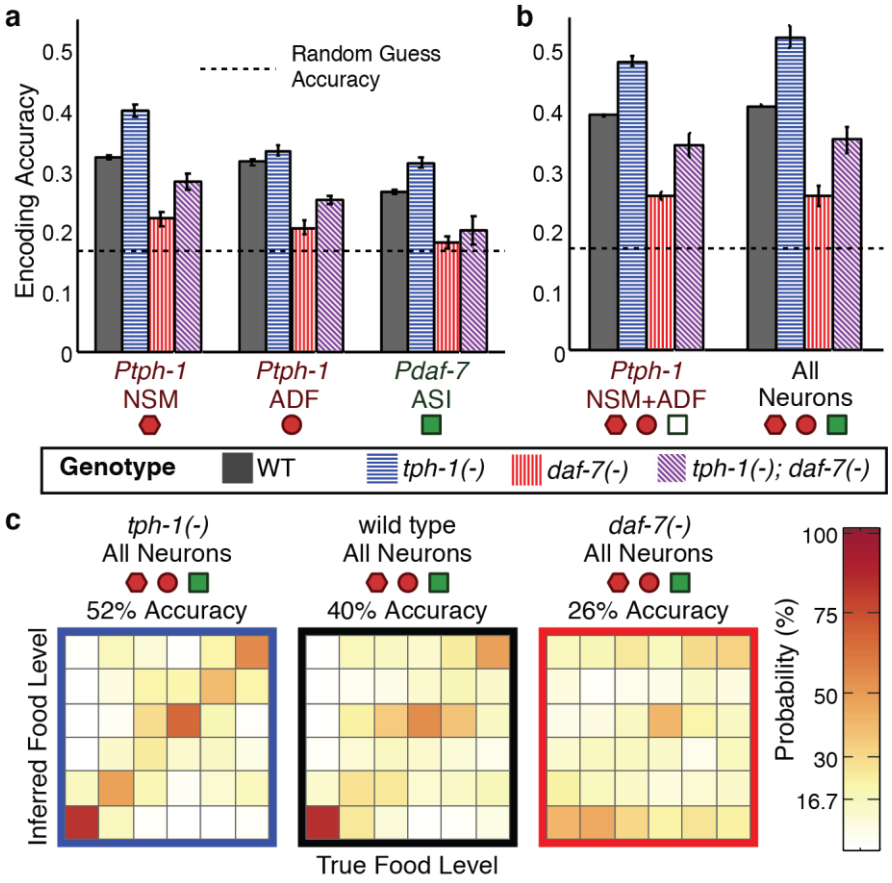

Figure 4.8: Cross- and self-regulation of tph-1 and daf-7 control the accuracy of internal representation of food levels. a) Encoding accuracy of individual neuron-specific expression readouts in wildtype and mutant populations, as indicated by the legend. Dotted line indicates the lower bound for encoding accuracy due to chance. b) Functional combinations of the neuron-specific expression readouts increase encoding accuracy in both wildtype and mutant populations. c) Matrices indicating the full encoding accuracy of the combination of all gene expression readouts in wildtype and mutant animals reveal a surprising increase in accuracy with the loss of *tph-1*.

The results in Figure 4.8c would seem to contradict the observation of decreased food responsiveness in the longevity outcomes of the *tph-1* mutants (Figure 4.1c). However, since these results accounts for both functional and non-functional genetic outputs in the mutants, they only indicate the theoretical encoding performances of the encoding system when regulatory connections are disrupted. The effect of these regulatory connections on

encoding fidelity are summarized in Figure 4.9a. However, despite the negative effect the presence of functional *tph-1* has on the dynamic range of the expression readouts, *tph-1* readouts in NSM and ADF encompass a large portion of the information carrying capacity in the system (Figure 4.8b). Thus, accounting for the loss of *tph-1* as a functional readout, *tph-1* mutants have diminished encoding accuracy (Figure 4.9b). In the case of the *daf-7* mutant, the effect of the loss of *daf-7* as an expression readout itself is not as significant as the effect of the loss of *daf-7* regulation on the encoding fidelity of the tph-1 readouts. Thus, excluding non-functional readouts in the *daf-7* mutant results in a similar level of accuracy as in Figure 4.8c. Finally, the losses in encoding accuracy observed in the mutants (Figure 4.9b) is consistent with the loss of lifespan responsiveness when the Bayesian framework is applied to the lifespan outputs of the mutants. (Figure 4.9c). These results indicate that encoding of environmental food information via the gene expression responses of *tph-1* and *daf-7* is important for DR-mediated lifespan responses. However, the persistence of some food responsiveness in the double mutant in Figure 4.9c indicates that additional players may be involved in representing food information within the worm.

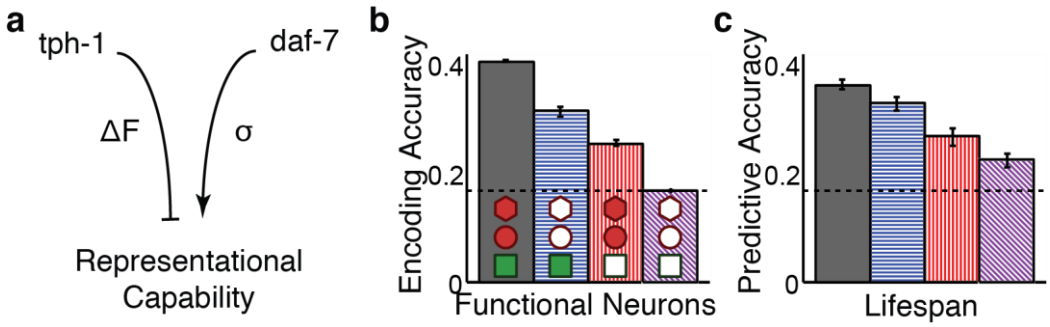

Figure 4.9: Loss of food representative capability in the *tph-1* and *daf-7* encoding system is consistent with attenuation of lifespan responsiveness to food. a) Schematic indicating the distinct mechanisms by which *tph-1* and *daf-7* control the representational capabilities of the system. *tph-1* and *daf-7* exert their effects largely via modulating dynamic range or variability in gene expression, respectively. b) Mutant animals show diminished encoding accuracy relative to wildtype when only functional expression readouts (filled symbols) are considered. For example, only *daf-7* expression in ASI ($Pdaf\text{-}7_{ASI}$) is a functional readout in the *tph-1(-)* mutant. c) Encoding accuracies of lifespan response in the mutants exhibit decreases that are consistent with the loss of representational capability in (b).

4.4: Discussion and Conclusions

This work demonstrates for the first time that food abundance is functionally encoded in vivo in *C. elegans* by the combinatorial expression of *tph-1* and *daf-7* in three neuron-pairs. The longevity phenotypes of *tph-1(-)* and *daf-7(-)* mutants reveal that rather than serving intrinsic roles in lifespan extension, serotonin and TGFβ constitute a new class of signals required for both food-dependent increases and decreases in lifespan. This bidirectional attenuation of DR-mediated lifespan responses is consistent with the disruption of food level representation by loss of these genetic outputs. Furthermore, *tph-1* and *daf-7* have established functional connections to conserved pathways for regulating metabolism, cellular maintenance, reproduction and longevity, such as the insulin/IGF pathway (*11, 17, 138*). Thus, this internal perception of food availability may facilitate

the coordination of energy utilization and appropriate physiological and behavioral responses to optimize survival in variable environments.

The analysis in this work also imply that *tph-1* and *daf-7* play distinct and vital roles in representing environmental information. While *tph-1* readouts comprise the major carriers of food information, its regulatory role with respect to its own response and that of *daf-7* limits the overall food-responsiveness of the system. Thus, *tph-1* is potentially a major functional output of a food encoding scheme that negatively feeds back on the rest of the system to maintain reasonable, homeostatic limits on serotonin signaling. On the other hand, *daf-7* readouts themselves carry only small amounts of food information. However, the regulatory effect of *daf-7* is necessary to maintain representational capacity in tph-1 outputs. Thus, while *daf-7* is not necessarily a major functional output of the food encoding scheme, it mediates the responsiveness of the rest of the system.

Ultimately, the parity in encoding performance between gene expression and lifespan (Figure 4.7b), along with the attenuation of lifespan response in the mutants, suggests that this neuronal representation has major functional information-carrying capacity. These results indicate that a limited number of molecular players can produce relevant physiological responses via spatial compartmentalization and complex regulatory interactions. Furthermore, this work characterizes the limits and directionality with which *tph-1* and *daf-7* outputs are altered by environmental food inputs. This serves as the starting point for designing interventional schemes to alter food-responsive physiological outputs such as longevity in the absence of changes in food inputs.

Finally, while the analysis in this work shows that the information carrying capacity of *tph-1* and *daf-7* is greater than the information carrying capacity of lifespan outputs themselves (Figure 4.7b), food information is necessary for specifying many internal processes and physiological outputs. Thus, the total ability of an organism to interpret and store environmental information is expected to be much greater than the information stored within any individual phenotypical output alone. Furthermore, unlike previous studies where the loss of single genetic outputs have fully abrogated the food response, even the loss of both *tph-1* and *daf-7* do not fully attenuate DR-mediated longevity responses (Figure 4.1c and 4.9c). Thus, *tph-1* and *daf-7* likely act upstream of previously identified regulators of longevity and the phenotypes observed in this study implicate other food sensors that act at the same level. This work also provides the framework for other such food sensors to be characterized and potentially targeted for interventional therapies.

4.5: Materials and Methods

4.5.1: Strain Construction and Transgenesis

The following parental strains were used to generate all other used in this study: N2 (wildtype), QL101 *tph-1(n4622)* II, QL282 *daf-7(ok3125)* III, EG6701 *ttTi4348* I; *unc-119(ed3)* III; *oxEx1580*, EG6699 *ttTi5605* II*; unc-119(ed3)* III; *oxEx1578*. Worms were cultured according to standard protocols (*89*).

Transcriptional reporters were generated from fosmid clones carrying the wildtype *tph-1* and *daf-7* genomic sequences obtained from Source Bioscience Lifesciences (UK). Collatorators Dr. Eugeni Entchev and Dr. Dhaval Patel in the Ch'ng Lab then used a

recombineering pipeline (*139*) to replace the coding sequence of the target gene in the fosmid with *C. elegans* optimized versions of either mCherry or Venus. These recombinant fosmids were then subcloned into pCFJ352 and pCFJ151 (*140*), to generate Venus and mCherry reporters that were flanked by the native 5' and 3' intergenic regions of *daf-7* and *tph-1*, respectively. These reporters were then integrated into defined positions of the C. elegans genome using MosSCI (*140*). *Ptph-1::mCherry* was integrated on chromosome I at the *ttTi4348* Mos locus and *Pdaf-7::Venus* was integrated on chromosome II at the *ttTi5605* Mos locus, the integrated constructs were designated *drcSi61* and *drcSi7*, respectively. Standard genetic techniques were then used to generate strains carrying both fluorescent reporters in various genetic backgrounds.

4.5.2: Preparation of Bacterial Food Source for Dietary Restriction

The dietary restriction protocol used in this study was derived from two previously published methods for dietary restriction on agar plates (*26, 141*). Briefly, the *E. coli* strain OP50 was cultured overnight in LB broth in a 37°C orbital shaker. Before being harvested, streptomycin was added to the overnight cultures to a final concentration of 50μg/ml. The culture was then allowed to continue shaking at 37°C for 30 minutes and then chilled on ice for 15 minutes. The bacteria was then harvested via centrifugation at 4500g for 25mins at 4°C. The supernatant was then decanted and the bacteria were resuspended in S Basal containing streptomycin (50μg/ml).

The volume of S Basal used for resuspension was determined by measuring the OD600 of a 10-fold dilution of the overnight culture prior to centrifugation and then calculating the volume required to give the resuspended culture a theoretical OD600 of 56, which

corresponds to a total cell count (live + dead) of ~$1x10^{10}$ cells/ml. All subsequent bacterial concentrations were generated through serial dilution of this high-density stock.

Stocks were stored at 4°C before being applied to NGM plates supplemented with both streptomycin (50μg/ml) and carbenicillin (50μg/ml). The use of two antibiotics ensured that bacteria were unable to proliferate and alter food density on the agar plates. The bacterial solutions were transferred onto the plates with a dispensing pipette to ensure that all plates received an equal volume of liquid. Plates were typically seeded with the bacterial solution 2-3 days before use to allow sufficient times for the solution to dry and form coherent bacterial lawns.

4.5.3: Maintenance and Culture of *C. elegans* for Lifespan Assays

Many *C. elegans* aging studies use fluoro-2'-deoxyuridine (FuDR) to inhibit the germline of experimental animals in order to eliminate progeny that may otherwise contribute to depleting food resources or cause premature modes of death due to reproductive complications. However, the use of FuDR is problematic as the germline in *C. elegans* is a major regulator of longevity (*142, 143*) and its use can cause gene-specific effects on lifespan (*144*). To eliminate these potential experimental complications, this work uses a novel method to eliminate production of progeny by inhibiting formation of the eggshell of fertilized *C. elegans* embryos through RNAi knockdown of *egg-5 (145, 146)*. While this permits normal germline function up to point of oocyte-to-embryo transition, the resulting embryos are not viable.

Lifespan assays were performed on 6cm CellStar (Greiner) plates at density of 15 worms per plate. Plates were always seeded with a single 225μl aliquot of bacterial solutions

prepared according to Section 4.5.2 at appropriate bacterial concentrations. During the course of the lifespan experiments, worms were passaged to fresh plates by manual transfer using a platinum wire pick. To avoid physical damage to the worms during transfer, animals were floated off the pick by immersing it into a 10µl droplet of S Basal + streptomycin on the surface of the new plate.

Animals for all strains were raised on live OP50 bacteria for two generations at 20°C. Synchronized L4-stage progeny of the F2 parents were manually transferred to NGM plates supplemented with 1mM IPTG and 50µg/ml carbenicillin that were seeded with HT115 bacteria expressing dsRNA targeting *egg-5*. Animals were exposed to *egg-5* RNAi for 24 hours before being transferred to NGM + streptomycin + carbenicillin plates seeded with a baseline food concentration of $2x10^9$ cell/ml. On day 2 of adulthood, animals were shifted to the desired DR food level and temperature. To avoid food depletion, animals were transferred every other day up until day 11 of adulthood and then a final transfer was performed on day 15 of adulthood. Animals were also scored for movement upon gentle prodding with a wire pick; failure of response was scored as death. Animals were scored for death at every transfer point and then daily after the last transfer point.

4.5.4: C. elegans Culture for Imaging

Imaging experiments were carried on 10cm CellStar (Greiner) to allow for a higher number of animals (~100 worms) than lifespan assays. Due to the greater number of worms in these assays, animals were transferred between plates by washing with S Basal

+ streptomycin. The 10cm plates were seeded with five 225µl aliquots of the bacterial solutions prepared according to Section 4.5.2 in a cross-like formation.

In the imaging experiments using the *daf-7* and *tph-1* reporters in a wildtype background, L1-stage larvae were synchronized by collecting animals that hatched in a 2-hour window. These larvae were transferred to fresh 10cm NGM plates seeded with live OP50 and reared at 20°C. The animals were then harvested 36 hours later once they had reached the L4 stage and washed on to plates for *egg-5* RNAi. After 24 hours on the RNAi plates the animals were washed to the baseline food level of $2x10^9$ cells/ml for one day before the initiation of DR on the 2nd day of adulthood. Animals were transferred to fresh plates on the 3rd and 5th days of adulthood and imaged on the 6th day.

Due to egg-laying defects, imaging experiments involving strains containing the *daf-7(ok3125)* mutation could not be treated as above. Instead, all strains used for these imaging sets were grown for 2 generations as before, and then the gravid F2 adults were collected and treated with Sodium Hypochlorite to break open the animals and liberate their eggs (*89*). The eggs were then deposited onto NGM plates seeded with OP50 for either 72 hours, in the case of strains in a *daf-7(ok3125)*-containing background, or 48 hours for non-*daf-7(ok3125)*-containing strains. L4-stage animals were then harvested after these respective intervals and then treated exactly as above.

4.5.5: Microfluidic Imaging

For the quantitative imaging studies, animals subjected to the dietary restriction protocol described in the previous sections were suspended in S Basal media on day 6 of adulthood and introduced into the custom microfluidic device via pressure driven flow.

All microfluidic devices were prepared according to procedures described in Appendix A. On the device, individual animals were sequentially directed into and trapped within an imaging channel gated by pressure-driven on-chip valves (*30*) under the control of custom LabVIEW software (Section 2.4). Dense, 1-micron fluorescent z-stacks through head of each worm were collected using a standard epifluorescence microscope (Nikon Ti-E inverted microscope) with a 40X oil objective (1.3 NA) and a Hamamatsu Orca R2 camera. Red and green fluorescent intensities for each our fluorescent reporters were collected simultaneously using an Optosplit II emission splitter and stored for analysis.

4.5.6: Image Processing

Z stacks from our quantitative imaging studies were loaded into MATLAB to be analyzed for single-cell expression. To identify neuron-pairs and their locations within the imaging plane, maximum projections were computed and a thresholding algorithm was utilized to locate individual fluorescent cells. Identifications of the cells were then computed based on relative distances and locations within the worm head. For quantification, the three dimensional volume around each cellular location was extracted from the full z-stack and intensity was integrated over a consistent number of the brightest pixels, which fully encapsulate the entire cell in all cases. To avoid potential interference from condition-specific changes in the gut auto-fluorescence, the background intensity was calculated for cell pairs near the gut (ADF, ASI), via estimation of the mode of the intensity distribution in a volume around the neuron. This background intensity value was subtracted from the integrated fluorescence to obtain the final output.

4.5.7: Encoding Analysis

To estimate the ability of the gene expression readouts and lifespan responses to encode information about the food inputs, a Bayes discriminator is applied with five-fold cross validation (*147*). To do this the data is first randomly partitioned into five test groups. For each test group, expression or lifespan probability distributions are computed for each food level based on the remaining data in the four other test groups (the training set). A multivariate Gaussian distribution is used to fit the expression data and a Weibull distribution is used for lifespan data. Using these probability distributions, the conditional probability that each member of the test group has their particular expression or lifespan outputs given each of the food levels is calculated. The encoding accuracy of these raw probability values can be found in Figure B.4 in Appendix B. To make a final inference about the food level each worm was subjected to, the animal was assumed to have come from the food level with the highest conditional probability. The encoding accuracy of this maximum likelihood model can be found in Figure B.5 in Appendix B.

In the encoding analysis for expression data, the full set of imaging data (Figure B.1-B.3 in Appendix B) is limited to animals with corresponding data from all three neuron pairs ($n \geq 726$ for WT, $n \geq 110$ for tph-1(-), $n \geq 83$ for daf-7(-) and $n \geq 54$ for tph-1(-);daf-7(-) for each food level). For the lifespan data, the pooled aggregate of all of the lifespan data (highlighted rows in Table B.1 for wildtype and pooled mutant data in Table B.2) is used.

CHAPTER 5: WORM CHAMBER ARRAY FOR CHEMICAL STIMULATION AND ASSESSMENT OF BEHAVIORAL OUTPUTS IN *C. ELEGANS*

This work has been previously published in Lab on a Chip and was performed in collaboration with Kwanghun Chung.

5.1: Introduction

Thus far, microfluidic, hardware and software technologies have been developed and applied for the purpose of assessing specific internal readouts in *C. elegans*. However, one of the advantages of the worm as a model organism is that it is capable of exhibiting complex behaviors that are relatable to functional metrics of health span in humans and can provide insight into organismal integrity and health with age. For example, the overall motility and activity of the worm and the ability of the worm to respond appropriately to stimuli can provide insight into sensory, neural and muscular integrity (*3, 148-154*). In combination with the tools developed in the previous chapters, the ability to assess these behavioral outputs can provide a comprehensive view of the aging process from the molecular to the organismal level and the relationship of these outputs to ultimate longevity.

However, the intrinsic mobility of the worm also hinders the observation of behavioral outputs in a large population in a longitudinal way. Chemotaxis assays which gauge the ability of worms to respond to environmental chemical cues are often done at the population level. These assays are typically accomplished by depositing a small amount of a chemical cue at a fixed location on an agar plate, allowing a spatial gradient to be

established form this source and then observing the positions of a population of animals relative to this source (*155*). While this type of assay is informative of the relative attraction of populations to certain chemical stimuli, the specific behaviors elicited by different concentrations of chemicals and the level of heterogeneity in the responses of the population are lost. Moreover, these assays lack temporal control of stimulus application or observations of temporal changes in behavior patterns. Alternatively, chemicals can be delivered to individual worms partially immobilized by adhesives (*156, 157*). However, this method adds confounding mechanical stimuli, limits the range of behaviors than can be exhibited by the worm, and is time-consuming and manually laborious.

Recent technological advancements have started to increase experimental accessibility to longitudinal behavior data with higher temporal resolution. For example, Ryu *et al.* and Luo *et al.* developed a microdroplet assay where odorants or temperature changes could be delivered with temporal resolution to individually encapsulated worms (*158, 159*). However, this process is still limited by the need for manual encapsulation and limitations in the types of chemicals that can be delivered. To address some of these problems, different types of microfluidic have been developed to allow on-chip trapping and stimulation of individual worms (*39, 44, 160, 161*). However, these platforms tend to accommodate only limited numbers of worms simultaneously, making it potentially difficult to ascertain subtle or noisy behavioral outputs.

As an alternative approach, image processing solutions have also been developed to enable the acquisition of longitudinal data via computational tracking of individual

worms without the need for physical isolation (*42, 51, 52, 162*). However, these methods are limited in the number of worms that can be tracked simultaneously and allow physical interaction between individual worms, which can confuse tracking software and introduce new experimental uncertainties. More importantly, single worm tracking is dependent on having continuous data acquisition at frame rates high enough such that the displacement of worms between frames is relatively low. While this is achievable in the short term, this is not a robust solution for long-term experiments, where the interruption of video acquisition for even a few seconds over hours or days can cause loss of worm identification.

Thus, there is still a need for technologies to address the need for robust longitudinal stimulation and behavioral tracking of large numbers of worms. Ideally, platforms should facilitate worm handling and loading with minimal manual intervention, be scalable to accommodate large numbers of worms, enable a high degree of temporal control in the application and removal of chemical stimuli, have low off-chip support system requirements, and be simple to use for non-experts. This chapter will discuss the development of a micro-scale, self-loading multi-well platform accommodates all of these needs (*163*). While this chapter will highlight the specific application of this platform for assaying chemically stimulated behavioral changes with high temporal resolution, the microfluidic technologies developed here are extendable to many other applications requiring highly parallelized individual housing of *C. elegans*.

5.2: Device Design and Operation

Figure 5.1a shows an overview of the microfluidic device. The device is fabricated with standard soft lithographic techniques (Appendix A) in one layer of PDMS and consists of a single main serpentine channel between two inlets (I1 and I2) and one outlet (O). As shown in Figure 5.1b, rows of worm loading channels and circular housing chambers are arranged between adjacent rows of the main serpentine flow path. Thus, as the main flow moves along the serpentine channel (a), small amounts of flow are diverted downwards towards the worm loading channel (b) and across to the next arm of the serpentine channel. Under low pressure, this small cross-flow directs worms into the loading channel (b) and stops them at a restriction (c). At this point, the worm occludes further flow and prevents the entry of additional worms. Under high pressure, the restriction (c) is designed to expand enough to allow passage of worms from the channel (b) to the main housing chamber (d). In the housing chamber, the worms are trapped by an array of small outlet channels that prevent escape while permitting continuous perfusion of media through the chamber and its outlet into the next serpentine arm (f).

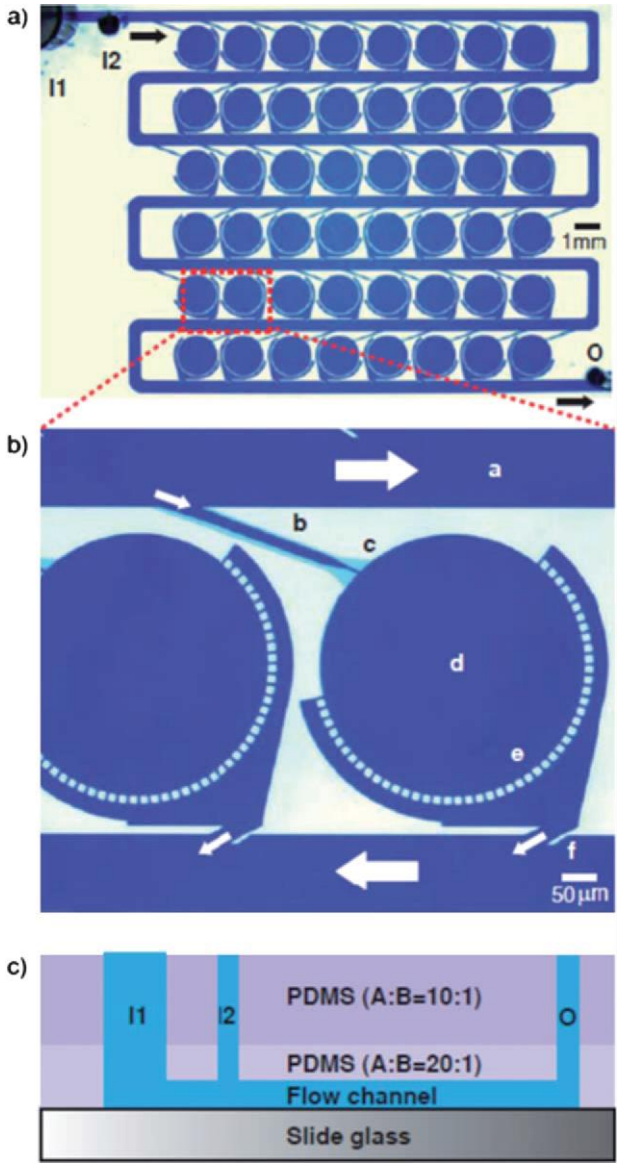

Figure 5.1: Optical micrographs of the worm chamber array device. a) Dye-filled image of the device showing array of 48 circular chambers connected between the arms of a main serpentine flow channel. Black arrows represent flow direction. I1, worm inlet; I2, chemical inlet; O, outlet. b) Zoomed in image of the boxed region in a showing microfluidic components to enable high-throughput single worm loading and chemical delivery: a, serpentine channel; b, single worm loading channel; c, worm loading restriction; d, circular chamber; e, array of small chamber outlets; f, outlet of chamber flow path into next serpentine arm. White arrows represent flow direction. c) Schematic drawing showing cross-section of the device.

The loading operation of the device depends upon the ability of the restriction (c) to sufficiently deform when pressurized and allow worms to enter into the chamber (d). PDMS at the standard lab 10:1 prepolymer to crosslinker ratio is too stiff to permit sufficient deformation. Thus, as shown in Figure 5.1c, the prepolymer to crosslinker ratio is altered to 20:1 in a thin ~2mm layer near the features in order to allow sufficient deformation. However, to facilitate handling of the resulting devices, another ~6-8 mm of 10:1 PDMS is cross-linked on top of this softer layer using the techniques described in Appendix A.

Figure 5.2 outlines the loading process for individually housing *C. elegans* worms within this array of chambers. Operation requires a large plug to close the large worm inlet (I1 in Figure 5.1), a small plug to close the small chemical inlet (I2 in Figure 5.1) and approximate 50 cm of tubing connected to the outlet (O in Figure 5.1) with a manual pinch valve to control flow on chip. Initially, the device is primed with M9 buffer, which is introduced with a syringe through the small inlet. With the large plug inserted and the outlet pinch valve closed, any remaining air can be removed via pressurizing the syringe for 5-10 minutes. After fully priming the device, the syringe can be removed and replaced with the small plug, the outlet pinch valve is closed and the large plug is removed to prepare for the introduction of worms (Figure 5.2a).

Once the device is ready, worms can be collected and suspended in M9 buffer. With the outlet pinch valve closed, these worms can be introduced into the device using the large inlet as a reservoir (Figure 5.2a). To begin the loading process, the pinch valve on the outlet is opened with the outlet roughly 50 cm below the height of the device. As shown

in Figure 5.2b, this allows low pressure, gravity driven flow to allow individual worms to dock into the single worm loading channels preceding the chambers. As the worms are loaded, additional clean buffer can be added to the large inlet reservoir to ensure the removal of all worms through the device. Once all worms have moved through the device, the large plug is then rapidly inserted into the worm inlet in order to induce a burst of high-pressure flow that pushes the worms through the restriction in between the loading channel and chamber (Figure 5.2c). After the plug has been inserted, single worms have been loaded into individual chambers, the worm inlet is closed and the device is ready for the introduction of chemical stimuli through the small chemical inlet. To do this, the small plug is first removed with the outlet pinch valve closed. For addition of a new media or chemical stimuli, a small droplet ~50 μL droplet of the sample can be pipetted on top of the open chemical inlet. Subsequently opening the outlet pinch valve for about 15 seconds is sufficient to fully exchange the volume of the device with the new fluid. Repeated changes in the media can be accomplished in the same manner with washing of the chemical inlet with M9 buffer in between different samples.

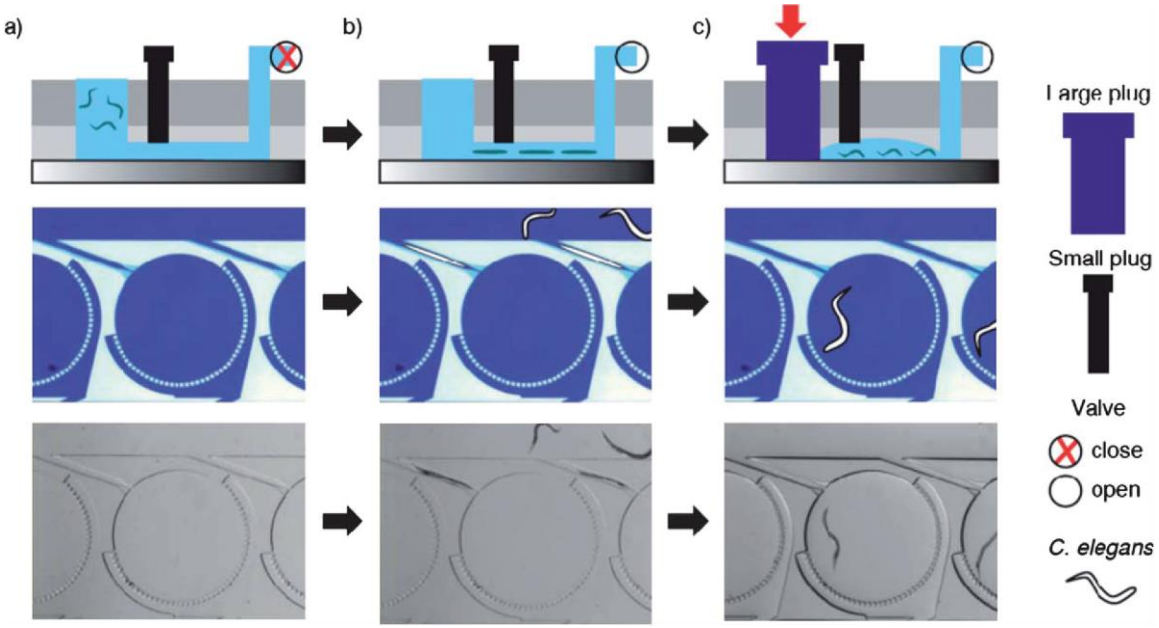

Figure 5.2: Device operation process: top, schematic drawing of the cross-section of the device; middle, illustration of single circular chamber; bottom, optical micrographs of the single circular chamber. a) After filling the device with buffer, outlet valve is closed, and worm suspension is pipetted in the worm inlet. b) To load the worms in the single worm loading channels, the outlet valve is open to allow low pressure, gravity-induced flow. c) Once the worms are in the single loading channels, the large plug is rapidly inserted into the worm inlet. This applies pressure to expand the stopper and push the worms through the stopper and into the chambers.

The ability to load worms in the manner described in Figure 5.2 depends on the ability of the restriction between the loading channels and the chambers themselves to both stop worm movement during low pressure loading in Figure 5.2b and allow worm movement during high pressure bursts in Figure 5.2c. In order to facilitate these two functions, the stepper is designed using a tall narrow channel superimposed on a shallow, wide channel on the bottom, as shown in Figure 5.3a. Under low pressure conditions, both the narrow portion of the channel and the shallow portion of the channel are not wide or tall enough to allow the passage of young adult worms that are roughly 40 μm in diameter. However, Figure 5.3b shows that pressurization of the device via insertion of the large plug visibly

deflects the structures in the restriction. Confocal imaging of the deflection using a fluorescent solution in the chamber reveals that the upward deflection of the shallow channels allows sufficient room for the passage of an adult worm (Figure 5.3c). In Figure 5.3d, confocal imaging under defined pressures shows that this restriction design simultaneously inhibits the passage of worms under low pressures (5.3d left) and permits the passage of worms under high pressures (5.3d right).

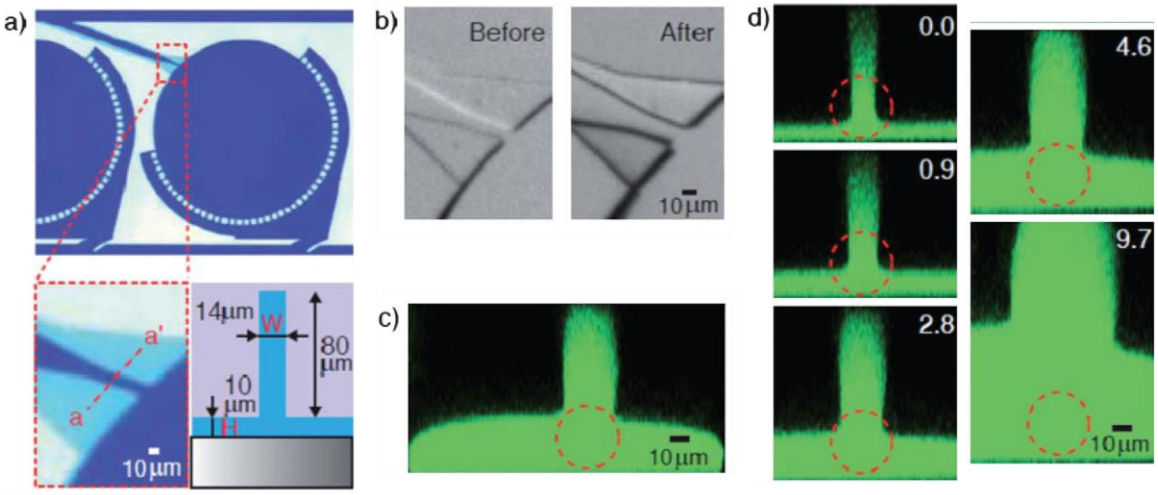

Figure 5.3: Expansion of the restriction region allows worm loading into the circular chambers. a) Top, optical micrograph of a single chamber; bottom left, zoomed-in image of the boxed region showing the restriction; bottom right, schematic of the cross-sectional view (a–a') of the restriction showing its dimensions. b) Optical micrograph of the restriction before (left) and after (right) the large plug is inserted. c) Confocal image of the cross-section (a–a') in a showing expansion of the restriction when the large plug is inserted. The outlet valve remained closed. Dotted red circle represents the cross-section of a young adult *C. elegans* (40 µm in diameter). d) Confocal image of the cross-section (a–a') in a at pressures 0, 0.9, 2.8, 4.6, and 9.7 psi.

5.3: Device Characterization

Figure 5.4 shows optical micrographics demonstrating the loading efficiency of the device. As shown in Figure 5.4a, worms are effectively guided into the single worm

loading channels by the small cross-flows into each of the chambers. However, by design, the entry of a worm both physically occludes the channel and stops further cross-flow, effectively preventing multiple loading of worms at this stage. Figure 5.4b shows that insertion of the plunger effectively pushes all of the worms docked in the single worm loading channels in Figure 5.4a into the attached chambers. Occasionally, at this stage of loading, additional worms which have not been washed out of the worm inlet can enter the loading channel as the previously loaded worm exits the channel into the chamber. This leads to rare instances of doubly loaded chambers, as indicated by the blue arrow in Figure 5.4b.

The loading procedure shown in Figures 5.2 and 5.4 takes only approximately 3 minutes. Over 17 independent operations of different devices, the average single worm loading success rate was 65%, corresponding to over 30 worms per experiment. Moreover, 16 out of the 17 trials resulted in 20 or more singly loaded chambers. Thus, the device permits robust loading of a relatively large sample of individually housed worms in a short amount of time.

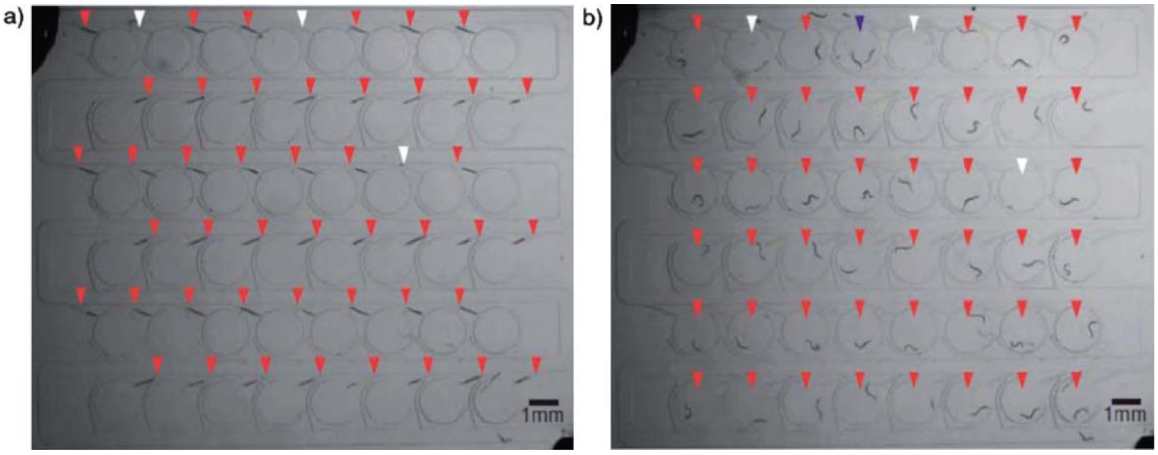

Figure 5.4: Optical photographs of *C. elegans* loaded in the single worm loading channels (a) and in the circular chambers (b). Red arrow head, successfully loaded single worms; white arrow head, empty channels/chambers; blue arrow head, multiple worms in single chambers.

After loading, the single worm loading channels and restrictions preceding the chamber are no longer occluded. The cross-flows across each chamber then serve the second purpose of allowing rapid media exchange through all of the chambers via a single chemical inlet and outlet. To characterize and visualize this media exchange, Figure 5.5 shows the exchange of media adulterated with a food dye. The media exchange process is schematically diagrammed in Figure 5.5a. As described in section 5.2, removal of the small plug creates an access port into the device. To conserve potentially valuable reagents, small droplets of new media can be directly pipetted onto this flow path. Entry of the media can then be controlled via the same outlet pinch valve. This process can be repeated as many times as necessary in order to assay multiple conditions over time.

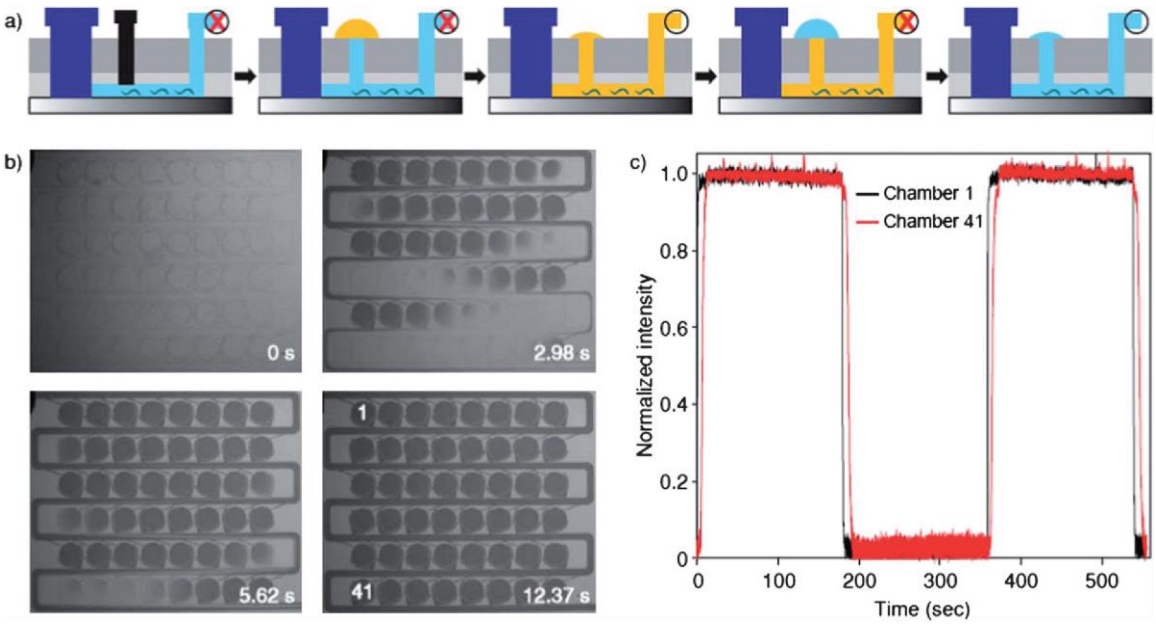

Figure 5.5: Rapid, low-volume media exchange on chip. a) Schematic drawing of the cross-section of the device describing the chemical delivery process. b) Optical photographs showing dye delivery. The device reaches a steady state concentration in all chambers in about 13 seconds, with chamber 41 being the last to reach steady state. c) Plot showing stepwise chemical delivery in chamber 1 and chamber 41 as a function of time.

Figure 5.5b shows optical micrographs of the progression of media exchange through the device. Since the chambers lie in sequence along the main serpentine flow path, media exchange occurs at slightly different times through the device. However, Figure 5.5b shows that full media exchange over all of the chambers can occur under 15 seconds. The time lag between media exchange in the first and last chambers along the serpentine flow path is shown in Figure 5.5c. Over experimental time-frames of several minutes to hours, the exchange lag between the chambers is relatively negligible.

5.4: Assessing Chemically Stimulated Behavioral Changes

5.4.1: Transient Responses to Anesthetic Application

To demonstrate the ability of the device to resolve transient behavioral responses to the application of a chemical, Figure 5.6 characterizes the time-dependent decrease in locomotion after the application of sodium azide. Figure 5.6a shows the population average of body bends per second before and after the application of 5 mM and 10 mM sodium azide. Although at both 5 mM and 10 mM concentrations, sodium azide ultimately results in immobilization of all of the worms, the temporal resolution afforded by the device allows the two concentrations to be distinguished via the speed of immobilization. As expected, 10 mM sodium azide results in a much faster rate of decrease in the body bend frequency.

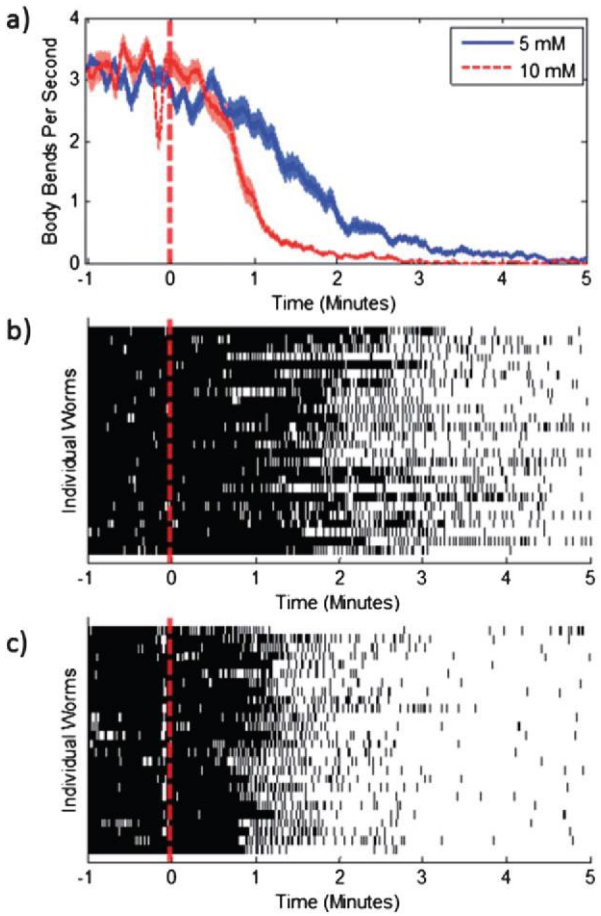

Figure 5.6: Quantification of body bending frequency under the influence of sodium azide. a) Population average (n=26 for both 5 mM and 10 mM conditions) of body bending frequency. Curves represent a 5 second running average of body bend frequency. The standard error for each curve is given in light blue and light red for 5mM and 10mM respectively. b) Raster plot showing incidences of body bending for all 26 animals under the influence of 5mM sodium azide. c) Raster plot showing incidences of body bending for all 26 animals under the influence of 10mM sodium azide. Red dashed lines indicate the time of sodium azide application (t=0).

In addition to temporal resolution, the ability to segregate the independent behavior profiles of individual worms allows for an understanding of behavioral subtleties that would be obscured by population-average data. For example, the gradual decrease in the average body bend frequency observed in Figure 5.6a can be attributed to either gradual decreases in the body bend frequency of each individual worm or sharp decreases in

some worms at different times. The ability of the device developed in this chapter to track many worms with single worm resolution permits the acquisition of longitudinal information for a large number of worms. The raster plots in Figure 5.6b and c show the individual incidences of body bends for each of the 26 worms assayed in both the 5 mM (b) and 10 mM (c) experiments, suggesting that individual worms exhibit a gradual decrease in body bend frequency as well.

In addition to applications in understanding the response time and latent effects of many chemicals, the ability to study initial responses to condition changes may provide mechanistic insights into behaviors such as chemotaxis, where time dependent changes in concentration alter worm locomotion (*159, 164-167*). Unlike conventional point source plate assays, the device developed here allows precise concentration control, temporal control, and permits observation of specific behavioral responses of many animals at a time.

5.4.2: Sex-specific Behavioral Responses to Chemical Stimuli

In addition to the monitoring of simple behaviors such as motility, the platform is also capable of being used to dissect more complex behavioral outputs that stem from physiologically relevant chemical signaling. In many organisms, population-density sensing and sexual attraction rely on small-molecule-based signaling systems (*168, 169*). In *C. elegans*, chemical cues secreted by young adult hermaphrodites has been demonstrated to be a potent male attractant (*170, 171*). In most previous studies, male response to conditioned medium was analyzed by measuring time spent within the vicinity of a point source of chemicals placed on an agar plate (*171*). Although this

attraction assay has been broadly used, it has several limitations. First, the exact concentration of the compounds tested in the scoring region is not well defined due to the diffusion of the chemicals into the agar. As a result of this diffusion, the effect of chemical concentration gradients also cannot be distinguished from the effect of absolute chemical concentrations. Second, chemicals cannot be added or removed during assays and responses to temporal changes cannot be delineated from responses to spatial gradients. Third, animals often crawl in and out of the field of view of a fixed imaging system, which makes it difficult to monitor behavioral response with single-worm resolution. Finally, only a small number of worms can be assayed simultaneously. The microfluidic device presented here, in comparison, allows monitoring up to 48 individual worms simultaneously. In addition, it allows the precise definition of chemical concentrations defined to each worm with high temporal resolution.

To demonstrate the potential of the chamber array to overcome the aforementioned limitations of conventional assays and provide new biological insight, the device was used to monitor male responses to hermaphrodite-conditioned medium containing secreted mating signals. Typical *C. elegans* male mating behavior consists of a set of sub-behaviors that include backward locomotion along a hermaphrodite and tight tail-first turns around the hermaphrodite body in search of the vulva (*172*). Within the liquid environment of the microfluidic device, male worms exhibit a specific behavior wherein the tail forms a tight coil back on a straightened body. This configuration, heretofore referred to as ‘‘male specific behavior’’ and shown in Figure 5.7a, occurs sporadically and persists for periods of several seconds before the worm returns to its normal

swimming behavior. Based on preliminary observations of male behavior in the device and prior demonstrations of the male specific effect of hermaphrodite-conditioned medium on solid agar substrate, it was hypothesized that exposure to hermaphrodite-conditioned medium would result in a higher incidence of male specific behavior.

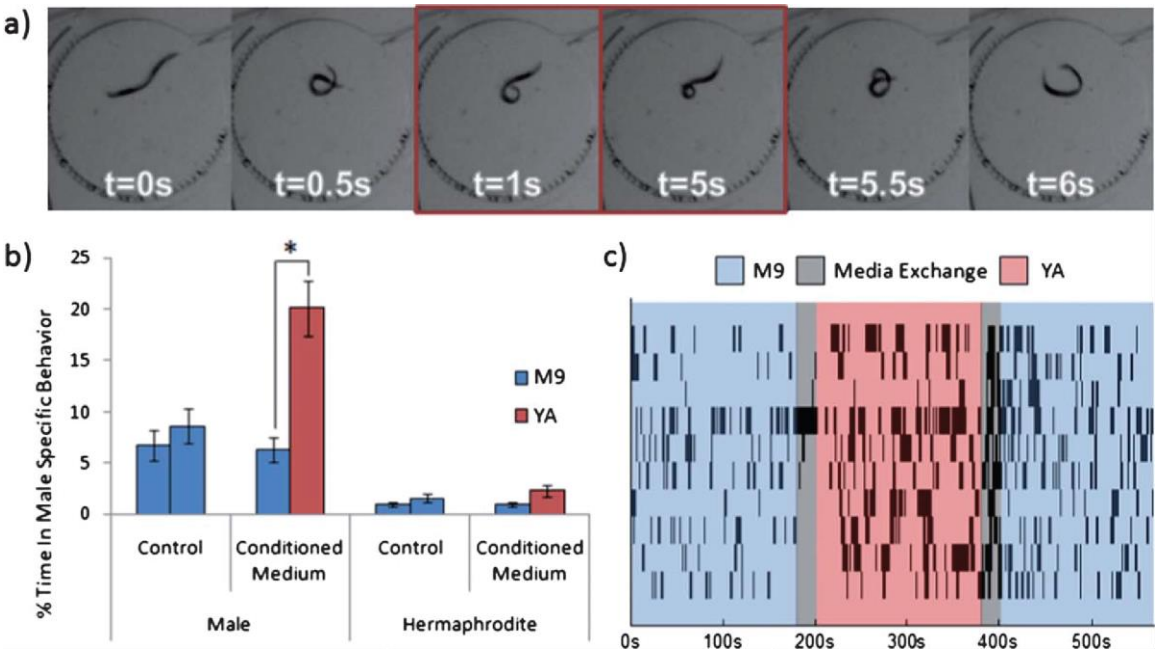

Figure 5.7: Quantification of male specific behavior under the influence of hermaphrodite-conditioned medium. a) Time lapse images showing a worm entering into, maintaining and exiting out of male specific behavior. Frames categorized as male specific behavior are outlined in red. b) Quantification of the percentage of time engaged in male specific behavior for males and hermaphrodites subjected to sequential treatment of M9 and M9 or M9 and YA (young adult conditioned medium). n=16 for male control, n=35 for male conditioned medium, n=20 for hermaphrodite control, n=19 for hermaphrodite-conditioned medium. *Statistically significant $P < 10^{-6}$. Other data pairs are not statistically significant (a=0.05). c) Raster plot showing incidences of male specific behavior for 10 male worms during a full experiment (3 min M9, 3 min conditioned medium, 3 min M9).

The loading and chemical exchange procedures outlined in Section 5.2 were used to expose *him-5* worms to M9 and young adult hermaphrodite-conditioned medium in

succession and measured the percentage of time males engaged in male specific behavior under each condition. The device facilitated the collection of a large quantity of data where many behavioral readouts, such as body bend frequency, turning frequency as well as other specific body configurations such as the male specific behavior in Figure 5.7a, can be tracked for individual worms over a long period of time. To facilitate efficient analysis of a large quantity of data and demonstrate accurate automated determination of behavioral readouts, determination of male specific behavior was performed using custom MATLAB code that detected coiling and body elongation in the worm (*173-175*). Validation of our image processing technique against a set of manually annotated images resulted in a specificity (true negative rate) of over 99% and a sensitivity (true positive rate) of over 94%.

The results in Figure 5.7b show that when subjected to hermaphrodite-conditioned medium, male worms show a significant increase in the percentage of time engaged in male specific behavior ($P < 10^{-6}$). Furthermore, in accordance with early qualitative assessments, hermaphrodites were very rarely observed to engage in male specific behavior in the assays. This indicates that chemical signals in hermaphrodite-conditioned medium trigger a specific behavioral response in male worms other than changes in locomotive behavior such as forward movement and pirouettes (*164-167*). Unlike assaying dwell times on plate, the device provides the means to easily dissect out specific components of behavioral response. This opens up exciting opportunities in ascertaining the specific behavioral effect of individual chemicals in complex mixtures such as hermaphrodite-conditioned medium.

Similar to individual tracking in the assays with anesthetics, Figure 5.7c shows a representative selection of individual worm behavior in response to conditioned medium. With high time resolution for many individual worms, it is observed that an increase in the incidence of male specific behavior happens within 30 seconds of introducing the conditioned medium. Interestingly, a less pronounced increase in the incidence of male specific behavior persists after conditioned medium has been replaced with M9. This may indicate that male responses to chemical cues from hermaphrodites are persistent past the removal of the initial stimulus.

5.5: Discussion and Conclusions

This chapter presents a microfluidic device that allows for the behavioral tracking of single worms and delivery of stimuli with precise temporal control. The capabilities of this device with respect to chemical screening and behavioral assessment were demonstrated by processing the behavioral response of a large number of individual worms to drugs and sex pheromones in hermaphrodite-conditioned medium. Unlike previously reported methods for chemical response assays, the method presented here permits rapid loading, the simultaneous longitudinal investigation of large numbers of freely moving worms, and excellent temporal control in the delivery of chemicals. Thus, this system is an advancement that can be used to facilitate numerous chemical screening studies on *C. elegans* including investigations into neurodegenerative disorders, diabetes, addiction, and aging related diseases.

In addition to its applications in chemical screening, the device presented here is a refinement and miniaturaization of the mutli-well platform that is frequently used across

a broad spectrum of biology. However, despite the convenience of the physical isolation afforded by multi-well platforms, traditional plates can be difficult to load with defined numbers of specimens. Furthermore, high-throughput fluid exchanges and imaging applications are difficult to perform without specialized liquid handlers or plate readers. Even with these expensive support systems in place, traditional multi-well plates have high volume requirements and limited amenability to parallel data acquisition due to the limited ability to fit macro-scale wells onto a small imaging field of view. The system presented here addresses all of these aforementioned problems by providing a mechanism for controlled loading of biological specimens on-chip and allowing rapid fluid exchange without the use of expensive liquid handlers. Furthermore, the miniaturization of the platform reduces reagent usage and permits a large number of individual wells to be assayed simultaneously using a fixed field of view. Thus, this systems also represents a technological advancement that can be generally applied to many other types of biological experimentation requiring a multi-well format.

5.6: Materials and Methods

5.6.1 Device and Hardware Fabrication

Microfluidic devices were manufactured using standard photolithographic and soft lithographic techniques outlined in Appendix A. 10 gauge needles (McMaster-Carr, Elmhurst, IL) were used to punch the large worm inlet (I1 in Figure 5.1a) and 19 gauge needles were used to punch the chemical inlet (I2) and the outlet (O). The small and large plugs used for device operation are constructed by filling the same needles with PDMS (Dow Corning Sylgard 184, Midland, MI) using a syringe and allowing the PDMS to

cure inside the pore of the needles to form a sealed plug. At the outlet, roughly 50 cm of polyethylene tubing (Scientific Commodities BB31695-PE/4, Lake Havasu City, AZ) with an acetal pinch valve (McMcaster-Carr 5031K11, Elmhurst, IL) was used to facilitate and control gravity driven flow through the device

5.6.2 Worm Maintenance and Culture

Wild-type *C. elegans* (N2 Bristol) and CB1490 *him-5(e1490)* were used in the experiments described in this chapter. All strains were maintained at 20°C. For all the assays, age-synchronized young adult worms were prepared as follows: embryos were obtained by bleaching adults using a solution containing about 1% NaOCl and 0.1 M NaOH, washed and allowed to hatch in M9 buffer, and cultured at 20°C on Nematode Growth Medium (NGM) plates seeded with OP50. To generate the liquid suspension of worms used in each experiment, 100 young adult worms were washed and suspended in M9 solution containing 0.02 wt% Triton X100 as a surfactant.

5.6.3: Experimental Image Acquisition and Processing

N2 (for anesthetic response experiments) or *him-5* (for male response experiments) young adults worms were loaded in the devices as described previously. After loading, fresh M9 without Triton X was introduced and the loaded worms were allowed to rest for 2 min. Then, images of the worms swimming in M9 were captured at an acquisition rate of 15 fps with an Infinity 2 CCD camera (1.4 Megapixel CCD monochrome camera) (Electron Microscopy Sciences, Hatfield, PA), mounted on a Zeiss Stemi SV11 dissecting microscope (Carl Zeiss Instruments, Germany). For all experiments, the

magnification was set such that all the chambers filled the field of view (18.13 mm x 13.54 mm).

For the anesthetic experiments, 2 min of M9 data was acquired before sodium azide was introduced. Behavior after the introduction of sodium azide was then recorded for 5 min. For the male behavioral response experiments, 3 min of M9 data was acquired before hermaphrodite-conditioned medium was delivered and the subsequent behavior of the worms was monitored for another 3 minutes. After these 3 minutes of data collection, the media was exchanged for fresh M9 and another 3 minutes of data was acquired. Once the assay was over, 10 mM sodium azide was introduced to immobilize the worms and then each worm was examined under higher magnification to determine the sex of individual worms. The hermaphrodite-conditioned medium used in these studies was prepared as described in previous publications (*168, 170, 171, 176-179*).

The captured images were analyzed with code developed in MATLAB. Each chamber was isolated and analyzed individually. First, features outside of the circular chamber were removed. Thresholding was then employed to segment out the worm body, which is substantially darker than the surrounding fluid. Using the resulting binary image, the eccentricity of an ellipse with the same second moments as the area occupied by the worm is calculated. Since the eccentricity is a measure of worm elongation, body bending during swimming causes periodic decreases in the eccentricity parameter. Thus, body bending frequency for each worm can be found by assessing the frequency of these decreases.

To identify the male specific behavior shown in Figure 5.7a, a circular Hough transform was performed on the original grayscale image in order to identify circles formed by tail coiling in the worm. A combination of the Hough transform circle identification result, eccentricity, and temporal relationship to other frames identified as male specific behavior was then used to identify incidences of this behavior in all of the video frames captured for each worm.

5.6.4: Characterization of Pressure-Induced Deflection on Chip

To characterize the deformation of the restriction that prevents worms from entering the chambers prior to pressurization, the device was first filled fluorescent dextran (molecular weight 70,000 Da Oregon Green; Invitrogen) solution as a contrast agent. The pressurized cross-section of the restriction region was then imaged using confocal microscopy (Zeiss LSM 510 VIS Confocal Microscope). For the pressure sequence in Figure 5.3d, the device was pressurized through the outlet while both inlets are plugged to maintain the pressure in the device during imaging. In actual device operation, the device expands when the plug is inserted and quickly shrinks back to its undeflected shape as liquid is displaced through the outlet. To assess the maximum stopper expansion in actual device operation, the large plug is inserted with the outlet closed. Then, the cross-section was imaged as before.

CHAPTER 6: LONG-TERM TRACKING OF HEALTH AND LONGEVITY IN *C. ELEGANS*

This work is planned for future submission to a peer reviewed journal.

6.1: Introduction

C. elegans is an important model organism for the investigation of the aging process and has historically furnished much of the initial evidence for the genetic regulation of aging (*180-182*). The worm's popularity as an aging model is a result of many biological traits that make it easy to apply both genetic and environmental perturbations and rapidly assess the outcomes of large populations over relatively short lifespans (Table 1.1). However, existing experimental techniques and technologies for aging assays in the worm have limited the ability to simultaneously offer fine control over environmental variables, high experimental temporal resolution, longitudinal tracking of individuals and large-scale experimentation. Thus, conventional techniques have not been capable of fully leveraging the capability of the *C. elegans* model for large-scale, high-content assessment of the health and longevity.

As described in Section 4.5.3, conventional methods of performing lifespan assays in *C. elegans* typically involve the culture of small populations of animals on agar plates. Environmental conditions such as different food and temperature inputs are applied via controlling the growth and density of the bacterial lawns on these plates and the use of incubators, respectively. To prevent food depletion over time, animals are manually transferred between plates outside of the incubator. Scoring of animals for health or

longevity also occurs manually outside the incubator. Thus, the degree of manual labor involved in these assays limits the ability to conduct assays with single worm resolution and perform large-scale experimentation. Moreover, these techniques do not permit fine and continuous control over environmental variables or high temporal resolution in data collection. The maintenance of food concentrations is limited by the frequency of transfers and the frequency of both transfers and data collection is limited by manual labor constraints and the deleterious experimental effects of interrupting temperature control.

Some specialized culture techniques have been demonstrated to address the issues of single-worm and temporal resolution. For example, Pincus *et al*. demonstrated the use of a patterned hydrogel array to spatially confine individual worms for lifelong assessment (*149*). While this system allows large-scale tracking of individual *C. elegans* via both spatial confinement and automated microscopy, the method of physical confinement does not permit the transfer of worms or food exchange and thus limits the ability to control a critical determinant of longevity (*6, 7, 92-94*). The ability to transfer or remove progeny within this platform also imposes experimental constraints that require inhibition of reproduction, which is also a regulator of longevity (*142, 183-187*). Furthermore, while the system lowers manual labor requirements and the throughput of assays via automated microscopy once slides are transferred onto the microscope, experimental data collection still requires manual physical manipulation of the experimental setup and removal from environmental control chambers. Thus, this system is still constrained with respect to experimental time resolution.

To address the environmental control and time resolution issue, Stroustrup *et al*. developed a fully automated data acquisition system using commercial scanners as a sensor system that could be scalable and integrated into commercial incubators (*188*). The system permits automated data acquisition without manual intervention and thus allows sub-hourly resolution in the determination of longevity. However, the low frame rate achievable by scanners prevents acquisition of many behavioral metrics that may be indicative of health. Additionally, the system also has no intrinsic mechanism for transferring worms, removing progeny, or exchanging food, again limiting control of food inputs and requiring inhibition of progeny production.

To achieve a higher degree of environmental control, microfluidic platforms allowing liquid culture of worms on chip have been demonstrated for lifespan and developmental assays (*44, 45, 189*). These systems typically have the intrinsic advantage of accommodating continuous food exchange and progeny removal. However, these microfluidic platforms lack mechanisms for fine temperature control and are difficult to integrate within commercial incubator systems. Furthermore, scalable and automated systems for accommodating operation of many experiments in parallel have not been demonstrated. Systems that accommodate larger sample sizes have done so at the expensive of single-worm resolution (*189*). As a result, the experimental data derived from these systems have been mainly limited to proof-of-concept demonstrations.

Thus, a *C. elegans* lifespan assay platform that addresses all of the experimental challenges hindering large-scale, longitudinal data collection and environmental control is still lacking. To fulfill this need, this chapter will discuss the integration of

microfluidics, hardware and software technologies to combine the specific advantages of physical isolation, high temporal resolution and continuous environmental control of the previously described systems. Moreover, leveraging the specific advantages of the microfluidic platform developed in Chapter 5, the platform developed in this work exceeds the capabilities of previous work by allowing the acquisition of behavioral metrics with the possibility for intermittent physical or chemical stimulation or rapid changes in environmental conditions. Thus, the system developed here has the potential to enable high-throughput high-content, long-term analysis of individual health outcomes with fine control of environmental conditions and the possibility for applying a large range of experimental interventions.

6.2: System Overview

Figure 6.1 shows an overview of the *C. elegans* long term culture and data acquisition platform presented in this chapter. This work adapts the capabilities of the microfluidic technology presented in Chapter 5 for long term physical isolation of individual worms cultured on a microfluidic chip. However, beyond the functionality of the microfluidic technology itself, this work develops the hardware and software ecosystem that enable automated and scalable experimentation under a large number of environmental conditions. Overall, the system as a whole permits the simultaneous investigation of up to 32 independent microfluidic chips each housing up to 60 worms. Both the longevity and behavioral attributes of these worms can be automatically monitored with sub-hourly experimental time resolution and at behavioral video acquisition speeds of up to 25 frames per second. For environmental control, these 32 chips can each be operated via

independent flow paths that permit the investigation of different food and chemical environments. Furthermore, the system accommodates up to 8 different temperature conditions for these chips.

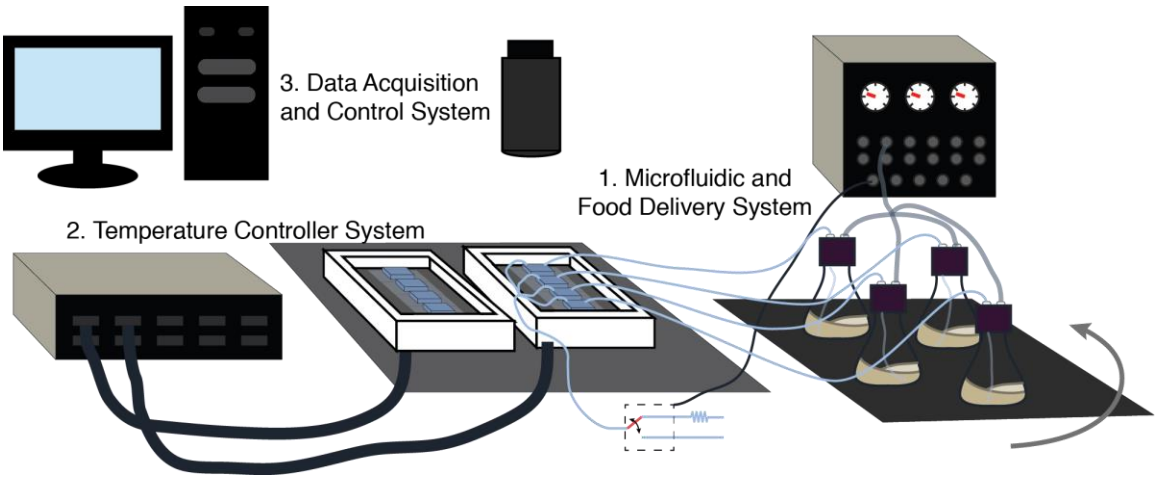

Figure 6.1: Overview of long-term culture and data acquisition system. The entire system consist of three major subsystems that enable control over two critical environmental variables and integrative control over data acquisition.

As shown in Figure 6.1, the platform is composed of three major subsystems. The first subsystem is the liquid handling system comprised of both the microfluidic chip itself and the off-chip support system for control of food and chemical delivery. The second subsystem enables continuous control of environmental temperatures on chip. The third and final subsystem enables automated control and perturbation of environmental variables by interfacing with the first two subsystems and automated data acquisition via control of camera and stage movement. Table 6.1 breaks down each of these subsystems further into their component parts, and outlines the requirements for each of these components. The following sections will outline the specific design of each of these components to meet these requirements.

Table 6.1: Overview of long-term culture subsystem components and requirements

Subsystem 1: Microfluidic and Food Delivery System	
Microfluidic Chip	• Efficient single worm loading • Long term physical isolation of 30-60 worms. • Controlled food and chemical delivery to each worm
Food Delivery System	• Scalable for many independent flow paths with different food or chemical environments • Maintenance of long term sterility • Prevention of particulate accumulation in microfluidic chip • Maintenance of continuous media replacement at reasonable media consumption rates (<1 ml/hour) • Capability for short-term rapid flow to facilitate chemical exchange or physically stimulate worms.
Subsystem 2: Temperature Control System	
Temperature Module	• Capable of interfacing with microfluidic chips for good thermal contact • Can at least accommodate temperature ranges from 12.5 to 27.5°C • Even temperature distribution across each independent module Permits continuous imaging
Temperature Controller	• Scalable for many independent temperature modules • Maintains proscribed temperature in the face of environmental variations
Subsystem 3: Data Acquisition and Control System	
Camera and Optics	• Magnification ranges that permit visualization of up to an entire microfluidic device within the field of view • Sufficient resolution to allow characterization of worm body shapes Frame rates that permit characterization of worm motion
Camera Motion System	• X,Y and Z positioning of the sensor to permit time-sharing amongst multiple simultaneous experiments • Large motion range to accommodate multiple temperature modules Ability scan range of motion with sub-hourly time resolution
Software Integration	• Programmatic control of worm loading • Programmatic control of food delivery system • Programmatic control of temperature controller with temperature feedback and data logging • Programmatic control of camera and motion system • Capability for long term, automated coordination of data acquisition and handling.

6.3: Adaptation of the Worm Chamber Array and Food Delivery

6.3.1: Refinement of Worm Chamber Array for Long Term Applications

The worm chamber array developed in Chapter 5 provides a method for automatically loading and spatially confining otherwise freely mobile worms for observation. In order to extend this design for long term encapsulation and food delivery, several refinements

to the initial design concept were made. Figure 6.2a shows an overview of the refined worm chamber array design, which is operated via one inlet (I) and one outlet (O). The replacement of the two distinct worm and chemical delivery inlets with one inlet was necessary to accommodate long term food delivery. Under long term delivery of a bacterial food source, small amounts of dead volume created by imperfect closure of the second inlet resulted in a flow stagnation point in which bacterial accumulation and proliferation occurred. As opposed to two on-chip inlets, the distinct delivery of worms and food and chemicals was accommodated by off-chip mechanisms as described in Section 6.3.3.

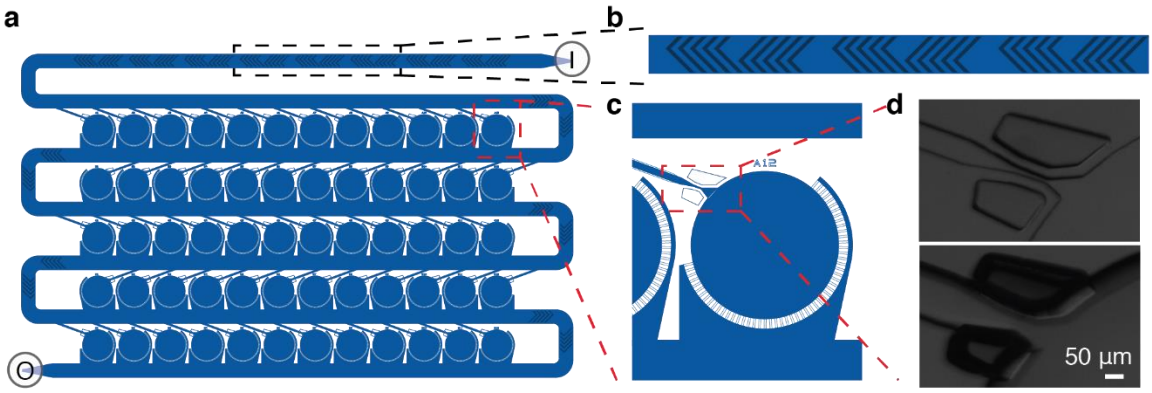

Figure 6.2: Refined worm chamber array for long-term culture and observation of *C. elegans*. a) Overview of device showing 60 chambers arranged along a serpentine channel with one inlet (I) and one outlet (O). b) Inset on inlet channel showing staggered herringbone structures for bacterial mixing. c) Inset on one chamber showing the loading channel, the restriction gating entry into the main chamber and the array of outlet channels to maintain chamber perfusion. d) Bright field images showing deflection new of loading channel restriction under pressure.

The second refinement to accommodate long term food delivery is shown in Figure 6.2b. Under low continuous flow rates to facilitate long term media replacement, small amounts of bacterial sedimentation in the flow lines and tubing off-chip can induce bacterial concentration gradients on chip (*190*). Thus, to promote robust and homogenous distribution of food throughout the array, staggered herringbone mixers (*191*) were integrated along an inlet flow segment to allow resuspension and mixing of any bacterial sedimentation. In addition to accommodating mixing functions, this inlet flow segment also permitted equilibration of the temperature of incoming fluid with the temperature module temperature before delivery to any of the chambers. This is described in more detail in Section 6.5.

Other refinements were made to the chamber design in order to facilitate both long term confinement and robust worm loading (Figure 6.2b). First, worms were found to

spontaneously exhibit crawling behaviors using the array of outlet channels in Figure 5.1b as highly restrictive pillars (*41, 42*). To prevent this behavior and potential escape of worms from the chamber over long culture times, the dimensions of the outlet channels were restricted to a height of 30 μm while the height of the remainder of the device remained at 80 μm to allow room for growth and the exhibition of swimming behaviors. This height restriction effectively prevented the lateral deflection of the outlet channels and the ability for worms to forcibly push themselves in and out of the chambers. Second, while the design of the loading channel restriction in Figure 5.3 permitted the robust entry of small, young adult worms, they occasionally resulted in physical damage to larger worms loaded into the device at different days of adulthood. To promote robust pressure-induced deflection of the restriction and damage-free entry of worms into the chamber, the concept of the laterally deflected membrane in Section 2.2 was adapted to enable outward expansion of the flow channel. Figure 6.2d shows that the creation of PDMS membranes on both sides of the restriction allowed sufficient pressure-induced opening of the restriction to permit entry of worms that are 50-60 μm in diameter.

6.3.2: Characterization of On-Chip Flow

For the chemical delivery applications described in Chapter 5, operation of the device was less sensitive to distributions in on-chip velocities and differences in flow rate for each chamber. The small differences between flow rates to each chamber would only result in slightly delayed fluid exchange in some chambers that were small relative to the time scales of the experiments. However, for long term applications, adequate on-chip velocities are necessary to prevent bacterial sedimentation under stagnant flow and

consistent flow rates into each chamber are necessary to ensure similar environmental conditions experienced by each worm. To address these two issues in microfluidic design process, a combination of finite element modeling and lumped element modeling was utilized to address both detailed evaluation of potential stagnation and assessment of bulk flow properties.

Figure 6.3a shows the result of a COMSOL model for flow velocities and streamlines within a single chamber operated at a 0.5 psi pressure difference between the inlet and the outlet of the chamber. The array of outlet channels located along the circumference of chambers distributes streamlines throughout each chamber and prevents stagnation points where bacterial accumulation may occur. In addition to providing detailed flow velocity distributions within the chamber, the pressure-flow characteristics derived from COMSOL were used to calculate a lumped hydraulic resistance parameter which characterizes the bulk resistance of this complex structure to flow. This parameter was then used in a higher-level lumped element analysis of the entire worm chamber array as shown in Figure 6.3b. The lumped element model permits the assessment of flow profiles throughout the chip in a computationally inexpensive manner.

Figure 6.3c shows the flow rates calculated for each chamber in the array via lumped element analysis with an inlet pressure of 5 psi. While flow rates for the middle 6 chambers are relatively consistent, nearly five-fold differences in flow occur across some rows. Design-wise, the differences in flow rates can be dampened by increasing the resistance of the flow path between each row of the serpentine channel. However, this also has the effect of reducing the space that can be occupied by chambers for each chip.

With the 5 row by 12 chamber configuration analyzed here, up to 60 worms can be housed per chip and roughly 30 of them experience relatively consistent flow rates. Additionally, the characterization provided by this analysis permits the post-hoc assessment of any correlations between media delivery and phenotypic outputs.

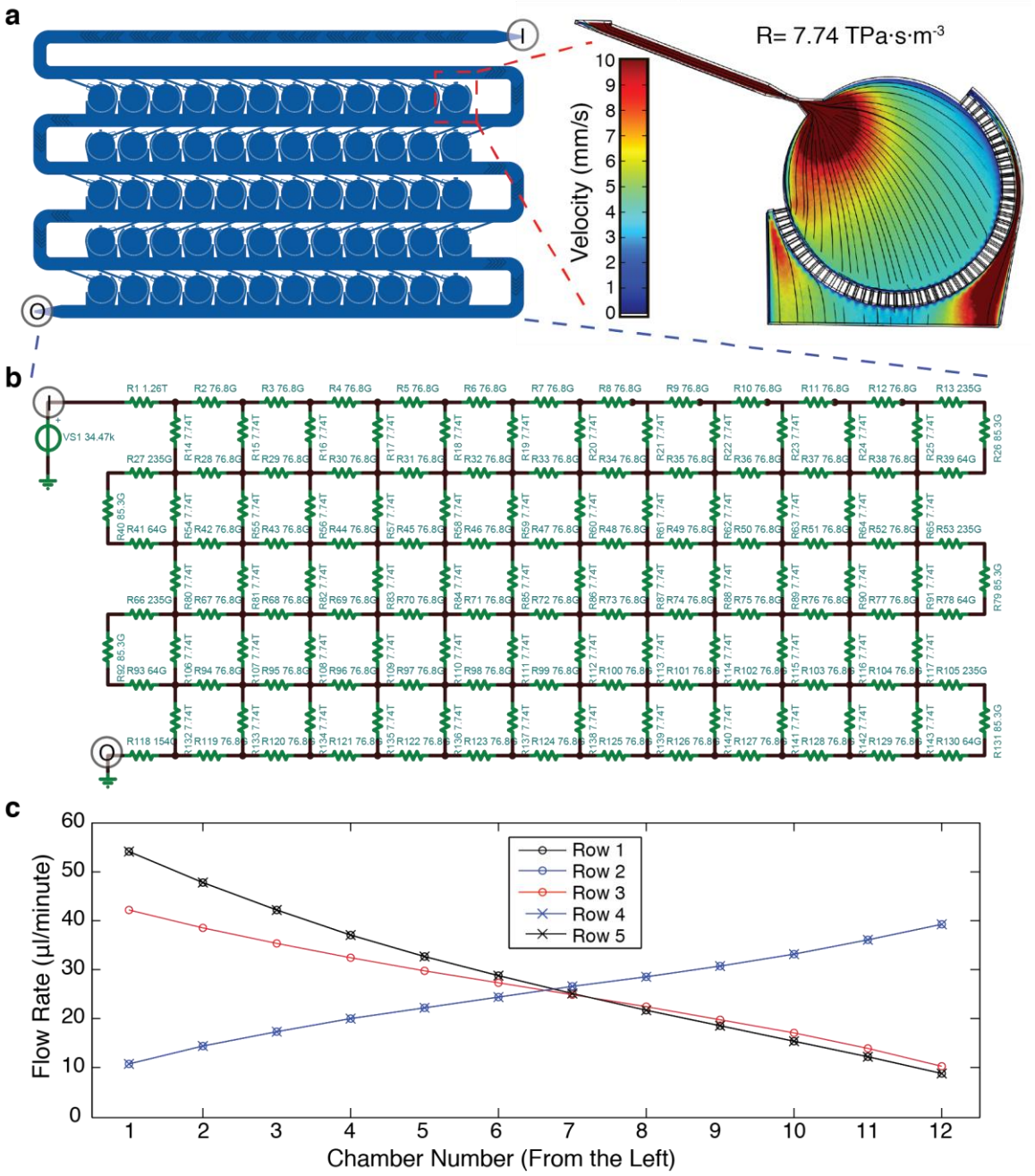

Figure 6.3: Characterization on on-chip flow via mutli-scale modeling. a) COMSOL finite element analysis of flow distributions within a single chamber reveals on-chip velocity distributions and a bulk hydraulic resistance for each chamber. b) Re-interpretation of the worm chamber array as a lumped element distributed resistance model using the hydraulic resistance from COMSOL models full-chip flow distributions in a computationally inexpensive manner. c) Flow rates for each chamber from lumped element modeling.

6.3.3: Off-Chip Food and Worm Delivery System

The ability to load worms and perfuse food into the microfluidic device and to maintain both sterility and consistent flow depends on off-chip flow systems. Figure 6.4 shows the distinct components of the off-chip flow system for food delivery (A), food filtration (B), worm delivery (C) and flow rate regulation (D). Initial worm loading functions are depending upon food delivery module (A), a macroporous filter module for particulate removal (B) and a worm loading modules (C). After worm loading is complete the worm loading module can be disconnected from the flow paths via luer connectors and the microfluidic device can be directly perfused from modules A and B. Additionally, flow rates of chip are regulated by the addition of a flow regulation module (D) at the outlet of the microfluidic device. To allow autoclave sterilization of all flow modules and permit gas exchange through the tubing (*192*), all flow lines use silicone tubing (Scientific Commodities BB518-25)

The food delivery module (A) consists of an air-tight flask with an inlet port for pressure inputs and an outlet port for pressure-driven flow delivery into the rest of the system. To permit repeated sterilization via autoclaving, these ports are constructed from polypropylene luer and tube adapters (Value Plastics XMTLL-6005 and TECS116-6005) screwed into holes drilled and tapped into a GL45 cap using silicone O-rings to maintain a seal (McMaster-Carr). As shown in module A in Figure 6.4, the air input is fed via an air line capped by a 0.2μm syringe filter to insulate the system from the potential contaminants and particulates in the air source and maintain sterility. The flow outlet of the food delivery module is connected to a male luer adapter (Value Plastics MTLL004-

6005) that permits sterile alterations in the flow path including exchanging the filter assembly (B) and connecting and disconnecting the worm loading module (C). Additionally, the flask is placed atop an orbital shaker that offers scalable agitation of many flasks in parallel. This agitation is necessary to prevent bacterial sedimentation within the bacterial reservoir over time and helps to aerate the media in a manner similar to agitators used for other liquid culture platforms.

The outlet of the food delivery module (A) is connected directly to a macroporous filter assembly (B) that permits filtration of both particulates and small bacterial clumps that may be present in the media. The filtration module is constructed from five polypropylene female to luer adapters (Value Plastics LC34-6005) that encapsulate four macroporous polyester meshes (Spectrum Labs) with diminishing pore dimensions and total flow cross-sections. Multi-stage filtration with a sequence of macroporous membranes was necessary to allow a final filtration pore size below the smallest dimension on the microfluidic device (20μm) without rapid occlusion of the filter. The meshes in the pre-filtration stages have higher total cross-sectional area for flow and can maintain flow through multiple days of food delivery even at high bacterial concentrations. The luer connections at the inlet and outlet of the filtration unit facilitates its periodic exchange throughout the course of an experiment to ensure continuous flow.

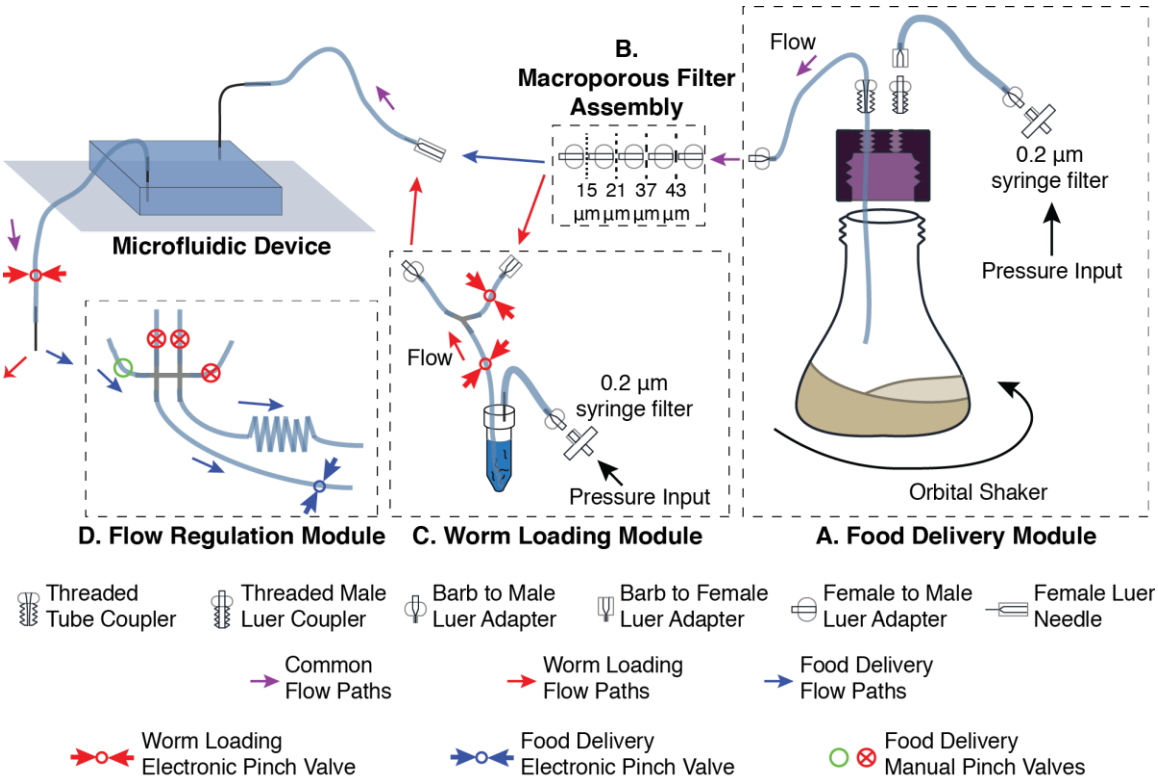

Figure 6.4: Off-chip flow modules for regulation of food and worm delivery. The functionality of the microfluidic device is dependent on initial worm loading operations (flow paths denoted by purple and red arrows) and long term food delivery (flow paths denoted by purple and blue arrows). Initial worm loading relies on the involvement of off-chip modules A, B, and C. Subsequent long-term flow regulation is dependent on modules A, B, and D. Maintenance of sterility in the system is enabled by luer adapters for flow paths that require disconnection or replacement.

The two modules discussed thus far are capable of delivering mixed, aerated and particulate-filtered media into the microfluidic device. However, initial loading of the device requires a separate flow module for worm delivery. This module (C in Figure 6.4) consists of an air-tight microcentrifuge tube (VWR 16466-058) for pressure-driven worm delivery. As discussed in the previous section (Section 6.3.1), continuous perfusion of bacterial solutions on chip without bacterial accumulation permits only one flow inlet into the microfluidic chip. Thus, separation of the worm and media inlets occurs off-chip

via a Y barb adapter (Value Plastics Y210-6005) as a part of this module. The two inlets of the Y adapter connect to the flow outlet of the worm reservoir tube and the flow outlet of the filtration unit during the loading process. The entry of either worms or media is gated by two independent, electronically activated pinch valves on these lines as shown in module C in Figure 6.4. During loading, the outlet of this Y adapter connects to the inlet of the microfluidic device, which is gated by a third electronically activated pinch valve at the outlet. In whole, module C permits the electronic control of both worm and media entry into the device and enables programmatic loading of worms into the chip, as described in Section 6.3.3.1

Once worms are loaded onto the chip, the flow paths provided by the worm loading module are no longer necessary. Using the luer connections in the system, the inlet to the microfluidic device can be removed from the worm loading module and adapted directly to the food delivery module without compromising sterility. This creates a single continuous flow path that prevents the formation of any stagnation points for bacterial accumulation. Furthermore, the outlet of the microfluidic device is then attached to a flow regulation module (D in Figure 6.4). The flow regulation module is a manifold that combines the flow of up to four devices and programmatically regulates the flow using two outlet paths of different resistances. Thus, two different flow rates can be programmatically achieved by opening and closing the outlet flow paths with an electronic pinch valve. Details on the operation of the flow regulation module can be found in Section 6.3.3.2.

6.3.3.1: Details of Worm Delivery

Figure 6.5 shows the sequence of valve operations for the initial preparation of devices and the loading of worms onto the microfluidic chip. For worm loading, the device is connected with modules A, B and C from Figure 6.4. The flow lines through the device are primed using media loaded into the food delivery module via the opening of electronic pinch valves as shown in Figure 6.5a. After the flow lines have been primed, the system must be pressurized to remove any lingering air bubbles on the microfluidic chip. As shown in Figure 6.5b, this can be done by applying high pressure through the food delivery module and subsequently closing all flow paths. The closure of the flow paths allows the flow paths and device to remain pressurized to eliminate air via diffusion through the PDMS. This normally takes about 10-15 minutes.

After this priming process, the system is ready for the introduction of worms. The empty microcentrifuge tube in the worm loading module is replaced with a tube containing a suspension of worms. This suspension can then be pressure injected into the microfluidic device at roughly 2.5 psi as shown in Figure 6.5c. Once the worms enter the device, excess worms can be removed from the flow lines and serpentine channel using the flow of media from the food delivery channel. This ensures that only the worms docked into the loading channels of the microfluidic device are pushed into the chambers during the pressurization step in Figure 6.5d. In the pressurization step, the worm loading restrictions shown in Figure 6.2d are deflected via the pressurization of the device through the food loading module and worms are allowed to flow through these deformed restrictions via the subsequent opening of the outlet pinch valve (Figure 6.5d).

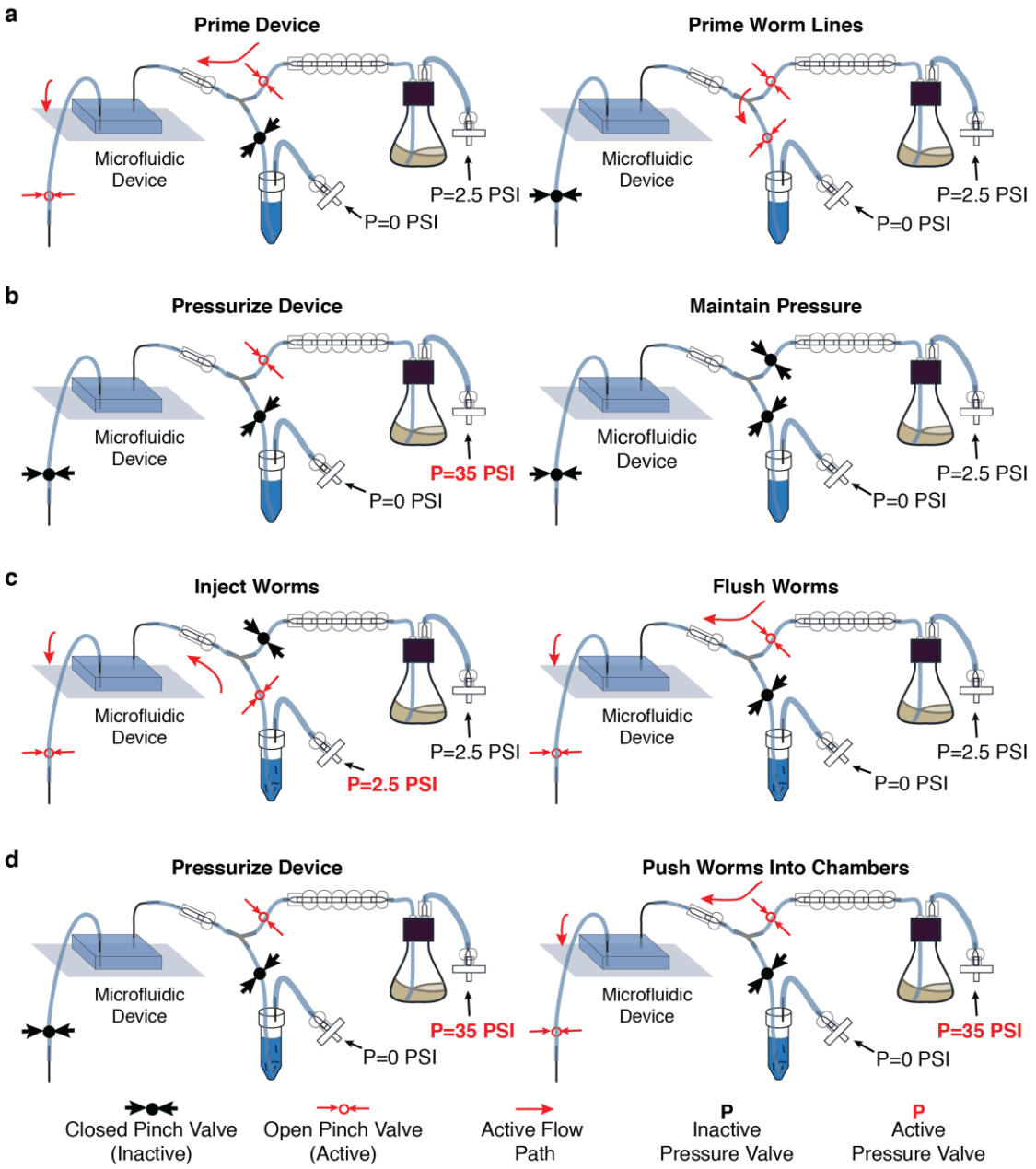

Figure 6.5: Sequence of pressure and pinch valve operations for priming and loading of the microfluidic device. a) The device itself and the flow lines in the worm delivery module are first primed with media from the food delivery flask. b) To fully eliminate air bubbles in the system, the device is pressurized via the food delivery module and any air is allowed to diffuse out from the PDMS device. c) With the device primed, worms are then added to the worm delivery module and pressure injected into the device at low pressure. The tubing and device are then washed out with fresh media from the food delivery module. d) To push the worms into the chambers on chip, the device is pressurized via the food delivery module.

6.3.3.2: Details of Food Delivery

After completion of the worm loading steps in Figure 6.5, the flow system can be reconfigured to a long-term flow delivery configuration consisting of modules A, B and D from Figure 6.4. As shown in Figure 6.6a, this module permits continuous flow of media through the device through a resistance flow path in the flow regulation module. The addition of a fluidic resistor to the flow path is necessary due to the low overall hydraulic resistance of the worm chamber array. Affordable pressure regulation systems cannot robustly operate below 1 psi and pressures near 5 psi are ideally utilized to permit precise regulation and tuning. However, both lumped element analysis (Figure 6.3b) and empirical flow measurements revealed flow rates of roughly 30 ml per hour under driving pressures of 5 psi. This is an unreasonable rate of media consumption. To regulate this media delivery to more reasonable flow rates under feasible operating pressures, microfluidic resistor chips are used (Figure 6.6b).

The calculations in Figure 6.6b show that under a constant channel height of 45μm, these devices can be dimensionally altered in width and length to achieve a range of flow rates. Additionally, since each flow delivery module accommodates the attachment of up to four devices, a range of fluidic resistances is necessary to achieve a constant flow rate of 0.3-0.5 ml/hour when one, two, three or four devices are connected. Figure 6.6b shows these flow designs. The hydraulic resistance of these fluidic resistance is theoretically calculated using $R = \frac{12\mu L}{WH^3(1-0.63\frac{H}{W})}$, where the limiting dimension, H, is assumed to be much lower than the width. They were also empirically verified via flow rate measurements in operation.

In addition to the constant rate of flow afforded by the constant pressure-driven, resistance-regulated flow path shown in Figure 6.6a, there is the potential need for rapid media exchange or physical agitation of the worms on chip. Thus, additional flow modes can be accommodated by the flow regulation module as shown in Figure 6.6c and d. Figure 6.6c shows that a pinch-valve regulated low-resistance flow path in the flow regulation module can be used to programmatically induce bursts of fast flow rates on chip. This flow mode can be utilized for rapid media exchange or physical agitation of the worms. Figure 6.6d shows a third flow mode wherein the food delivery module can be programmatically pressurized to momentarily induce higher rates of flow. However, due to the fluidic capacitance of the system, rapid pressurization and de-pressurization can induce back-flow. While this pulsatile back-flow can be advantageous in terms of worm agitation, potential contamination from too much flow reflux from the outlet into the device and potential escape of worms through the worm loading channels fundamentally limit the range of flow rates achievable in this mode.

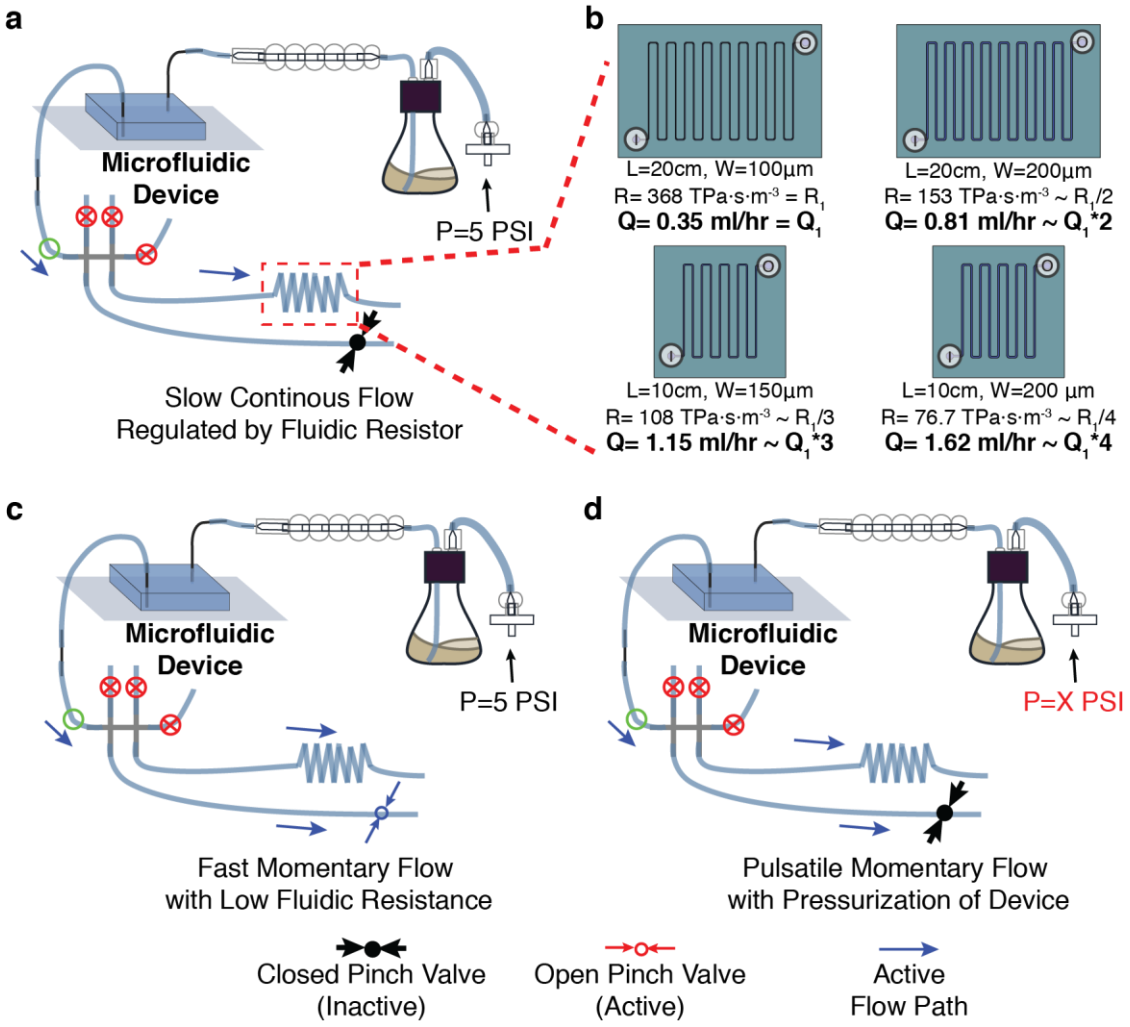

Figure 6.6: Modes of food and chemical delivery into the device. a) The flow regulation module has two outlets and permits continuous delivery of new media to the device at a low flow rate that is regulated by a fluidic resistor at one of the outlets. b) The microfluidic resistor governing flow rates during continuous delivery can be dimensionally altered to accommodate different flow rates and numbers of devices attached to the four-input flow regulation module. c) An electronic pinch valve at the other, low resistance outlet can open to induce momentary flow at a high flow rate for rapid fluid exchange or physical agitation of the worms. d) Flow rates can also be pulsed on chip by increasing the pressure to the food delivery module using a pneumatic valve.

6.3.3.3: Electronics for Programmatic Pressure and Flow Control

All of the components of the off-chip flow system for worm and food delivery are designed to accommodate programmatic control of these processes with minimal manual intervention. Compare to the manual operation procedures described in Chapter 5, the establishment of electronic control is necessary both to maintain closed flow paths and sterility and facilitate downstream automation. Additionally, programmatic operation lowers the learning curve for device operation and affords a level of repeatability and robustness not achievable using manual operation. However, the actuation mechanisms described in Figure 6.4 and the previous sections requires additional support systems to mediate their functions. Towards this end, the technologies and concepts developed in Section 2.3.1 were adapted to create a modified pressure and valve controller system to support the loading functions in Figure 6.5 and the distinct flow modes in Figure 6.6.

The adapted system is shown in Figure 6.7a. The system includes three distinct pressure controllers for generating a high pressure source for pushing worms into chambers during loading and pulsatile food delivery (P_A), a pressure regulator for generating a ~5 psi output to drive continuous food delivery (P_B), and a pressure regulator for generating a ~2.5 psi output to driven worm loading functions (P_C). These three pressure sources are regulated by three-way pneumatic valves into 3 distinct types of outputs as shown in Figure 6.7b. The worm loading valve is connected in a typical configuration where the default air path releases to atmospheric pressure. However, to permit rapid pressurization of the device to higher pressures during loading and pulsatile food delivery, the other valves are connected to either the food delivery pressure (P_B) or the loading pressure (P_C)

when not activated and connected to a high pressure (P_A) when activated. In addition to these pneumatic functions, the system offers 12 voltage outputs to drive the pinch valves for regulating worm loading and fluid regulation.

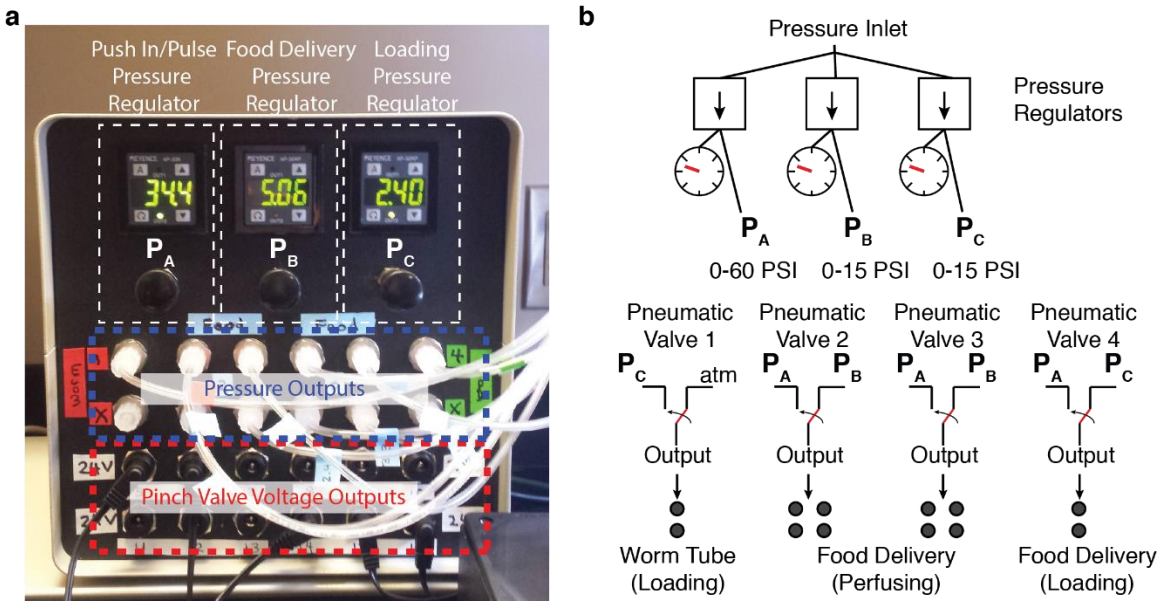

Figure 6.7: Modified pressure and valve controller to allow loading and long term food delivery to worms on the worm chamber array. a) Picture of the front panel of the modified box shows the three distinct pressures necessary for loading (P_A and P_C) and food delivery (P_B), pressure output ports and electronic outputs to control the pinch valves for loading and flow modulation. b) Schematic diagram of the operation of the pneumatic system within the box.

6.4: Microfluidic Temperature Controller

One of the intrinsic advantages of microfluidic technologies is the high degree of environmental control they can enable owing to highly controlled flow profiles, small volumes and low thermal masses. However, control of these environmental variables also depends on off-chip support systems to interface with on-chip functionality. In particular, support systems to mediate continuous and precise temperature control of microfluidic

chips are lacking. Thus, while the system described in Figure 6.5b facilitates a high degree of control over the chemical environmental on chip, it is not easily subjected to temperature control using commercial incubation or environmental control units. Furthermore, utilization of incubators typically prevents continuous or automated monitoring of experiments. To address these challenges, a specialized temperature controller was developed to both enable temperature control on chip and permit continuous imaging using dark-field microscopy.

Figure 6.8a shows a schematic overview of the design of the temperature control system. The basic system consists of a copper temperature distribution platform that is in thermal contact with an underlying peltier module. Application of voltage from a control unit to the peltier heats or cools the copper platform, whose temperature is monitored by a sensor and reported back to the control unit. Additionally, to facilitate the maintenance of set temperatures on one side of the peltier module, waste heat from the opposing side of the peltier module is removed using a heat sink mounted to an aluminum heat sink plate. The temperature module can be compression mounted together to maintain thermal contact between each of the elements by using the lower heat sink plate and a plastic retainer as shown by the assembly in Figure 6.8a. Furthermore, the physical implementation of the temperature module concept can be sized to accommodate different chip sizes and different numbers of chips. For this application, a rectangular temperature module was designed such that each module could accommodate up to four worm chamber devices arranged along its length.

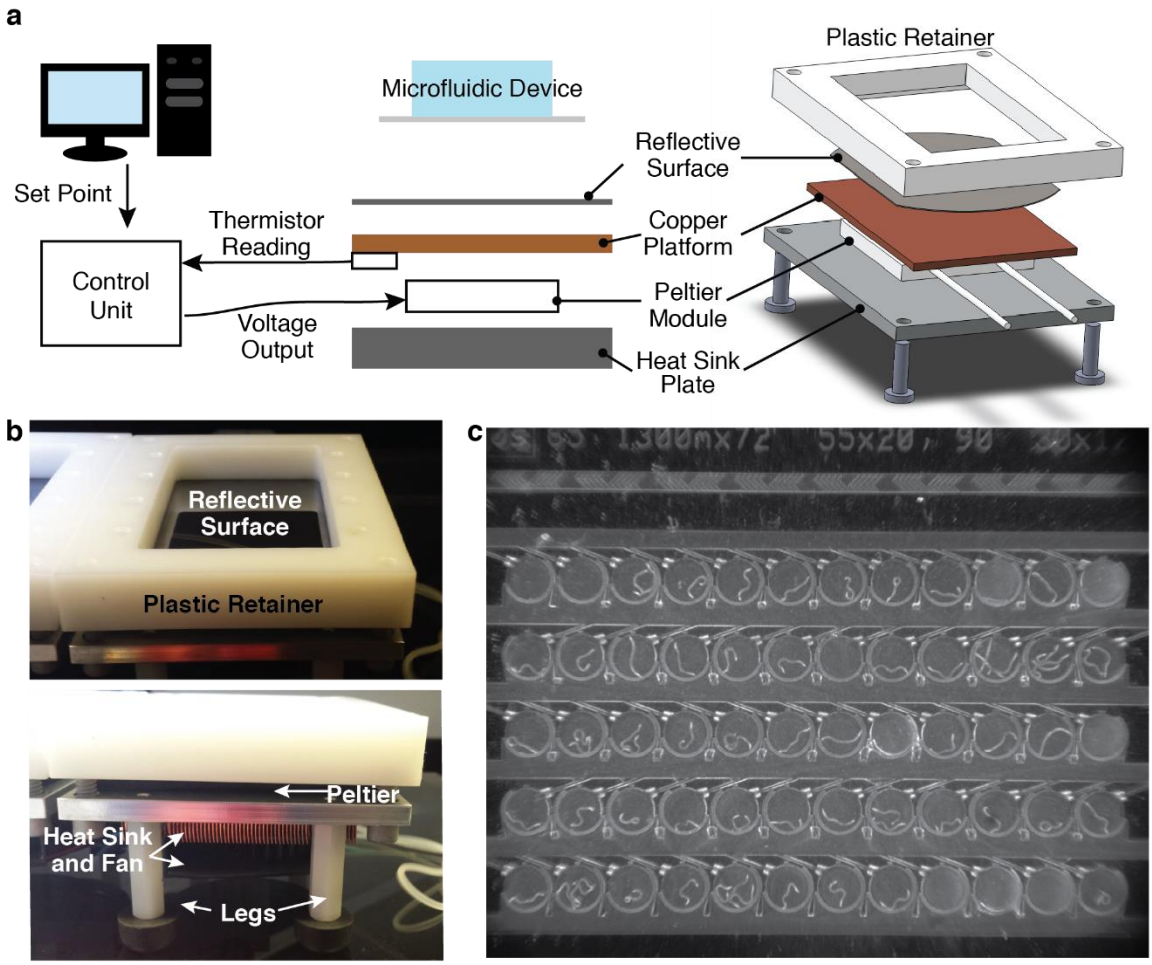

Figure 6.8: Overview of microfluidic temperature controller. a) Schematic of functional elements of the temperature controller system and mechanism for assembling the temperature module. b) Pictures of assembled temperature module showing functional elements in a. c) Image taken with top-down illumination with an LED ring demonstrating the level of contrast available via dark-field reflective illumination.

While this setup provides a scalable mechanism to control the temperature of many overlying microfluidic chips, the temperature control system outlined in Figure 6.8a does not maintain optical clarity on both sides of a microfluidic chip for imaging functions using transmitted light. Thus, a reflective surface in the form of a polished silicon wafer is also added on top of the copper platform to permit dark-field imaging via reflected

light. A picture of the assembled temperature module with its reflective imaging surface is shown in Figure 6.8b. As shown in Figure 6.8c, the reflective surface in combination with a ring LED light source affords a high contrast imaging modality for assessing worm mobility.

6.4.1: Electronic Temperature Control

Control of the temperature module requires the ability to both read out module temperature at the copper platform and a method of programmatically adjusting the voltage to the peltier to account for changes in either set points or ambient temperatures. To do this in a scalable and computer-controllable way, an Arduino MEGA 2560 microcontroller was chosen as the control mechanism. The Arduino permits the measurement of analog voltage inputs and the generation of both digital and analog pulse width modulated (PWM) voltage outputs for multiple independent channels. Thus, a single Arduino controller and its serial computer interface is sufficient to control the temperature of up to 10 independent temperature modules. Figure 6.9a shows pictures of the user interface and the interior of the temperature control unit with one Arduino controller controlling multiple buffered outputs for driving up to 10 peltier modules in parallel.

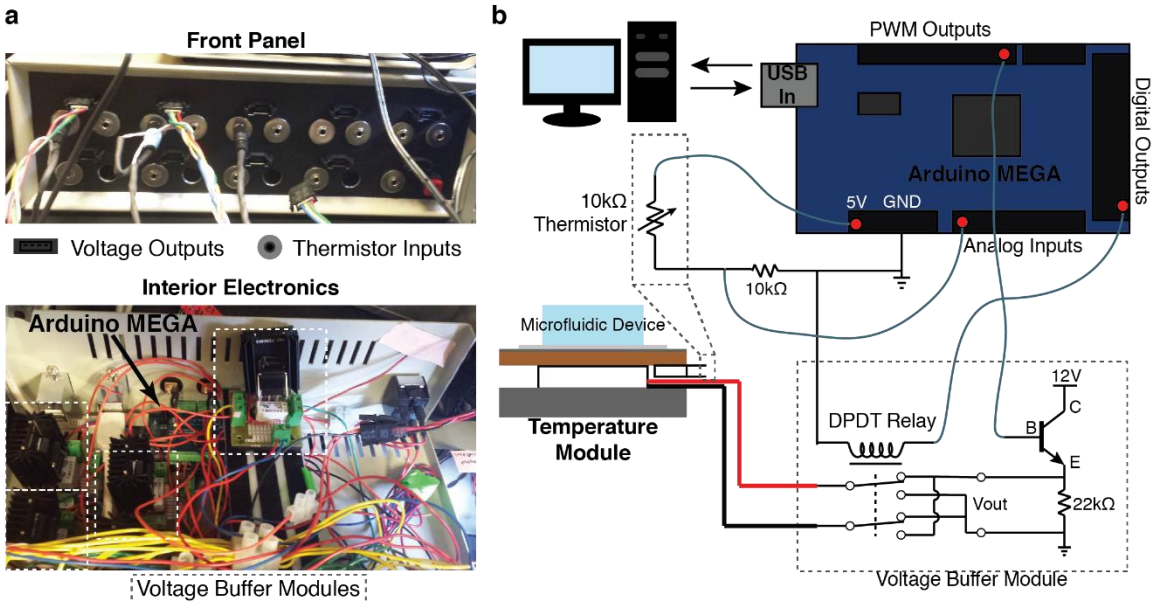

Figure 6.9: Temperature control unit electronics. a) Temperature control unit box. The front user interface shows voltage output and thermistor input connections and the interior view shows one Arduino MEGA controller and multiple voltage buffer modules for each output channel. b) Detailed operation of one output channel showing connections between the Arduino microcontroller, there thermistor inputs and the voltage buffer module.

The details of how a single temperature control channel is driven using the combination of an analog input channel, a digital output channel and a PWM analog output channel is shown in Figure 6.9b. The temperature at the copper platform is measured via resistance changes in a 10 kΩ thermistor (Omega SA2F-TH-44031-40). These resistance changes are measured using one of the analog inputs of the Arduino MEGA and a voltage divider circuit as shown in Figure 6.9b. The analog measurement in terms of voltage is then converted to a temperature measurement on the Arduino board using a look up table (see accompanying code and LUT in Appendix C.1). This measurement is reported back to the computer and an appropriate voltage output is calculated either via a PID controller operating independently on the Arduino board or on the computer and communicated

back to the Arduino board. The board then modulates the output level of one of the PWM analog outputs to the magnitude of the voltage and changes one of the digital outputs to reflect the sign of the voltage. As before, the high current requirements of the peltier modules require a voltage buffering stage after the PWM output (Figure 6.9b). Additionally, the use of the digital output allows the temperature module to both heat and cool by alternating the polarity of its connection to the buffered PWM signal using a DPDT relay. The code implemented on the Arduino microcontroller to allow both serial communication of temperature and voltages for up to 10 independent channels in provided in Appendix C.1.

The PID controller parameters on the Arduino board were tuned to reduce initial temperature overshoots, maximize long term stability of the temperature, and maintain low steady state error rates. While achieving these goals, the set of parameters reflected in the implementation Appendix C.1 also slow the response time of the system to perturbations or alterations in set points. Figure 6.10a and b show the response times of a module from ambient temperature to higher and lower temperature set points. The system generally stabilizes to set point temperatures in roughly 10 minutes. For applications requiring much faster response times or oscillatory outputs, alternative models involving the direct measurement of the ambient temperature can be utilized. Figure 6.10c shows that the current implementation maintains high temperature stability despite fluctuations in ambient temperatures over the course of a day.

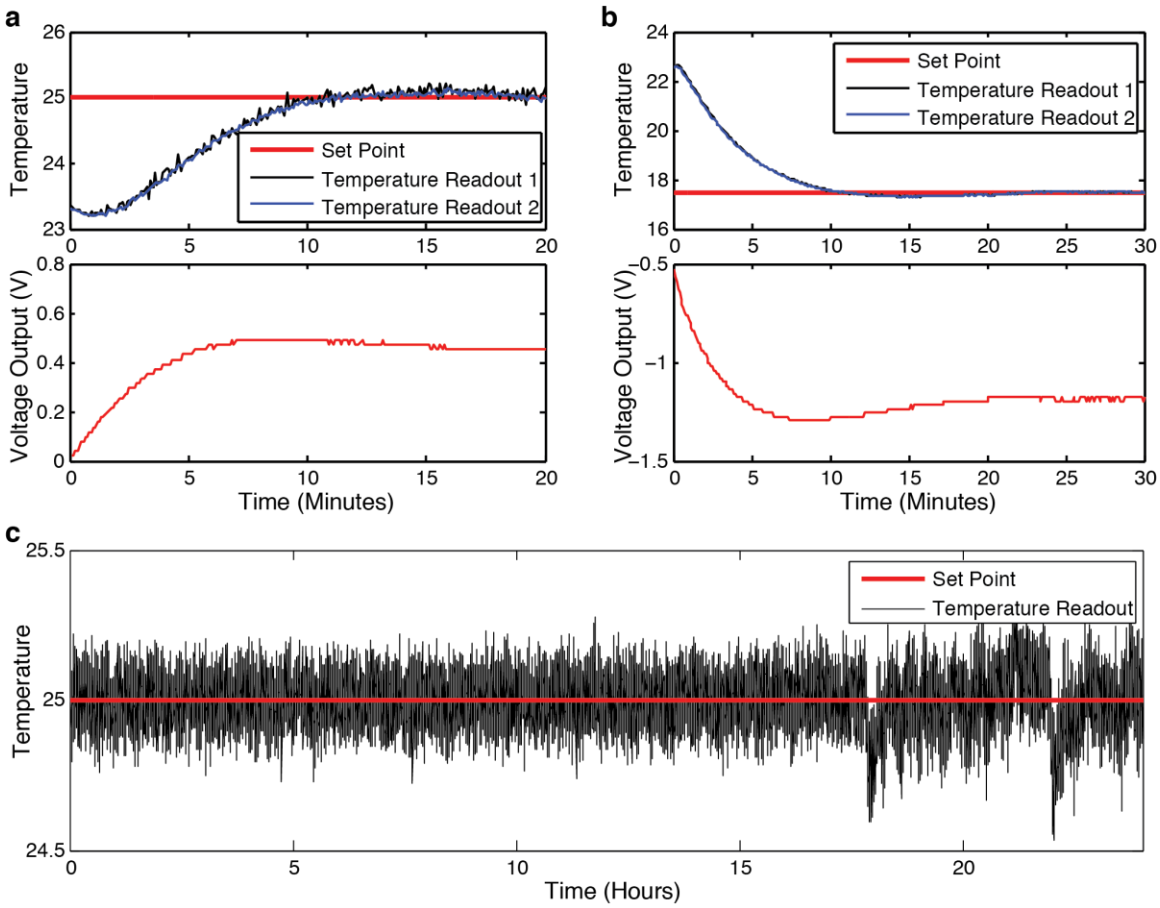

Figure 6.10: Response times and stability of temperature control system. a) Heating response to a temperature set point roughly 2°C above ambient. b) Cooling response to a temperature set point roughly 5°C below ambient, c) Temperature stability over the course of a 24 hour operation period.

Additionally, in Figure 6.10a and b, the temperature module was equipped with two thermistors attached on opposing sides of the copper module. Four different temperature measurement channels were also used to measure each one of the temperature readouts shown. The consistency between the readouts undergoing temperature modulation demonstrates the high temperature uniformity throughout the operational area of the module. Additionally, that is consistency is maintained despite the use of different

readout channels demonstrates the consistency of temperature readout electronics on the different channels of the control unit.

6.4.2: Microfluidic Interface and On-Chip Temperature Characterization

The control unit described in the previous section only ensures high fidelity of the temperature module itself to the set point temperature. On-chip temperatures, as experienced by the worms within the chambers, depends on both the influx of new media and thermal transfer across the glass interface between the temperature module and the liquid layer and from the liquid layer to the surrounding air. To promote intimate thermal contact between the chip and the temperature module, chips are mated to the module using custom compression Z-clips as shown in Figure 6.11a. In this configuration, the maintenance of set point temperatures on chip were validated using a thermocouple probe. However, these probes have the potential to change temperature profiles via their own thermal mass and thermal conductivity. Additionally, insertion of these probes into the device alters flow profiles and they are not appropriate for assessing the impact of media replenishment on temperature stability.

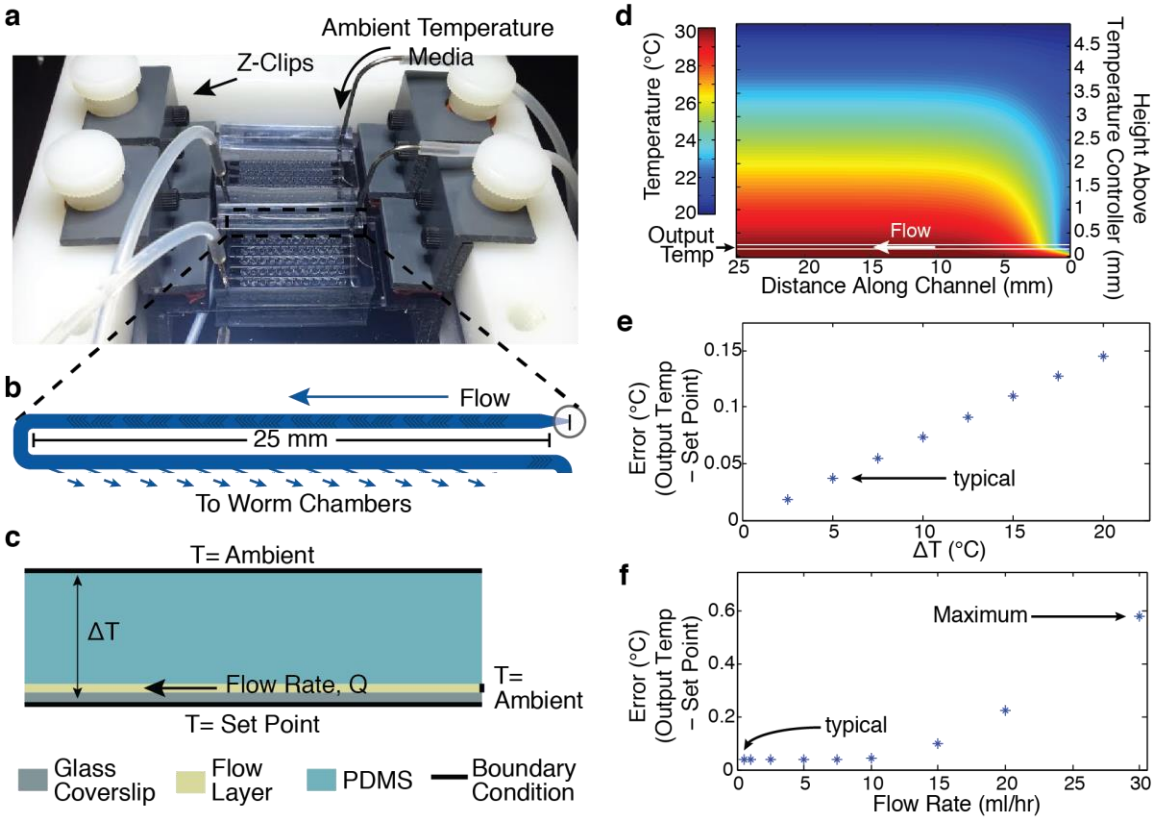

Figure 6.11: Characterization of on-chip temperature control. a) Picture of chips mounted atop temperature module using custom Z-clips to maintain thermal contact. The chip is perfused with incoming ambient temperature media at a defined flow rate. b) Incoming media is directed along a 25 mm channel before flowing into experimental worm chambers. c) Profile view of flow in entry channel showing parameters affecting on chip temperature. d) Temperature distribution through the glass coverslip, flow layer and PDMS modeled using COMSOL. The flow layer is demarcated by white lines and the output temperature is considered as the temperature at the end of the 25 mm channel. e) Flow outlet temperature errors for different differentials between the set point and ambient temperature at a flow rate of 1 ml/hour. The typical error is indicated with an arrow. f) Flow outlet temperature errors for different flow rates. Typical steady state flow rates and the maximum flow rate without a resistance device are indicated by arrows.

To ensure compatibility of the media delivery system with the maintenance of temperatures on chip, a COMSOL model was used to assess the impact of changes in flow rate and ambient temperatures. As shown in Figure 6.11a, the food delivery system

ensures continual delivery of media at ambient temperature into the chip. Figure 6.11b shows that this flow is directed along a 25 mm long channel along the chip before reaching any experimental chambers containing worms. A profile view of this thermal transfer system with the relevant variables indicated is shown in Figure 6.11c. To evaluate temperature profiles within the system, a 2D COMSOL model was constructed and used to calculate the temperature of the liquid leaving the entry channel. Figure 6.11d shows the full 2D temperature distribution calculated for a flow rate of 5 ml per hour and a differential temperature of 10°C.

Based on a series of models for different temperature and flow parameters, Figure 6.11e and f indicate the robustness of the system against the relevant perturbations. Figure 6.11e shows an expected linear increase in error with higher differentials between the set point and ambient temperatures at a relatively low flow rate of 1 ml/hr. With this flow rate, the temperature has reached its equilibrium value before exiting the channel and the errors are determined by the thermal transfer through the coverslip, liquid layer and PDMS. A typical error is indicated. Because this source of error is consistent and well-defined by the properties of the physical system, it can be accounted for during control calculations and eliminated.

Figure 6.11f shows the temperature output errors associated with different flow rates for a typical temperature differential of 5°C. For flow rates lower than roughly 10 ml/hour the temperature of the liquid reaches its equilibrium value prior to exiting the channel. As a result, the error within this regime is due to the thermal transfer effects shown in Figure 6.11e alone. Above this regime, it becomes dependent on the flow rate and the maximum

temperature error as a result flow through the device at 5 psi without a resistance module (a mode of flow shown in Figure 6.6c) is indicated with an arrow. The results here show that the normal operating conditions established in Section 6.3 induce low temperature errors that can be programmatically eliminated. Furthermore, temperature errors under maximal flow rates that may only be utilized intermittently are still below 0.6 °C

6.5: Data Acquisition and Software Integration

6.5.1: Data Acquisition Hardware

Thus far, subsystems for achieving a high degree of environmental control have been discussed. Both of these technologies are compatible with continuous monitoring of an experiment without interruption of control. However, camera sensors have inherently limited field of view and resolution that limit the number of experiments they can monitor continuously and the application of dedicated camera sensors for each experiment limits scalability and is not cost effective. To simultaneously account for the need for scalability and temporal resolution, Figure 6.12 shows the construction of a time-sharing mechanism such that a single sensor can monitor multiple experiments quickly and automatically.

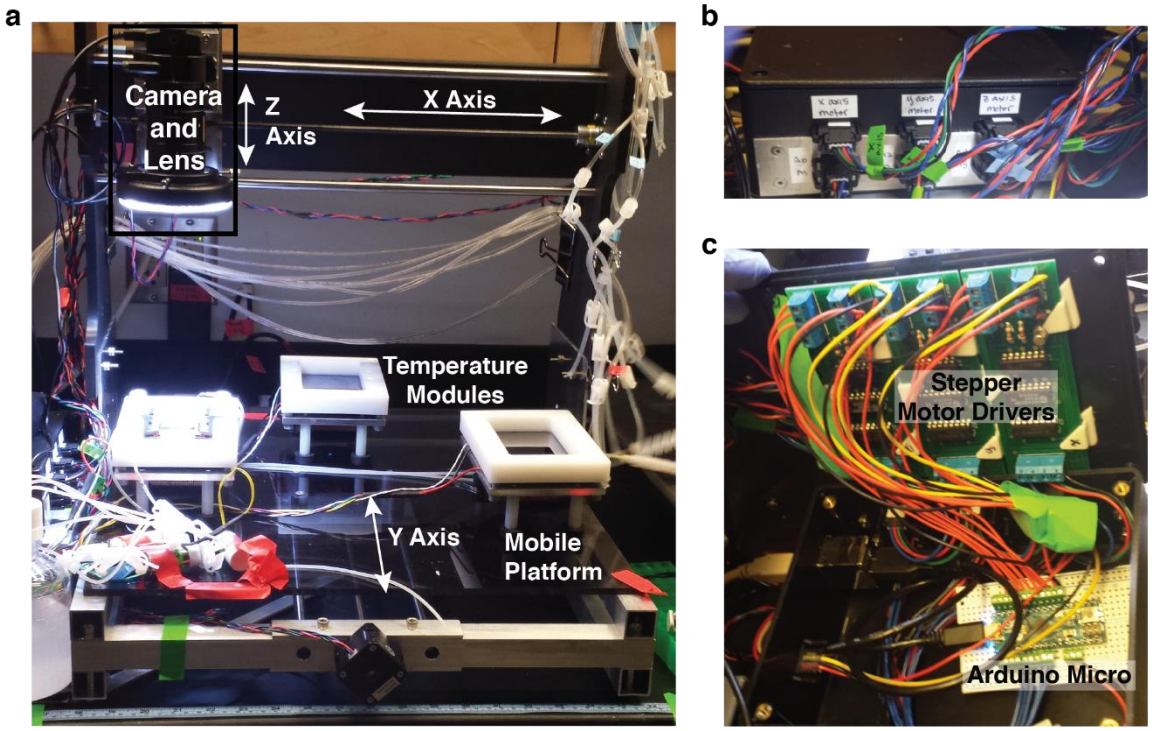

Figure 6.12: Camera motion system for automated data acquisition. a) Overview of modified CNC machining platform for camera motion to support data acquisition. The X and Z axis stepper motor controls move the camera relative to the temperature modules on a platform below. The Y axis stepper motor moves the platform relative to the camera. b) Exterior of control box for motion control shown motor and axis limit switch connections. c) Interior of control box shows a single Arduino Micro with a USB computer interface integrating control of three stepper motor drivers for the three axes.

While commercial optomechanical setups for moving sensors exist, typical commercial setups are for high-precision positioning applications with limited range of motion. For monitoring of multiple chips positioned atop multiple temperature modules, a range of motion of several feet in the X and Y directions and several inches in the Z direction is necessary. This range of motion is more aligned with the range of motion for computer-controlled machining applications than most optical applications. Thus, the data acquisition system in Figure 6.12 is modified from a commercial kit for a home-built computer numerical controlled (CNC) machining platform (MyDIYCNC PB6). Figure

6.12a shows an overview of the system indicating the axes of motion. The camera is mounted on a mobile head capable of X and Z motion by using two stepper motors to turn two orthogonal threaded axis rods. For Y positioning, the motion of an underlying platform using a third stepper motor actuation system is used. The CNC kit provides a X range motion of roughly 15 inches, a Y motion of roughly 13 inches, a Z motion of roughly 3 inches, and a resolution of below 10 μm per step for each direction. This is sufficient to accommodate up to 10 independent temperature modules and 40 different chips within the range of motion.

For driving the stepper motors via an integrated computer interface, an Arduino Micro microcontroller is utilized to drive the three stepper motor drivers (MyDIYCNC UBSMDM) for each axis. The interface and interior of the control box for the motion system is shown in Figure 6.12b and c, respectively. The Arduino microcontroller sends out digital pulses to the motor drivers in response to motion commands from the computer. Additionally, the Arduino continuously monitors two Hall effect proximity sensors that indicate the end of each axis and terminates motion whenever these sensors activate or are disconnected. Integrating limit switch control at the level of the Arduino controller adds a layer of protection against physical equipment damage in the event of interrupted computer connections. The code implemented on the Arduino Micro to permit computer directed position control is provided in Appendix C.2.

The stepper motors and the control electronics are capable of driving each axis at speeds of up to 10 inches per minute. Microfluidic chips within a temperature module are spaced roughly 1 inch apart and the modules are 4 inches apart. Thus, with efficient scan paths,

the system has to travel roughly 52 inches in total to monitor all experiments. At maximum speed, the system requires only 5.2 minutes of total travel time at full capacity. Thus, even with per-experiment acquisition times up to 45 seconds, each individual experiment can be examined twice per hour. Even with a single sensor, the temporal resolution of this system can exceed previously reported longevity experiments (*188*).

For the image acquisition system itself, the system in Figure 6.12 uses a Thorlabs DCC1545M camera with a close focus zoom lens (Edmund Optics #54-363). The Thorlabs camera has a sensor area of 6.66mm by 5.32 mm divided into 1280 x 1024 pixels. In combination with the low magnifications ranges of the zoom lens (<0.8X), all of the chambers on a single microfluidic device can be captured within a single field of view at a resolution of roughly 17.5 μm per pixel. This resolution and the maximum frame rate of the camera (25 frames per second) are sufficient for quantitative analysis of swimming behaviors (*50*). Thus, not only is the system capable of assessing longevity outputs and healthspan metrics in terms of worm bulk worm displacements, it is capable of assessing more detailed behavior profiles with high frame rates during each acquisition period.

6.5.2: Software Integration

Full functionality of the platform depends on integrated computer control over all of the subsystems described in the previous sections. Each of the subsystems have been developed with this need for computer interfacing in mind. Control of the worm and food loading system discussed in Section 6.3 was integrated via the PacDrive LED controller in the modified pressure and valve control unit. Control of the temperature control

functions described in Section 6.4 was integrated via the Arduino MEGA microcontroller, which has a serial interface to the computer via a USB connection. Finally, control of the data acquisition system described in the previous section is afforded by the computer interface on the Arduino Micro microcontroller and USB ThorLabs camera. Figure 6.13 shows the user interface of a LabVIEW program that uses all of these computer interfaces to control and automatically utilize the functions encompassed by all of these subsystems in parallel.

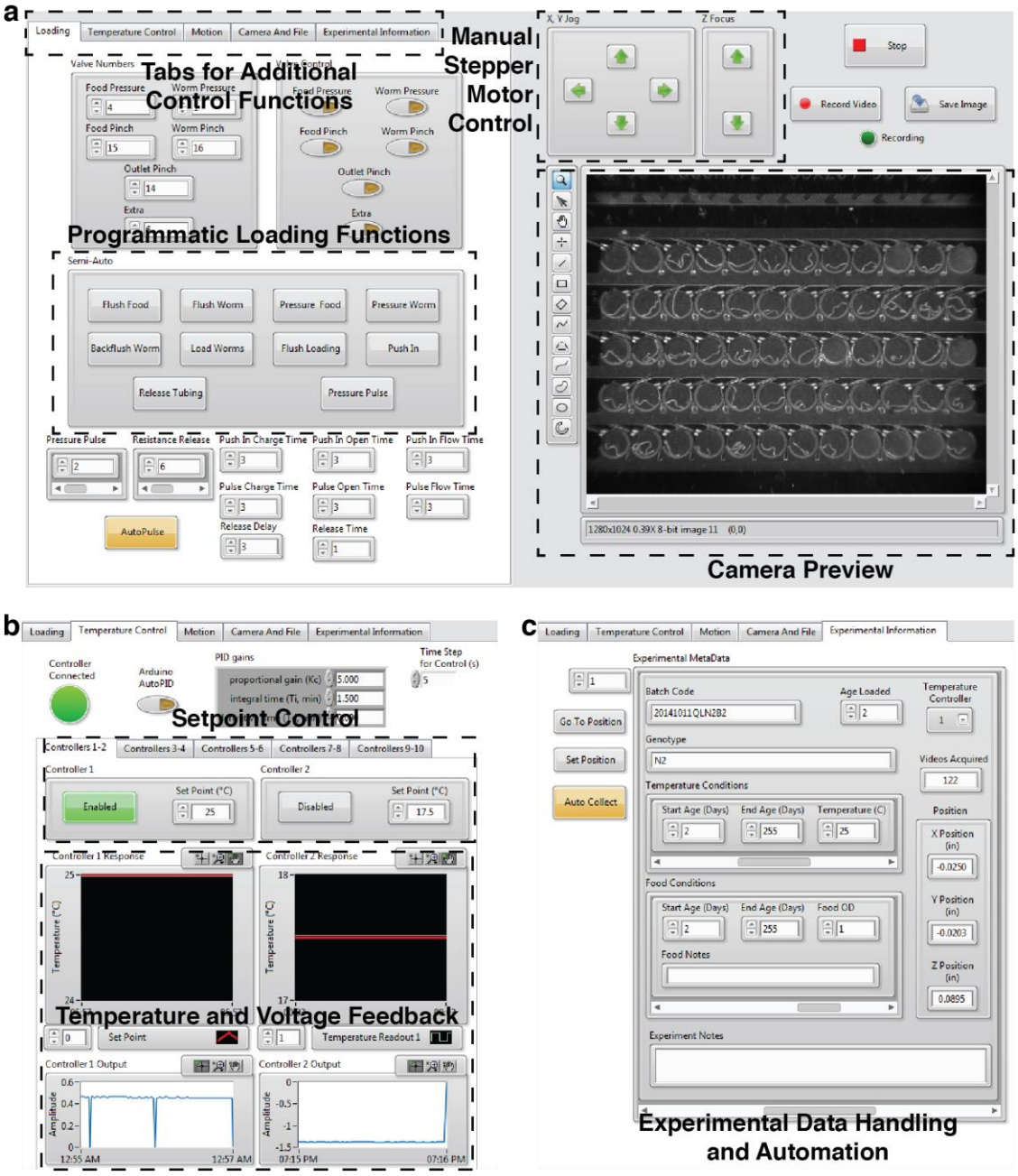

Figure 6.13: User interface of LabVIEW program for integrating control of all the subsystems for long-term culture. a) Overview of user interface. The user controls for valve control, worm loading and food delivery are shown on the left. Additional functions are accessed via different subpanels tabulated at the top. b) Subpanel for control of temperature control units. c) Subpanel for control of experimental data acquisition.

Figure 6.13a shows an overview of the user interface. A camera preview and buttons to manually jog the X, Y and Z stepper motors are consistently displayed on the right hand side. The set of functions displayed on the left are selectable via tabs at the top. These tabs allowed the display of different groups of user interface functions to control the distinct subsystems of the long term culture platform. Figure 6.13b shows the subpanel for temperature control. Set point temperatures inputted into these controls are communicated to the Arduino microcontroller. When a temperature control channel is enabled, the Arduino communicates the temperature readout and voltage outputs for that channel back to the computer. Figure 6.13c shows the subpanel for experimental data handling. Meta data for each chip as well as the X, Y and Z locations for each chip are controlled via this panel to allow for automated movement to each experiment and subsequent data collection.

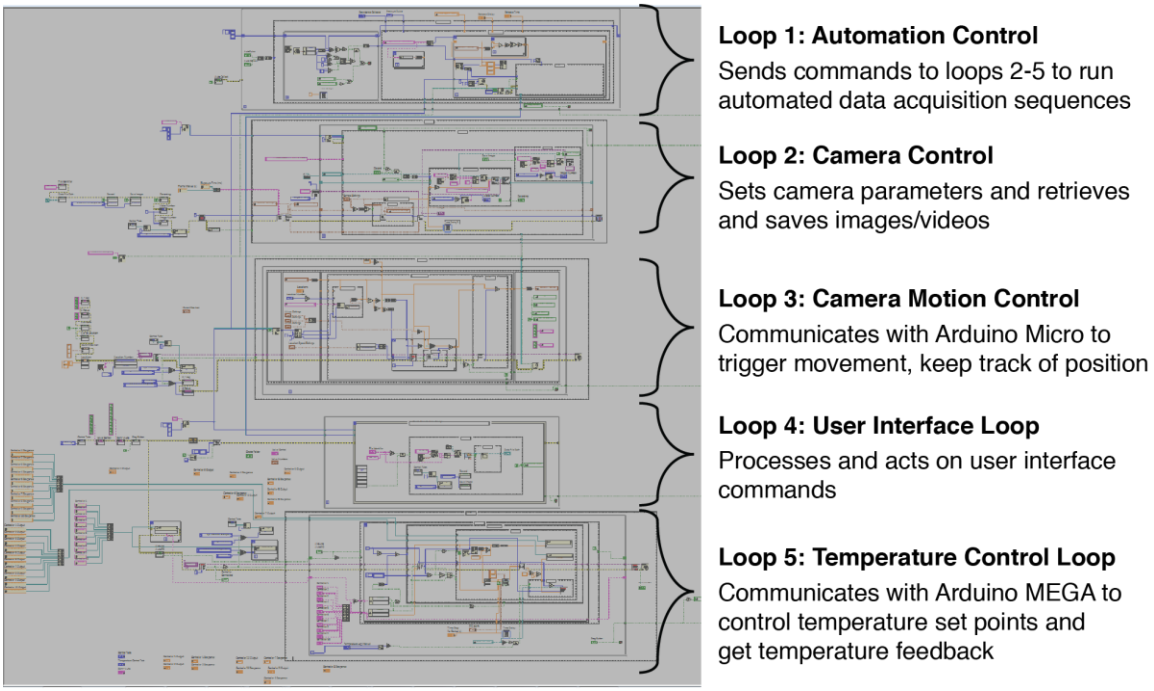

Figure 6.14: Block diagram of LabVIEW program showing underlying control loops. Each loop directs the operation of a different subsystem. The automation loop (Loop 1) interacts with the subsystem loops to run action sequences for automated data acquisition.

Figure 6.14 shows the LabVIEW code directing the operation of the connected subsystems. The operation of subsystems such as camera control, stepper motor control and temperature control are operated via independent loops that allow them to operate in parallel at different time intervals. In addition to coordinating general user face commands, the user interface loop (Loop 4) is responsible for communicating with the PacDrive LED controller to coordinate valve operations. Finally, to enable automation, a dedicated loop (Loop 1) is used to send commands to the other 4 loops to enable automated action sequences for controlling food delivery modes, stage movement and data acquisition.

6.6: Validation of Long-Term Culture on Chip

In order to validate the long-term culture platform for life-long maintenance of *C. elegans* on chip, lifespan assays on chip were tested against comparable liquid culture controls in multi-well plate (See Section 6.8.3 for methods). Figure 6.15 shows the effect of two different food levels on longevity of *C. elegans* reared at 25 °C. Figure 6.15a shows the survival of populations of worms reared in a 48-well plate. Median survival times of 19.9 and 22.4 days, respectively, were observed when food was limited from an OD of 2.5 to an OD of 1, resulting in a 12.5% DR-induced lifespan extension. Figure 6.15b shows the survival of populations of worms reared on the microfluidic culture platform developed in this chapter. Robust diet-induced lifespan extension was still observed on chip. However, the longevity of worms under both conditions and the degree of the diet-induced lifespan extension was reduced relative to multi-well.

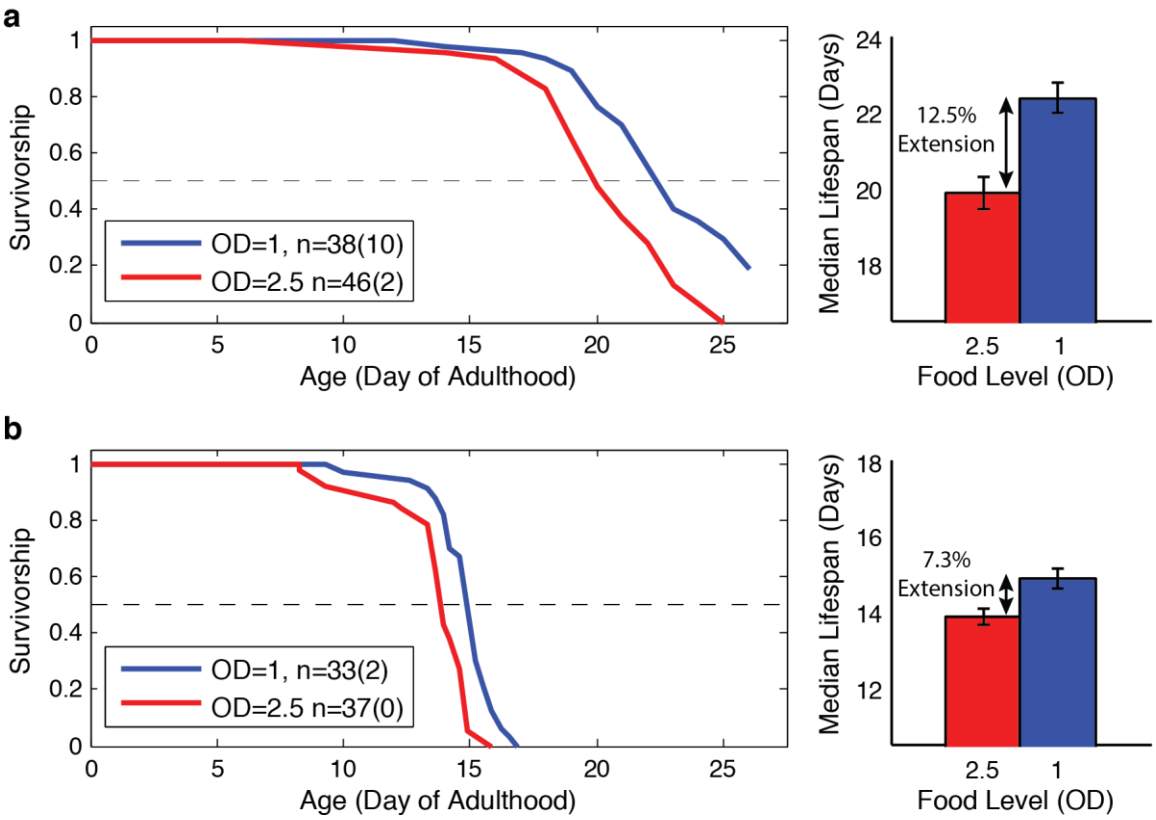

Figure 6.15: Comparison of multi-well and on-chip longevity outputs in response to food at 25°C. a) Liquid dietary restriction experiment using multi-well culture showing a 12.5% lifespan extension with a decrease in food abundance. b) Liquid dietary restriction experiment using microfluidic system showing a 7.3% lifespan extension with a decrease in food. Dashed lines indicate the median (Survivorship=0.5). Error bars on right are standard error.

While the longevities observed on chip are not as high as those observed in multi-well plates, they are within the range of longevities typically observed in *C. elegans* studies (*26, 149*). Furthermore, they are comparable to lifespan assays conducted under similar conditions using a similar protocol on solid NGM media in the Ch'ng lab (See Figure B.6 in Appendix B and methods in Section 4.5.3). There are several possible causes for the discrepancy observed between the mutli-well assays and assays conducted both on solid media and on chip. First, the physical environment and how it affects worm mobility may

be a determinant of longevity. In this case, the liquid environment provided on the microfluidic chip is a thin 80 μm film that is scarcely larger than the 60-70 μm diameter of the adult worm. This environmental constraint is likely to limit a worm's range of motion in a manner similar to that of solid media. Second, lower oxygen environments have been linked to increased longevity (*193*). Potentially, the aeration of bulk liquid media in a multi-well format is less efficient than the aeration of thin liquid films either on device or in solid culture. Thus, differences in oxygen availability may also partially account for some of the longevity differences generally observed between solid and liquid culture in *C. elegans* and explain the similarity of the microfluidic platform results to those of solid culture. Finally, despite the discrepancies noted above, the results in Figure 6.15 show that the platform is capable of sustaining worms throughout their lifespans and replicate well-documented longevity effects.

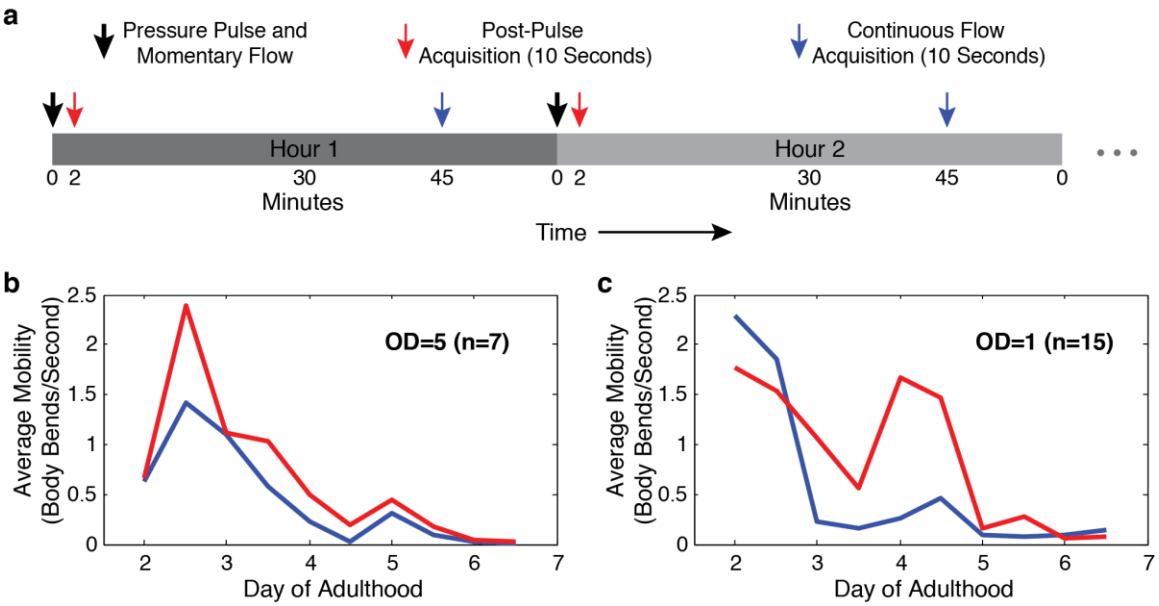

Figure 6.16: Age-related declines in stimulated and spontaneous mobility. a) Schematic of automated experimental acquisition sequence with hourly pressure- and flow-induced physical stimulation. b) Average stimulated (red line) and unstimulated (blue line) mobility of a small selection of worms reared at an OD of 5. b) Average stimulated (red line) and unstimulated (blue line) mobility of a small selection of worms reared at an OD of 1.

In addition to assessing longevity outputs, the platform developed in this chapter is capable of potentially delivering both chemical and physical stimuli via off-chip flow control and acquiring periodic videos to assess behavioral responses. In order to validate the capabilities of the system for assessing age-related behavioral declines, the experimental acquisition sequence shown in Figure 6.16a was tested on two populations of worms reared at an OD of 5 and an OD of 1. The acquisition sequence utilizes hourly operation of the pulsatile and resistance-release flow modes shown in Figure 6.6c and 6.6d to physically agitate the worms on chip. Two minutes after this agitation, a 10 second video is acquired to assess the stimulated mobility of the worms. 45 minutes after the resumption of steady flow, another 10-second video is acquired to assess

unstimulated mobility. A small fraction of the recorded cohorts were then manually assessed for body bending frequency at 12-hour intervals.

Consistent with previous literature, Figure 6.16b and c show that populations of worms show age-related loss in both stimulated and spontaneous movement (*3, 148-154*). Furthermore, physical stimulation generated by the possible flow modes of the system elicits responses in the form of altered mobility under both conditions. Also consistent with recent evidence, the age-related changes in the response profiles of stimulated and spontaneous mobility also appear to be food-dependent (*194*). Thus, unlike previous platforms for assessing longevity, this platform is capable of dissecting multiple components of health span via the application of stimuli and measurement of detailed behavioral outputs using video acquisition. However, both the inter-individual variability and the temporal variability of behavioral responses per individual were high, resulting in low ability to resolve significant differences with the small sample sizes and temporal sampling in Figure 6.16 b and c. This demonstrates the importance of the scalability and high temporal resolution of the long-term culture platform in assessing behavioral metrics.

6.7: Discussion and Conclusions

The platform described in this chapter extends the microfluidic technology developed in Chapter 5 to the performance of long-term assays with a high degree of environmental control. The worm chamber array as a technological component addresses one of the fundamental challenges of performing cost- and labor- effective longitudinal assays in freely moving *C. elegans*. The microfluidic technology enables the continual physical

isolation of many individual worms within a small form factor, the potential for continuous food delivery and passive removal of small progeny via flow. However, the off-chip support systems that enable these functions in a robust and scalable way and permit the control of other biologically critical environmental factors such as temperature have been lacking. Thus, many previous demonstrations of microfluidic technologies for longevity applications have been limited in scope. Instead, competing techniques and technologies that adapt manual culture techniques to permit physical isolation (*149*)or permit long-term individual worm tracking with new sensor systems have been developed. Yet, compared with the capabilities of microfluidics, these systems offer lower degrees of labor reduction and environmental control. To create an integrative long-term culture platform that combines the specific advantages of each of these competing technologies, this work fills the technology gap in terms of food delivery, temperature control and data acquisition support systems for microfluidics.

The final system is capable of accommodating the fine, continuous control of both food, chemical and temperature conditions in a scalable manner such that many different conditions can be assayed in parallel. The incorporation of electronic control for adjusting flow through the microfluidic device also permits the acute physical or chemical stimulation of worms via rapid fluid exchange. Additionally, the ability to effectively time-share one acquisition sensor amongst these parallel assays permits the use of a single high-quality sensor to acquire detailed behavioral outputs at high frame rates and spatial resolution. Together, these capabilities permit the tracking of multiple stimulation and behavior-based health metrics and permit multidimensional, longitudinal

assessment of health and longevity trajectories. Moreover, by leveraging integrative computer control of all of the support systems for automation, the system can achieve these goals with sub-hourly experimental resolution while requiring little manual intervention. Thus, the work in this chapter effectively addresses several of the experimental challenges for large-scale experimentation in *C. elegans* and has the capability for increasing both the throughput and informativeness of experimentation.

6.8: Materials and Methods

6.8.1: Preparation of Microfluidic Devices and Off-Chip Components

Microfluidic devices were manufactured using standard photolithographic and soft lithographic techniques outlined in Appendix A. To facilitate deformation of the worm loading restriction under pressure (Figure 6.2d), a pre-polymer to crosslinker ratio of 17.5:1 was utilized near the microfluidic features using the techniques described in Appendix A.2.

Inlet and outlet lines for the device assembly were prepared by injecting a 10% bleach solution into the tubing, allowing it to sit for 15 minutes and then rinsing thoroughly with deionized water. These lines were then inserted in the device and the female luer adapter at the inlet line was then capped with a male luer plug (Value Plastics MTLLP-6005) to prevent contamination during handling. The worm loading assembly described as module C in Figure 6.4 was also prepared by applying a 10% bleach solution through all flow paths for 15 minutes and rinsing all flow lines thoroughly with deionized water. All of the male luer inlets and outlets in the assembly were then capped with 0.2 μm polypropylene syringe filters (VWR 28145-483). The female luer inlet was capped with a male luer plug

as before. Both the assembled device and the prepared worm loading tubes were then packaged in a sterilization pouch (VWR 89140-802) and autoclave-sterilized before use.

Food reservoir vessels described as module A in Figure 6.4 were prepared by applying a 10% bleach solution in the vessel and flow paths for 15 minutes. The vessel and flow lines were then rinsed with deionized water and washed with a 1% Alconox detergent solution. Finally, the vessel and flow lines were thoroughly rinsed again with deionized water and the ends of the air inlet and flow outlet lines were capped with 0.2 μm polypropylene syringe filters. These assemblies were then autoclave-sterilized before use.

The macroporous food filters described as module B in Figure 6.4 were cleaned by applying a 10% bleach solution for 15 minutes. The filters were then rinsed with deionized water, capped with a 0.2 μm polypropylene syringe filter on the male end and a male luer plug on the female end and sterilized via autoclaving.

6.8.2: Preparation of Bacterial Food Sources

To prepare liquid media for the worms, the *E. coli* strain OP50 was cultured overnight in LB media using an incubated orbital shaker at 37 °C. After approximately 16 hours of culture, streptomycin was added to the culture to a final concentration of 50 μg/ml and the culture was shaken at 37 °C for another 30 minutes. The culture was then placed on ice for 15-30 minutes before being harvested by centrifugation at 4000g for 20 minutes at 4 °C. The supernatant was removed and the culture was washed once in chilled S Basal and centrifuged again. After removal of the supernatant, the resulting bacterial pellet was resuspended in S Media supplemented with 50 μg/ml carbenicillin and 50 μg/ml streptomycin. The final volume of S Media used was determined via measurement of the

optical density of a five-fold dilution of the initial bacterial culture in LB at 600nm. Generally, bacteria was resuspended to an OD of 5 or 10 and required experimental concentrations were made from serial dilution of this stock.

To prepare liquid media for RNAi knockdown of *egg-5* in the worms, HT115 expressing dsRNA targeting *egg-5* was cultured overnight in LB media supplemented with 0.2% β-lactose and 50 μg/ml carbenicillin. After approximately 16 hours of culture, the culture was placed on ice for 15-30 minutes and the bacteria was harvested as described previously. The bacterial pellet was resuspended in S media supplemented with 1mM IPTG and 50 μg/ml carbenicillin to a final OD of 5.

6.8.3: Worm Maintenance and Culture

Animals were raised on live OP50 bacteria on NGM plates for at least two generations at 20°C. During this time, animals were roughly synchronized and propagated by picking 15-20 L4 animals and allowing them to lay eggs overnight before removing them from the plate. After two days at 20°C, finely age-synchronized populations of worms were obtained by washing gravid adults and L1s off of these plates and then washing freshly hatched L1s from these plates after a 1 hour interval. The L1s obtained in this process were suspended in 10 ml of OD 5 OP50 liquid media in a 25 cm^2 cell culture flask (Greiner 690-175) at a density of 200-300 worms per flask. These worms were cultured at 20°C on a rocker for 40 hours until they reached L4. At that point, worms were isolated from these flasks via gravity sedimentation in a culture tube, washed with fresh S basal and resuspended in a new flask with 10ml of OD 5 *egg-5* RNAi liquid media. After 32 hours, worms were transferred to a new flask with 10ml of OD 5 OP50 liquid media

as day 1 adults. Worms harvested from these flasks were loaded into the microfluidic platform or multi-well plates and subjected to experimental food levels one day later at day 2 of adulthood.

For lifespan assays on conventional 48-well plates (Greiner 677180), individual worms were manually transferred into wells filled with 0.5 ml of media containing the correct bacterial concentrations. Worms were then placed into an incubator at the experimental temperature and agitated on a rocker. Worms were transferred every other day onto fresh multi-well plates until day 14 of adulthood when the transfer frequency was lowered to once every 4 days. Worms were scored for survival via lifting individuals out of the media with a sterilized platinum pick and then assessing mobility when they were moved back into liquid. Worms that did not respond to this physical stimulation over a period of three days were considered to have died the first day they stopped responding. Scoring occurred every other day at the transfer points up to day 14 and then was performed daily thereafter.

For on chip culture, worms were loaded into devices and continuously fed with liquid media as described in Section 6.3. Continuous flow rates per chip were maintained at roughly 0.3-0.4 ml/hour. However, on an hourly basis, a 1 second burst of fast momentary flow was delivered as described in Figure 6.6b. This physically agitates the worms similar to the scoring method employed for the multi-well assay. The worms were allowed to rest for 5 minutes after this pulse and a 10 second video was recorded of the chip to assess mobility. Accounting for this momentary flow, roughly 0.5-0.6 ml of media was consumed per device per hour. For the assays, each 200 ml food delivery flask

was filled with roughly 75 ml of media initially. The flasks were replaced every 4 days to replenish diminished media. Additionally, the macroporous filters capturing particulate matter and bacterial clumps were replaced every other day.

CHAPTER 7: OVERALL CONCLUSIONS AND FUTURE DIRECTIONS

Aging is a complex process arising from the interplay between environmental, genetic and stochastic factors. Many different environmental inputs are directly or indirectly sensed by discrete genetic pathways and then processed either at a specific-cell or tissue level to coordinate holistic changes within an organism with time. Thus, to understand this process and identify important biological subsystems that may be the sites for pathogenesis or clinical intervention, there is a need to experimentally dissect specific internal outputs and gauge health outputs within an organism under well-defined system perturbations. Furthermore, the documented inter-individual variability in aging outcomes suggests the importance of performing longitudinal tracking of individuals both to unmask relationships that may otherwise be obscured by population metrics and begin to understand the sources of this variability.

The model organism, *Caenorhabditis elegans*, has many convenient biological traits that partially enable the type of experimentation described above (Table 1.1). As a result, much of the current knowledge about the aging process has been derived from studies in this small worm (*180-182*). This strong basis of knowledge serves as a powerful starting point for more detailed, quantitative investigations. Yet, the conventional experimental techniques routinely used by the worm research community have impeded truly large-scale, quantitative and longitudinal experimentation. In whole, the work presented in this thesis address many of these current impediments by developing, refining, and applying new experimental techniques and technologies to overcome these barriers. The hardware

and computational technologies presented in Chapters 2 and 3 address the problems with high-throughput physical manipulation of the small worm and quantitative extraction of cell- and tissue- specific readouts in large datasets. The work in Chapter 4 demonstrates the power of the combining these technologies for deriving new biological insight about an important modulator of the aging process. Chapter 5 and 6 present a distinct set of technologies that enable the large-scale longitudinal measurement of whole-organism health outputs. The combined ability to apply controlled perturbations, quantitatively investigate internal readouts and assess individual health outputs represented by all of these technologies ultimately enable unprecedented levels of control, throughput and content-richness in aging experimentation.

Beyond the specific biological applications that have motivated this work, the technologies developed in this work also have the capability to address other biological questions. The systems developed in Chapter 2 are currently being applied to the investigation of other genetic pathways and functional outputs of aging such as alterations in synaptic morphology. The image processing techniques presented in Chapter 3 are broadly relevant to information extraction within biological datasets in general and will likely form the basis of future work to automatically dissect other types of biological information. The application of these technologies in Chapter 4 provide indications of how specific biological perturbations can potentially mimic dietary restriction effects but also sets forth a framework for other pathways and biological outputs to be investigated as well. Finally, the set of technologies developed in Chapters 5 and 6 provide critical and generalizable experimental functionality in terms of enabling

longitudinal assays and environmental control. Combining this set of hardware technologies with new data extraction algorithms generated from the framework in Chapter 2 has the potential to quickly provide new biological insights about environmental determinants of behavior and health. Thus, in whole, this thesis advances high-throughput, quantitative analysis in *C. elegans* via both technological innovations that remove experimental bottlenecks at the data acquisition and data processing levels and scientific insights that contribute to the broad base of knowledge to inform new studies.

APPENDIX A: FABRICATION METHODS FOR PDMS MICRODEVICES

Appendix A.1: Fabrication of Masters for Replica Molding

All masters used for the molding of the PDMS devices used in this work were fabricated using SU-8 negative photoresist (MicroChem, Westborough, MA) using standard photolithographic techniques(*195*). Figure A.1 diagrams the fabrication process. Briefly, SU-8 photoresist of specified viscosity was applied to a substrate silicon wafer via spin coating. This resulted in a uniform film of defined thickness depending on the choice of SU-8 viscosity and spin coating speed (Figure A.1a). The wafer was then briefly baked on a hot plate to remove excess solvent and was exposed with UV light through a photomask with a design pattern. As shown in Figure A.1b, in this photolithographic process, exposure through the photomask renders portions of the SU-8 insoluble to a developer solvent. After baking, the exposure wafer was either developed to achieve a single layer pattern or subjected to repeated application of SU-8 via spin coating. Figure A.1c shows how repetitive application of spin coating and photolithography was used to generate mutli-layer structures.

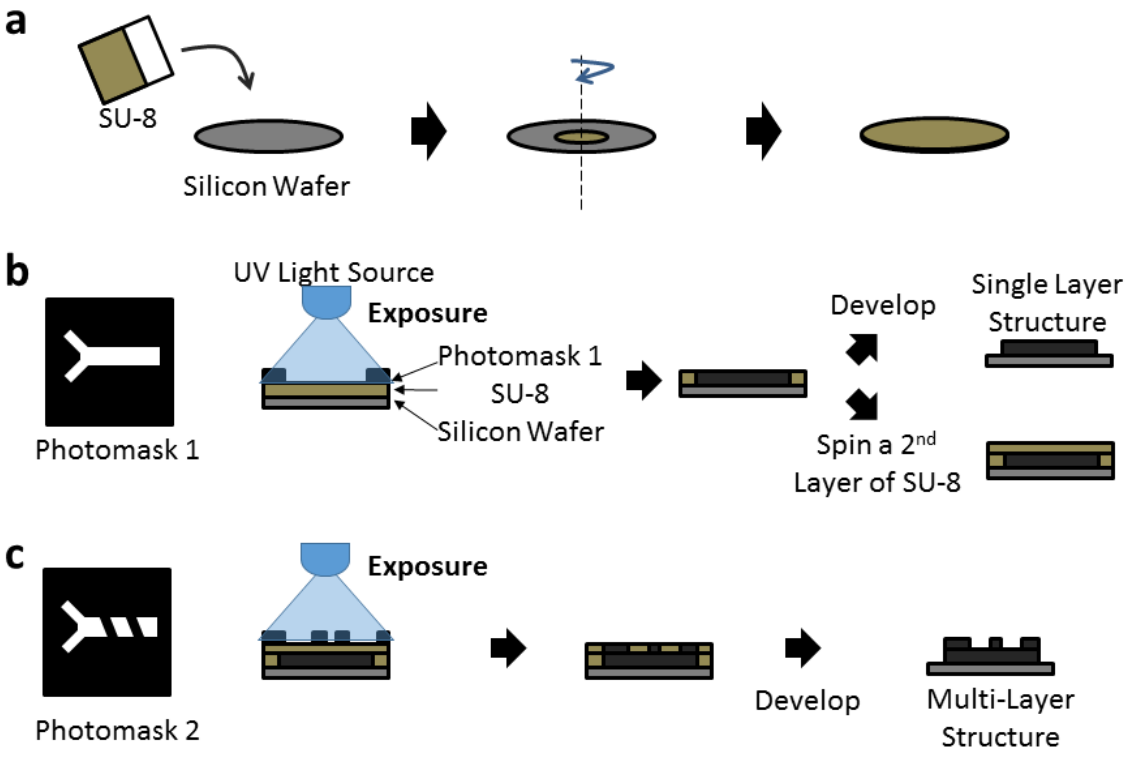

Figure A.1: Fabrication of masters for soft lithographic replica molding of PDMS. a) In the first step, SU-8, a negative photoresist is deposited onto a silicon wafer via spin coating. The thickness of the film and the resulting structure is determined by the viscosity of the SU-8 and the spin coating speed. b) The SU-8 is patterned via photolithographic transfer of a pattern on a printer photomask. After the transfer of the pattern, the wafer can be developed to generate a single layer master or additional layers of SU-8 can be added for multi-layer fabrication. c) Schematic of the fabrication of multi-layer masters via repeated application of SU-8 and photolithography.

After development of the wafer to produce the patterned master, the wafer surface was treated with tridecafluoro 1,1,2,2-tetrahydrooctyl-1-trichlorosilane vapor (United Chemical Technologies, Inc, Bristol, PA) in a vacuum dessicator to facilitate release of PDMS from the mold.

Appendix A.2: Single Layer Replica Molding and Device Fabrication in PDMS

The PDMS microdevices used in this work were fabricated using standard soft lithographic techniques (*28*). For single layer fabrication, a mixture of PDMS pre-

polymer and crosslinker (Dow Corning Sylgard 184, Midland, MI) was poured directly onto the wafer surface and cured for several hours at 70°C to achieve final device thickness of 7 to 10 mm (Figure A.2a). The pre-polymer to crosslinker ratio was typically 10:1 by weight. When more deformability of the PDMS feature layer was necessary, higher ratios of up to 20:1 were used. However, when used for the entire PDMS device, these ratios resulted in devices that were difficult to handle. Thus, when pre-polymer to crosslinker ratios exceeding 10:1 were used, thin 3mm layers were applied and cured for at least 30 minutes at 70°C to create a deformable feature layer for the device. After this, additional 10:1 PDMS mixture was added and cured for several hours to create a rigid handling layer for the device (Figure A.2b)

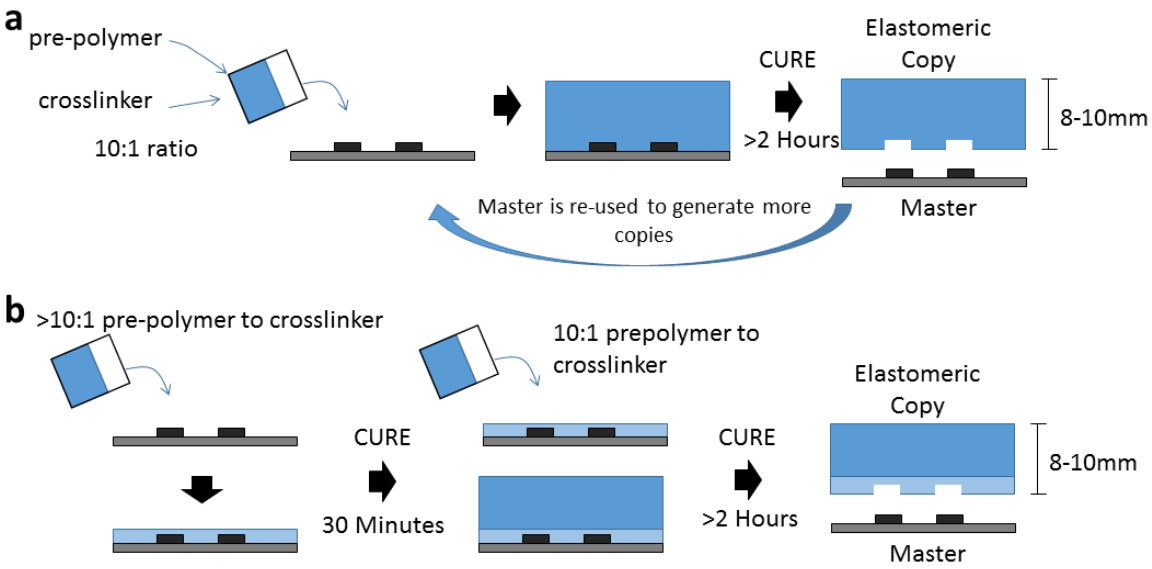

Figure A.2: Soft lithographic replica molding of PDMS microdevices. a) Replica molding in 10:1 pre-polymer to cross-linker PDMS results in a device with uniform mechanical properties. b) For higher deformability of the feature layer, a thin feature layer is formed with higher pre-polymer to crosslinker ratios and a bulk handling layer is cured on top using 10:1 PDMS.

After curing, PDMS devices were cut to size and access ports were created via puncturing the cured PDMS with sharpened 18-21 gauge needles (Figure A.3a). The prepared devices were then cleaned with scotch tape and exposure to air plasma for 20 seconds before being mated and covalently bonded to a glass surface to create closed channels (Figure A.3b).

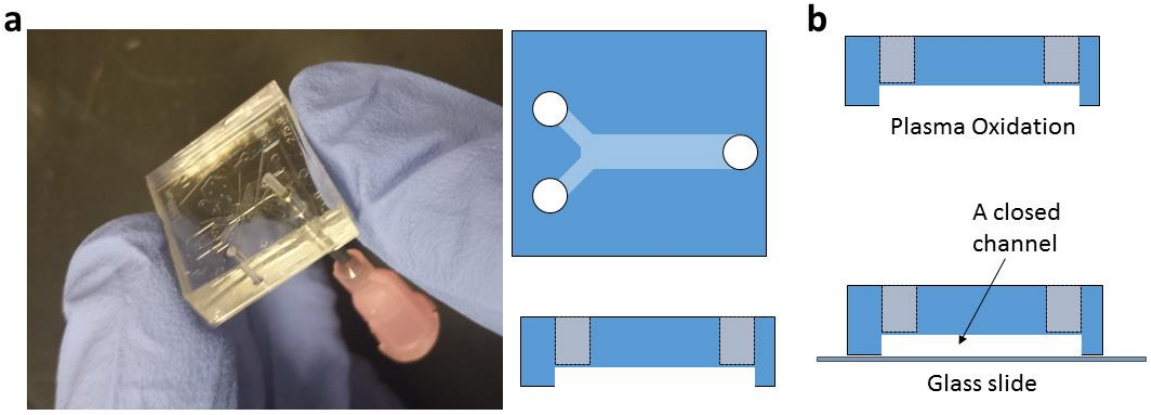

Figure A.3: The creation of access ports and closed channels in PDMS microdevices. a) Access ports are created by puncturing the PDMS device with a sharpened 18-21 gauge needle. b) The feature surface of the prepared PDMS device is then oxidized by air plasma exposure and covalently bonding to a glass slide to create closed channels.

Appendix A.3: Two Layer Replica Molding and Device Fabrication in PDMS

The multi-layer soft lithography process (*30*) for creating the two-layer PDMS microdevices described in Chapter 2 is diagrammed in Figure A.4. In this process, PDMS was deposited on to the bottom and top feature layer masters via different mechanisms. For the bottom or flow layer of features, PDMS was deposited via spin coating to create a thin and controlled layer of PDMS between the two layers in the final device (*196*). For the top or control layer, 10:1 PDMS was directly poured onto the master to create a thick

and mechanically rigid handle layer. Both layers were then placed into a 70°C oven for 20-30 minutes until the control layer PDMS was rigid but sticky to the touch. At that point, the top or control layer is not fully cured and there is still free cross-linker available within the PDMS structure. The availability of this cross-linker was used to crosslink the control and flow layers together after they were manually aligned and mated as shown in Figure A.4b.

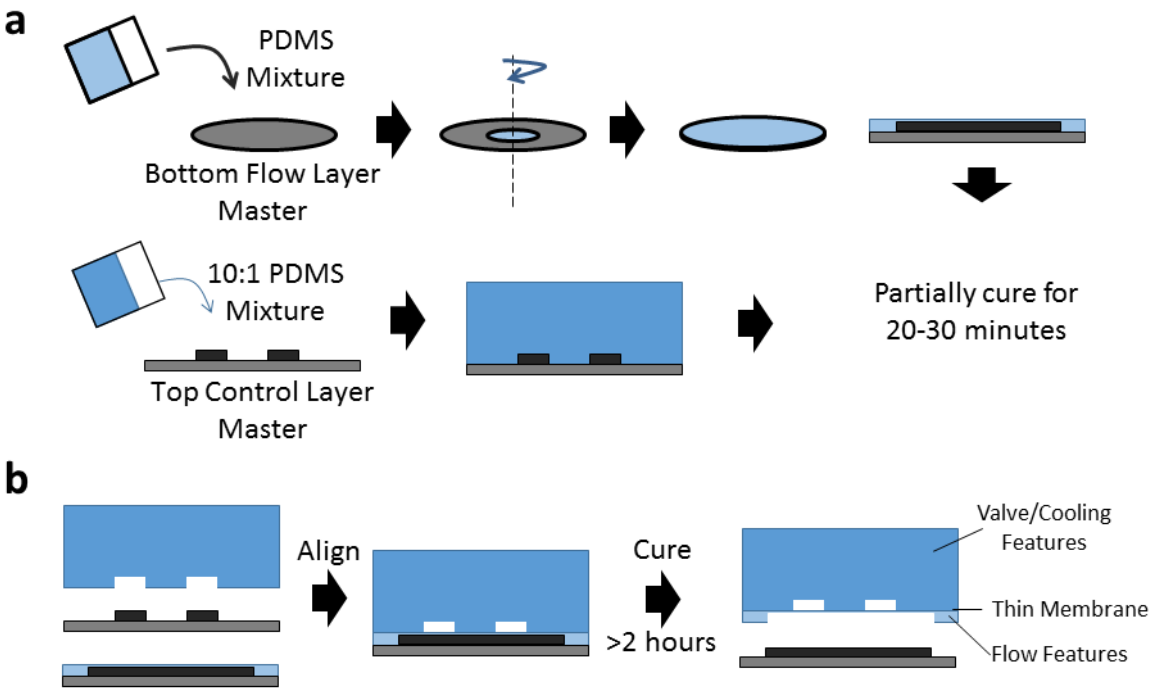

Figure A.4: Multi-layer soft lithography process for two layer fabrication in PDMS. a) PDMS deposition via two distinct methods onto the top and bottom feature layer masters. b) Assembly of two layers via alignment of the partially cured top layer PDMS onto the bottom layer master and curing.

APPENDIX B: DETAILED LIFESPAN AND IMAGING DATA FROM CHAPTER 4

Table B.1: Pooled wildtype lifespan data for Figure 4.1. Datasets used for the Bayesian analysis in Section 4.3 are highlighted in yellow.

All Wildtype Lifespans Pooled				
Food Level (cells/ml)	**N (Died)**	**N (Censored)**	**Mean Lifespan (Days)**	**SEM (+/- Days)**
S Basal	229	71	41.05	0.44
2.00E+04	102	18	41.34	0.73
2.00E+05	161	19	41.25	0.53
2.00E+06	103	17	42.88	0.56
6.32E+06	96	24	43.11	0.72
2.00E+07	384	151	40.50	0.29
3.56E+07	100	20	40.22	0.39
6.32E+07	394	132	31.48	0.34
1.12E+08	72	33	31.21	0.65
2.00E+08	215	85	25.92	0.30
3.56E+08	81	39	25.95	0.54
6.32E+08	383	141	23.78	0.20
1.12E+09	80	40	27.53	0.56
2.00E+09	613	122	32.10	0.30
3.56E+09	107	13	35.56	0.64
6.32E+09	271	29	26.49	0.37
1.12E+10	285	60	25.91	0.33
2.00E+10	41	4	24.00	0.65
3.56E+10	33	12	23.73	0.91

Table B.2: Mutant lifespan data for Figure 4.1. Datasets used for the Bayesian analysis in Section 4.3 are highlighted in yellow

			Food Level					
			S Basal	2 x 10^7	6.32 x 10^7	6.32 x 10^8	2 x 10^9	1.12 x 10^{10}
			Mean Lifespan ± SEM (Days) N Died (N Censored)	Mean Lifespan ± SEM (Days) N Died (N Censored)	Mean Lifespan ± SEM (Days) N Died (N Censored)	Mean Lifespan ± SEM (Days) N Died (N Censored)	Mean Lifespan ± SEM (Days) N Died (N Censored)	Mean Lifespan ± SEM (Days) N Died (N Censored)
Trial 1	Genotype	N2	38.77 ±1.27 31 (14)	39.81 ±0.94 26 (19)	30.91 ±1.24 32 (13)	22.14 ±0.69 37 (8)	31.53 ±1.21 38 (7)	24.55 ±0.71 40 (5)
		tph-1(-)	38.00 ±2.04 4 (0)	38.35 ±1.16 17 (28)	32.48 ±0.87 31 (14)	26.03 ±0.81 39 (6)	33.60 ±0.91 35 (10)	25.00 ±0.95 43 (2)
		daf-7 (-)	38.00 ±1.57 36 (9)	36.87 ±1.00 39 (6)	33.13 ±1.14 38 (7)	27.03 ±1.06 40 (5)	30.71 ±1.08 43 (2)	30.82 ±1.04 40 (5)
		tph-1(-); daf-7(-)	33.54 ±0.95 35 (10)	33.74 ±1.38 33 (12)	31.90 ±1.40 30 (15)	28.54 ±1.12 39 (6)	29.24 ±1.06 41 (4)	29.30 ±0.95 44 (1)
Trial 2	Genotype	N2	37.41 ±1.72 22 (23)	41.00 ±1.76 18 (27)	33.69 ±1.72 26 (20)	24.50 ±0.81 28 (16)	35.84 ±1.34 31 (14)	23.44 ±0.91 35 (10)
		tph-1(-)	33.50 ±1.96 16 (29)	42.56 ±1.01 18 (27)	32.59 ±1.38 28 (17)	26.76 ±0.71 38 (7)	34.10 ±1.08 38 (7)	24.00 ±0.93 37 (8)
		daf-7 (-)	36.74 ±1.63 37 (8)	39.98 ±1.72 35 (10)	33.03 ±1.47 32 (13)	29.44 ±1.22 32 (13)	33.92 ±0.97 41 (4)	31.09 ±1.18 40 (5)
		tph-1(-); daf-7(-)	31.77 ±1.38 35 (10)	35.97 ±1.56 37 (8)	34.17 ±1.63 34 (11)	30.03 ±1.15 37 (8)	31.76 ±1.18 41 (4)	31.42 ±1.12 43 (2)
Trial 3	Genotype	N2	41.62 ±0.91 40 (5)	38.39 ±0.87 33 (12)	31.16 ±1.09 35 (10)	23.48 ±0.75 37 (8)	32.81 ±1.43 42 (3)	28.94 ±0.84 35 (10)
		tph-1(-)	34.41 ±1.15 29 (16)	37.94 ±0.81 31 (14)	33.82 ±1.06 34 (11)	27.12 ±0.72 43 (2)	36.56 ±0.71 41 (4)	29.25 ±0.95 37 (8)
		daf-7 (-)	36.23 ±1.43 42 (3)	34.55 ±1.39 42 (3)	33.51 ±1.16 41 (4)	26.13 ±1.04 40 (5)	32.16 ±1.13 43 (2)	28.07 ±1.11 41 (4)
		tph-1(-); daf-7(-)	35.04 ±1.72 40 (5)	35.79 ±1.27 39 (6)	32.40 ±1.20 35 (10)	27.45 ±0.92 40 (5)	31.00 ±1.22 42 (3)	30.83 ±1.19 41 (4)
Trial 4	Genotype	N2	42.25 ±1.08 29 (16)	42.27 ±1.04 30 (15)	31.06 ±1.05 32 (13)	25.00 ±0.58 33 (12)	32.46 ±1.28 37 (8)	27.28 ±0.87 43 (2)
		tph-1(-)	30.51 ±1.80 19 (26)	35.28 ±1.73 22 (23)	33.37 ±0.99 27 (18)	26.78 ±0.75 37 (8)	34.24 ±0.93 40 (5)	27.42 ±0.72 41 (3)
		daf-7 (-)	37.08 ±2.08 30 (15)	35.24 ±1.52 37 (8)	35.11 ±1.29 31 (14)	28.70 ±1.04 37 (8)	33.77 ±1.12 39 (6)	33.22 ±1.13 41 (4)
		tph-1(-); daf-7(-)	33.68 ±1.49 36 (9)	35.74 ±1.17 31 (14)	32.78 ±1.23 36 (9)	28.31 ±1.12 32 (13)	34.17 ±1.19 41 (4)	30.74 ±1.25 42 (3)
Pooled	Genotype	N2	40.32 ±0.61 122 (58)	40.26 ±0.56 107 (73)	31.59 ±0.63 125 (56)	23.70 ±0.36 135 (44)	33.03 ±0.67 148 (32)	26.05 ±0.45 153 (27)
		tph-1(-)	33.38 ±0.85 68 (71)	38.25 ±0.65 88 (92)	33.08 ±0.54 120 (60)	26.68 ±0.37 157 (23)	34.67 ±0.46 154 (26)	26.39 ±0.47 158 (21)
		daf-7 (-)	36.94 ±0.82 145 (35)	36.55 ±0.72 153 (27)	33.66 ±0.62 142 (38)	27.71 ±0.55 149 (31)	32.60 ±0.54 166 (14)	30.80 ±0.57 162 (18)
		tph-1(-); daf-7(-)	33.54 ±0.72 146 (34)	35.34 ±0.68 140 (40)	32.84 ±0.68 135 (45)	28.58 ±0.54 148 (32)	31.55 ±0.59 165 (15)	30.56 ±0.56 170 (10)

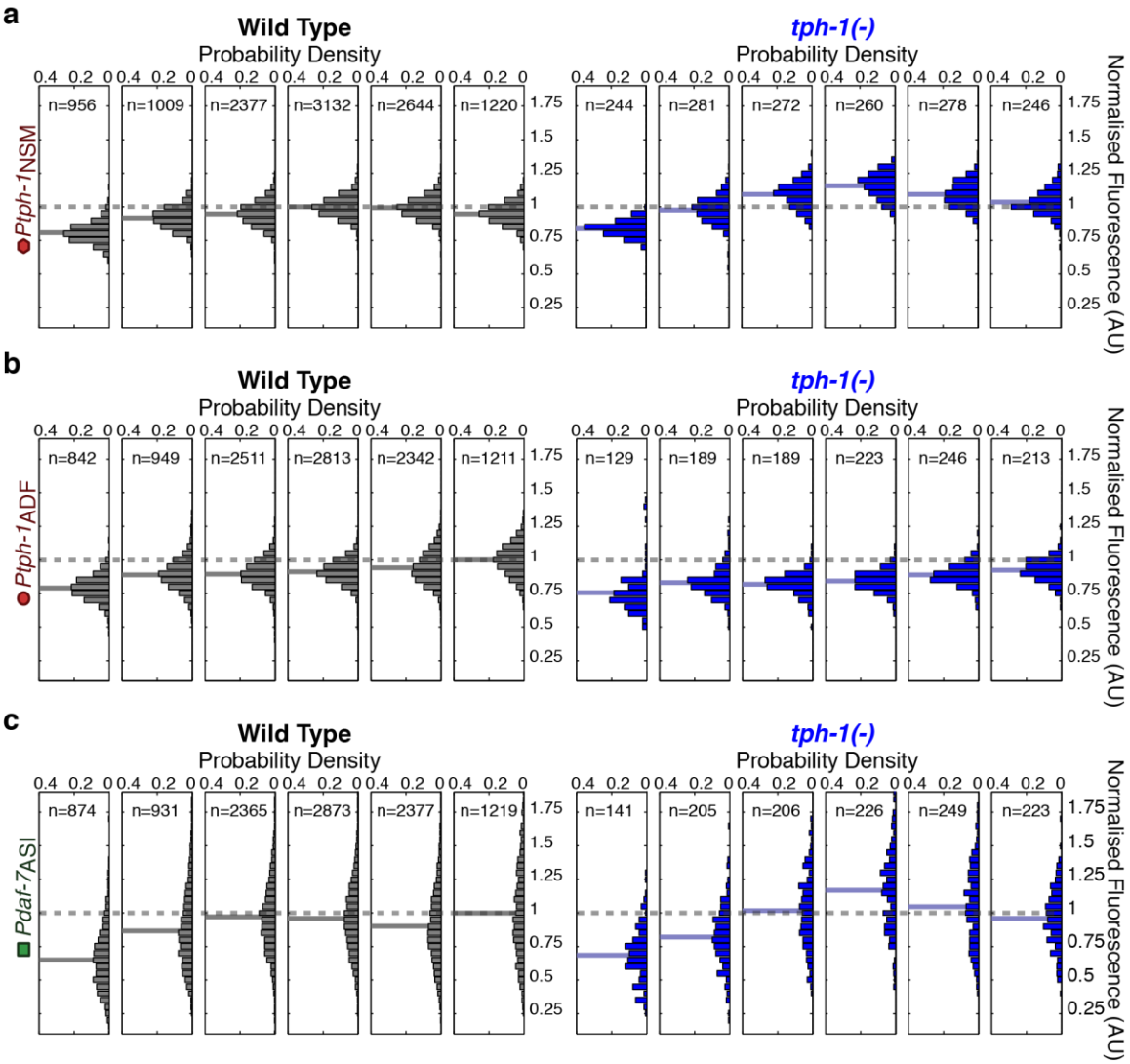

Figure B.1: Neuron-specific expression distributions for *tph-1(-)* mutants. Distributions of NSM, ADF and ASI expression intensities in the in the *tph-1(-)* mutants compared with corresponding distributions in the wild type animals. Values represent the sum of the expression intensities in both cells of the neuron-pair.

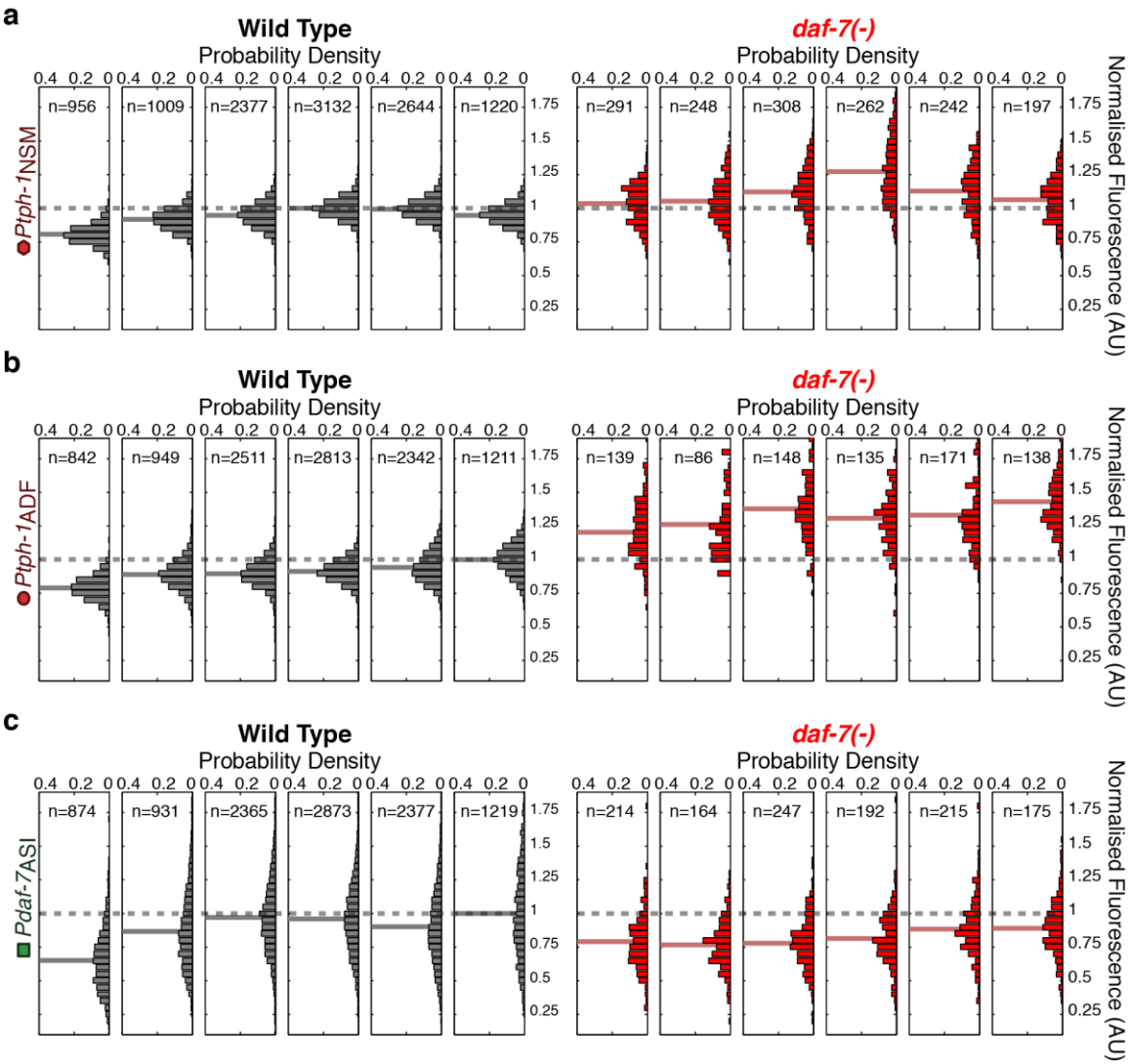

Figure B.2: Neuron-specific expression distributions for *daf-7(-)* mutants. Distributions of NSM, ADF and ASI neuronal expression intensities in the in the *daf-7(-)* mutants compared with corresponding distributions in the wild type animals. Values represent the sum of the expression intensities in both cells of the neuron-pair.

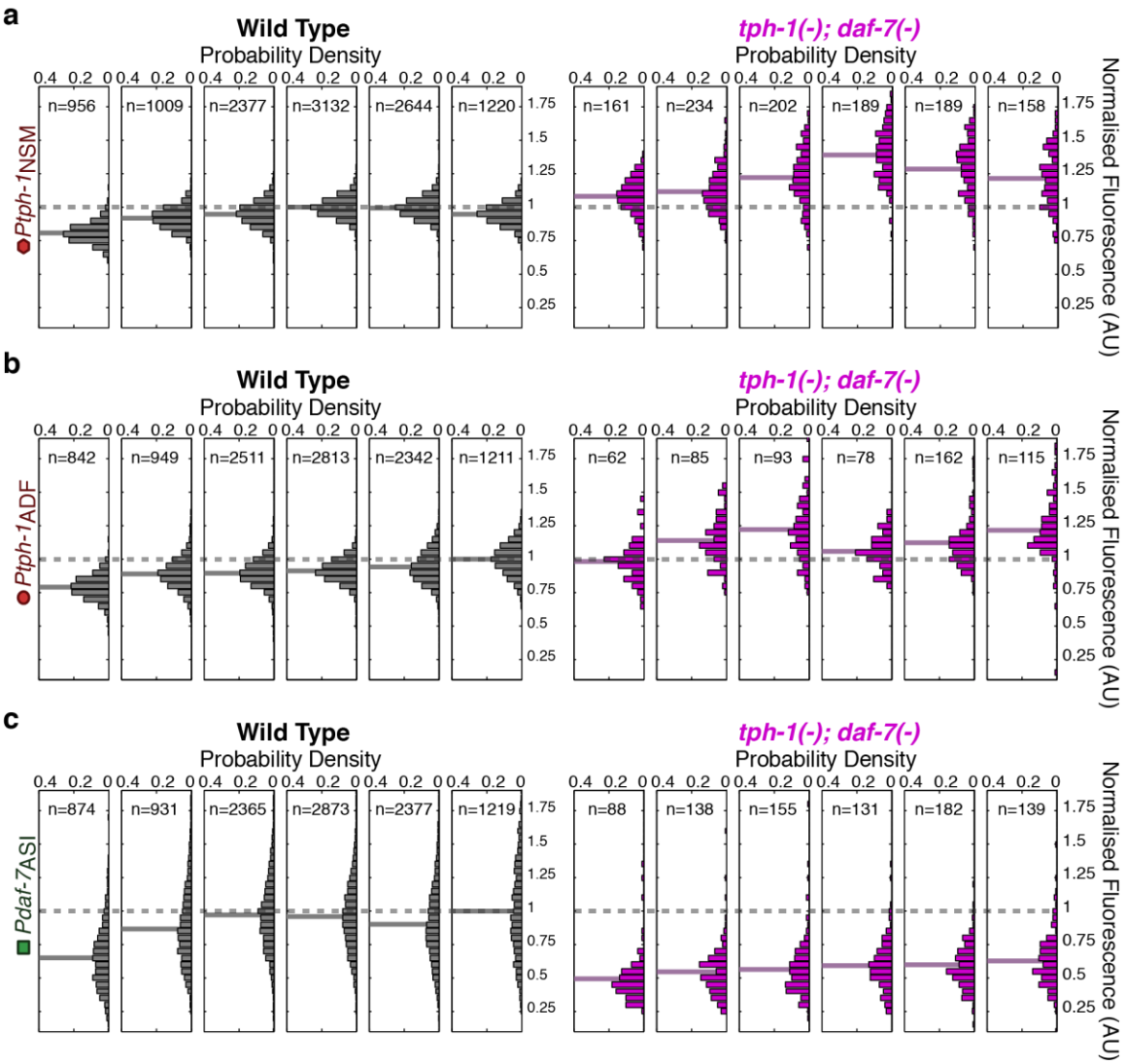

Figure B.3: Neuron-specific expression distributions for *tph-1(-); daf-7(-)* double mutants. Distributions of NSM, ADF and ASI neuronal expression intensities in the in the *tph-1(-);daf-7(-)* double mutants compared with corresponding distributions in the wild type animals. Values represent the sum of the expression intensities in both cells of the neuron-pair.

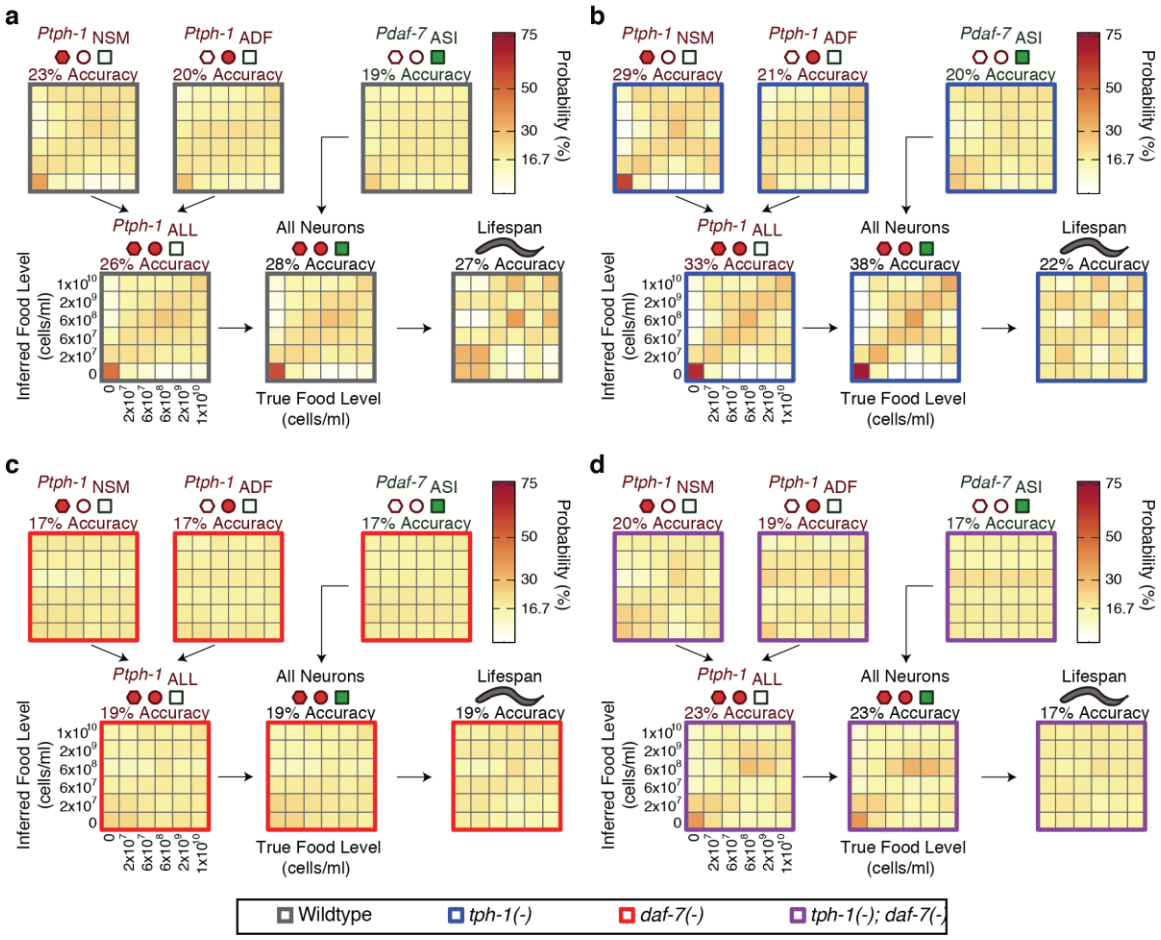

Figure B.4: Matrices of probability-based food encoding fidelity for single and combined neuronal outputs and lifespan outputs in the wildtype and mutant animals. These results are based on distributing the calculated raw probabilities of animals being from each food condition before assigning animals to particular food levels based on maximum likelihood. Genotype is denoted by the colored borders around the matrices as indicated by legend.

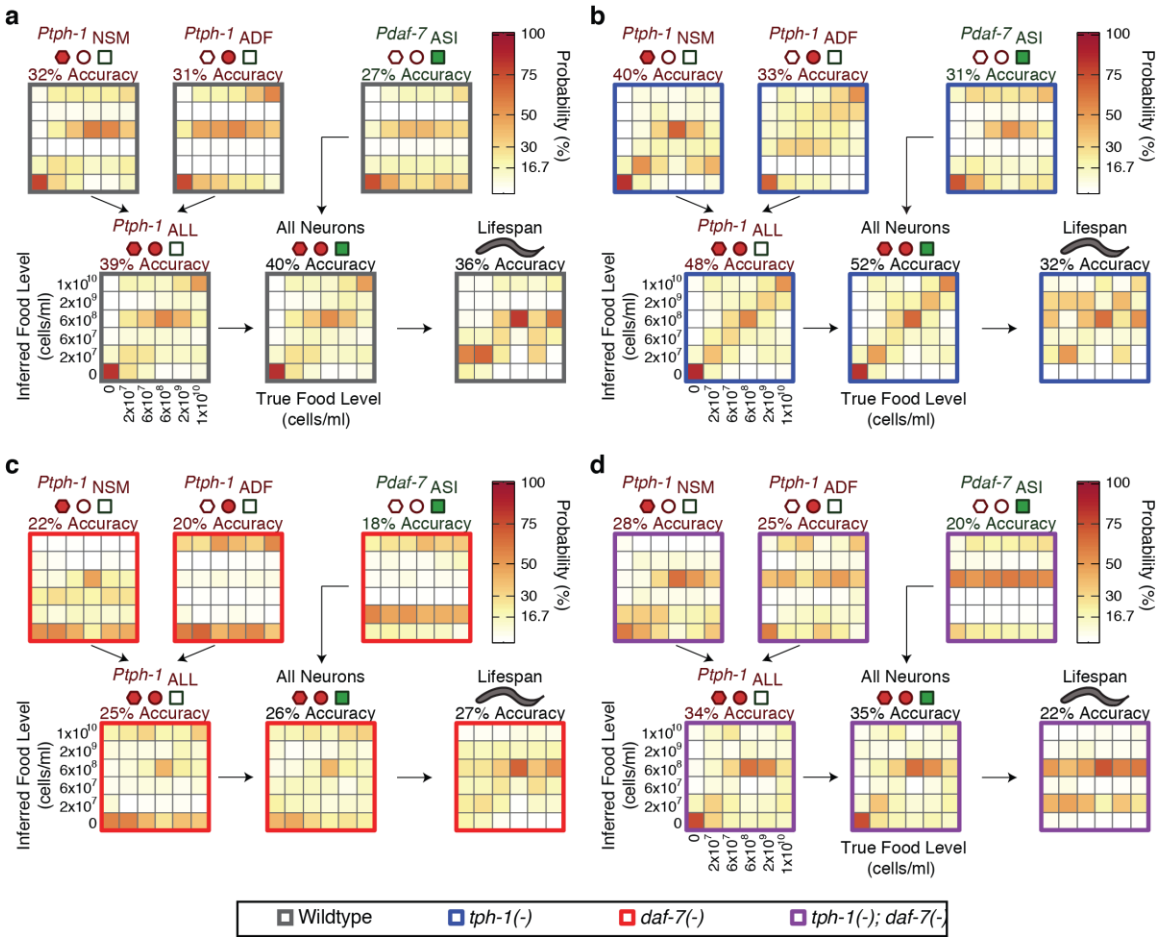

Figure B.5: Matrices of maximum likelihood-based food encoding fidelity for single and combined neuronal outputs and lifespan outputs in the wild type and mutant animals. Genotype is denoted by the colored borders around the matrices as indicated by legend.

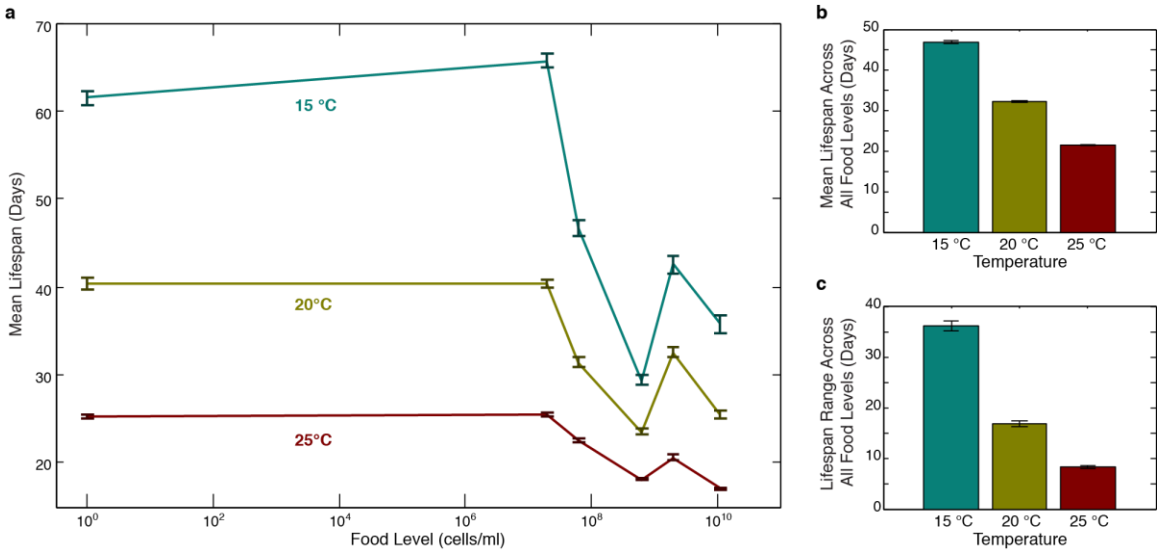

Figure B.6: Robustness of the dietary restriction response to temperature conditions. a) A similar pattern of lifespan modulation by food abundance is observed throughout the typical range of rearing temperatures for *C. elegans*. b) Rather than changing the shape of the food response, temperature changes shift the response, with higher mean lifespans observed at lower temperatures. c) Temperature also modulates the dynamic range of the food response, with higher ranges observed at lower temperatures.

APPENDIX C: ARDUINO CODE FOR INSTRUMENT CONTROL AND LABVIEW INTERFACE

Appendix C.1: Temperature Control Code and LUT for Thermistor Readout

The main Arduino code for deployment on the Arduino MEGA is provided below.

```
/*****************************************************************************
 **
 ** Includes.
 **
 *****************************************************************************/
// Standard includes.  These should always be included.
#include <QueueArray.h>
#include "TempLUT.h"


/*****************************************************************************
 **  setup()
 **
 **  Initialize the Arduino and setup serial communication.
 **
 **  Input:  None
 **  Output: None
 *****************************************************************************/
//Declare Global Variables
signed long SetPoint[10]={20, 20, 20, 20, 20, 20, 20, 20, 20, 20};
byte Output[10]={0, 0, 0, 0, 0, 0, 0, 0, 0, 0};
int analogIn[10]={A0, A2, A4, A6, A8, A10, A11, A12, A13, A14};
int analogIn2[5]={A1, A3, A5, A7, A9};
int analogOut[10]={2, 3, 4, 5, 6, 7, 8, 9, 10, 11};
int digitalOut[10]={30, 32, 34, 36, 38, 40, 42, 44, 46, 48};

//signed long LUT[1024];

byte ChanEnable[10]={0, 0, 0, 0, 0, 0, 0, 0, 0, 0};
byte PIDReInit[10]={0, 0, 0, 0, 0, 0, 0, 0, 0, 0};
signed long TempCurrent[10]={-27315000, -27315000, -27315000, -27315000, -27315000, -27315000, -
27315000, -27315000, -27315000, -27315000};
signed long TempCurrent2[10]={-27315000, -27315000, -27315000, -27315000, -27315000, -27315000, -
27315000, -27315000, -27315000, -27315000};
byte TempMode[10]={0, 0, 0, 0, 0, 0, 0, 0, 0, 0};
int IntCount[10]={0, 0, 0, 0, 0, 0, 0, 0, 0, 0};
QueueArray <double> Error[10];
double ErrorInt[10]={0, 0, 0, 0, 0, 0, 0, 0, 0, 0};
double ErrorCurr[10]={0, 0, 0, 0, 0, 0, 0, 0, 0, 0};

unsigned char LoopResponse[12];
byte AutoPID=0;


void setup()
{

  // Initialize Serial Port With The Default Baud Rate
  Serial.begin(115200);
  Serial.flush();

  //Configure Pins
  analogReference(DEFAULT);
  for(int k=0; k<10; k++)
  {
    pinMode(analogOut[k], OUTPUT);
    pinMode(digitalOut[k], OUTPUT);
    pinMode(analogIn[k], INPUT);
  }
```

```
  //Configure PWM Frequencies
  TCCR1B = TCCR1B & 0b11111000 | 0x01;
  TCCR2B = TCCR2B & 0b11111000 | 0x01;
  TCCR3B = TCCR3B & 0b11111000 | 0x01;
  TCCR4B = TCCR4B & 0b11111000 | 0x01;

}


/********************************************************************************
 **  loop()
 **
 **  The main loop.  This loop runs continuously on the Arduino.  It
 **  receives and processes serial commands from LabVIEW.
 **
 ********************************************************************************/


void loop()
{
  // Declare Loop Variables
    int COMMANDLENGTH=60;
    unsigned char Command[COMMANDLENGTH];
    unsigned char AutoPIDResponse[102];

    double Gain=10; //Proportional multiplier in PID Controller
    double TempProcess=0;
    double TempN=0;
    double SignedOutput;

    unsigned long LoopTime=5000; //Loop time in milliseconds
    unsigned long IntegrationTime=90000; //Integration Time for PID Controller in milliseconds
    unsigned long IntegrationCount=IntegrationTime/LoopTime; //Number of discrete loop cycles for
integration
    signed long TempSum=0; //Temperature summation for data averaging
    signed long SetPointTemp=20;


  //Auto-PID
  if (AutoPID==1)
  {
    AutoPIDResponse[0]=240;
    AutoPIDResponse[101]=241;
    for(int i=0; i<10; i++)
    {
      if (ChanEnable[i]==1)
      {
        //Read Temperature from Input 1
        TempSum=0;
        for(int j=0; j<50; j++)
        {
          TempSum=TempSum+LUT[analogRead(analogIn[i])];
        }
        TempCurrent[i]=TempSum/50;

        //Read Temperature from Input 2 if applicable
        if (i<=4)
        {
          TempSum=0;
          for(int j=0; j<50; j++)
          {
            TempSum=TempSum+LUT[analogRead(analogIn2[i])];
          }
          TempCurrent2[i]=TempSum/50;
        }

        TempProcess=0;
        TempN=0;

        if (TempCurrent[i]>0)
        {
          TempProcess=TempProcess+double(TempCurrent[i]);
          TempN=TempN+1;
        }
        if (TempCurrent2[i]>0)
        {
          TempProcess=TempProcess+double(TempCurrent2[i]);
          TempN=TempN+1;
```

```
        }
        if (TempN>0)
        {
          TempProcess=TempProcess/TempN;
          ErrorCurr[i]=(double(SetPoint[i])-TempProcess)/100000;
          Error[i].enqueue(ErrorCurr[i]);
//          if (PIDReInit[i]==1)
//          {
//            ErrorInt[i]=0;
//          }
          ErrorInt[i]=ErrorInt[i]+ErrorCurr[i]/IntegrationCount;

          SignedOutput=Gain*(ErrorCurr[i]+ErrorInt[i]);
          Output[i]=byte(abs(SignedOutput));
          if (Output[i]>25)
          {
            TempMode[i]=SignedOutput>0;
          }
          if (Output[i]>100)
          {
            Output[i]=100;
          }
        }
      }
      else
      {
        TempCurrent[i]=-27315000;
        TempCurrent2[i]=-27315000;
        Output[i]=0;
      }

        digitalWrite(digitalOut[i], TempMode[i]);
        analogWrite(analogOut[i], Output[i]);
        AutoPIDResponse[10*i+1]=char((signed long)TempCurrent[i]>>24);
        AutoPIDResponse[10*i+2]=char((signed long)TempCurrent[i]>>16);
        AutoPIDResponse[10*i+3]=char((signed long)TempCurrent[i]>>8);
        AutoPIDResponse[10*i+4]=char(TempCurrent[i]);
        AutoPIDResponse[10*i+5]=char((signed long)TempCurrent2[i]>>24);
        AutoPIDResponse[10*i+6]=char((signed long)TempCurrent2[i]>>16);
        AutoPIDResponse[10*i+7]=char((signed long)TempCurrent2[i]>>8);
        AutoPIDResponse[10*i+8]=char(TempCurrent2[i]);
        AutoPIDResponse[10*i+9]=Output[i];
        AutoPIDResponse[10*i+10]=TempMode[i];
      }
      delay(LoopTime);
    }
//    Serial.write(AutoPIDResponse, 102);
//    Serial.flush();


  // Check for commands from LabVIEW and process them.

    int bufferBytes = Serial.available();

    if(bufferBytes >= COMMANDLENGTH)
    {
      // New Command Ready, Process It
      // Build Command From Serial Buffer
      for(int i=0; i<COMMANDLENGTH; i++)
      {
        Command[i] = Serial.read();
      }
      if (Command[0]==0xFF && Command[COMMANDLENGTH-1]==0xFE)
      {
        switch (Command[1])
        {
          case 0x00:
            Serial.flush();
            Serial.print("SyncTemperature");
            Serial.flush();
            break;

          case 0x01:
            if (Command[2]>=0 && Command[2]<10 && (Command[3]==0 || Command[3]==1))
            {
              ChanEnable[Command[2]]=Command[3];
              if (ChanEnable[Command[2]]==1)
              {
```

```
              SetPoint[Command[2]]=(signed long)(long(Command[4]) << 24)+(long(Command[5]) <<
16)+(long(Command[6]) << 8) + long(Command[7]);
              TempSum=0;
              for(int i=0; i<50; i++)
              {
                TempSum=TempSum+LUT[analogRead(analogIn[Command[2]])];
              }
              TempCurrent[Command[2]]=TempSum/50;
              if (Command[2]<=4)
              {
                TempSum=0;
                for(int i=0; i<50; i++)
                {
                  TempSum=TempSum+LUT[analogRead(analogIn2[Command[2]])];
                }
                TempCurrent2[Command[2]]=TempSum/50;
              }
            }
            else
            {
              TempCurrent[Command[2]]=0;
            }
            LoopResponse[0]=250;
            LoopResponse[1]=char((signed long)TempCurrent[Command[2]]>>24);
            LoopResponse[2]=char((signed long)TempCurrent[Command[2]]>>16);
            LoopResponse[3]=char((signed long)TempCurrent[Command[2]]>>8);
            LoopResponse[4]=char(TempCurrent[Command[2]]);
            LoopResponse[5]=char((signed long)TempCurrent2[Command[2]]>>24);
            LoopResponse[6]=char((signed long)TempCurrent2[Command[2]]>>16);
            LoopResponse[7]=char((signed long)TempCurrent2[Command[2]]>>8);
            LoopResponse[8]=char(TempCurrent2[Command[2]]);
            LoopResponse[9]=Output[Command[2]];;
            LoopResponse[10]=TempMode[Command[2]];
            LoopResponse[11]=251;
            Serial.flush();
            Serial.write(LoopResponse, 12);
            Serial.flush();
          }
          break;

        case 0x02:
          if (Command[2]>=0 && Command[2]<10 && (Command[4]>=0 && Command[4]<3))
          {
            if (ChanEnable[Command[2]]==1)
            {
              Output[Command[2]]=Command[3];
              if (Output[Command[2]]>25 && TempMode[Command[2]]!=(Command[4]>1))
              {
                TempMode[Command[2]]=Command[4]>1;
              }
              digitalWrite(digitalOut[Command[2]], TempMode[Command[2]]);
              analogWrite(analogOut[Command[2]], Output[Command[2]]);
            }
            else
            {
              Output[Command[2]]=0;
              analogWrite(analogOut[Command[2]], Output[Command[2]]);
            }
            LoopResponse[0]=250;
            LoopResponse[1]=char((signed long)TempCurrent[Command[2]]>>24);
            LoopResponse[2]=char((signed long)TempCurrent[Command[2]]>>16);
            LoopResponse[3]=char((signed long)TempCurrent[Command[2]]>>8);
            LoopResponse[4]=char(TempCurrent[Command[2]]);
            LoopResponse[5]=char((signed long)TempCurrent2[Command[2]]>>24);
            LoopResponse[6]=char((signed long)TempCurrent2[Command[2]]>>16);
            LoopResponse[7]=char((signed long)TempCurrent2[Command[2]]>>8);
            LoopResponse[8]=char(TempCurrent2[Command[2]]);
            LoopResponse[9]=Output[Command[2]];
            LoopResponse[10]=TempMode[Command[2]];
            LoopResponse[11]=251;
            Serial.flush();
            Serial.write(LoopResponse, 12);
            Serial.flush();
          }
          break;

        case 0x03:
          if (Command[2]==0 || Command[2]==1)
          {
```

```
            AutoPID=Command[2];
          }
          Serial.write("AutoPIDSet");
          Serial.flush();
          break;

        case 0x04:
          if (Command[2]==0 || Command[2]==1)
          {
            if (AutoPID!=Command[2])
            {
              for (int i=0; i<10; i++)
              {
                PIDReInit[i]=1;
              }
            }
            AutoPID=Command[2];
            for(int i=0; i<10; i++)
            {
              SetPointTemp=(signed long)(long(Command[i*5+4]) << 24)+(long(Command[i*5+5]) <<
16)+(long(Command[i*5+6]) << 8) + long(Command[i*5+7]);
              if (ChanEnable[i]==Command[i*5+3] && SetPoint[i]==SetPointTemp && PIDReInit[i]==0)
              {
                PIDReInit[i]=0;
              }
              else
              {
                PIDReInit[i]=1;
              }
              ChanEnable[i]=Command[i*5+3];
              SetPoint[i]=SetPointTemp;
              if (ChanEnable[i]==0)
              {
                Output[i]=0;
                analogWrite(analogOut[i], Output[i]);
                TempCurrent[i]=0;
              }
            }
            AutoPIDResponse[0]=239;
            AutoPIDResponse[101]=240;
            Serial.write(AutoPIDResponse, 102);
            Serial.flush();
          }

          Serial.flush();
          break;

        case 0x05:
          if (Command[2]>=0 && Command[2]<10 && (Command[3]==0 || Command[3]==1))
          {
            SetPointTemp=(signed long)(long(Command[4]) << 24)+(long(Command[5]) <<
16)+(long(Command[6]) << 8) + long(Command[7]);
            if (AutoPID!=Command[8] || ChanEnable[Command[2]]!=Command[3] ||
SetPoint[Command[2]]!=SetPointTemp)
            {
              PIDReInit[Command[2]]=1;
            }
            else
            {
              PIDReInit[Command[2]]=0;
            }
            ChanEnable[Command[2]]=Command[3];
            SetPoint[Command[2]]=SetPointTemp;
            AutoPID=Command[8];
            AutoPIDResponse[0]=239;
            AutoPIDResponse[101]=240;
            Serial.write(AutoPIDResponse, 102);
            Serial.flush();
          }
          break;

        case 0x06:
          AutoPIDResponse[0]=240;
          AutoPIDResponse[101]=241;
          Serial.write(AutoPIDResponse, 102);
          Serial.flush();
          break;

       case 0x07:
```

```
//            AutoPID=0;
//            for(int i=0; i<10; i++)
//            {
//              ChanEnable[i]=0;
//              TempMode[i]=0;
//              Output[i]=0;
//              digitalWrite(digitalOut[i], TempMode[i]);
//              analogWrite(analogOut[i], Output[i]);
//
//            }
            Serial.write("DeInited");
            Serial.flush();
            break;


          default:
            Serial.flush();
            break;
        }
      }
      else
      {
        Serial.flush();
      }
      }
    else
    {
    }
}
```

The LUT for temperature readout is shown below. Temperatures are multiplied by 10^5 and stored and communicated as signed long integers.

```
signed long LUT[1024]=
{-27315000, -9293318, -8451025, -7932632, -7552417, -7250003, -6997826, -6780903, -6590153, -6419638,
-6265259, -6124061, -5993843, -5872920, -5759971, -5653941,
-5553976, -5459372, -5369542, -5283991, -5202301, -5124110, -5049108, -4977023, -4907617, -4840683, -
4776033, -4713504, -4652948, -4594232, -4537237, -4481856,
-4427990, -4375550, -4324456, -4274631, -4226008, -4178524, -4132120, -4086744, -4042345, -3998876, -
3956296, -3914564, -3873643, -3833498, -3794096, -3755407,
-3717401, -3680053, -3643336, -3607226, -3571701, -3536740, -3502322, -3468428, -3435041, -3402142, -
3369716, -3337746, -3306219, -3275121, -3244437, -3214155,
-3184264, -3154750, -3125604, -3096814, -3068371, -3040264, -3012485, -2985024, -2957873, -2931024, -
2904468, -2878198, -2852207, -2826488, -2801033, -2775838,
-2750894, -2726196, -2701738, -2677515, -2653522, -2629752, -2606201, -2582863, -2559736, -2536812, -
2514089, -2491562, -2469226, -2447078, -2425114, -2403330,
-2381722, -2360287, -2339021, -2317921, -2296984, -2276206, -2255585, -2235117, -2214800, -2194631, -
2174606, -2154724, -2134982, -2115377, -2095907, -2076569,
-2057361, -2038281, -2019327, -2000496, -1981786, -1963196, -1944722, -1926364, -1908120, -1889987, -
1871963, -1854048, -1836238, -1818533, -1800931, -1783431,
-1766030, -1748727, -1731520, -1714409, -1697392, -1680466, -1663632, -1646887, -1630230, -1613661, -
1597177, -1580777, -1564461, -1548226, -1532073, -1515999,
-1500003, -1484085, -1468244, -1452478, -1436786, -1421168, -1405622, -1390147, -1374742, -1359407, -
1344141, -1328942, -1313809, -1298743, -1283742, -1268805,
-1253931, -1239119, -1224370, -1209681, -1195052, -1180483, -1165973, -1151520, -1137125, -1122786, -
1108503, -1094275, -1080102, -1065982, -1051916, -1037902,
-1023940, -1010029,  -996169,  -982359,  -968599,  -954887,  -941224,  -927608,  -914040,  -900519,  -
887043,  -873614,  -860229,  -846889,  -833593,  -820341,
 -807131,  -793965,  -780840,  -767757,  -754716,  -741715,  -728754,  -715834,  -702952,  -690110,  -
677306,  -664541,  -651813,  -639123,  -626469,  -613852,
 -601272,  -588727,  -576217,  -563743,  -551303,  -538897,  -526525,  -514187,  -501882,  -489610,  -
477371,  -465163,  -452988,  -440844,  -428731,  -416649,
 -404598,  -392577,  -380586,  -368625,  -356692,  -344789,  -332915,  -321069,  -309252,  -297462,  -
285699,  -273965,  -262257,  -250576,  -238921,  -227293,
 -215690,  -204114,  -192562,  -181037,  -169536,  -158059,  -146607,  -135180,  -123776,  -112396,  -
101040,   -89707,   -78397,   -67110,   -55845,   -44603,
  -33383,   -22184,   -11008,      147,    11281,    22393,    33485,    44556,    55606,    66637,
77647,    88637,    99608,   110559,   121491,   132404,
  143298,   154173,   165029,   175868,   186688,   197490,   208274,   219041,   229790,   240522,
251236,   261934,   272615,   283279,   293927,   304559,
  315174,   325774,   336357,   346925,   357478,   368015,   378537,   389044,   399536,   410013,
420476,   430925,   441359,   451778,   462184,   472576,
```

482955, 493320, 503671, 514009, 524334, 534646, 544945, 555231, 565505, 575766,
586015, 596251, 606476, 616689, 626889, 637078,
647256, 657422, 667577, 677720, 687852, 697974, 708085, 718184, 728274, 738353,
748421, 758479, 768527, 778565, 788594, 798612,
808621, 818620, 828610, 838590, 848561, 858523, 868477, 878421, 888356, 898283,
908201, 918111, 928012, 937905, 947790, 957667,
967536, 977397, 987250, 997096, 1006934, 1016764, 1026588, 1036404, 1046213, 1056015,
1065810, 1075598, 1085379, 1095154, 1104922, 1114684,
1124439, 1134188, 1143931, 1153668, 1163399, 1173124, 1182843, 1192556, 1202264, 1211966,
1221663, 1231354, 1241040, 1250721, 1260397, 1270068,
1279734, 1289395, 1299052, 1308703, 1318351, 1327993, 1337632, 1347266, 1356896, 1366521,
1376143, 1385761, 1395375, 1404985, 1414591, 1424194,
1433793, 1443389, 1452981, 1462570, 1472156, 1481739, 1491318, 1500895, 1510469, 1520040,
1529608, 1539174, 1548737, 1558298, 1567856, 1577412,
1586966, 1596517, 1606067, 1615614, 1625160, 1634704, 1644246, 1653786, 1663325, 1672862,
1682398, 1691932, 1701465, 1710997, 1720527, 1730057,
1739586, 1749113, 1758640, 1768166, 1777692, 1787217, 1796741, 1806265, 1815788, 1825312,
1834835, 1844357, 1853880, 1863403, 1872926, 1882449,
1891972, 1901496, 1911020, 1920544, 1930069, 1939595, 1949121, 1958648, 1968176, 1977704,
1987234, 1996765, 2006297, 2015830, 2025364, 2034900,
2044437, 2053976, 2063516, 2073058, 2082602, 2092148, 2101695, 2111244, 2120796, 2130349,
2139905, 2149463, 2159023, 2168586, 2178151, 2187719,
2197289, 2206862, 2216438, 2226016, 2235598, 2245183, 2254770, 2264361, 2273955, 2283553,
2293154, 2302758, 2312366, 2321977, 2331592, 2341211,
2350834, 2360461, 2370091, 2379726, 2389365, 2399008, 2408655, 2418307, 2427963, 2437624,
2447289, 2456959, 2466634, 2476314, 2485999, 2495688,
2505383, 2515083, 2524788, 2534498, 2544214, 2553935, 2563662, 2573394, 2583133, 2592876,
2602626, 2612382, 2622144, 2631912, 2641686, 2651466,
2661253, 2671046, 2680846, 2690652, 2700465, 2710285, 2720111, 2729945, 2739785, 2749633,
2759488, 2769350, 2779219, 2789096, 2798980, 2808872,
2818772, 2828679, 2838595, 2848518, 2858449, 2868389, 2878336, 2888292, 2898256, 2908229,
2918210, 2928200, 2938199, 2948207, 2958223, 2968249,
2978283, 2988327, 2998380, 3008442, 3018514, 3028595, 3038687, 3048787, 3058898, 3069019,
3079149, 3089290, 3099441, 3109602, 3119774, 3129956,
3140148, 3150352, 3160566, 3170791, 3181027, 3191274, 3201533, 3211802, 3222084, 3232376,
3242680, 3252996, 3263324, 3273663, 3284015, 3294378,
3304754, 3315143, 3325543, 3335956, 3346382, 3356821, 3367272, 3377736, 3388214, 3398704,
3409208, 3419726, 3430257, 3440801, 3451359, 3461931,
3472517, 3483118, 3493732, 3504361, 3515004, 3525661, 3536334, 3547021, 3557723, 3568440,
3579172, 3589920, 3600683, 3611461, 3622255, 3633065,
3643891, 3654733, 3665590, 3676465, 3687355, 3698263, 3709186, 3720127, 3731085, 3742059,
3753051, 3764061, 3775087, 3786132, 3797194, 3808274,
3819372, 3830488, 3841623, 3852776, 3863947, 3875138, 3886347, 3897575, 3908823, 3920090,
3931376, 3942682, 3954008, 3965353, 3976719, 3988105,
3999512, 4010939, 4022387, 4033856, 4045346, 4056857, 4068389, 4079943, 4091519, 4103116,
4114736, 4126378, 4138042, 4149729, 4161439, 4173172,
4184927, 4196706, 4208509, 4220335, 4232185, 4244059, 4255957, 4267880, 4279827, 4291799,
4303796, 4315818, 4327866, 4339939, 4352038, 4364162,
4376313, 4388491, 4400695, 4412925, 4425183, 4437468, 4449780, 4462120, 4474488, 4486884,
4499309, 4511761, 4524243, 4536753, 4549293, 4561862,
4574461, 4587090, 4599749, 4612438, 4625158, 4637909, 4650691, 4663505, 4676350, 4689227,
4702136, 4715077, 4728052, 4741059, 4754099, 4767173,
4780281, 4793422, 4806598, 4819809, 4833054, 4846335, 4859651, 4873002, 4886390, 4899814,
4913275, 4926773, 4940308, 4953880, 4967491, 4981139,
4994826, 5008552, 5022317, 5036122, 5049966, 5063851, 5077776, 5091742, 5105750, 5119799,
5133889, 5148022, 5162198, 5176417, 5190679, 5204985,
5219335, 5233730, 5248169, 5262654, 5277185, 5291762, 5306385, 5321055, 5335773, 5350539,
5365352, 5380215, 5395126, 5410087, 5425099, 5440160,
5455273, 5470437, 5485652, 5500920, 5516241, 5531615, 5547043, 5562526, 5578063, 5593655,
5609304, 5625008, 5640770, 5656589, 5672466, 5688402,
5704397, 5720451, 5736566, 5752741, 5768978, 5785277, 5801639, 5818064, 5834553, 5851106,
5867725, 5884409, 5901160, 5917978, 5934864, 5951819,
5968842, 5985936, 6003100, 6020335, 6037643, 6055024, 6072478, 6090006, 6107610, 6125289,
6143045, 6160879, 6178792, 6196783, 6214855, 6233007,
6251242, 6269559, 6287959, 6306445, 6325015, 6343673, 6362417, 6381250, 6400172, 6419185,
6438289, 6457485, 6476775, 6496160, 6515640, 6535217,
6554892, 6574666, 6594540, 6614516, 6634594, 6654776, 6675063, 6695456, 6715957, 6736567,
6757288, 6778120, 6799065, 6820124, 6841299, 6862592,
6884003, 6905535, 6927188, 6948965, 6970867, 6992896, 7015053, 7037340, 7059758, 7082310,
7104997, 7127822, 7150785, 7173889, 7197136, 7220527,
7244065, 7267752, 7291589, 7315580, 7339726, 7364029, 7388491, 7413115, 7437904, 7462859,
7487984, 7513280, 7538750, 7564397, 7590223, 7616232,
7642425, 7668807, 7695379, 7722144, 7749107, 7776270, 7803635, 7831207, 7858989, 7886984,
7915195, 7943627, 7972283, 8001166, 8030281, 8059632,
8089221, 8119055, 8149137, 8179470, 8210061, 8240913, 8272031, 8303420, 8335086, 8367032,
8399264, 8431788, 8464609, 8497733, 8531166, 8564913,
8598981, 8633377, 8668106, 8703176, 8738593, 8774365, 8810499, 8847002, 8883883, 8921149,
8958809, 8996872, 9035345, 9074239, 9113562, 9153325,

```
 9193537,  9234210,  9275353,  9316977,  9359096,  9401719,  9444860,  9488532,  9532747,  9577520,
9622865,  9668796,  9715329,  9762480,  9810265,  9858702,
 9907809,  9957604, 10008107, 10059338, 10111318, 10164069, 10217614, 10271978, 10327185, 10383261,
10440234, 10498132, 10556986, 10616827, 10677688, 10739604,
10802610, 10866746, 10932052, 10998570, 11066344, 11135422, 11205854, 11277692, 11350992, 11425812,
11502215, 11580267, 11660039, 11741606, 11825046, 11910445,
11997894, 12087489, 12179334, 12273541, 12370229, 12469526, 12571571, 12676513, 12784515, 12895750,
13010409, 13128700, 13250847, 13377098, 13507722, 13643018,
13783313, 13928969, 14080389, 14238020, 14402362, 14573977, 14753496, 14941636, 15139212, 15347155,
15566537, 15798601, 16044796, 16306824, 16586707, 16886862,
17210218, 17560361, 17941746, 18359997, 18822341, 19338268, 19920566, 20586998, 21363201, 22287993,
23423961, 24881065, 26878270, 29949568, 36044018, -27315000
};
```

Appendix C.2: Stepper Motor Control Code for Camera Control

```
/*****************************************************************************
 **
 ** Includes.
 **
 *****************************************************************************/
// Standard includes.  These should always be included.


/*****************************************************************************
 **  setup()
 **
 **  Initialize the Arduino and setup serial communication.
 **
 **  Input:  None
 **  Output: None
 *****************************************************************************/
//Declare Global Variables
signed long Position[3]={0,0,0};
unsigned char MovementResponse[7];
int analog[6]={A0, A1, A2, A3, A4, A5};

void setup()
{
  // Initialize Serial Port With The Default Baud Rate
  Serial.begin(115200);
  Serial.flush();
  for(int i=2; i<13; i++)
  {
    pinMode(i, OUTPUT);
  }
  for(int i=0; i<6; i++)
  {
    pinMode(analog[i], INPUT_PULLUP);
  }


}


/*****************************************************************************
 **  loop()
 **
 **  The main loop.  This loop runs continuously on the Arduino.  It
 **  receives and processes serial commands from LabVIEW.
 **
 **  Input:  None
 **  Output: None
 *****************************************************************************/


void loop()
{
  // Declare Loop Variables
    int COMMANDLENGTH=15;
    unsigned char Command[COMMANDLENGTH];
    unsigned long StepsMoved=0;
    unsigned long StepsToMove=0;
    unsigned long MaxMovement=75000;
    boolean LimitSwitch=true;
    int breakloopbytes=0;
    int n=0;
```

```
    float timedelay=0;
    float timedelayacc=0;
    unsigned char PositionResponse[14];


  // Check for commands from LabVIEW and process them.

    int bufferBytes = Serial.available();

    if(bufferBytes >= COMMANDLENGTH)
    {
      // New Command Ready, Process It
      // Build Command From Serial Buffer
      for(int i=0; i<COMMANDLENGTH; i++)
      {
        Command[i] = Serial.read();
      }
      if (Command[0]==0xFF && Command[COMMANDLENGTH-1]==0xFE)
      {
        switch (Command[1])
        {
          case 0x00:
            Serial.flush();
            Position[0]=0;
            Position[1]=0;
            Position[2]=0;
            Serial.print("Sync");
            break;

          case 0x01:
            if ((Command[8]==0 || Command[8]==1) && (Command[7]>=0 && Command[7]<=2)) //Check for
variable compatibility
            {
              Serial.print("OK");
              digitalWrite(Command[2], HIGH); //Write to Enable
              digitalWrite(Command[3], Command[8]); //Write to Direction
              digitalWrite(Command[4], LOW); //Ensure Step is low before looping
              timedelay=7500/float(Command[9]); //Calculate time delay from speed specification
              StepsMoved=0;
              breakloopbytes=0;
              LimitSwitch=digitalRead(analog[Command[5+Command[8]]]); //Query whether axis is already
at limit in this direction
              while (breakloopbytes==0 && LimitSwitch==1 && StepsMoved<MaxMovement)
              {
                if (StepsMoved<100)
                {
                  timedelayacc=timedelay+float(100-StepsMoved)*(10000-timedelay)/100;
                }
                else
                {
                  timedelayacc=timedelay;
                }
                digitalWrite(Command[4], HIGH);
                delayMicroseconds(long(timedelayacc));
                digitalWrite(Command[4], LOW);
                delayMicroseconds(long(timedelayacc));
                StepsMoved++;
                LimitSwitch=digitalRead(analog[Command[5+Command[8]]]);
                breakloopbytes=Serial.available();
              }
              digitalWrite(Command[2], LOW); //Disable Axis
              switch (Command[8])
              {
                case 0x00:
                  Position[Command[7]]=Position[Command[7]]-StepsMoved;
                  break;
                default:
                  Position[Command[7]]=Position[Command[7]]+StepsMoved;
                  break;
              }
              MovementResponse[0]=250;
              MovementResponse[1]=char((unsigned long)StepsMoved>>24);
              MovementResponse[2]=char((unsigned long)StepsMoved>>16);
              MovementResponse[3]=char((unsigned long)StepsMoved>>8);
              MovementResponse[4]=char(StepsMoved);
              MovementResponse[5]=LimitSwitch;
              MovementResponse[6]=251;
              Serial.flush();
              Serial.write(MovementResponse, 7);
```

```
            }
            break;

          case 0x02:
            if ((Command[8]==0 || Command[8]==1) && (Command[7]>=0 && Command[7]<=2)) //Check for
variable compatibility
            {
              Serial.print("OK");
              digitalWrite(Command[2], HIGH); //Write to Enable
              digitalWrite(Command[3], Command[8]); //Write to Direction
              digitalWrite(Command[4], LOW); //Ensure Step is low before looping
              timedelay=(60/(float(Command[9])*4000)/2*1000000);
              StepsToMove=(unsigned long)(long(Command[10]) << 24)+(long(Command[11]) <<
16)+(long(Command[12]) << 8) + long(Command[13]);
              StepsMoved=0;
              breakloopbytes=0;
              LimitSwitch=digitalRead(analog[Command[5+Command[8]]]); //Query whether axis is already
at limit in this direction
              while (breakloopbytes==0 && LimitSwitch==1 && StepsMoved<StepsToMove)
              {
                digitalWrite(Command[4], HIGH);
                delayMicroseconds(long(timedelay));
                digitalWrite(Command[4], LOW);
                delayMicroseconds(long(timedelay));
                StepsMoved++;
                LimitSwitch=digitalRead(analog[Command[5+Command[8]]]);
                breakloopbytes=Serial.available();
              }
              digitalWrite(Command[2], LOW); //Disable Axis
              switch (Command[8])
                {
                  case 0:
                    Position[Command[7]]=Position[Command[7]]-(signed long)StepsMoved;
                    break;
                  default:
                    Position[Command[7]]=Position[Command[7]]+(signed long)StepsMoved;
                    break;
                }
              MovementResponse[0]=250;
              MovementResponse[1]=char((unsigned long)StepsMoved>>24);
              MovementResponse[2]=char((unsigned long)StepsMoved>>16);
              MovementResponse[3]=char((unsigned long)StepsMoved>>8);
              MovementResponse[4]=char(StepsMoved);
              MovementResponse[5]=LimitSwitch;
              MovementResponse[6]=251;
              Serial.flush();
              Serial.write(MovementResponse, 7);
            }
            break;

          case 0x03:
            Serial.flush();
            Serial.write(MovementResponse, 7);
            break;

          case 0x04:
            PositionResponse[0]=240;
            PositionResponse[13]=241;
            Serial.flush();
            for(int j=0; j<3; j++)
            {
              PositionResponse[1+4*j]=char(Position[j]>>24);
              PositionResponse[2+4*j]=char(Position[j]>>16);
              PositionResponse[3+4*j]=char(Position[j]>>8);
              PositionResponse[4+4*j]=char(Position[j]);
            }
            Serial.write(PositionResponse, 14);
            break;

          default:
            Serial.flush();
            break;
        }
      }
      else
      {
        Serial.flush();
      }
      }
```

```
    else
    {

    }
}
```

REFERENCES

1. T. B. Kirkwood, C. E. Finch, Ageing: the old worm turns more slowly. *Nature* **419**, 794-795 (2002); published online EpubOct 24 (10.1038/419794a).

2. T. B. L. Kirkwood, M. Feder, C. E. Finch, C. Franceschi, A. Globerson, C. P. Klingenberg, K. LaMarco, S. Omholt, R. G. J. Westendorp, What accounts for the wide variation in life span of genetically identical organisms reared in a constant environment? *Mechanisms of ageing and development* **126**, 439-443 (2005)10.1016/j.mad.2004.09.008).

3. L. A. Herndon, P. J. Schmeissner, J. M. Dudaronek, P. A. Brown, K. M. Listner, Y. Sakano, M. C. Paupard, D. H. Hall, M. Driscoll, Stochastic and genetic factors influence tissue-specific decline in ageing C. elegans. *Nature* **419**, 808-814 (2002); published online EpubOct 24 (10.1038/nature01135).

4. M. Tatar, A. Bartke, A. Antebi, The endocrine regulation of aging by insulin-like signals. *Science* **299**, 1346-1351 (2003); published online EpubFeb 28 (10.1126/science.1081447).

5. C. Kenyon, The plasticity of aging: insights from long-lived mutants. *Cell* **120**, 449-460 (2005); published online EpubFeb 25 (10.1016/j.cell.2005.02.002).

6. L. Fontana, L. Partridge, V. D. Longo, Extending healthy life span—from yeast to humans. *Science* **328**, 321-326 (2010).

7. W. Mair, A. Dillin, Aging and survival: the genetics of life span extension by dietary restriction. *Annual review of biochemistry* **77**, 727-754 (2008)10.1146/annurev.biochem.77.061206.171059).

8. S. J. Lee, C. Kenyon, Regulation of the longevity response to temperature by thermosensory neurons in Caenorhabditis elegans. *Curr Biol* **19**, 715-722 (2009); published online EpubMay 12 (10.1016/j.cub.2009.03.041).

9. B. Conti, M. Sanchez-Alavez, R. Winsky-Sommerer, M. C. Morale, J. Lucero, S. Brownell, V. Fabre, S. Huitron-Resendiz, S. Henriksen, E. P. Zorrilla, L. de Lecea, T. Bartfai, Transgenic mice with a reduced core body temperature have an increased life span. *Science* **314**, 825-828 (2006); published online EpubNov 3 (10.1126/science.1132191).

10. C. Kenyon, J. Chang, E. Gensch, A. Rudner, R. Tabtiang, A C. elegans mutant that lives twice as long as wild type. *Nature* **366**, 461-464 (1993); published online EpubDec 2 (10.1038/366461a0).

11. W. M. Shaw, S. Luo, J. Landis, J. Ashraf, C. T. Murphy, The C. elegans TGF-beta Dauer pathway regulates longevity via insulin signaling. *Curr Biol* **17**, 1635-1645 (2007); published online EpubOct 9 (10.1016/j.cub.2007.08.058).

12. H. Murakami, S. Murakami, Serotonin receptors antagonistically modulate Caenorhabditis elegans longevity. *Aging cell* **6**, 483-488 (2007); published online EpubAug (10.1111/j.1474-9726.2007.00303.x).

13. J. Apfeld, C. Kenyon, Regulation of lifespan by sensory perception in Caenorhabditis elegans. *Nature* **402**, 804-809 (1999); published online EpubDec 16 (10.1038/45544).

14. J. Alcedo, C. Kenyon, Regulation of C. elegans longevity by specific gustatory and olfactory neurons. *Neuron* **41**, 45-55 (2004); published online EpubJan 8 (

15. N. A. Bishop, L. Guarente, Two neurons mediate diet-restriction-induced longevity in C. elegans. *Nature* **447**, 545-549 (2007); published online EpubMay 31 (10.1038/nature05904).

16. M. Estevez, A. O. Estevez, R. H. Cowie, K. L. Gardner, The voltage-gated calcium channel UNC-2 is involved in stress-mediated regulation of tryptophan hydroxylase. *Journal of Neurochemistry* **88**, 102-113 (2004)10.1046/j.1471-4159.2003.02140.x).

17. B. Liang, M. Moussaif, C.-J. Kuan, J. J. Gargus, J. Y. Sze, Serotonin targets the DAF-16/FOXO signaling pathway to modulate stress responses. *Cell Metabolism* **4**, 429-440 (2006); published online Epub12// (10.1016/j.cmet.2006.11.004).

18. P. Ren, C. S. Lim, R. Johnsen, P. S. Albert, D. Pilgrim, D. L. Riddle, Control of C. elegans larval development by neuronal expression of a TGF-beta homolog. *Science* **274**, 1389-1391 (1996); published online EpubNov 22 (

19. W. S. Schackwitz, T. Inoue, J. H. Thomas, Chemosensory Neurons Function in Parallel to Mediate a Pheromone Response in C. elegans. *Neuron* **17**, 719-728 (1996); published online Epub10// (10.1016/S0896-6273(00)80203-2).

20. W. Li, S. G. Kennedy, G. Ruvkun, daf-28 encodes a C. elegans insulin superfamily member that is regulated by environmental cues and acts in the DAF-2 signaling pathway. *Genes & development* **17**, 844-858 (2003); published online EpubApr 1 (10.1101/gad.1066503).

21. S. Honjoh, T. Yamamoto, M. Uno, E. Nishida, Signalling through RHEB-1 mediates intermittent fasting-induced longevity in C. elegans. *Nature* **457**, 726-730 (2009); published online EpubFeb 5 (10.1038/nature07583).

22. H. T. Schwartz, A protocol describing pharynx counts and a review of other assays of apoptotic cell death in the nematode worm Caenorhabditis elegans. *Nat. Protocols* **2**, 705-714 (2007); published online Epub03//print (

23. R. Pulak, Techniques for analysis, sorting, and dispensing of C. elegans on the COPAS flow-sorting system. *Methods in molecular biology (Clifton, N.J.)* **351**, 275-286 (2006); published online Epub/ (

24. M. O. Casanueva, A. Burga, B. Lehner, Fitness trade-offs and environmentally induced mutation buffering in isogenic C. elegans. *Science* **335**, 82-85 (2012); published online EpubJan 6 (10.1126/science.1213491).

25. S. L. Rea, D. Wu, J. R. Cypser, J. W. Vaupel, T. E. Johnson, A stress-sensitive reporter predicts longevity in isogenic populations of Caenorhabditis elegans. *Nature genetics* **37**, 894-898 (2005); published online EpubAug (10.1038/ng1608).

26. E. L. Greer, A. Brunet, Different dietary restriction regimens extend lifespan by both independent and overlapping genetic pathways in C. elegans. *Aging cell* **8**, 113-127 (2009).

27. M. Zhan, L. Chingozha, H. Lu, Enabling Systems Biology Approaches Through Microfabricated Systems. *Analytical Chemistry* **85**, 8882-8894 (2013); published online Epub2013/10/01 (10.1021/ac401472y).

28. D. C. Duffy, J. C. McDonald, O. J. Schueller, G. M. Whitesides, Rapid prototyping of microfluidic systems in poly (dimethylsiloxane). *Analytical chemistry* **70**, 4974-4984 (1998).

29. J. C. McDonald, G. M. Whitesides, Poly (dimethylsiloxane) as a material for fabricating microfluidic devices. *Accounts of chemical research* **35**, 491-499 (2002).

30. M. A. Unger, H.-P. Chou, T. Thorsen, A. Scherer, S. R. Quake, Monolithic Microfabricated Valves and Pumps by Multilayer Soft Lithography. *Science* **288**, 113-116 (2000); published online EpubApril 7, 2000 (10.1126/science.288.5463.113).

31. H.-P. Chou, M. A. Unger, S. R. Quake, A microfabricated rotary pump. *Biomedical Microdevices* **3**, 323-330 (2001).

32. K. Chung, M. M. Crane, H. Lu, Automated on-chip rapid microscopy, phenotyping and sorting of C. elegans. *Nature methods* **5**, 637-643 (2008); published online EpubJul (10.1038/nmeth.1227).

33. C. B. Rohde, F. Zeng, R. Gonzalez-Rubio, M. Angel, M. F. Yanik, Microfluidic system for on-chip high-throughput whole-animal sorting and screening at

subcellular resolution. *Proceedings of the National Academy of Sciences of the United States of America* **104**, 13891-13895 (2007); published online EpubAug 28 (10.1073/pnas.0706513104).

34. T. V. Chokshi, A. Ben-Yakar, N. Chronis, CO2 and compressive immobilization of C. elegans on-chip. *Lab on a chip* **9**, 151-157 (2009); published online EpubJan 7 (10.1039/b807345g).

35. C. L. Gilleland, C. B. Rohde, F. Zeng, M. F. Yanik, Microfluidic immobilization of physiologically active Caenorhabditis elegans. *Nat. Protocols* **5**, 1888-1902 (2010); published online Epub11//print (

36. F. Zeng, C. B. Rohde, M. F. Yanik, Sub-cellular precision on-chip small-animal immobilization, multi-photon imaging and femtosecond-laser manipulation. *Lab on a chip* **8**, 653-656 (2008); published online EpubMay (10.1039/b804808h).

37. M. M. Crane, J. N. Stirman, C.-Y. Ou, P. T. Kurshan, J. M. Rehg, K. Shen, H. Lu, Autonomous screening of C. elegans identifies genes implicated in synaptogenesis. *Nature methods* **9**, 977-980 (2012).

38. I. Caceres, N. Valmas, M. A. Hilliard, H. Lu, Laterally orienting C. elegans using geometry at microscale for high-throughput visual screens in neurodegeneration and neuronal development studies. *PloS one* **7**, e35037 (2012)10.1371/journal.pone.0035037).

39. T. V. Chokshi, D. Bazopoulou, N. Chronis, An automated microfluidic platform for calcium imaging of chemosensory neurons in Caenorhabditis elegans. *Lab on a chip* **10**, 2758-2763 (2010); published online EpubOct 21 (10.1039/c004658b).

40. N. Chronis, M. Zimmer, C. I. Bargmann, Microfluidics for in vivo imaging of neuronal and behavioral activity in Caenorhabditis elegans. *Nature methods* **4**, 727-731 (2007); published online EpubSep (10.1038/nmeth1075).

41. S. R. Lockery, K. J. Lawton, J. C. Doll, S. Faumont, S. M. Coulthard, T. R. Thiele, N. Chronis, K. E. McCormick, M. B. Goodman, B. L. Pruitt, Artificial dirt: microfluidic substrates for nematode neurobiology and behavior. *Journal of neurophysiology* **99**, 3136-3143 (2008).

42. D. R. Albrecht, C. I. Bargmann, High-content behavioral analysis of Caenorhabditis elegans in precise spatiotemporal chemical environments. *Nature methods* **8**, 599-605 (2011).

43. J. Larsch, D. Ventimiglia, C. I. Bargmann, D. R. Albrecht, High-throughput imaging of neuronal activity in Caenorhabditis elegans. *Proceedings of the National Academy of Sciences of the United States of America* **110**, E4266-4273 (2013); published online EpubNov 5 (10.1073/pnas.1318325110).

44. S. E. Hulme, S. S. Shevkoplyas, A. P. McGuigan, J. Apfeld, W. Fontana, G. M. Whitesides, Lifespan-on-a-chip: microfluidic chambers for performing lifelong observation of C. elegans. *Lab on a chip* **10**, 589-597 (2010); published online EpubMar 7 (10.1039/b919265d).

45. J. Krajniak, H. Lu, Long-term high-resolution imaging and culture of C. elegans in chip-gel hybrid microfluidic device for developmental studies. *Lab on a chip* **10**, 1862-1868 (2010); published online EpubJul 21 (10.1039/c001986k).

46. H. Wen, W. Shi, J. Qin, Multiparameter evaluation of the longevity in C. elegans under stress using an integrated microfluidic device. *Biomedical microdevices* **14**, 721-728 (2012).

47. A. E. Carpenter, T. R. Jones, M. R. Lamprecht, C. Clarke, I. H. Kang, O. Friman, D. A. Guertin, J. H. Chang, R. A. Lindquist, J. Moffat, CellProfiler: image analysis software for identifying and quantifying cell phenotypes. *Genome biology* **7**, R100 (2006).

48. C. Wählby, L. Kamentsky, Z. H. Liu, T. Riklin-Raviv, A. L. Conery, E. J. O'Rourke, K. L. Sokolnicki, O. Visvikis, V. Ljosa, J. E. Irazoqui, An image analysis toolbox for high-throughput C. elegans assays. *Nature methods* **9**, 714-716 (2012).

49. C. A. Schneider, W. S. Rasband, K. W. Eliceiri, NIH Image to ImageJ: 25 years of image analysis. *Nature methods* **9**, 671-675 (2012).

50. C. Restif, C. Ibáñez-Ventoso, M. M. Vora, S. Guo, D. Metaxas, M. Driscoll, CeleST: Computer Vision Software for Quantitative Analysis of <italic>C. elegans</italic> Swim Behavior Reveals Novel Features of Locomotion. *PLoS Comput Biol* **10**, e1003702 (2014)10.1371/journal.pcbi.1003702).

51. N. A. Swierczek, A. C. Giles, C. H. Rankin, R. A. Kerr, High-throughput behavioral analysis in C. elegans. *Nature methods* **8**, 592-598 (2011).

52. D. Ramot, B. E. Johnson, T. L. Berry Jr, L. Carnell, M. B. Goodman, The Parallel Worm Tracker: a platform for measuring average speed and drug-induced paralysis in nematodes. *PloS one* **3**, e2208 (2008).

53. N. Kwon, J. Pyo, S.-J. Lee, J. H. Je, 3-D worm tracker for freely moving C. elegans. *PloS one* **8**, e57484 (2013).

54. M. M. Crane, K. Chung, H. Lu, Computer-enhanced high-throughput genetic screens of C. elegans in a microfluidic system. *Lab on a chip* **9**, 38-40 (2009); published online EpubJan 7 (10.1039/b813730g).

55. A. San-Miguel, H. Lu, Microfluidics as a tool for C. elegans research. *WormBook : the online review of C. elegans biology*, 1-19 (2013)10.1895/wormbook.1.162.1).

56. M. Baker, Digital PCR hits its stride. *Nature methods* **9**, 541 (2012).

57. M. Schwertner, M. Booth, M. Neil, T. Wilson, Measurement of specimen-induced aberrations of biological samples using phase stepping interferometry. *Journal of microscopy* **213**, 11-19 (2004).

58. S. Hell, G. Reiner, C. Cremer, E. H. K. Stelzer, Aberrations in confocal fluorescence microscopy induced by mismatches in refractive index. *Journal of Microscopy* **169**, 391-405 (1993)10.1111/j.1365-2818.1993.tb03315.x).

59. M. J. Booth, M. Neil, T. Wilson, Aberration correction for confocal imaging in refractive-index-mismatched media. *Journal of Microscopy* **192**, 90-98 (1998).

60. Z. Wang, A. A. Volinsky, N. D. Gallant, Crosslinking effect on polydimethylsiloxane elastic modulus measured by custom-built compression instrument. *Journal of Applied Polymer Science* **131**, (2014).

61. A. R. Abate, J. J. Agresti, D. A. Weitz, Microfluidic sorting with high-speed single-layer membrane valves. *Applied Physics Letters* **96**, 203509 (2010).

62. S. Lee, J. C. Chan, K. Maung, E. Rezler, N. Sundararajan, Characterization of laterally deformable elastomer membranes for microfluidics. *Journal of Micromechanics and Microengineering* **17**, 843 (2007).

63. N. Sundararajan, D. Kim, A. A. Berlin, Microfluidic operations using deformable polymer membranes fabricated by single layer soft lithography. *Lab on a chip* **5**, 350-354 (2005).

64. M. M. Crane, Automated quantitative phenotyping and high-throughput screening in c. elegans using microfluidics and computer vision. (2011).

65. H. Lee, M. M. Crane, Y. Zhang, H. Lu, Quantitative screening of genes regulating tryptophan hydroxylase transcription in Caenorhabditis elegans using microfluidics and an adaptive algorithm. *Integrative Biology* **5**, 372-380 (2013).

66. S. W. Hell, Toward fluorescence nanoscopy. *Nature biotechnology* **21**, 1347-1355 (2003).

67. P. Török, S. Hewlett, P. Varga, The role of specimen-induced spherical aberration in confocal microscopy. *Journal of microscopy* **188**, 158-172 (1997).

68. W. E. Brant, C. A. Helms, *Fundamentals of diagnostic radiology*. (Lippincott Williams & Wilkins, 2012).

69. L. Fenno, O. Yizhar, K. Deisseroth, The development and application of optogenetics. *Annual review of neuroscience* **34**, 389-412 (2011).

70. A. E. Palmer, Y. Qin, J. G. Park, J. E. McCombs, Design and application of genetically encoded biosensors. *Trends in biotechnology* **29**, 144-152 (2011).

71. K. W. Eliceiri, M. R. Berthold, I. G. Goldberg, L. Ibanez, B. S. Manjunath, M. E. Martone, R. F. Murphy, H. Peng, A. L. Plant, B. Roysam, N. Stuurman, J. R. Swedlow, P. Tomancak, A. E. Carpenter, Biological imaging software tools. *Nat Meth* **9**, 697-710 (2012); published online Epub07//print (

72. V. Ljosa, K. L. Sokolnicki, A. E. Carpenter, Annotated high-throughput microscopy image sets for validation. *Nat Meth* **9**, 637-637 (2012); published online Epub07//print (

73. M. Sonka, V. Hlavac, R. Boyle, *Image processing, analysis, and machine vision*. (Cengage Learning, 2014).

74. A. Ben-Hur, C. S. Ong, S. Sonnenburg, B. Schölkopf, G. Rätsch, Support vector machines and kernels for computational biology. *PLoS computational biology* **4**, e1000173 (2008).

75. L. Shamir, J. D. Delaney, N. Orlov, D. M. Eckley, I. G. Goldberg, Pattern recognition software and techniques for biological image analysis. *PLoS computational biology* **6**, e1000974 (2010).

76. D. Zhang, G. Lu, Review of shape representation and description techniques. *Pattern recognition* **37**, 1-19 (2004).

77. C.-C. Chang, C.-J. Lin, LIBSVM: a library for support vector machines. *ACM Transactions on Intelligent Systems and Technology (TIST)* **2**, 27 (2011).

78. J. N. Stirman, M. M. Crane, S. J. Husson, S. Wabnig, C. Schultheis, A. Gottschalk, H. Lu, Real-time multimodal optical control of neurons and muscles in freely behaving Caenorhabditis elegans. *Nature methods* **8**, 153-158 (2011).

79. A. M. Leifer, C. Fang-Yen, M. Gershow, M. J. Alkema, A. D. Samuel, Optogenetic manipulation of neural activity in freely moving Caenorhabditis elegans. *Nature methods* **8**, 147-152 (2011).

80. U. T. Brunk, A. Terman, Lipofuscin: mechanisms of age-related accumulation and influence on cell function. *Free radical biology & medicine* **33**, 611-619 (2002); published online EpubSep 1 (

81. L. Avery, J. H. Thomas, in *C. elegans II*, B. T. Riddle DL, Meyer BJ, et al., Ed. (Cold Spring Harbor Laboratory Press, Cold Spring Harbor, NY, 1997), chap. 24.

82. C.-W. Hsu, C.-C. Chang, C.-J. Lin. (2003).

83. J. G. White, E. Southgate, J. N. Thomson, S. Brenner, The structure of the nervous system of the nematode Caenorhabditis elegans. *Philosophical Transactions of the Royal Society of London. B, Biological Sciences* **314**, 1-340 (1986).

84. E. R. Troemel, B. E. Kimmel, C. I. Bargmann, Reprogramming chemotaxis responses: sensory neurons define olfactory preferences in C. elegans. *Cell* **91**, 161-169 (1997).

85. A. Cornils, M. Gloeck, Z. Chen, Y. Zhang, J. Alcedo, Specific insulin-like peptides encode sensory information to regulate distinct developmental processes. *Development* **138**, 1183-1193 (2011).

86. C. I. Bargmann, H. R. HORvITZ, Control of larval development by chemosensory neurons in Caenorhabditis elegans. *Science* **251**, 1243-1246 (1991).

87. T.-F. Wu, C.-J. Lin, R. C. Weng, Probability estimates for multi-class classification by pairwise coupling. *The Journal of Machine Learning Research* **5**, 975-1005 (2004).

88. M. A. Bray, A. N. Fraser, T. P. Hasaka, A. E. Carpenter, Workflow and metrics for image quality control in large-scale high-content screens. *Journal of biomolecular screening* **17**, 266-274 (2012); published online EpubFeb (10.1177/1087057111420292).

89. T. Stiernagle, Maintenance of C. elegans. *WormBook : the online review of C. elegans biology*, 1-11 (2006)10.1895/wormbook.1.101.1).

90. E. R. Dougherty, R. A. Lotufo, T. I. S. f. O. E. SPIE, *Hands-on morphological image processing*. (SPIE press Bellingham, 2003), vol. 71.

91. B. Scholkopft, K.-R. Mullert, Fisher discriminant analysis with kernels. *Neural networks for signal processing IX*, (1999).

92. E. J. Masoro, Overview of caloric restriction and ageing. *Mechanisms of ageing and development* **126**, 913-922 (2005).

93. N. A. Bishop, L. Guarente, Genetic links between diet and lifespan: shared mechanisms from yeast to humans. *Nature Reviews Genetics* **8**, 835-844 (2007).

94. D. A. Sinclair, Toward a unified theory of caloric restriction and longevity regulation. *Mechanisms of ageing and development* **126**, 987-1002 (2005).

95. S.-J. Lin, M. Kaeberlein, A. A. Andalis, L. A. Sturtz, P.-A. Defossez, V. C. Culotta, G. R. Fink, L. Guarente, Calorie restriction extends Saccharomyces cerevisiae lifespan by increasing respiration. *Nature* **418**, 344-348 (2002).

96. S.-J. Lin, P.-A. Defossez, L. Guarente, Requirement of NAD and SIR2 for life-span extension by calorie restriction in Saccharomyces cerevisiae. *Science* **289**, 2126-2128 (2000).

97. W. Mair, P. Goymer, S. D. Pletcher, L. Partridge, Demography of dietary restriction and death in Drosophila. *Science* **301**, 1731-1733 (2003).

98. L. Partridge, M. D. Piper, W. Mair, Dietary restriction in< i> Drosophila</i>. *Mechanisms of ageing and development* **126**, 938-950 (2005).

99. G. Walker, K. Houthoofd, J. R. Vanfleteren, D. Gems, Dietary restriction in< i> C. elegans</i>: From rate-of-living effects to nutrient sensing pathways. *Mechanisms of ageing and development* **126**, 929-937 (2005).

100. W. Mair, S. H. Panowski, R. J. Shaw, A. Dillin, Optimizing dietary restriction for genetic epistasis analysis and gene discovery in C. elegans. *PloS one* **4**, e4535 (2009).

101. R. Weindruch, R. L. Walford, Dietary restriction in mice beginning at 1 year of age: effect on life-span and spontaneous cancer incidence. *Science* **215**, 1415-1418 (1982).

102. R. Weindruch, R. L. Walford, S. Fligiel, D. Guthrie, The retardation of aging in mice by dietary restriction: longevity, cancer, immunity and lifetime energy intake. *J Nutr* **116**, 641-654 (1986).

103. I. Shimokawa, Y. Higami, G. B. Hubbard, C. A. McMahan, E. J. Masoro, B. P. Yu, Diet and the suitability of the male Fischer 344 rat as a model for aging research. *J Gerontol* **48**, B27-32 (1993); published online Epub1993/01// (

104. J. A. Mattison, G. S. Roth, T. M. Beasley, E. M. Tilmont, A. M. Handy, R. L. Herbert, D. L. Longo, D. B. Allison, J. E. Young, M. Bryant, Impact of caloric restriction on health and survival in rhesus monkeys from the NIA study. *Nature*, (2012).

105. N. L. Bodkin, T. M. Alexander, H. K. Ortmeyer, E. Johnson, B. C. Hansen, Mortality and morbidity in laboratory-maintained Rhesus monkeys and effects of long-term dietary restriction. *The Journals of Gerontology Series A: Biological Sciences and Medical Sciences* **58**, B212-B219 (2003).

106. R. J. Colman, R. M. Anderson, S. C. Johnson, E. K. Kastman, K. J. Kosmatka, T. M. Beasley, D. B. Allison, C. Cruzen, H. A. Simmons, J. W. Kemnitz, Caloric

restriction delays disease onset and mortality in rhesus monkeys. *Science* **325**, 201-204 (2009).

107. I. Messaoudi, J. Warner, M. Fischer, B. Park, B. Hill, J. Mattison, M. A. Lane, G. S. Roth, D. K. Ingram, L. J. Picker, Delay of T cell senescence by caloric restriction in aged long-lived nonhuman primates. *Proceedings of the National Academy of Sciences* **103**, 19448-19453 (2006).

108. M. Lane, D. Ingram, G. Roth, Calorie restriction in nonhuman primates: effects on diabetes and cardiovascular disease risk. *Toxicological Sciences* **52**, 41-48 (1999).

109. N. V. Patel, M. N. Gordon, K. E. Connor, R. A. Good, R. W. Engelman, J. Mason, D. G. Morgan, T. E. Morgan, C. E. Finch, Caloric restriction attenuates Abeta-deposition in Alzheimer transgenic models. *Neurobiol Aging* **26**, 995-1000 (2005); published online Epub2005/07// (10.1016/j.neurobiolaging.2004.09.014).

110. D. M. Kristan, Calorie restriction and susceptibility to intact pathogens. *Age (Dordr)* **30**, 147-156 (2008); published online Epub2008/09// (10.1007/s11357-008-9056-1).

111. L. Fontana, T. E. Meyer, S. Klein, J. O. Holloszy, Long-term calorie restriction is highly effective in reducing the risk for atherosclerosis in humans. *Proceedings of the National Academy of Sciences of the United States of America* **101**, 6659-6663 (2004).

112. T. E. Meyer, S. J. Kovács, A. A. Ehsani, S. Klein, J. O. Holloszy, L. Fontana, Long-term caloric restriction ameliorates the decline in diastolic function in humans. *Journal of the American College of Cardiology* **47**, 398-402 (2006).

113. A. Witte, M. Fobker, R. Gellner, S. Knecht, A. Flöel, Caloric restriction improves memory in elderly humans. *Proceedings of the National Academy of Sciences* **106**, 1255-1260 (2009).

114. J. F. Trepanowski, R. E. Canale, K. E. Marshall, M. M. Kabir, R. J. Bloomer, Impact of caloric and dietary restriction regimens on markers of health and longevity in humans and animals: a summary of available findings. *Nutr J* **10**, 107 (2011).

115. D. K. Ingram, M. Zhu, J. Mamczarz, S. Zou, M. A. Lane, G. S. Roth, R. DeCabo, Calorie restriction mimetics: an emerging research field. *Aging cell* **5**, 97-108 (2006).

116. E. L. Greer, D. Dowlatshahi, M. R. Banko, J. Villen, K. Hoang, D. Blanchard, S. P. Gygi, A. Brunet, An AMPK-FOXO Pathway Mediates Longevity Induced by a

Novel Method of Dietary Restriction in< i> C. elegans</i>. *Current biology* **17**, 1646-1656 (2007).

117. K. Jia, B. Levine, Autophagy is required for dietary restriction-mediated life span extension in C. elegans. *Autophagy* **3**, 597 (2007).

118. S. H. Panowski, S. Wolff, H. Aguilaniu, J. Durieux, A. Dillin, PHA-4/Foxa mediates diet-restriction-induced longevity of C. elegans. *Nature* **447**, 550-555 (2007).

119. K. A. Steinkraus, E. D. Smith, C. Davis, D. Carr, W. R. Pendergrass, G. L. Sutphin, B. K. Kennedy, M. Kaeberlein, Dietary restriction suppresses proteotoxicity and enhances longevity by an hsf-1-dependent mechanism in Caenorhabditis elegans. *Aging cell* **7**, 394-404 (2008).

120. D. Gems, S. Pletcher, L. Partridge, Interpreting interactions between treatments that slow aging. *Aging cell* **1**, 1-9 (2002)10.1046/j.1474-9728.2002.00003.x).

121. M. Hansen, A. Chandra, L. L. Mitic, B. Onken, M. Driscoll, C. Kenyon, A role for autophagy in the extension of lifespan by dietary restriction in C. elegans. *PLoS genetics* **4**, e24 (2008).

122. M. V. Blagosklonny, Calorie restriction: decelerating mTOR-driven aging from cells to organisms (including humans). *Cell cycle* **9**, 683-688 (2010).

123. D. Van Heemst, M. Beekman, S. P. Mooijaart, B. T. Heijmans, B. W. Brandt, B. J. Zwaan, P. E. Slagboom, R. G. Westendorp, Reduced insulin/IGF-1 signalling and human longevity. *Aging cell* **4**, 79-85 (2005).

124. S. Wullschleger, R. Loewith, M. N. Hall, TOR signaling in growth and metabolism. *Cell* **124**, 471-484 (2006).

125. S. Oldham, E. Hafen, Insulin/IGF and target of rapamycin signaling: a TOR de force in growth control. *Trends in cell biology* **13**, 79-85 (2003).

126. A. R. Saltiel, C. R. Kahn, Insulin signalling and the regulation of glucose and lipid metabolism. *Nature* **414**, 799-806 (2001).

127. M. Kaeberlein, Resveratrol and rapamycin: are they anti-aging drugs? *Bioessays* **32**, 96-99 (2010).

128. J. Y. Sze, M. Victor, C. Loer, Y. Shi, G. Ruvkun, Food and metabolic signalling defects in a Caenorhabditis elegans serotonin-synthesis mutant. *Nature* **403**, 560-564 (2000).

129. D. G. Albertson, J. Thomson, The pharynx of Caenorhabditis elegans. *Philosophical Transactions of the Royal Society of London. Series B, Biological Sciences*, 299-325 (1976).

130. J. D. Meisel, O. Panda, P. Mahanti, F. C. Schroeder, D. H. Kim, Chemosensation of Bacterial Secondary Metabolites Modulates Neuroendocrine Signaling and Behavior of C. elegans. *Cell* **159**, 267-280 (2014); published online EpubOct 9 (10.1016/j.cell.2014.09.011).

131. T. Noble, J. Stieglitz, S. Srinivasan, An Integrated Serotonin and Octopamine Neuronal Circuit Directs the Release of an Endocrine Signal to Control C. elegans Body Fat. *Cell Metabolism* **18**, 672-684 10.1016/j.cmet.2013.09.007).

132. Y. Zhang, H. Lu, C. I. Bargmann, Pathogenic bacteria induce aversive olfactory learning in Caenorhabditis elegans. *Nature* **438**, 179-184 (2005).

133. R. Pocock, O. Hobert, Hypoxia activates a latent circuit for processing gustatory information in C. elegans. *Nature neuroscience* **13**, 610-614 (2010).

134. A. J. Chang, N. Chronis, D. S. Karow, M. A. Marletta, C. I. Bargmann, A Distributed Chemosensory Circuit for Oxygen Preference in C. elegans. *PLoS Biol* **4**, e274 (2006)10.1371/journal.pbio.0040274).

135. Y. Qin, X. Zhang, Y. Zhang, A neuronal signaling pathway of CaMKII and Gqα regulates experience-dependent transcription of tph-1. *The Journal of Neuroscience* **33**, 925-935 (2013).

136. E. M. Myers, Gα_o and Gα_q Regulate the Expression of <italic>daf-7</italic>, a TGFβ-like Gene, in <italic>Caenorhabditis elegans</italic>. *PloS one* **7**, e40368 (2012)10.1371/journal.pone.0040368).

137. E. R. Greer, C. L. Pérez, M. R. Van Gilst, B. H. Lee, K. Ashrafi, Neural and Molecular Dissection of a< i> C. elegans</i> Sensory Circuit that Regulates Fat and Feeding. *Cell metabolism* **8**, 118-131 (2008).

138. S. D. Narasimhan, K. Yen, A. Bansal, E.-S. Kwon, S. Padmanabhan, H. A. Tissenbaum, PDP-1 links the TGF-β and IIS pathways to regulate longevity, development, and metabolism. *PLoS genetics* **7**, e1001377 (2011).

139. M. Sarov, S. Schneider, A. Pozniakovski, A. Roguev, S. Ernst, Y. Zhang, A. A. Hyman, A. F. Stewart, A recombineering pipeline for functional genomics applied to Caenorhabditis elegans. *Nature methods* **3**, 839-844 (2006).

140. C. Frokjaer-Jensen, M. W. Davis, C. E. Hopkins, B. J. Newman, J. M. Thummel, S. P. Olesen, M. Grunnet, E. M. Jorgensen, Single-copy insertion of transgenes in Caenorhabditis elegans. *Nature genetics* **40**, 1375-1383 (2008); published online EpubNov (10.1038/ng.248).

141. T.-T. Ching, A.-L. Hsu, Solid Plate-based Dietary Restriction in Caenorhabditis elegans. *Journal of visualized experiments: JoVE*, (2011).

142. H. Hsin, C. Kenyon, Signals from the reproductive system regulate the lifespan of C. elegans. *Nature* **399**, 362-366 (1999); published online EpubMay 27 (10.1038/20694).

143. K. Lin, H. Hsin, N. Libina, C. Kenyon, Regulation of the Caenorhabditis elegans longevity protein DAF-16 by insulin/IGF-1 and germline signaling. *Nature genetics* **28**, 139-145 (2001).

144. L. Aitlhadj, S. R. Stürzenbaum, The use of FUdR can cause prolonged longevity in mutant nematodes. *Mechanisms of ageing and development* **131**, 364-365 (2010).

145. K. C.-C. Cheng, R. Klancer, A. Singson, G. Seydoux, Regulation of MBK-2/DYRK by CDK-1 and the pseudophosphatases EGG-4 and EGG-5 during the oocyte-to-embryo transition. *Cell* **139**, 560-572 (2009).

146. J. M. Parry, N. V. Velarde, A. J. Lefkovith, M. H. Zegarek, J. S. Hang, J. Ohm, R. Klancer, R. Maruyama, M. K. Druzhinina, B. D. Grant, EGG-4 and EGG-5 Link Events of the Oocyte-to-Embryo Transition with Meiotic Progression in< i> C. elegans</i>. *Current Biology* **19**, 1752-1757 (2009).

147. P. Dayan, L. Abbott, Theoretical neuroscience: computational and mathematical modeling of neural systems. *Journal of Cognitive Neuroscience* **15**, 154-155 (2003).

148. C. F. Glenn, D. K. Chow, L. David, C. A. Cooke, M. S. Gami, W. B. Iser, K. B. Hanselman, I. G. Goldberg, C. A. Wolkow, Behavioral deficits during early stages of aging in Caenorhabditis elegans result from locomotory deficits possibly linked to muscle frailty. *The Journals of Gerontology Series A: Biological Sciences and Medical Sciences* **59**, 1251-1260 (2004).

149. Z. Pincus, T. Smith-Vikos, F. J. Slack, MicroRNA predictors of longevity in Caenorhabditis elegans. *PLoS genetics* **7**, e1002306 (2011).

150. C. Huang, C. Xiong, K. Kornfeld, Measurements of age-related changes of physiological processes that predict lifespan of Caenorhabditis elegans. *Proceedings of the National Academy of Sciences of the United States of America* **101**, 8084-8089 (2004).

151. J. J. Collins, C. Huang, S. Hughes, K. Kornfeld, The measurement and analysis of age-related changes in Caenorhabditis elegans. *WormBook : the online review of C. elegans biology*, 1-21 (2008)10.1895/wormbook.1.137.1).

152. R. Hosono, Age dependent changes in the behavior of Caenorhabditis elegans on attraction to Escherichia coli. *Experimental gerontology* **13**, 31-36 (1978); published online Epub// (http://dx.doi.org/10.1016/0531-5565(78)90027-X).

153. R. Hosono, Y. Sato, S.-I. Aizawa, Y. Mitsui, Age-dependent changes in mobility and separation of the nematode Caenorhabditis elegans. *Experimental gerontology* **15**, 285-289 (1980); published online Epub// (http://dx.doi.org/10.1016/0531-5565(80)90032-7).

154. T. E. Johnson, Aging can be genetically dissected into component processes using long-lived lines of Caenorhabditis elegans. *Proceedings of the National Academy of Sciences* **84**, 3777-3781 (1987); published online EpubJune 1, 1987 (

155. S. Ward, Chemotaxis by the nematode Caenorhabditis elegans: identification of attractants and analysis of the response by use of mutants. *Proceedings of the National Academy of Sciences* **70**, 817-821 (1973).

156. D. B. Dusenbery, Responses of the nematodeCaenorhabditis elegans to controlled chemical stimulation. *Journal of comparative physiology* **136**, 327-331 (1980).

157. R. Kerr, V. Lev-Ram, G. Baird, P. Vincent, R. Y. Tsien, W. R. Schafer, Optical Imaging of Calcium Transients in Neurons and Pharyngeal Muscle of< i> C. elegans</i>. *Neuron* **26**, 583-594 (2000).

158. W. S. Ryu, A. D. Samuel, Thermotaxis in Caenorhabditis elegans analyzed by measuring responses to defined thermal stimuli. *The Journal of neuroscience* **22**, 5727-5733 (2002).

159. L. Luo, C. V. Gabel, H.-I. Ha, Y. Zhang, A. D. Samuel, Olfactory behavior of swimming C. elegans analyzed by measuring motile responses to temporal variations of odorants. *Journal of neurophysiology* **99**, 2617-2625 (2008).

160. W. Shi, H. Wen, Y. Lu, Y. Shi, B. Lin, J. Qin, Droplet microfluidics for characterizing the neurotoxin-induced responses in individual Caenorhabditis elegans. *Lab on a chip* **10**, 2855-2863 (2010).

161. J. A. Carr, A. Parashar, R. Gibson, A. P. Robertson, R. J. Martin, S. Pandey, A microfluidic platform for high-sensitivity, real-time drug screening on C. elegans and parasitic nematodes. *Lab on a chip* **11**, 2385-2396 (2011).

162. S. J. Husson, W. S. Costa, C. Schmitt, A. Gottschalk, Keeping track of worm trackers. *WormBook : the online review of C. elegans biology*, 1-17 (2012)10.1895/wormbook.1.156.1).

163. K. Chung, M. Zhan, J. Srinivasan, P. W. Sternberg, E. Gong, F. C. Schroeder, H. Lu, Microfluidic chamber arrays for whole-organism behavior-based chemical screening. *Lab on a chip* **11**, 3689-3697 (2011).

164. J. T. Pierce-Shimomura, T. M. Morse, S. R. Lockery, The fundamental role of pirouettes in Caenorhabditis elegans chemotaxis. *The journal of neuroscience* **19**, 9557-9569 (1999).

165. J. T. Pierce-Shimomura, M. Dores, S. R. Lockery, Analysis of the effects of turning bias on chemotaxis in C. elegans. *Journal of experimental biology* **208**, 4727-4733 (2005).

166. A. C. Miller, T. R. Thiele, S. Faumont, M. L. Moravec, S. R. Lockery, Step-response analysis of chemotaxis in Caenorhabditis elegans. *The journal of neuroscience* **25**, 3369-3378 (2005).

167. Y. Iino, K. Yoshida, Parallel use of two behavioral mechanisms for chemotaxis in Caenorhabditis elegans. *The Journal of Neuroscience* **29**, 5370-5380 (2009).

168. C. Dulac, A. T. Torello, Molecular detection of pheromone signals in mammals: from genes to behaviour. *Nature Reviews Neuroscience* **4**, 551-562 (2003).

169. A. Camilli, B. L. Bassler, Bacterial small-molecule signaling pathways. *Science* **311**, 1113-1116 (2006).

170. J. M. Simon, P. W. Sternberg, Evidence of a mate-finding cue in the hermaphrodite nematode Caenorhabditis elegans. *Proceedings of the National Academy of Sciences* **99**, 1598-1603 (2002).

171. J. Srinivasan, F. Kaplan, R. Ajredini, C. Zachariah, H. T. Alborn, P. E. Teal, R. U. Malik, A. S. Edison, P. W. Sternberg, F. C. Schroeder, A blend of small molecules regulates both mating and development in Caenorhabditis elegans. *Nature* **454**, 1115-1118 (2008).

172. M. M. Barr, L. R. Garcia, Male mating behavior. *WormBook : the online review of C. elegans biology*, 1-11 (2006)10.1895/wormbook.1.78.1).

173. C. J. Cronin, J. E. Mendel, S. Mukhtar, Y.-M. Kim, R. C. Stirbl, J. Bruck, P. W. Sternberg, An automated system for measuring parameters of nematode sinusoidal movement. *BMC genetics* **6**, 5 (2005).

174. K. Hoshi, R. Shingai, Computer-driven automatic identification of locomotion states in< i> Caenorhabditis elegans</i>. *Journal of neuroscience methods* **157**, 355-363 (2006).

175. K.-M. Huang, P. Cosman, W. R. Schafer, Machine vision based detection of omega bends and reversals in< i> C. elegans</i>. *Journal of neuroscience methods* **158**, 323-336 (2006).

176. C. Pungaliya, J. Srinivasan, B. W. Fox, R. U. Malik, A. H. Ludewig, P. W. Sternberg, F. C. Schroeder, A shortcut to identifying small molecule signals that

regulate behavior and development in Caenorhabditis elegans. *Proceedings of the National Academy of Sciences* **106**, 7708-7713 (2009).

177. J. W. Golden, D. L. Riddle, The< i> Caenorhabditis elegans</i> dauer larva: Developmental effects of pheromone, food, and temperature. *Developmental biology* **102**, 368-378 (1984).

178. J. W. Golden, D. L. Riddle, A pheromone-induced developmental switch in Caenorhabditis elegans: Temperature-sensitive mutants reveal a wild-type temperature-dependent process. *Proceedings of the National Academy of Sciences* **81**, 819-823 (1984).

179. J. Q. White, T. J. Nicholas, J. Gritton, L. Truong, E. R. Davidson, E. M. Jorgensen, The Sensory Circuitry for Sexual Attraction in< i> C. elegans</i> Males. *Current Biology* **17**, 1847-1857 (2007).

180. C. J. Kenyon, The genetics of ageing. *Nature* **464**, 504-512 (2010).

181. A. Antebi, Genetics of aging in Caenorhabditis elegans. *PLoS genetics* **3**, e129 (2007).

182. C. Kenyon, The first long-lived mutants: discovery of the insulin/IGF-1 pathway for ageing. *Philosophical Transactions of the Royal Society B: Biological Sciences* **366**, 9-16 (2011).

183. D. Crawford, N. Libina, C. Kenyon, Caenorhabditis elegans integrates food and reproductive signals in lifespan determination. *Aging cell* **6**, 715-721 (2007); published online EpubOct (10.1111/j.1474-9726.2007.00327.x).

184. D. Dalfó, D. Michaelson, E. J. A. Hubbard, Sensory regulation of the C. elegans germline through TGF-β-dependent signaling in the niche. *Current biology : CB* **22**, 712-719 (2012)10.1016/j.cub.2012.02.064).

185. A. Ghazi, S. Henis-Korenblit, C. Kenyon, A Transcription Elongation Factor That Links Signals from the Reproductive System to Lifespan Extension in <italic>Caenorhabditis elegans</italic>. *PLoS Genet* **5**, e1000639 (2009)10.1371/journal.pgen.1000639).

186. A. Mukhopadhyay, H. A. Tissenbaum, Reproduction and longevity: secrets revealed by C. elegans. *Trends in Cell Biology* **17**, 65-71 (2007); published online Epub2// (10.1016/j.tcb.2006.12.004).

187. M. Tatar, Regulation of Aging by Germline Stem Cells. *Sci. Aging Knowl. Environ.* **2002**, pe2- (2002); published online EpubJanuary 23, 2002 (10.1126/sageke.2002.3.pe2).

188. N. Stroustrup, B. E. Ulmschneider, Z. M. Nash, I. F. López-Moyado, J. Apfeld, W. Fontana, The Caenorhabditis elegans lifespan machine. *Nature methods* **10**, 665-670 (2013).

189. B. Xian, J. Shen, W. Chen, N. Sun, N. Qiao, D. Jiang, T. Yu, Y. Men, Z. Han, Y. Pang, WormFarm: a quantitative control and measurement device toward automated Caenorhabditis elegans aging analysis. *Aging cell* **12**, 398-409 (2013).

190. X.-B. Zhang, Z.-Q. Wu, K. Wang, J. Zhu, J.-J. Xu, X.-H. Xia, H.-Y. Chen, Gravitational Sedimentation Induced Blood Delamination for Continuous Plasma Separation on a Microfluidics Chip. *Analytical Chemistry* **84**, 3780-3786 (2012); published online Epub2012/04/17 (10.1021/ac3003616).

191. A. D. Stroock, S. K. Dertinger, A. Ajdari, I. Mezić, H. A. Stone, G. M. Whitesides, Chaotic mixer for microchannels. *Science* **295**, 647-651 (2002).

192. R. Barrer, H. Chio, in *Journal of Polymer Science Part C: Polymer Symposia*. (Wiley Online Library, 1965), vol. 10, pp. 111-138.

193. T. Liu, D. Cai, *Counterbalance between BAG and URX neurons via guanylate cyclases controls lifespan homeostasis in C. elegans*. (2013), vol. 32, pp. 1529-1542.

194. K. Lüersen, U. Faust, D.-C. Gottschling, F. Döring, Gait-specific adaptation of locomotor activity in response to dietary restriction in Caenorhabditis elegans. *The Journal of experimental biology*, jeb. 099382 (2014).

195. A. Del Campo, C. Greiner, SU-8: a photoresist for high-aspect-ratio and 3D submicron lithography. *Journal of Micromechanics and Microengineering* **17**, R81 (2007).

196. A. Mata, A. Fleischman, S. Roy, Characterization of Polydimethylsiloxane (PDMS) Properties for Biomedical Micro/Nanosystems. *Biomedical Microdevices* **7**, 281-293 (2005); published online Epub2005/12/01 (10.1007/s10544-005-6070-2).